UILU-ENG 92-3602

Report No. 161

FATIGUE AND STRESS ANALYSES OF ROLLING CONTACT

A Collection of Reports

prepared for
Association of American Railroads
1990–1991

by

Y. Roger Jiang
and
Huseyin Sehitoglu

A Report of the

MATERIALS ENGINEERING—MECHANICAL BEHAVIOR

College of Engineering, University of Illinois at Urbana-Champaign

February 1992

Contact Fatigue Life Prediction Methods

Y. Roger Jiang
and
Huseyin Sehitoglu

Report No.1 prepared for
Association of American Railroads

March 1990

Report No. 1 prepared for Association of American Railroads

Contact Fatigue Life Prediction Methods

Huseyin Sehitoglu, Associate Professor
Roger Jiang, Research Assistant
Department of Mechanical and Industrial Engineering
University of Illinois at Urbana-Champaign
1206 West Green Street
Urbana, IL 61801

Abstract

Contact fatigue life estimates are reported using four different multiaxial fatigue criteria. The first class of models is characterized by second invariant of deviatoric stress amplitude or maximum shear stress amplitude modified by the hydrostatic stresses. The second class of models is based on the critical plane approach incorporating the shear stress range or shear strain range and the normal stresses and strains on the critical plane. The predicted lives are reported over several p_o/σ'_y ratios in the range 1 to 3 (peak Hertzian pressure normalized by yield strength) and q/p (shear to normal traction) ratios in the range 0 to 0.4. Depending on the model the estimated fatigue lives varied with q/p ratio from 0 to 0.4, in the range 10^2 to 10^9 cycles. The limitations of these models in handling both the compressive normal stresses and the non-proportionality of normal and shear stress components are discussed. The distinction is made between cases where the shear stress direction is fixed in the critical plane and the situations when the shear stress vector may vary within the critical plane. The fundamental differences between subsurface versus surface crack initiation and the influence of plastic deformation on the results are discussed.

Nomenclature

a	Half Contact Patch
α,β	Euler angles used to describe the orientation of any plane
α', β'	Constants in Crossland-Sines Criteria
$\Delta\gamma$	Shear Strain Range on the critical plane
$\Delta\varepsilon_n$	Normal strain range on the critical plane
$\Delta\tau_{xz}$	Orthogonal Shear Stress Range
$\Delta\tau^Q_{max}$	Maximum shear stress range on an arbitrary plane Q
$\Delta\tau_{max}$	Maximum shear stress range on the critical plane, the largest shear stress range in the body obtained by surveying all possible planes Q.
$\varepsilon_1,\varepsilon_2,\varepsilon_3$	Principal Strains
ε_n	Normal strain amplitude on the critical plane
γ	Shear strain amplitude on the critical plane
J_1,J_2	First and Second Invariant of Deviatoric Stress
$(J_2)^{1/2}_{alt}$	Alternating component of J_2
$(J_1)_{stat}$	Static or mean value of J_1
μ	Poisson's Ratio
n	Unit normal on an arbitrary plane Q
N_f	Cycles to Failure
p_o, q_o	Hertzian peak normal and shear tractions respectively
p, q	Normal and shear tractions on the contact patch
$\sigma_x,\sigma_y,\sigma_z,\tau_{xz}$	Orthogonal Stresses
σ,τ	Normal and shear stresses on an arbitrary plane Q at a given time
$\sigma_1,\sigma_2,\sigma_3$	Principal Stresses
σ'_y	Yield Strength (=430MPa)
σ_n	Mean stress on the critical plane
σ_{na}	Normal stress amplitude on the critical plane
σ_{nmax}	Maximum normal stress on the critical plane
τ_a	Shear stress amplitude on the critical plane
τ_{max}	Maximum shear stress obtained in the body obtained by surveying all possible planes Q
τ^Q_{max}	Maximum Shear Stress on an arbitrary plane Q
$\tau_1,\tau_2,\tau_3,\tau_4$	Shear Stress Vectors at times 1,2,3,4 on an arbitrary plane Q

Introduction

Wheel shelling is believed to occur as a result of rolling contact fatigue. Spalling is believed to be due to coalescence of thermal cracks under rolling contact loading and thermal loading resulting in loss of material. Under rolling contact loading conditions the material suffers from reversed shear superimposed with compressive mean normal stresses. It is difficult to simulate these conditions in the laboratory specimens yet the multiaxial fatigue models designed for compressive mean stresses are needed.

Under rolling contact fatigue conditions of two bodies, the normal stresses in the vicinity of the contact patch are highly compressive. This is evident from the early work of Hertz [1] , Razimovsky [2] and are summarized in the text Contact Mechanics by K.L.Johnson[3]. In the presence of shear tractions, tensile normal stresses in the tangential direction develop.

Smith and Liu [4] determined the magnitude of maximum shear stress and discussed the variation of shear stress direction with time on the plane of maximum shear stress. Furthermore, they illustrated graphically how the range of maximum shear stress on a plane is determined. Their work quantified the influence of tangential tractions on increasing the maximum shear stress and on moving the location of the maximum shear stress to the surface. Their results noted the presence of tensile normal stress on the surface of the contact when there are combined normal and tangential tractions. Kannel and Tevaarwerk [5] performed a similar analysis. However their results are not in agreement with Smith and Liu [4]. Furthermore, their conclusions that the maximum shear stress range occurs beneath the surface on the orthogonal plane irrespective of shear tractions is contradictory to the results presented in our study. In the presence of tangential tractions, the plane of maximum shear stress range differs from the orthogonal plane.
Smith and Liu [4] provide the stress history of a material element as the normal plus tangential contact load approaches the material point, reaches the material point and passes the material point. These results indicate that the deformation history of an element at the surface and below the surface is non-proportional. Under non-proportional loading the plane of maximum

shear stress usually rotates as the wheel rolls over the rail. The critical plane where crack nucleation would occur is not known a priori. The orientation of the critical plane needs to be determined and damage on this plane or lifetime needs to be predicted.

Despite many studies in fatigue and in multiaxial fatigue, the understanding of crack nucleation under reversed shear loading superimposed with compressive mean normal stresses is not developed. Early experiments studied the effect of tensile mean (normal) stresses on fatigue [6-8]. Tensile stresses on the crack(critical) plane facilitated shear growth by providing a Mode I type opening hence decreasing the asperity contact of crack surfaces. The mechanism of growth when the normal stresses are highly compressive is not very well known.

In certain class of materials, crack nucleation and growth is confined to well defined planes called 'critical plane'. The critical plane defined by Stulen Cummins Findley is the plane where the linear combination of shear stress range and normal stress range reaches a maximum value. The relationship proposed by Stulen-Cummins-Findley [9-11] included a shear stress term determined for the critical plane with the normal stress on the plane having a modifying influence. These models have been modified using strain based approaches by Miller and co-workers [7] and Socie and co-workers [8,12-13] who defined the critical plane as the plane of maximum shear stress or shear strain range.

On the other hand, models exist that utilize shear stress range and normal stress range averaged over all the planes in the material. The model proposed by Crossland-Sines [14-16] and other equivalent stress[17] approaches fall into this category and are designated as bulk damage models.

In this study, analysis of shear stresses and compressive stresses under wheel-rail contact conditions will be considered. We will consider (a) normal Hertzian loading and (b) combined normal and shear tractions. Fatigue lives will be determined using critical plane models and bulk fatigue models.

Contact Stress Analysis

The line contact of width 2a is considered in this study. The coordinate system and the orthogonal stresses are indicated in Fig.1. Both normal and tangential loads are assumed to vary over the area of contact in the following form,

$$p=-p_o\sqrt{1-\frac{x^2}{a^2}} \quad ; \quad q = f \cdot p$$

where p_o denotes the peak Hertzian pressure and q is the shear traction, f is the ratio of shear to normal tractions. The shear traction variation is proportional to normal load variation. Plane strain -elastic deformations are considered.

Shear Stress Variation on a Plane

Representation of an arbitrary plane Q by its normal **n** is demonstrated in Figure 2. The direction cosines of the normal are written in terms of the Euler angles α and β. The normal stress on plane Q is denoted as σ and the shear stress is denoted as τ.

The orientation of the plane which has the maximum range of shear stress is determined in this study. This is different than Smith and Liu's work where in their study the shear stress range on the plane of maximum shear stress was determined. However, the orientations of the plane of maximum shear stress and the plane of maximum shear stress range are not the same, nor are the values of maximum shear stress ranges on those two planes. A computer program is written to determine the plane which has the maximum shear stress range. All possible planes are traced by varying α and β in incremental form and calculating the maximum $\Delta\tau$ on each plane. Finally, the maximum shear stress range $\Delta\tau_{max}$ is established with this procedure. To illustrate this further, consider Figure 3 which describes general shear stress variation on an arbitrary plane Q. τ_ξ, τ_ψ represent maximum shear stress direction and direction perpendicular to it on plane Q respectively. The shear stress will

change its magnitude as well as direction with time. Shear stresses $\tau_1,\tau_2,\tau_3,\tau_4$ correspond to times 1,2,3 and 4 respectively. τ^Q_{max} is the maximum shear stress on the plane Q and $\Delta\tau^Q_{max} = \tau_1-\tau_4$ is the maximum shear stress range on this plane. It should be noted that the direction of the maximum shear stress range, $\Delta\tau^Q_{max}$, usually does not coincide with the direction of the maximum shear stress, τ^Q_{max}, as illustrated in Figure 3. Note that $\Delta\tau^Q_{max}$ is usually larger than τ^Q_{max}. Upon considering all planes and establishing $\Delta\tau^Q_{max}$ on all possible planes, the largest value of $\Delta\tau^Q_{max}$ is identified as $\Delta\tau_{max}$. The plane corresponding to the maximum shear stress range, $\Delta\tau_{max}$,is the so-called 'critical plane'.

Orthogonal stresses, Principal stresses and Stress Deviators

The variation of orthogonal stresses $\sigma_x,\sigma_y,\sigma_z,\tau_{xz}$ with position x/a are plotted for the case q/p=0 and 0.3 at depths of z/a=0 and z/a=0.5 in Figure 4. All the stress quantities are normalized with respect to maximum Hertzian pressure p_o .Note that the maximum σ_x and σ_y components are tensile at the trailing edge of the contact for the q/p=0.3 case.

The results are shown in terms of the principal components, σ_1,σ_2 and σ_3 in Figure 5. We note that the the σ_1 component undergoes almost a complete reversal of stress for the q/p=0.3 case on contact surface while the σ_2 and σ_3 components are primarily in the compressive stress regime.

The variation of first invariant of deviatoric stress, $J_1/3$, second invariant, $(J_2)^{1/2}$, and maximum shear stress τ_{max} is plotted in Figure 6. The results are presented for q/p= 0, 0.3 and z/a = 0, 0.5 locations respectively.

Orthogonal Shear Stress Range versus Maximum Shear Stress Range

The orthogonal shear stress range $\Delta\tau_{xz}$ as a function of q/p ratio (0 to 0.3) and depth z/a is given in Figure 7 . It is important to note that $\Delta\tau_{xzmax}$ (maximum value of $\Delta\tau_{xz}$) is invariant to q/p ratio at depths below z/a =0.15 and $\Delta\tau_{xzmax} = 0.5p_o$ occurs at the location z/a=0.5 . However, $\Delta\tau_{xzmax}$, in general, is smaller than the maximum shear stress range, $\Delta\tau_{max}$, which is shown in Figure 8 . The orientation of the maximum shear stress range is indicated in Table 1. The magnitude of $\Delta\tau_{max}$ /po, τ_{max}/po , their location (z/a) and their orientation ($\alpha°$, $\beta°$) are given in columns 1 and 2. For the case q/p=0, the plane of τ_{max} is $\alpha°$ =0 and $\beta°$=45 and the plane of $\Delta\tau_{max}$ is α=0°and β=90°. It is noted that $\Delta\tau_{max}$ and maximum of $\Delta\tau_{xz}$ values correspond only for the case of pure rolling contact, q/p=0. The plane of $\Delta\tau_{max}$ changes with increasing q/p ratio such that α decreases from 90° to 45°. For example, for the case q/p=0.2, the plane of maximum shera stress range is α=0°and β=79°.

To illustrate the difference between maximum shear stress and maximum shear stress range, the stress variations on those two planes are investigated. Maximum shear stress occurs at z/a=0.786 at the orientation of α=0° and β=45° in q/p=0 case (Poisson's ratio μ=0.3, see Figure .9). In Figure 9(b) the cycle begins at point A, point B corresponds to maximum shear stress and point D corresponds to minimum shear stress, and the cycle is completed at point A. The shear stress range on this plane is τ_B-τ_D=0.30- (-0.64))p_o =0.364p_o and is obtained from Figure 9b. Note that the normal stresses corresponding to points A, B, C and D are in the compressive regime. The plane of maximum shear stress range coincides with the the orthogonal plane in q/p=0 case with α=0° and β=90° and the results on this plane are illustrated in Figure 10. The maximum shear stress range is obtained from Figure 10(a) as 0.5p_o . Note that at point B the shear stress is 0.25p_o which is less than the maximum shear stress given in Figure 9(a). However, the minimum shear stress in Figure 10(a) is -0.25po and the range of shear stress is 0.5po which is higher than the shear stress range shown in Figure 9(b). Note that the location of maximum shear stress range is at 0.5625a. The corresponding normal stresses are illustrated in Figure 10(b) and it is noted that these compressive normal stresses are higher in magnitude compared to those in

Figure 9(b). This is expected due to the closer proximity of the plane of maximum shear stress range to the surface.

The variation of shear stress on the plane of maximum shear stress is indicated in Figure 11(a) for the case $q/p=0.3$. This plane has orientation $\alpha=128°$ and $\beta=-24°$, $z=0$ and maximum $\Delta\tau$ on this plane is $0.514p_o$. In this case, the shear stress vector rotates on the $\alpha=128°$ and $\beta=-24°$ plane such that the shear stress vector is pointed towards A, B, C, D and E during the cycle. Note that Fig.11(a) is consistent with the analysis of Smith and Liu. However, the $0.514p_o$ is not the maximum shear stress range when all the planes are surveyed.
The relation between normal stress and shear stress magnitude on this plane is given in Figure 11(b). Note that the normal stress is tensile at point B and compressive at point D. Therefore, when τ_{max} is reached, the normal stress is a minimum. The relation between normal strain and shear strain magnitude on this plane is given in Figure 11(c) for the $p_o/\sigma'_y=1$ case. The results are similar to the $\sigma-\tau$ plot however the normal strain is influenced by all normal stress components.

The plane of maximum shear stress range (critical plane) is determined for $q/p=0.3$ case and its orientation is found as $\alpha=0°$ and $\beta=45°$. This plane is termed the 'critical plane'. The variation of shear stress on this plane is given in Figure12(a). Note that $\Delta\tau_{max}=0.6p_o$ which is higher than $\Delta\tau=0.514p_o$ on the maximum shear stress plane. The relation between normal stress and shear stress magnitude on this plane is indicated in Figure 12(b). Note that the normal stress is tensile during a portion of the cycle. However, the mean stress of the cycle is highly compressive. The normal strain and shear strain variation on the critical plane is given in Figure 12(c). It is interesting to note that the normal strain range shown in Figure 12(c) is much higher than that shown in Figure 11(c).

Comparison of Results to Smith-Liu's Work

Smith and Liu [4] were the first to demonstrate the rotation of the shear stress vector on a given plane. However, they did not determine the maximum shear stress range in their analysis. Their results showing the variations of shear stress on the plane of maximum shear stress and the plane of maximum octahedral shear stress are accurate with the exception of few errors on the shear stress ranges. In our study, the magnitude of the maximum shear stress on the plane of maximum shear stress was determined as $0.43p_o$ (μ=0.25 and q/p=1/3 case) which agrees with Smith and Liu's result. However, the shear stress range on this plane is found to be $0.62p_o$ instead of $0.53p_o$ as reported by Smith and Liu. The maximum shear stress range on the maximum octahedral shear plane is determined as $0.59p_o$ instead of $0.63p_o$ as reported by Smith and Liu. Therfore, their conclusion that the shear stress range on the plane of maximum octahedral shear stress is larger than shear stress range on the maximum shear stress plane is not correct in view of the corrected results. It is worth noting that the maximum shear stress plane is not the plane of maximum shear stress range (See Table 1 and Figure 11(a), 12(a)) . Based on our calculation, for the μ=1/4 and q/p=1/3 case the maximum shear stress range is $0.667p_o$ and the orientation of the plane is $\alpha=0°$ and $\beta=45°$. It should be noted that this result, $\Delta\tau_{max}=0.667p_o$, is different from that presented in Figure .12 of this report due to the different μ and q/p levels used.

Multiaxial fatigue

There are a number of multiaxial fatigue criteria developed over the past three decades. The effective stress range modified by hydrostatic stresses is proposed by Crossland-Sines [14-16]. Findley, McDiarmid, Miller and Socie developed critical plane approaches[6-13,18] based on the earlier ideas of Guest[19] and Gough [20]. The limitation of all these models lies in handling of compressive mean stress effects where very few experimental data is available and in handling of non-propotional loading cases where the maximum normal stress and maximum shear stress in the cycle does not coincide.

Crossland and Sines proposed independently the following criterion:

$$(J_2)^{1/2}_{alt} + \alpha'(J_1)_{stat} = f(N_f) \qquad (1)$$

where α' is a constant which may also depend on fatigue life [14,15] and the $f(N_f)$ denotes a function incorporating cycles to failure. If used in non-proportional loadings, the terms in Eq.(1) are defined:

$$(J_2)^{1/2}_{alt} = \frac{1}{2}\left\{\frac{1}{6}[(\Delta\sigma_{11}-\Delta\sigma_{22})^2+(\Delta\sigma_{11}-\Delta\sigma_{22})^2+(\Delta\sigma_{11}-\Delta\sigma_{22})^2+6(\Delta\sigma_{12}^2+\Delta\sigma_{23}^2+\Delta\sigma_{31}^2)]\right\}^{1/2}$$

which is maximized with respect to time and where

$\Delta\sigma_{ij}=\sigma_{ij}(t_1)-\sigma_{ij}(t_2)$
$\sigma_{ij}(t_1)$=stress component at time t_1
$\sigma_{ij}(t_2)$=stress component at time t_2

$$(J_1)_{stat}=\frac{1}{2}(J_{1max}-J_{1min})$$
$$J_1=\sigma_{11}(t)+\sigma_{22}(t)+\sigma_{33}(t)$$

Sines and Ohgi[15] gave a physical interpretation of this criterion as average of the shear stress over all planes modified by a linear function of the static normal stress averaged over all planes.
For multiaxial fatigue under non-proportional loading, the parameter has been modified to [15]

$$\frac{\Delta\tau_{max}}{2}+\beta'(J_1)_{stat}=f(N_f) \qquad (2)$$

where $\frac{\Delta\tau_{max}}{2}$ is the maximum shear stress amplitude and β' is a constant. Eq.(1) and Eq.(2) are directly related to the Mises equivalent stress range and Tresca equivalent stress range, respectively, with consideration of the

hydrostatic stress effect. There is experimental evidence to support these criteria based on pressure experiments performed by Crossland [16]. These two criteria predict no effect of mean torsional stress on fatigue. Note that $(J_2)^{1/2}_{alt}$ is always a positive scalar and is a function of stress amplitude and is independent of mean stresses.

The critical plane approaches [6-13] take into consideration of the observed damage of crack initiation and propagation. The basic impetus of critical plane approaches is local(resolved) shear and and normal stress and strain parameters on the plane of crack initiation/propagation describe the fatigue damage. The earlier expressions for critical plane approach were stress based, suitable for high cycle fatigue research studies,

$$\tau_a + C_1 \sigma_{na} = f(N_f) \qquad (3)$$

where τ_a and σ_{na} are shear stress and normal stress amplitudes, respectively, on the critical plane, C_1 is a material constant. This parameter predicts that the shear stress on the critical plane governs the fatigue life, with the normal mean stress on that plane having a modifying influence. This expression is similar to Stulen and Cumming's criterion [11] and those proposed by Findley[9-10] and McDiarmid [6]. Note, however that the critical plane defined by Stulen and Findley is not necessarily the plane of maximum shear stress but the plane where $\tau_a + C_1 \sigma_n$ is a maximum.

Brown and Miller [7] developed a critical plane approach based on strain. Both the maximum shear strain and the tensile strain acting across the maximum shear strain plane influence the damage. Kandil, Brown and Miller[18] proposed,

$$\Delta\gamma + S\Delta\varepsilon_n = f(N_f) \qquad (4)$$

where $\Delta\gamma$ is shear strain range on the plane experiencing the maximum range of shear, $\Delta\varepsilon_n$ is the normal strain range on this plane, and S is a material constant. This criterion could be applied to cases where the principal axes are rotating but the critical plane is not known a priori. The

parameter $\Delta\gamma$ has to be calculated on every possible plane and the plane where $\Delta\gamma$ is a maximum is determined and termed the 'critical plane'. Then, the the normal strain range on that plane is determined and Equation (4) is used to estimate life.

Lohr and Ellison [21] reasoned that crack nucleation is facilitated on shear planes that emerge at the specimen surface(and not confined within the bulk material) and used the ε_1-ε_2 plane and strain ranges on this plane to characterize cracks growing into the thickness of the specimen. This parameter correlated the tension and torsion test data very satisfactorily.

Based upon the observations that mean stress effect influences the development of microcracks on the maximum shear plane, Socie et al [22] modified Brown and Miller's parameter by seting S=1 and including a mean stress correction in the form:

$$\gamma+\varepsilon_n+\frac{\sigma_n}{E} = f(N_f) \qquad (5)$$

where γ is the maximum shear strain amplitude, ε_n is the strain amplitude perpendicular to the plane of maximum shear strain amplitude, σ_n is the mean stress perpendicular to this plane. In subsequent work, Fatemi and Socie[22],Fatemi and Kurath[23] and Morrow[24]modified this shear based parameter to,

$$\gamma(1+K\frac{\sigma_{nmax}}{\sigma'_y})=f(N_f) \qquad (6)$$

where γ has the same meaning as in previous model, σ_{nmax} is the maximum normal stress on the critical plane, K is a constant and σ'_y is the yield strength of the material.

Since the basic concept behind the critical plane models is that the bulk parameters must be consistent with localized damage, it is not surprising that a shear based model is not particularly successful in predicting life for a material that developed tensile cracks. Instead, it was shown that the Smith,

Watson, and Topper[25] model(TWS parameter) applied to multiaxial loading resulted in a better fatigue life correction of components which developed tensile cracks. TWS expression is well known

$$\frac{\Delta\varepsilon_1\sigma_1}{2} = f(N_f) \qquad (7)$$

where $\Delta\varepsilon_1$ is the maximum value of principal strain range and σ_1 is the maximum stress on the plane of maximum principal strain amplitude.

Illustration of Multiaxial Fatigue Parameters

The normalized $(J_2)^{1/2}_{alt}$, $(J_1/3)$ and $[(J_2)^{1/2}_{alt} + \alpha'(J_1)_{stat}]$ parameter (Equation 1) for the case of different shear tractions are plotted as a function of depth for different values of α' in Figure 14. The horizontal axis is normalized with respect to p_o. The curves on the far right represent $(J_2)^{1/2}_{alt}$ and the curves on the far left represent the $(J_1/3)_{stat}$. Note that as q/p ratio increases the location of maxixmum $(J_1/3)_{stat}$ moves from the surface to the interior. The three curves between the $(J_2)^{1/2}_{alt}$ and $(J_1/3)$ are the $[(J_2)^{1/2}_{alt} + \alpha'(J_1)_{stat}]$ parameter. At q/p=0.1 the location of maximum value of the $[(J_2)^{1/2}_{alt} + \alpha'(J_1)_{stat}]$ parameter is below the surface and at q/p=0.3 the maximum $[(J_2)^{1/2}_{alt} + \alpha'(J_1)_{stat}]$ location moves to the surface.

The $\Delta\tau_{max}$, $(J_1)_{stat}/3$ and the parameter $[\Delta\tau_{max}/2 + \beta'(J_1)_{stat}]$ (Equation 2) is indicated on Figure 15 . The trends are similar to that shown in Figure. 14. At q/p=0.3 the location of maximum value of $[\Delta\tau_{max}/2 + \beta'(J_1)_{stat}]$ is at the surface. When q/p is smaller than 0.240 (μ=0.3), the maximum value of $(J_2)^{1/2}_{alt}$ is almost constant and occurs at subsurface at about a depth of z/a=0.4. The maximum shear stress range is unchanged with q/p ratio and occurs on the subsurface at about z/a=0.45 when q/p<0.225. The maximum shear stress and maximum $(J_2)^{1/2}$ have different behavior than the maximum shear stress range and $(J_2)^{1/2}_{alt}$. The maximum values of $(J_2)^{1/2}_{max}$ and τ_{max} change continuously with q/p ratio. The maximum shear stress, τ_{max} , occurs on the surface when q/p>0.25. The maximum $(J_2)^{1/2}_{max}$ occurs on the surface when q/p>0.265.

The critical plane parameter, $[\gamma+\varepsilon_n+\frac{\sigma_n}{E}]$ (Equation 5), and the individual components of this parameter are plotted for the case $p_o/\sigma'_y = 1$ in Figure 16. The horizontal axis represents a strain quantity in these cases. It is interesting to note that rapid changes occur in this parameter near the surface when q/p ratio exceeds 0.2.

The recently proposed critical plane parameter, $\gamma(1+K\sigma_{nmax}/\sigma'_y)$ (Equation 6), for values of K=0.5 and 1 is given in Figure 17. Note that the normal stress term in $\gamma(1+K\sigma_{nmax}/\sigma'_y)$ has no effect for $q/p < 0.1$.

1070 Steel Properties

The strain amplitude versus fatigue life data from this investigation and from early investigations on Class U and Class C steels are summarized in Figure 18. There are approximately 60 tests reported in this figure obtained from References [26-29]. Coarse refers to a coarse pearlitic structure while fine refers to a fine pearlitic structure. Class C (coarse) designate specimens obtained from a Class C wheel that has been subject to tread braking. 'Class C, This Study' designates recent results on a fine pearlitic structure obtained from a Class C wheel. 'This Study' refers to 2.5 " diameter 1070 bars obtained for the multiaxial testing program. The Class C behavior is represented with the upper bound curve and the Class U behavior is represented with the lower bound curve. In both cases the strain life behavior is represented with a double linear representation.

Similarly, the stress-life curves are illustrated in Figure 19 for the Class C and Class U materials.The Class U exhibits shorter lives in the high cycle fatigue regime. Similarly, the upper solid line represents the Class C behavior while the lower solid line represents the Class U behavior.

The parameters, $(J_2)^{1/2}_{alt} + \alpha'(J_1)_{stat}$, $\Delta\tau_{max}/2 + \beta'(J_1)_{stat}$, $\gamma+\varepsilon_n+\frac{\sigma_n}{E}$, and $\gamma(1+K\sigma_{nmax}/\sigma'_y)$, versus fatigue lives are plotted in Figures 20 through 23

based on uniaxial tests. In all those plots, the lower bound represents Class U lives and the upper bound represents Class C lives for these 1070 steels. Double linear relations as indicated in the figures are employed for both Class C and Class U materials in contact life prediction.

Contact Fatigue Life Prediction

Class U- Steel

Fatigue life prediction for crack nucleation is performed using $[(J_2)^{1/2}_{alt}+\alpha'(J_1)_{stat}]$ parameter (Equation1), $[\Delta\tau_{max}/2+\beta'(J_1)_{stat}]$ parameter (Equation2), $[\gamma+\varepsilon_n+\frac{\sigma_n}{E}]$ parameter (Equation 5), and $\gamma(1+K\sigma_{nmax}/\sigma'_y)$ parameter (Equation 6). The results are shown in Figures 24 through 28. In the bulk approach, the parameters α' and β' are in the range of 0.1 to 0.2. When 0.2 is used, the bulk models predict fatigue lives exceeding 10^9 cycles. Therefore, $\alpha'=0.1$ and $\beta'=0.1$ are used in the fatigue life predictions. Life predictions are made for the cases p_o/σ'_y= 1., 1.5, 2.0, 2.5, and 3 using the four parameters. If we consider Figures 24-25 based on the bulk parameters, the predicted lives are in the range 10^2 to 10^9 depending on the p_o/σ'_y ratio and q/p ratio. It is interesting to note that for the same conditions the predict lives are in a narrower range (2. 10^4 to 3.10^6) cycles when the summation parameter is used. This result is expected since the γ and ε_n used in this model are strain amplitudes and whether the strain is in compression versus tension regimes is not reflected. Furthermore, the effect of the shear tractions on fatigue life is least pronounced with the $[\gamma+\varepsilon_n+\frac{\sigma_n}{E}]$ parameter compared to other three parameters. In Figure 27 $\gamma(1+K\sigma_{nmax}/\sigma'_y)$ parameter predicts the longest lives (10^6 to 10^9) compared to other models. A summary of the predicted results with different models for Class U material is shown in Figure 28 for $p_o/\sigma'_y=2$ case. In this case, $[\Delta\tau_{max}/2+\beta'(J_1)_{stat}]$ parameter predicts shortest lives while $\gamma(1+K\sigma_{nmax}/\sigma'_y)$ parameter predicts longest lives.

Class C- Steel

Fatigue life predictions obtained for Class C steel are summarized in Figures 29-33 using the four parameters. It is noted that the same value of σ'_y (=430 MPa) is used for the normalization in all results. The $[\gamma+\varepsilon_n+\frac{\sigma_n}{E}]$ parameter predicts longest lives for q/p=0.3 case while the $[(J_2)^{1/2}_{alt}+\alpha'(J_1)_{stat}]$ parameter results in longest lives when q/p ratio is zero. It is interesting to note that the results somewhat converge when q/p ratio is 0.4. and they diverge rapidly when q/p ratio is below 0.3. Overall, the fatigue lives are substantially longer in Class C material compared to the Class U material.

Discussion of Results

Limitations of the Models under Compressive Mean Stresses

The models proposed for multiaxial fatigue rely on tensile mean stress data and multiaxial fatigue with sufficient compressive mean stresses have not been considered. Therefore, the available models are severely limited in their generality and in handling compressive mean stresses. The experiments have been conducted under plane stress conditions (thin walled cylinders), therefore the triaxiality of normal stress components cannot be achieved. Under these circumstances, any attempts to impose mean stresses a fraction of yield strength would result in rapid fracture of the specimen or rapid relaxation of mean stresses. This triaxiality of stresses in real contact situations differs than the stress states previously considered in laboratory specimens.

Only experiments where the tensile mean stress on the critical planes were systematically varied were those conducted by Morrow [24] and Fatemi - Kurath on 1045 steel [22]. A static tensile hoop stress was imposed on the specimen and the axial strain was cycled. It was found that the mean stress in the axial direction did not relax with cycles and the effect of mean stress on life was evaluated.

Variation of the Shear Stress within a Critical Plane

In contact fatigue situations, the shear stress direction may rotate on the critical plane The critical plane is defined as the plane that undergoes the maximum shear stress range. Only in the case, when $\alpha°=0$, the direction of shear within the critical plane is confined to a single direction. In non-proportional loading of laboratory specimens the critical plane is rotating however the direction of shear stress on the critical plane does not change. Consider the formation of a embedded circular crack on the critical plane which undergoes the shear stress variation as shown in Figure 11(a). Every point on the crack front undergoes Mode II type of shearing during a portion of the history and the same point undergoes Mode III type of shearing during another portion of the cycle. Therefore, any point on the crack front undergoes a combination of Mode II and Mode III in the same cycle. In the case when the shear direction does not change, such as in Figure 10(a) the same point on the crack front experiences either Mode II or Mode III components but not both.

The Nonconcurrence of Maximum Normal Stress and Maximum Shear Stress on the Critical Plane

Under non-proportional loading the maximum shear stress and the maximum normal stress does not coincide. When the shear stress has reached its maximum, the normal stress may be minimum and vice versa. In the current life models, the maximum shear stress(strain) range and the normal stress(strain) range on the critical plane are used in a manner that is consistent when the loading is in-phase. The influence of this procedure on fatigue life prediction has not been discussed. If the normal mean stresses are primarily in the compressive regime we would expect the damage to be lower than if the mean normal stresses were zero or tensile. However, if the the shear stress reversal coincides with the portion of the cycle when the normal stress level is zero or slightly tensile, the damage due to shear could be very effective. This is illustrated in Figure 34 where normal stress σ_n versus τ is plotted on the critical plane. For path ACBCACB the shear stress range CB occurs when the normal stress is zero. For path ADBDADB the maximum shear stress range, AD, coincides with the maximum tensile

normal stress in the cycle. Path II would be more damaging than Path I. However, the critical plane approaches predict the same life for these two loading paths.

Influence of Residual Stresses and Plastic Deformation on Contact Fatigue Results

The results presented in this study are based on the classical Hertz theory and are a result of elastic calculations. If the strains and stresses are increased such that plastic deformation occurs, upon unloading, residual stresses and residual strains develop as a function of distance from the contact surface. The residual stresses are compressive, and the effect of these stresses would be to decrease the life parameters in both type of models considered in this study. At large values of p_o/σ'_y, the residual shear strains may increase progressively in the rolling direction and this ratchetting phenomena is expected to have a detrimental effect on fatigue lives.

Merwin and Johnson [30] analysed the variation in orthogonal stress components with multiple passes. Because of ideal plasticity model used, and since the strain ranges are not known at all depths it is difficult to use their results and conduct a fatigue analysis at this time. Their assumption of total strain in the elastic and elastic-plastic problem being the same provides accurate results as later confirmed by finite element studies [31]. Therefore, the strain based fatigue models used in our analysis would be still applicable for the elastic-plastic case however the mean stresses need to be modified to reflect the residual stresses.

Crack Initiation at Subsurface versus at Surface

It is noted that in laboratory experiments the crack initiation often occurs at intrusions and extrusions emanating from the surface . In the case of pure torsion the maximum shear stress planes are inclined 0° and 90° to the specimen axis. It is more difficult to initiate cracks on these planes since the slip planes are confined within the material and no slip steps emerge at the surface. Shear planes inclined 45° to the specimen surface undergo lower resolved shear stresses, however crack are preferentially found on these

planes [24]. These results indicate that whether the slip planes are emanating at the surface or not influences fatigue lives. Therefore, when the cracks are initiated on subsurface, the constraint prevailing on these planes could result in longer lives than predicted based on our life analysis.

Comparison with other Models

Lundberg and Palmgren's model [32] is a maximum shear stress theory which incorporates the effects of contact configuration and the position of the maximum shear stress. It should be noted that the shear stress used in this model is orthogonal shear stress. Pure rolling cases were considered with this model. Moyar and Morrow[33] modified Lundberg and Palmgren's model by incorporating the hydrostatic stress effect on the fatigue limit. Chiu, Tallian and McCool have a model [34] which incorporates the hydrostatic stress, the presence of inclusions at the subsurface, the shear stress at the inclusion location and a Coffin-Manson type equation. There is no explicit consideration of shear traction effects nor the multiaxial fatigue concepts in their model. It is difficult to make a direct comparison of these models with the results presented here. It is worth pointing out that depending on how compressive mean stresses are handled the predicted life could vary orders of magnitude.

Summary

A contact life prediction procedure is developed based on the bulk approaches and the critical plane approaches to multiaxial fatigue. The results indicate that depending on the criteria used, predicted lives could differ by orders of magnitude. Experiments are needed to establish which criteria is accurate when compressive mean stresses are present.

Future Work

1. There have been no reversed shear experiments performed with compressive mean stresses. Crack nucleation and crack growth under these conditions is extremely relevant to wheel shelling. The 1070 steel bars have been purchased and tubular specimens have been machined for this purpose. Experiments under combined axial -shear loading in the compressive range are currently conducted on tubular specimens.

2. Several experiments will be conducted under the simultaneous action of external pressure and axial compressive loading and shear loading. The advantages of these experiments are (a) all potential critical planes in this case are undergoing compressive normal stresses which are independently controlled and (b) high hydrostatic stresses are achievable.
This part of the project will be a substantial experimental effort involving computer control of axial load, external pressure and torsional loading. The specimen design has to be suited to handle high compressive hydrostatic stresses. The difference between this work and previous studies is that high normal stresses (typically observed under contact conditions) will be considered in this work. Since the experiments are expensive they will be of probing nature where the value of $\Delta\tau_{max}$ that results in crack initiation under different values of normal stress will be determined. There are no such experiments reported as of todate. A specialized vessel that encloses the fatigue specimen is designed and a high pressure hydraulic power unit that is capable of producing 100 ksi pressure is being purchased. This pressure unit will provide external pressure for smooth specimens testing and for tubular specimen testing.

3. A rational model incorporating thermo-mechanical fatigue, rolling-sliding contact fatigue, transformation induced martensite cracking and the associated wheel cracking , shelling and spalling should be an ultimate goal as outlined in Reference[35]. Our study will attempt to provide answer to some basic questions which would aid in the development of such a model.

Acknowledgements

This work is supported by Association of American Railroads (AAR), Technical Center, Chicago, Ill. Dr. Dan Stone, Executive Director, is the research monitor. Discussions with Dr. Dan Stone and Mr. Michael Fec of AAR and Dr. Gerald Moyar are appreciated.

References

1. Hertz, H., " Ueber die Beruehrung fester elastischer Koerper(On the Contact of Solids), J. reine und angewandte Mathematik, Vol.92, pp.156-171, 1882

2. Radzimovsky, E.I."Stress Distribution and Strength Condition of Two Rolling Cylinders Pressed Together", University of Illinois Engineering Experiment Station, Bulletin Series No.408, 1953

3. Johnson, K.L. " Contact Mechanics", Cambridge University Press, 1987

4. Smith, J.O. and Liu, C.K., " Stresses due to Tangential and Normal Loads on an Elastic Solid with Application to Some Contact Stress Problems", Journal Applied Mechanics, Vol.20, June 1953, pp.157-166.

5. Kannel, J.W. and Tevaarwerk, J.L.," Subsurface Stress Evaluations under Rolling/Sliding Contacts", Journal of Tribology, Trans. ASME, Vol.106, Jan.1984, pp.96-103

6. McDiarmid, D.L., " Fatigue Criteria and Cumulative Damage in Fatigue under Multi-Axial Stress Conditions", Ph.D Thesis, City University, London, 1972.

7. Brown,M.W. anf Miller, K.J.,"A Theory for Fatigue Failure under Multiaxial Stress-Strain Conditions", Proc. Instn. Mech. Engrs, Vol.187, 1973, pp.745-755

8. Bannantine, Julie Ann,"A Variable Amplitude Multiaxial Fatigue Life Prediction Method", PhD Thesis, Mechanical Engineering Department,University of Illinois,1989, See also Materials Engineering Report #151, 1989.

9. Findley, W.N.,"A Theory for the Effect of Mean Stress on Fatigue of Metals under Combined Torsion and Axial Load or Bending", Journal of Engineering for Industriy, Trans. ASME, Nov. 1959, pp.302-305

10. Findley, W.N. and Mathur, P.N.," Modified Theories of Fatigue under Combined Stress", A.E.S.A. Proc., Vol.XIV, No.1, 1956, pp.35-46

11. Stulen, F.B. and Cummings, H.N., " A Fatigue Criterion for Multiaxial Fatigue Stress", in Proceedings, American Society for Testing and Materials, Philodelphia, 1954, pp.822-835

12. Socie, D.F. and Shield, T.W.,"Mean Stress Effects in Biaxial Fatigue of Inconel 718", Journal of Engineering Materials and Technology, Trans. ASME, Vol.106, July 1984, pp.227-232.

13. Socie, D.F. and Bannantine, J., "Bulk Deformation Fatigue Damage Models", Materials Science and Engineering, A103, 1988, pp.3-13

14. Sines,G.,"Failure of Materials under Combined Repeated Stresses with Superimposed Static Stresses", Technical Note 3495, National Advisory Council for Aeronautics, Washington,D.C.,1955m6.

15. Sines,George and Ohgi,George,"Fatigue Criteria Under Combined Stresses or Strains",Journal of Engineering Materials and Technology, Trans. ASME, April 1981, Vol.103, pp.82-90

16. Crossland,B.,"The Effect of Pressure on the Fatigue of Metals", Chapter 7 in The Mechanical Behavior of Materials under Pressure", H.LP.D.Pugh, Ed., Elsevier Publishing Company, Limited, 1970

17. Krempl, E., "The Influence of State of Stress on Low-Cycle Fatigue of Structural Materials: A Literature Survey and Interpretive Report, STP 549, American Society for Testing and Materials, Philadelphia, 1974.

18. Kandil, F.A., Brown, M.W., and Miller, K.J., "Biaxial Low-Cycle Fatigue Fracture of 316 Stainless Steel at Elevated temperatures", Book 280, The Metals Society, London, 1982, pp.203-210

19. Guest, J.J., "On the Strength of Ductile Materials under Combined Stress", Philosophical Magazine, Vol.50, July 1900, pp.69-132

20. Gough, H.J., Pollard, H.V., and Clenshaw, W.J.," Some Experiments on the Resistance of Metals to Fatigue under Combined Stresses", Aero. Research Council, R. and M 2522. HMSO, London, 1951

21. Lohr, R.D. and Ellison, E.G., "A Simple Theory for Low Cycle Multiaxial fatigue", Fatigue of Engineering Materials and Structures, Trans ASME, Vol.3, No.1, 1980, pp.1-17

22. Fatemi, Ali, Socie, D.F.," A Critical Plane Approach to Multiaxial Fatigue Damage Including Out-of-Phase Loading", Fatigue and Fracture of Materials and Structures, Vol.11, No.3, 1988, pp.149- 165

23. Fatemi,A. and Kurath,P.,"Multiaxial Fatigue Life Prediction under the Influence of Mean-Stresses", Journal of Engineering Materials and Technology, Trans.ASME, Vol.110, 1988,pp.380-388

24. D.Morrow, " Biaxial-Tension Fatigue of Inconel 718 ", Materials Engineering Report #147, College of Engineering, University of Illinois, 1989

25. Smith,R.N., Watson, P., and Topper,T.H.," A stress strain Function for the Fatigue of Metals", Journal of Materials, JMLSA, Vol.5, No.4, 1970, pp.767-778

26. Sehitoglu, H. " Characterization of Thermo-mechanical Fatigue", Department of Theoretical and Applied Mechanics, PhD Thesis, University of Illinois, 1983

27. Karasek, M.L., ' An Investigation into Isothermal and Thermal-Mechanical Fatigue Damage at Elevated Temperatures', Report No.132, Materials Engineering-Mechanical Behaviors, College of Engineering, University of Illinois at Urbana-Champaign, 1986.

28. Fec, M.C., D.Utrata" Elevated Temperature Fatigue Behavior of Class B,C and U Wheel Steels, Proceedings of the 1985 Joint ASME- IEEE Railroad Conference, ASME, New York, 1985,

29. Park, Y.J. and Stone, D.H., ' Cyclic Behavior of Class U Wheel', ASME Paper No. 80-WA/RT-9, Presented at ASME Winter Annual Meeting, 1980

30. Merwin, J.E. and Johnson, K.L.,"An Analysis of Plastic Deformation in Rolling Contact", Proc Instn Mech Engrs, Vol.177, No.25, 1963, pp.676-685

31. Bhargava,V., Hahn, G.T., and Rubin, C.A.," An Elasto-Plastic Finite Model of Rolling Contact; Part 1: Analysis of Single Contact, Part 2: Analysis of Repeated Contact", Journal of Applied Mechanics, Trans. ASME, Vol.52, March 1985, pp.67-82

32. Lundberg, G. and Palmgren, A., 'Dynamic capacity of rolling bearings', ACTA Polytechnica, Mechanical Engineering Series, Vol.1,N.3, 1947 ,

33. Moyar,G.J and Morrow J.,'Surface Failure of Bearings and Other Rolling Elements',Engineering Experiment Station Bulletin 468, University of Illinois at Urbana-Champaign, College of Engineering, Urbana, Il., 1964.

34. Chiu, Y.P., Tallian, T.E., and McCool, J.I., 'An Engineering Model of Spalling Fatigue Failure in Rolling Contact ,I. The subsurface model', II. The surface model, Engineering discussion and Illustrative examples',Wear, Vol.17, 1971, pp.433-480.

35. G.J.Moyar, D.H.Stone, "An Analysis of the Thermal Contributions to Railway Wheel Shelling", 3rd. International Symposium on Contact Mechanics and Wear of Rail/Wheel Systems, Cambridge, 1990

Table I. Summary of Calculated Results

q/p			τ_{max}/p_o	Max Shear Stress Range $\Delta\tau_{max}/p_o$	$(J_2)_{alt}^{1/2}/p_o$
0	Magnitude		0.300	0.50	0.250
	Location, z/a		0.786	0.5	0.5
	Orien-	$\alpha°$	0	0	-
	tation	$\beta°$	45	90	-
0.1	Magnitude		0.305	0.50	0.251
	Location, z/a		0.738	0.50	0.492
	Orien-	$\alpha°$	0	0	-
	tation	$\beta°$	31	90	-
0.2	Magnitude		0.319	0.506	0.254
	Location, z/a		0.600	0.4375	0.468
	Orien-	$\alpha°$	0	0	-
	tation	$\beta°$	16	79	-
0.3	Magnitude		0.359	0.600	0.314
	Location, z/a		0	0	0
	Orien-	$\alpha°$	128	0	-
	tation	$\beta°$	-24	45	-
0.4	Magnitude		0.415	0.800	0.4146
	Location, z/a		0	0	0
	Orien-	$\alpha°$	129.7	0	-
	tation	$\beta°$	-23.3	45	-

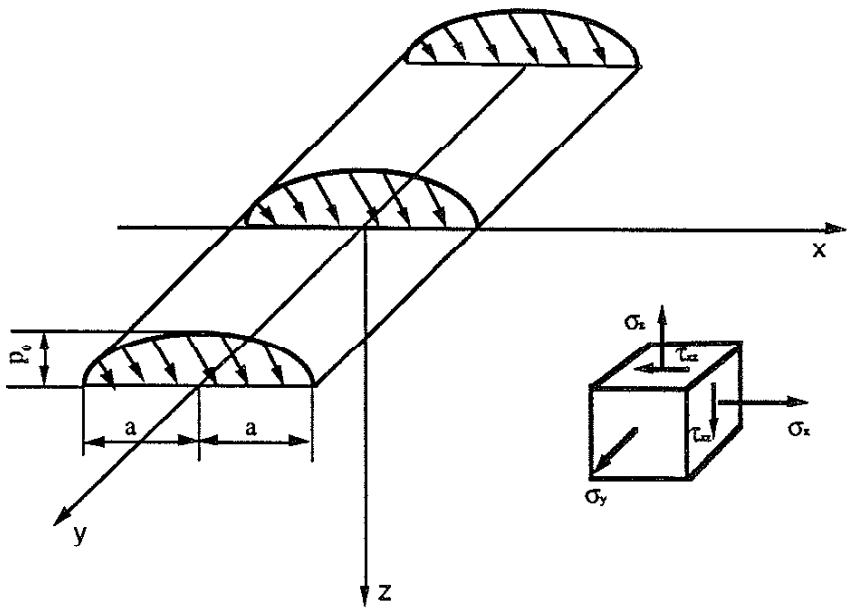

Fig.1 Line Contact, Coordinate System, and Orthogonal Stresses

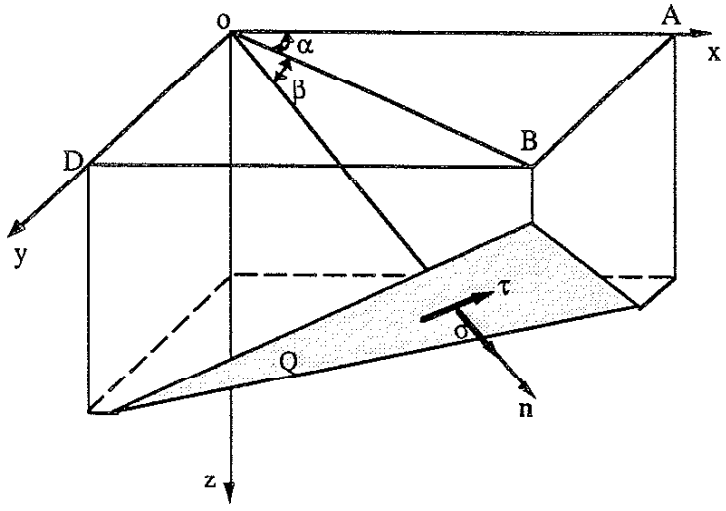

Representation of an arbitary plane Q by its unit normal n

$n = i\cos\alpha\cos\beta + j\sin\alpha\cos\beta + k\sin\beta$

σ and τ are normal stress and shear stress, respectively, on plane Q .

Fig.2 Representation of a Plane by Its Normal

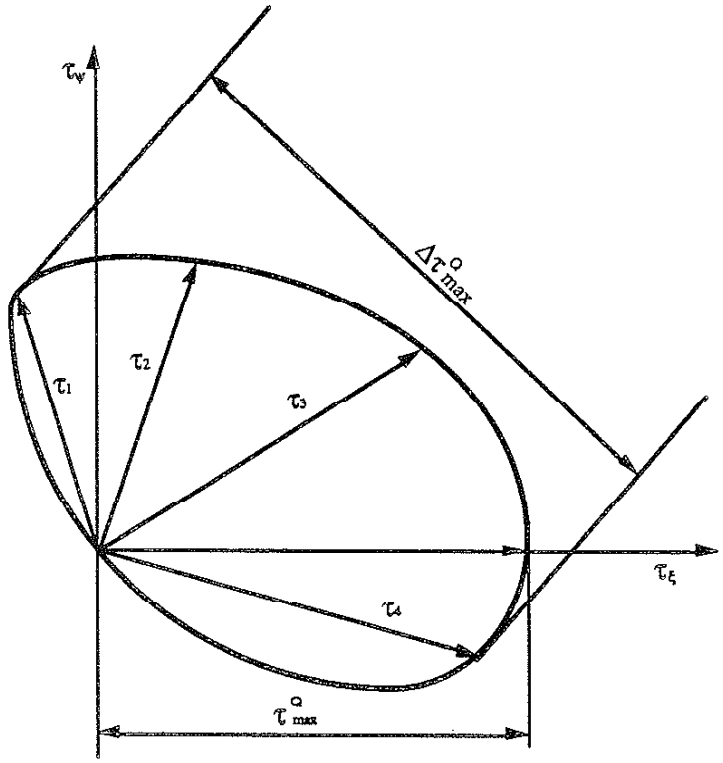

τ_1, τ_2, τ_3, and τ_4 are shear stresses at time 1,2,3, and 4 , respectively. τ^Q_{max} is the maximum shear stress on this plane. $\Delta\tau^Q_{max}$ is the maximum shear stress range on the plane Q

τ_ξ is the direction of maximum shear stress and τ_w is the direction perpendicular to it

$\Delta\tau^Q_{max} = \tau_4 - \tau_1$

Fig.3 A Schematic Illustruation of Shear Stress Variation (Direction and Magnitude) on an Arbitrary Plane, Q

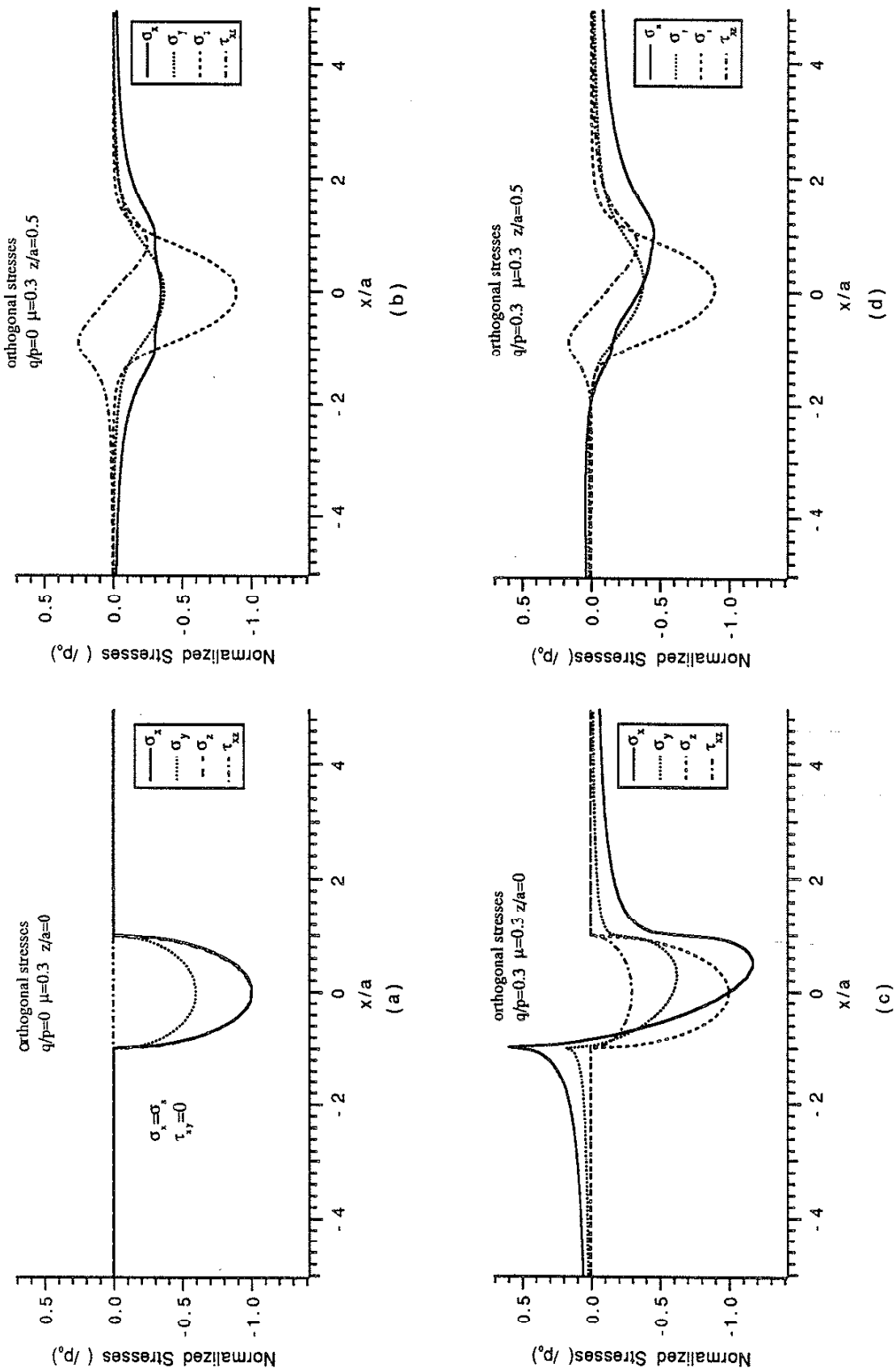

Fig.4 Orthogonal Stresses under q/p=0 and 0.3 Conditions at z/a=0 and 0.5

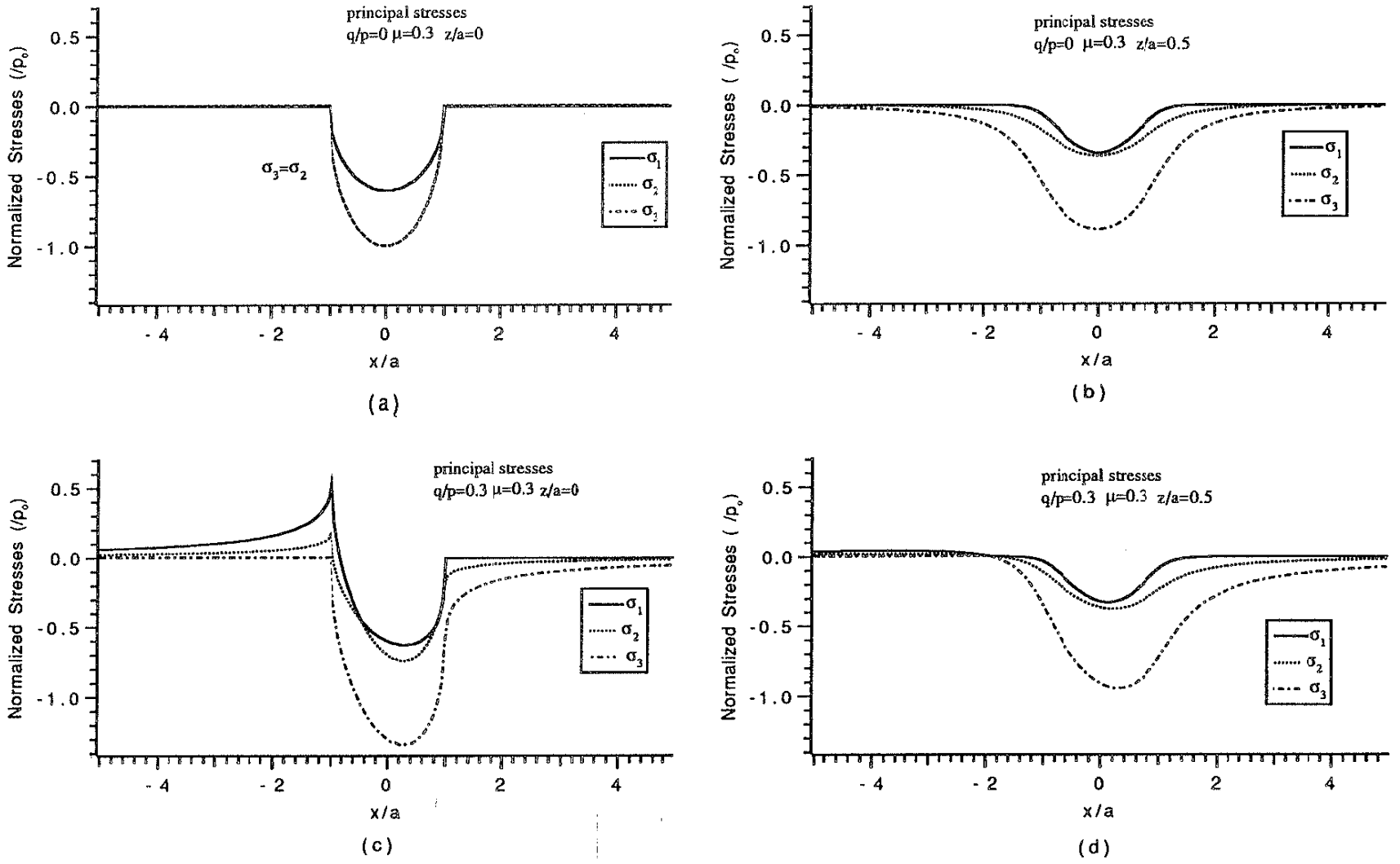

Fig.5 Principal Stresses under q/p=0 and 0.3 Conditions at z/a=0 and 0.5

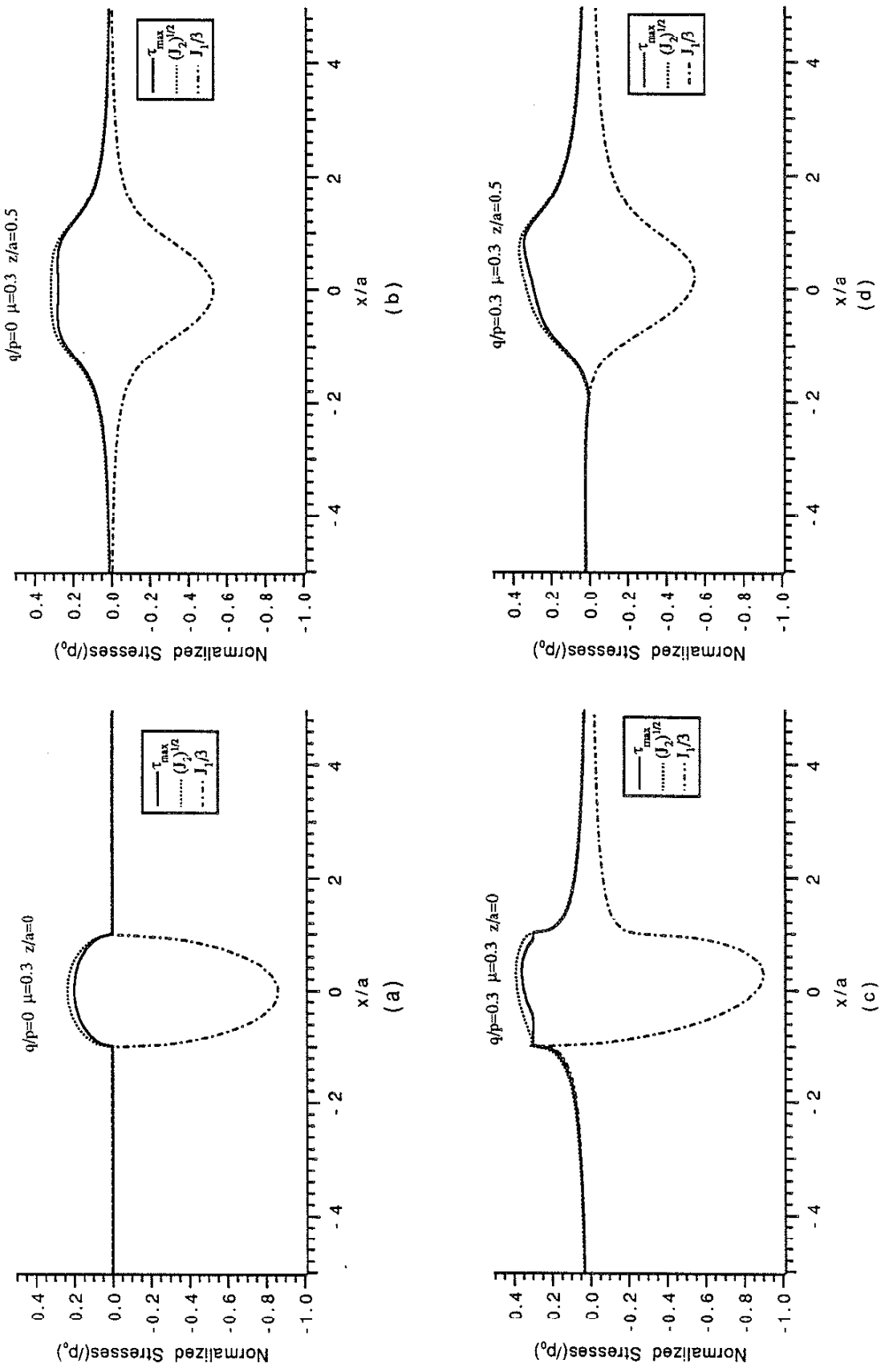

Fig.6 First Invariant, Second Invariant, and Maximum Shear Stress under q/p=0 and 0.3 Conditions at z/a=0 and 0.5

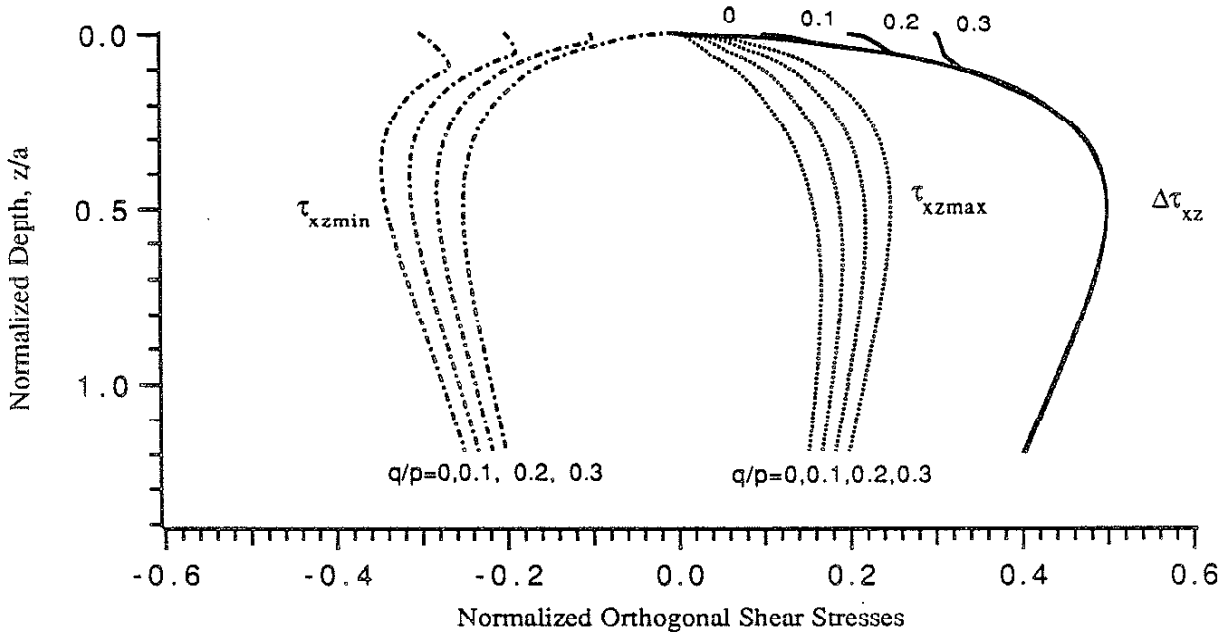

Fig.7 Variation of τ_{xzmax}, τ_{xzmin}, and $\Delta\tau_{xz}$ along z-axis with Different q/p Ratios (μ=0.3). Note that maximum value of $\Delta\tau_{xz}$ is not influenced by q/p ratio.

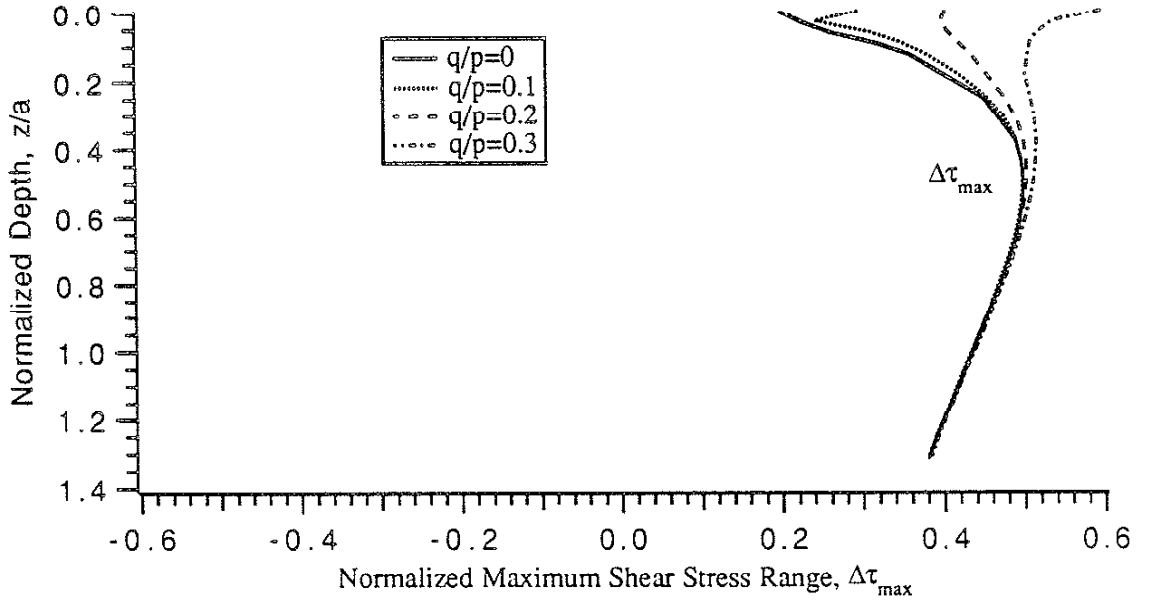

Fig.8 Variation of Maximum Shear Stress Range along z-axis with Different q/p Ratios (μ=0.3) Note that $\Delta\tau_{max}/p_0$=0.6 at surface for q/p=0.3 case

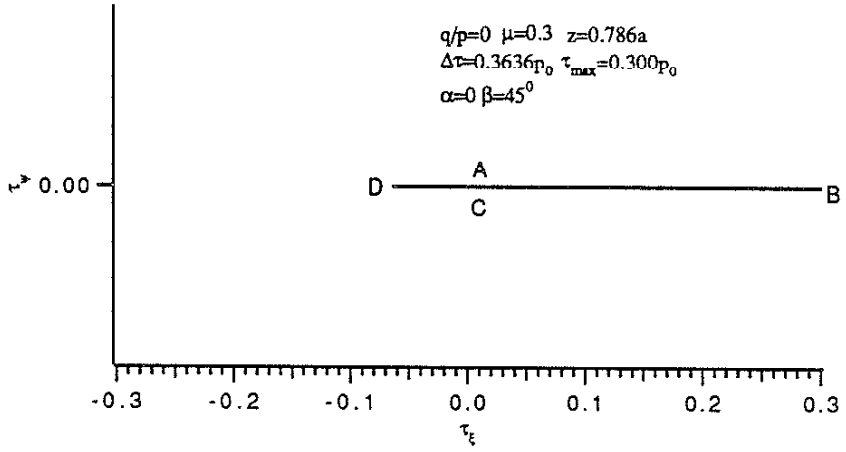

(a) Shear Stress Variation on the Plane of Maximum Shear Stress

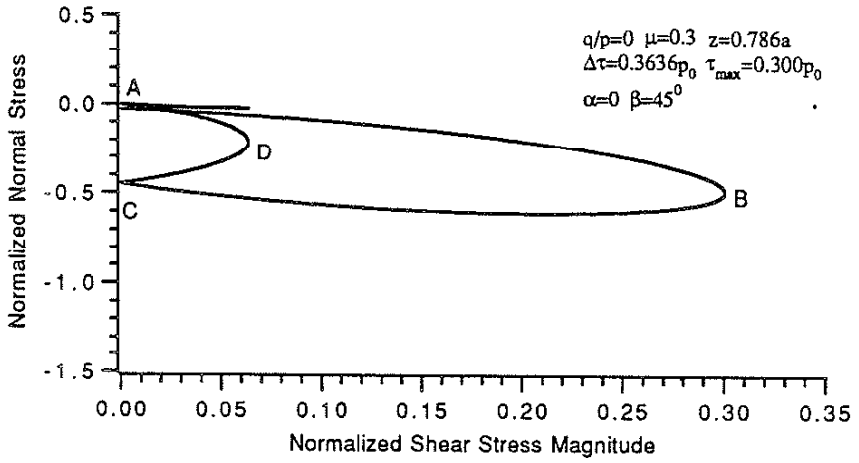

(b) Relation between Normal Stress and Shear Stress Magnitude on the Plane of Maximum Shear

Fig.9 Stress Variations on the Plane of Maximum Shear Stress(q/p=0,μ=0.3)

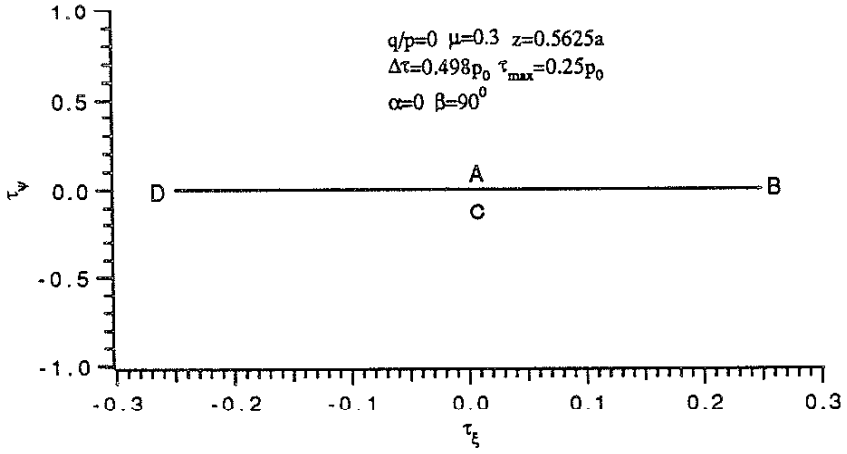

(a) Shear Stress Variation on the Plane of Maximum of Shear Stress Range

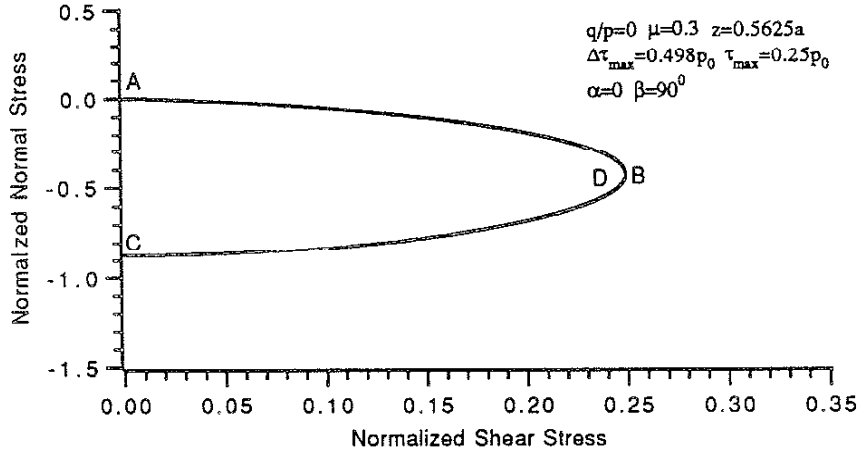

(b) Relation between Normal Stress and Shear Stress Magnitude on the Plane of Maximum Shear Stress Range

Fig.10 Stress Variations on the Plane of Maximum of Shear Stress Range(Critical Plane), (q/p=0,μ=0.3)

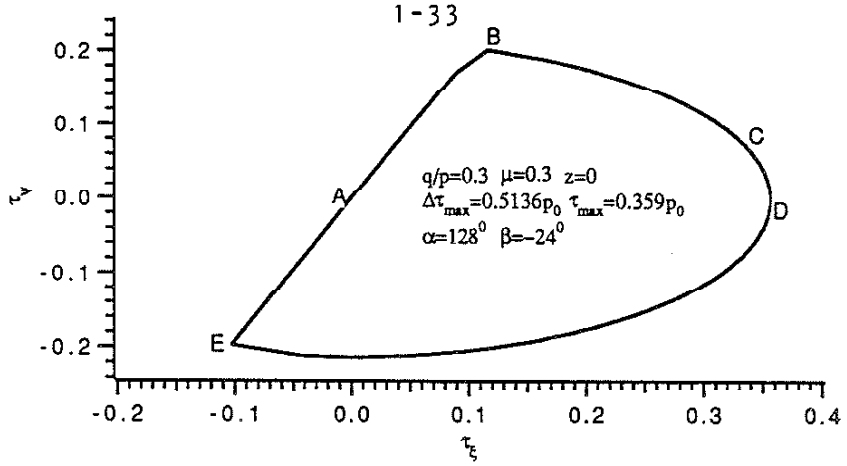

(a) Shear Stress Variation on the Plane of Maximum Shear Stress

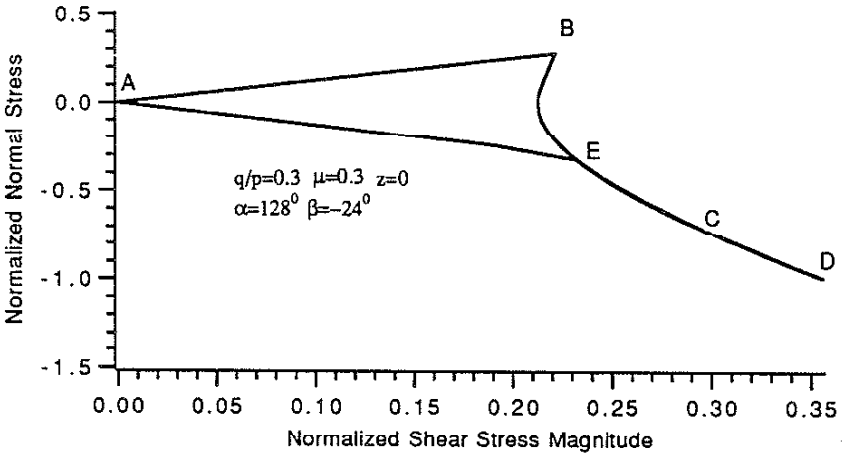

(b) Relation of Normal Stress and Shear Stress Magnitude the Plane of Maximum Shear Stress

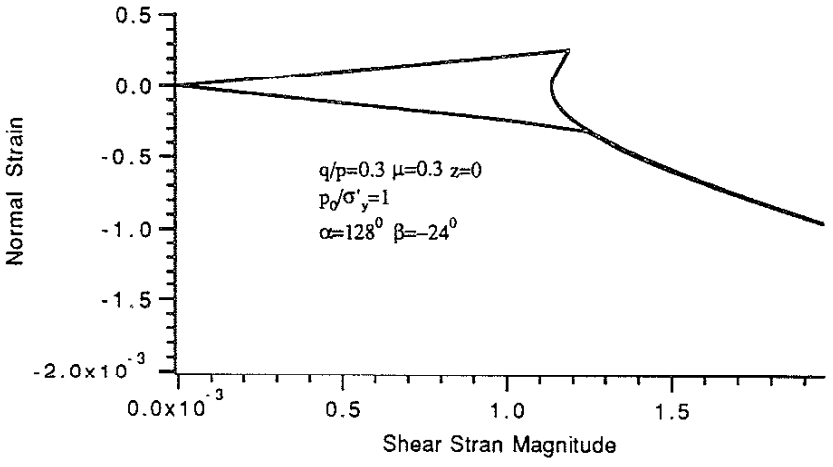

(c)Relation of Normal Strain and Shear Strain Magnitude on the Plane of Maximum Shear Stress

Fig.11 Stress and Strain Variations on the Plane of Maximum Shear, (q/p=0.3, μ=0.3)

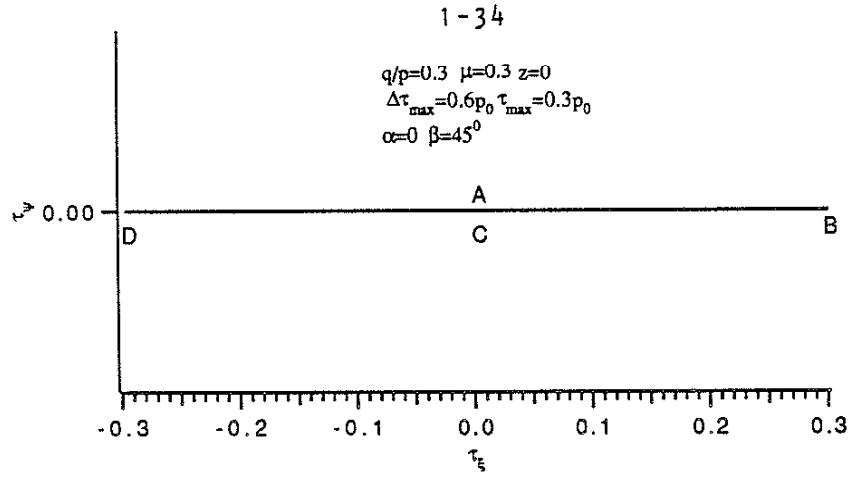

(a) Shear Stress Variation on the Plane of Maximum Shear Stress Range

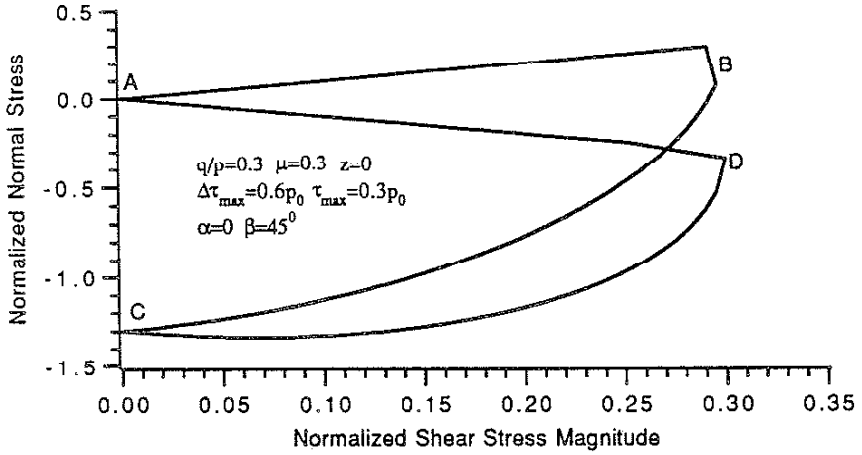

(b) Relation between Normal Stress and Shear Stress Magnitude on the Plane of Maximum Shear Stress Range

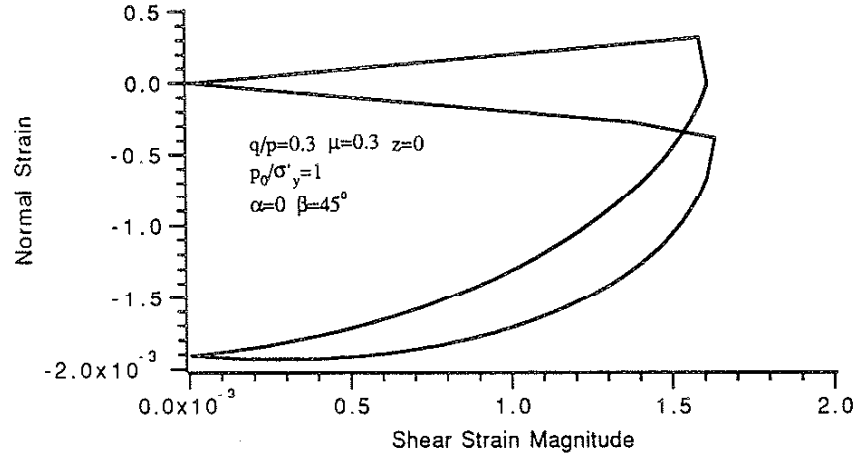

(c) Relation between Normal Strain and Shear Strain Magnitude on the Plane of Maximum Shear Stress Range

Fig.12 Stress and Strain Variations on the Plane of Maximum Shear Stress Range(Critical Plane),(q/p=0.3, μ=0.3)

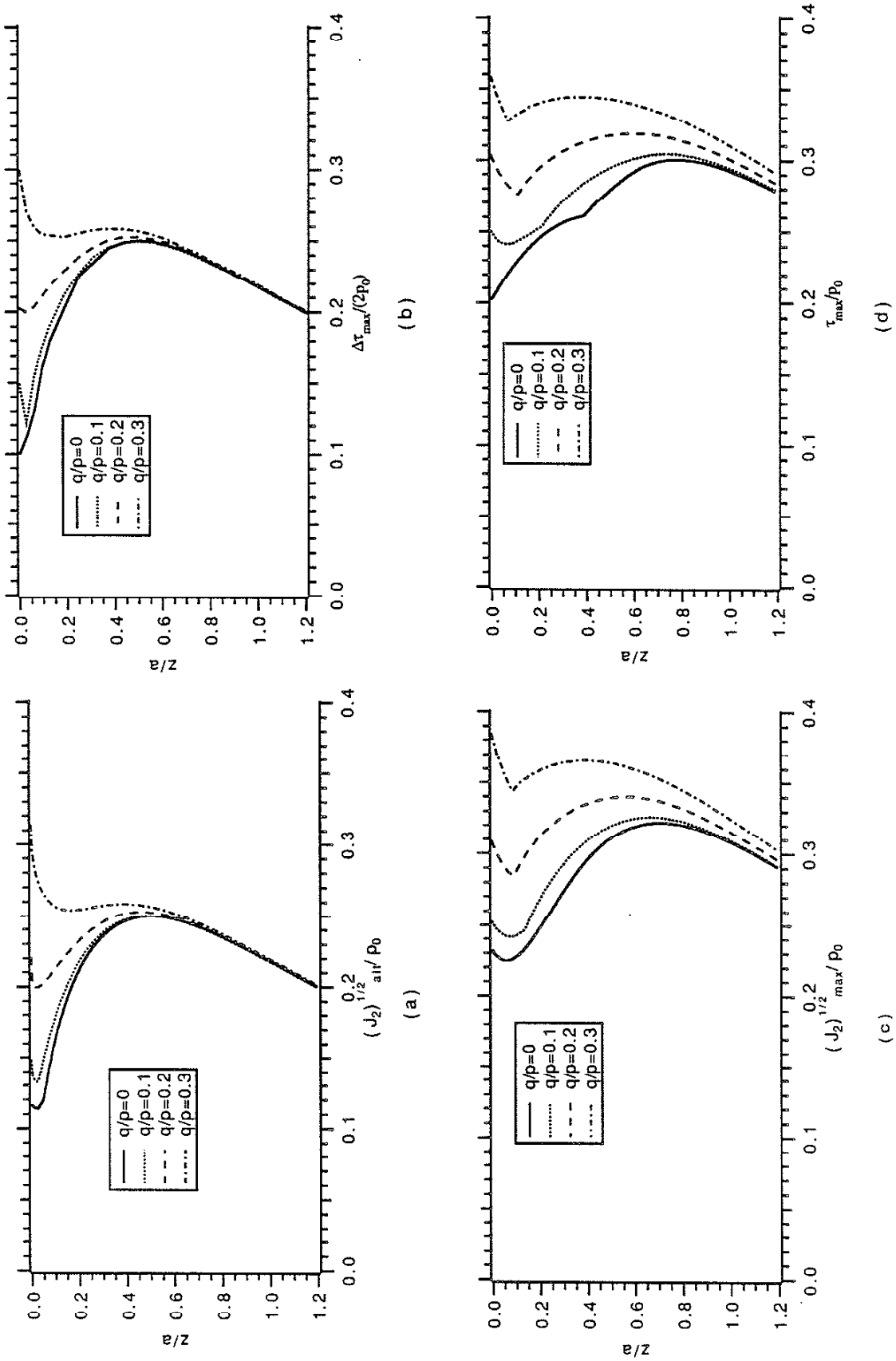

Fig.13 Variations of $(J_2)^{1/2}_{all}$, $\Delta\tau_{max}$, $(J_2)^{1/2}_{max}$, τ_{max}, and $(J_1)_{stat}$ along z-axis(μ=0.3)

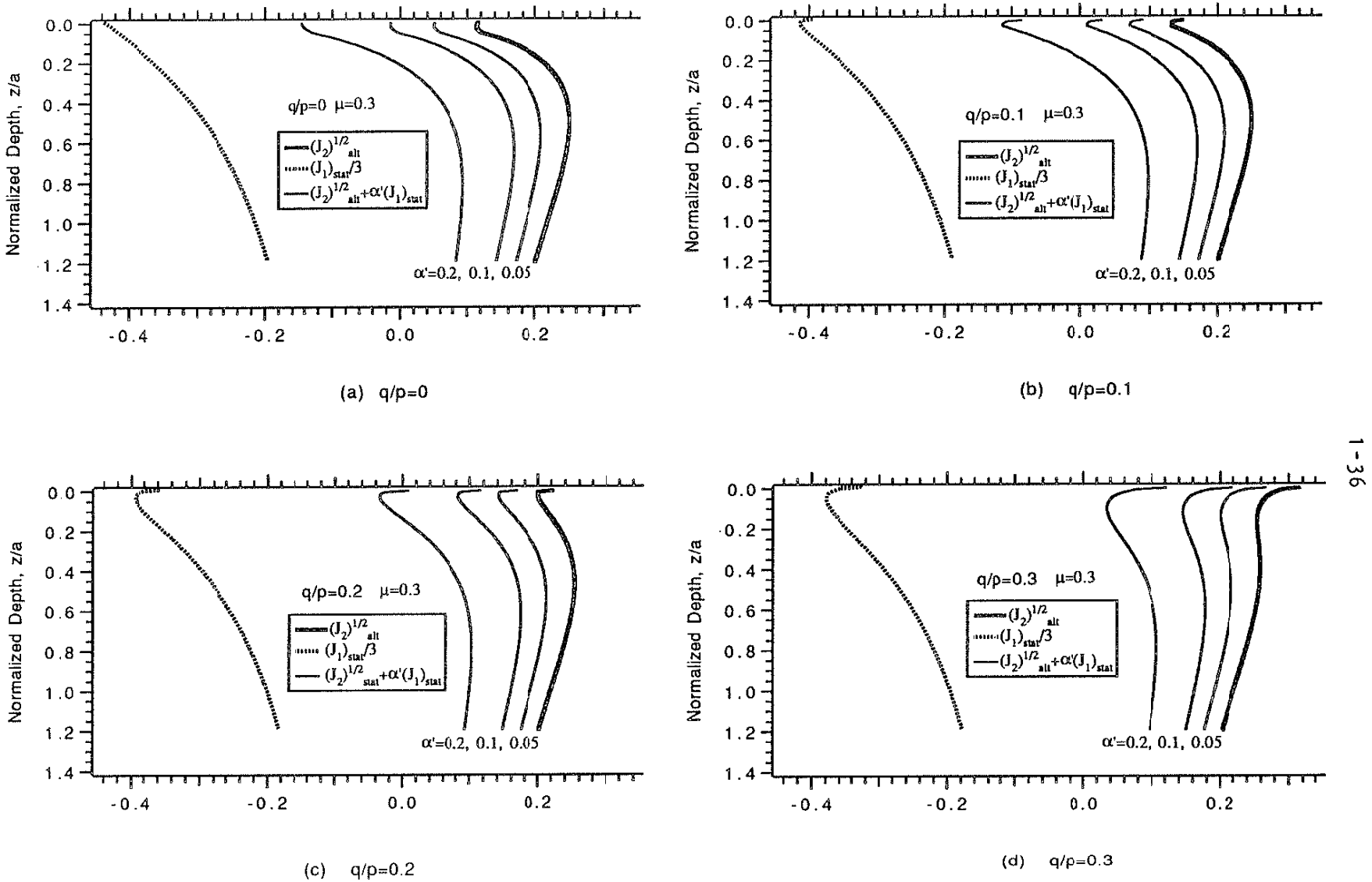

Fig.14 Variation of $(J_2)^{1/2}_{alt}-\alpha'(J_1)_{stat}$ Parameter along z-axis

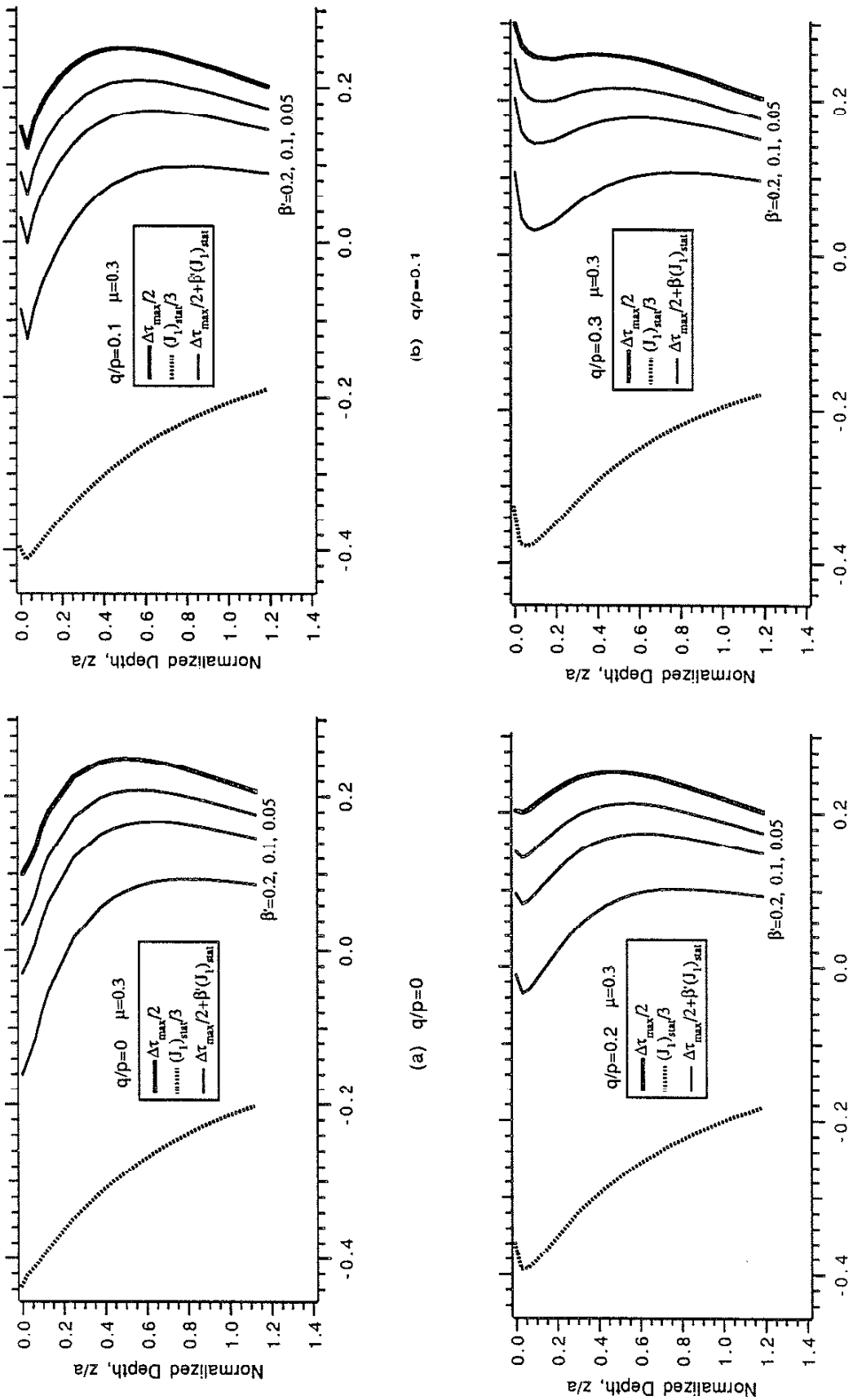

Fig.15 Variation of $\Delta\tau_{max}/2+\beta'(J_1)_{stat}$ Parameter along z-axis

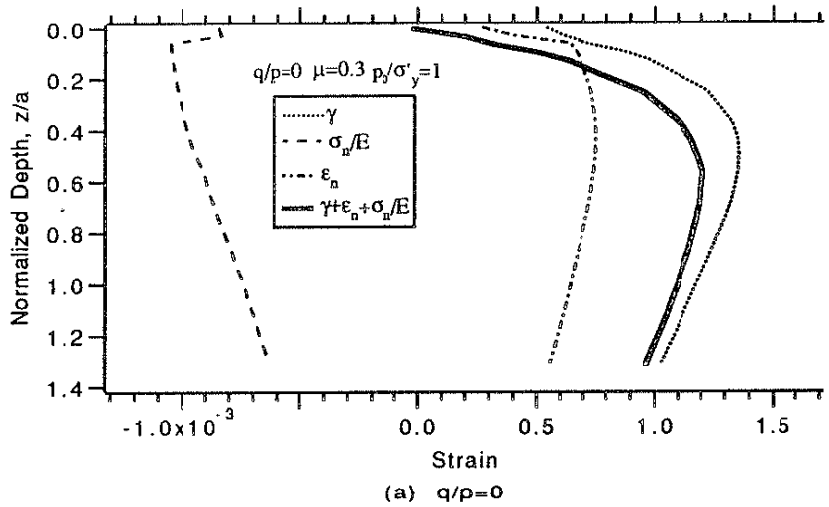

(a) q/p=0

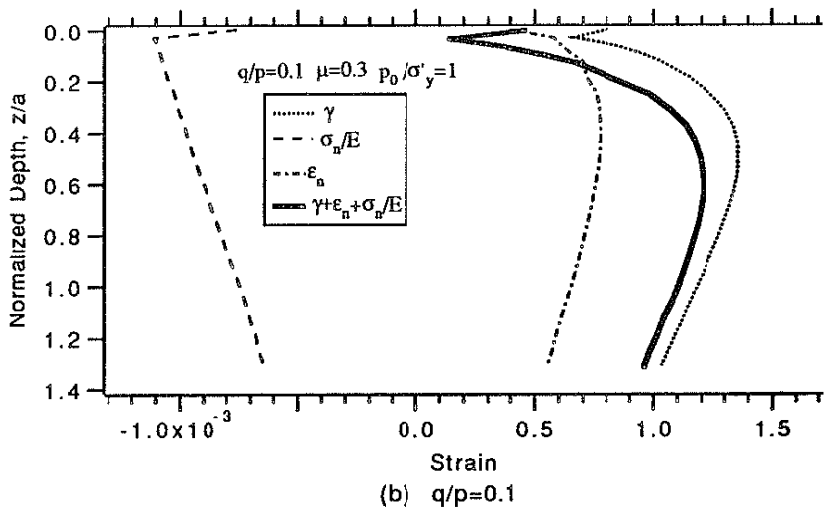

(b) q/p=0.1

(Note stains are all of the order of 10^{-3} which is in the high cycle fatigue regime)

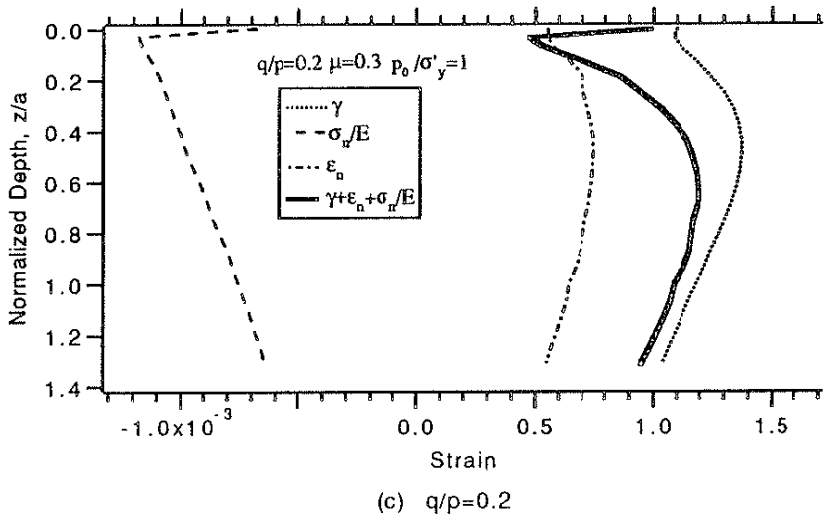

(c) q/p=0.2

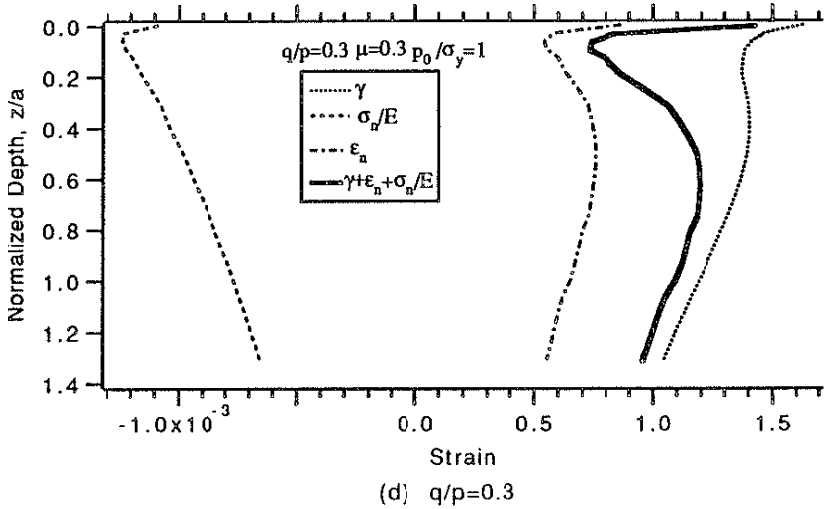

(d) q/p=0.3

Fig.16 Variation of $\gamma+\varepsilon_n+\sigma_n/E$ Parameter(dark line) along z-axis ($p_0/\sigma'_y=1$)

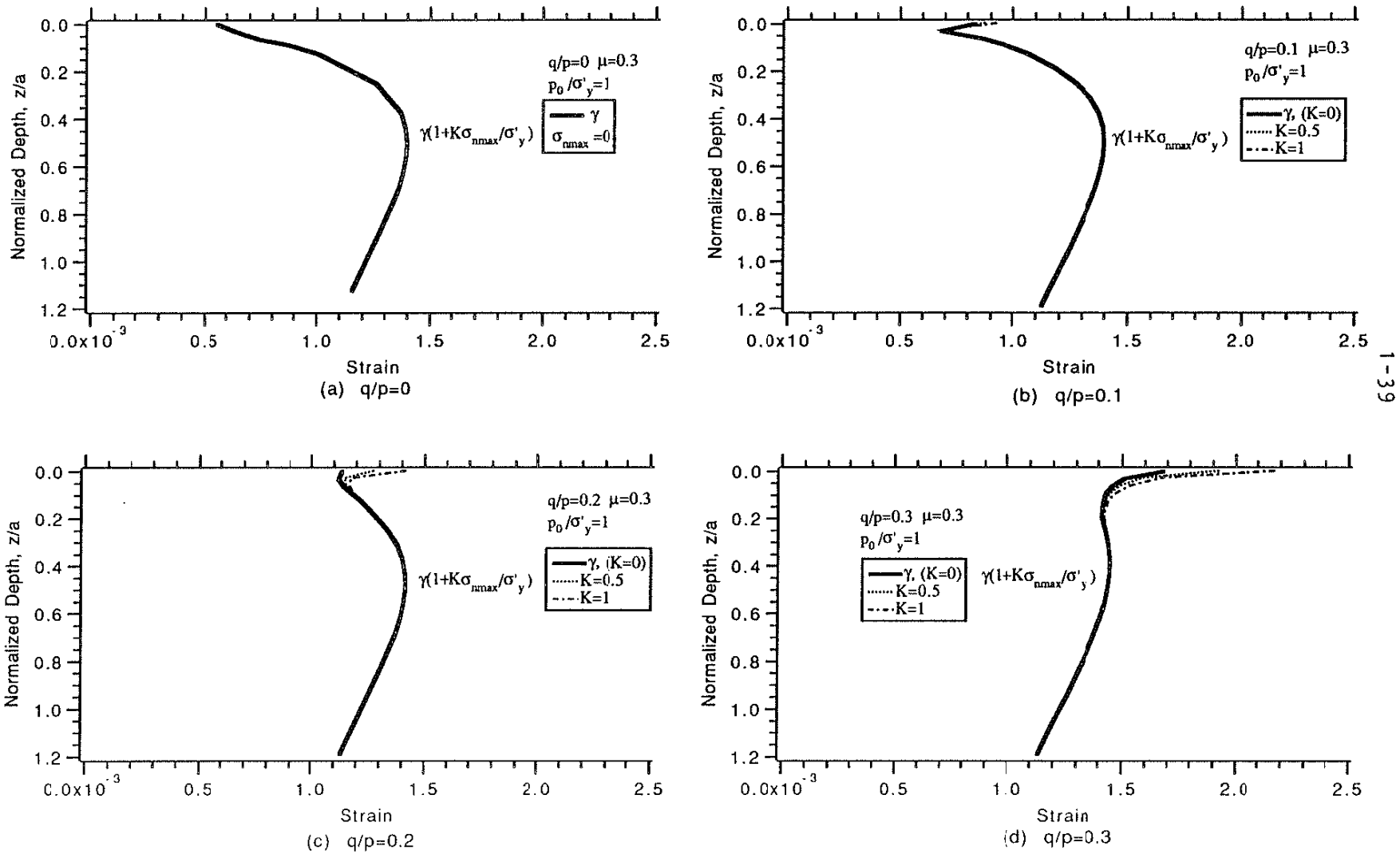

Fig.17 Variation of $\gamma(1+K\sigma_{nmax}/\sigma'_y)$ Parameter along z-axis ($p_0/\sigma'_y=1$)

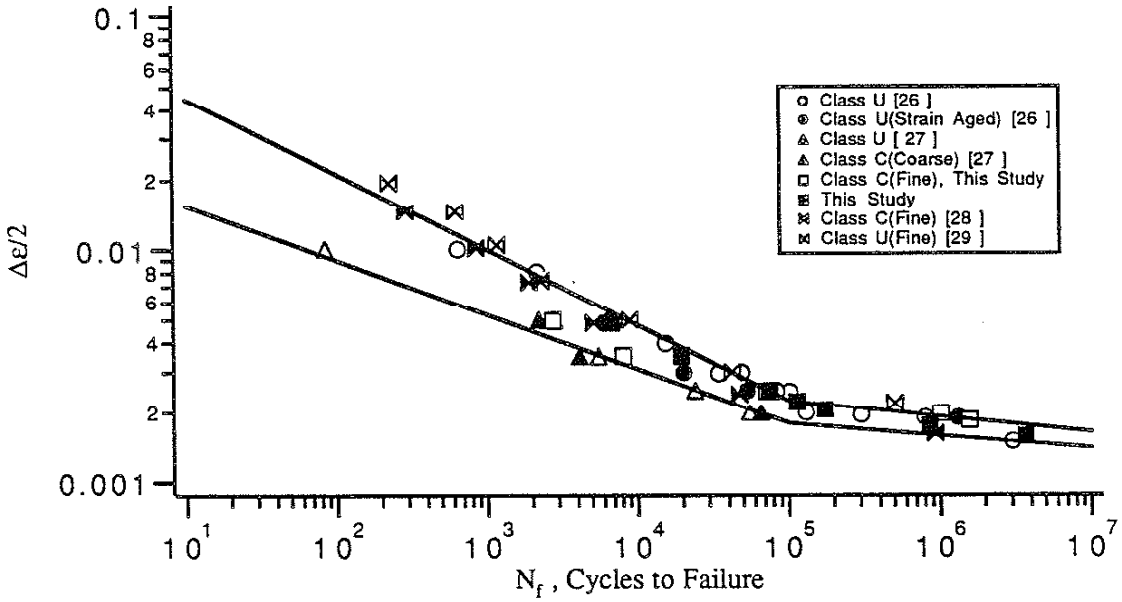

Fig.18 Strain versus Cycles to Failure for Various 1070 Steels.
The lower bound represents Class U and the upper bound represents Class C properties.

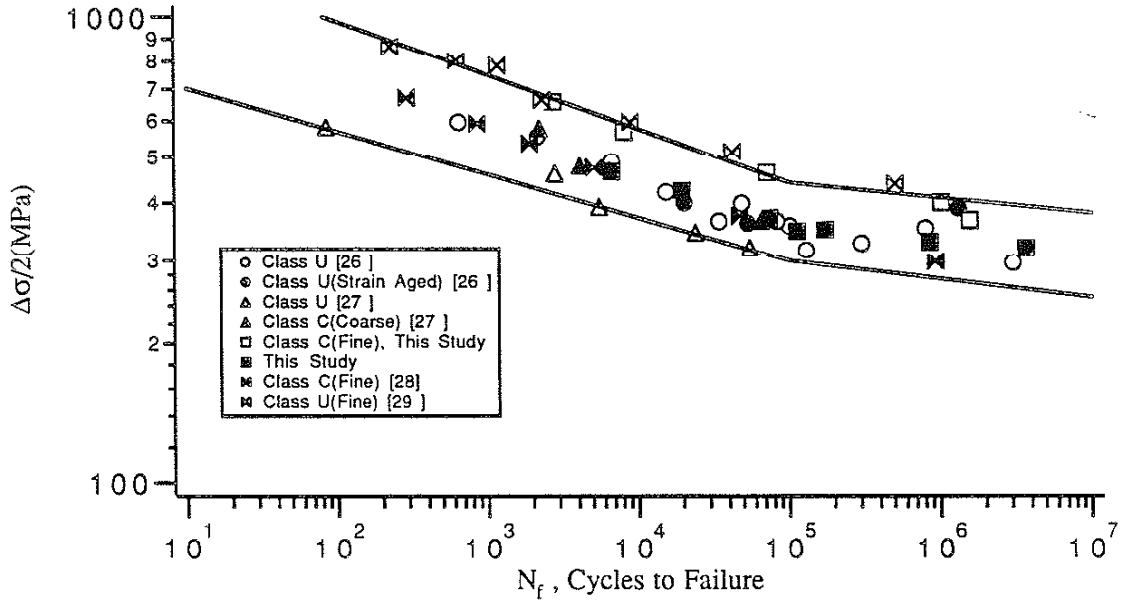

Fig.19 Stress Amplitude versus Cycles to Failure for Various 1070 Steels.
The lower bound represents Class U and the upper bound represents Class C steels.

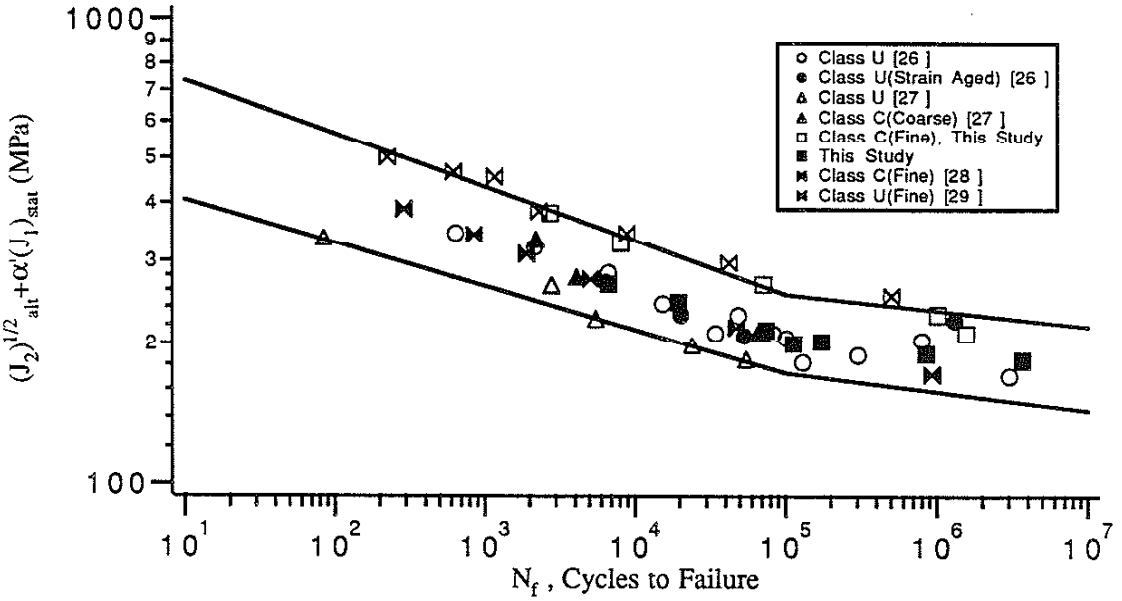

Fig.20 $(J_2)^{1/2}_{alt}+\alpha'(J_1)_{stat}$ Parameter versus Cycles to Failure for Various 1070 Steels.The lower bound represents Class U and the upper bound represents Class C Steels.

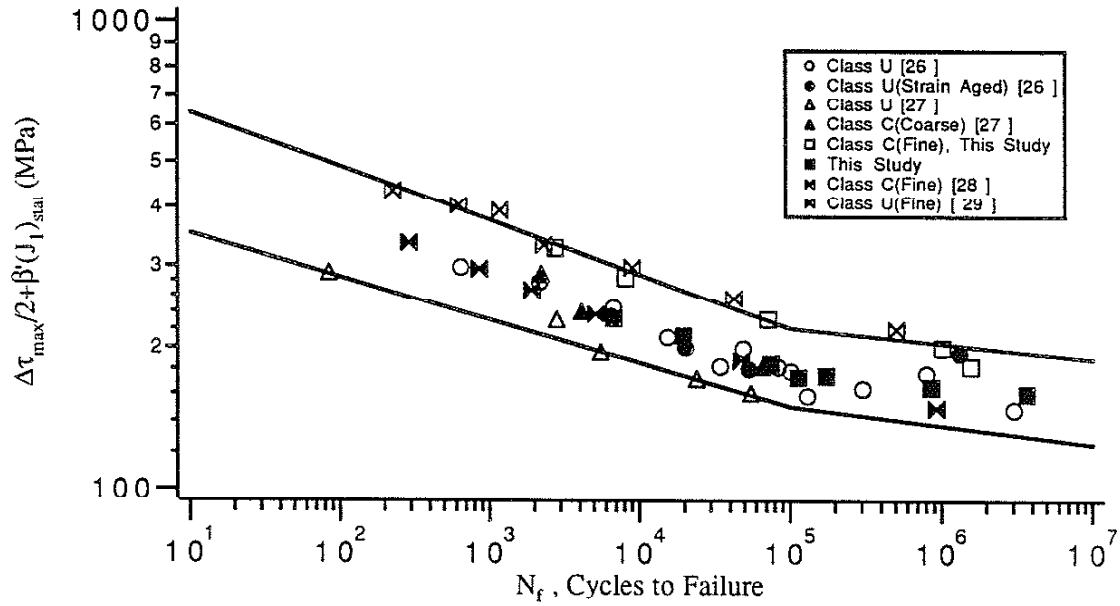

Fig.21 $\Delta\tau_{max}/2+\beta'(J_1)_{stat}$ Parameter versus Cycles to Failure for Various 1070 Steels. The lower bound represents Class U and the Upper Bound represents Class C properties.

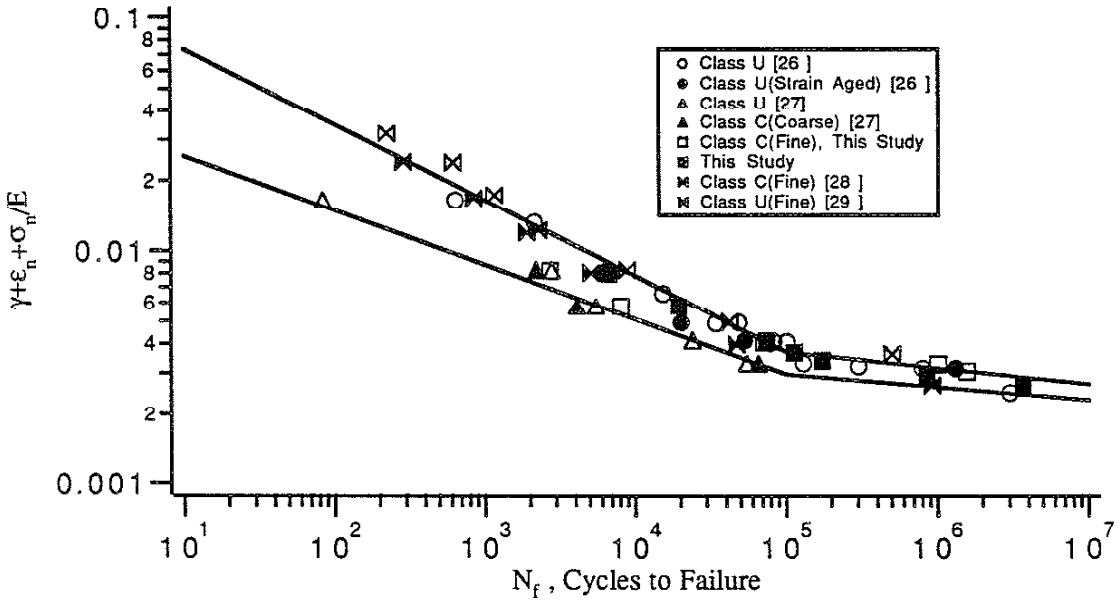

Fig.22 $\gamma+\varepsilon_n+\sigma_n/E$ Parameter versus Cycles to Failure for Various 1070 Steels.
The Lower bound represents Class U and the upper bound represents Class C properties.

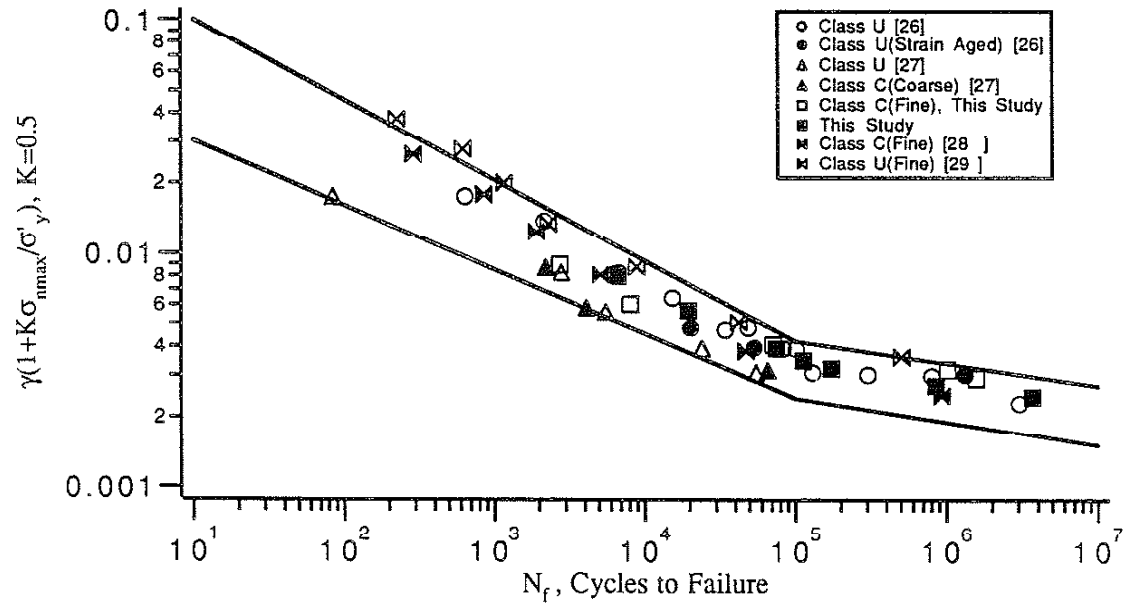

Fig.23 $\gamma(1+K\sigma_{nmax}/\sigma'_y)$ Parameter versus Cycles to Failure for Various 1070 Steels.
The lower bound represents Class U and the upper bound represents Class C properties.

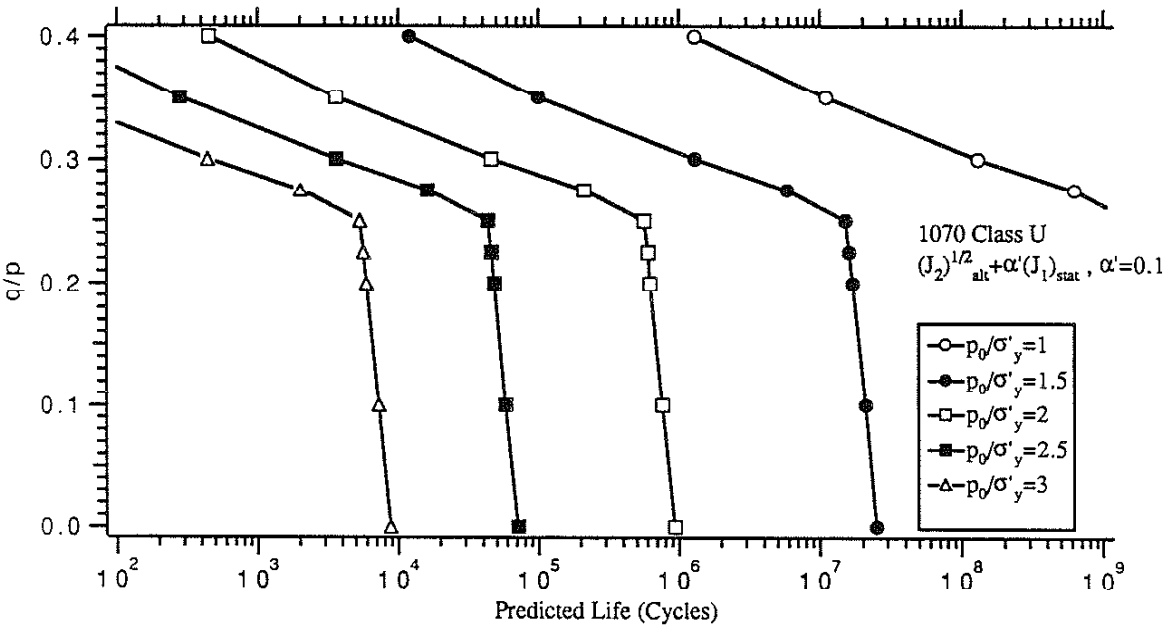

Fig.24 Fatigue Life Prediction Using $(J_2)^{1/2}_{alt}+\alpha'(J_1)_{stat}$ Parameter for Class U Material, $\alpha'=0.1$

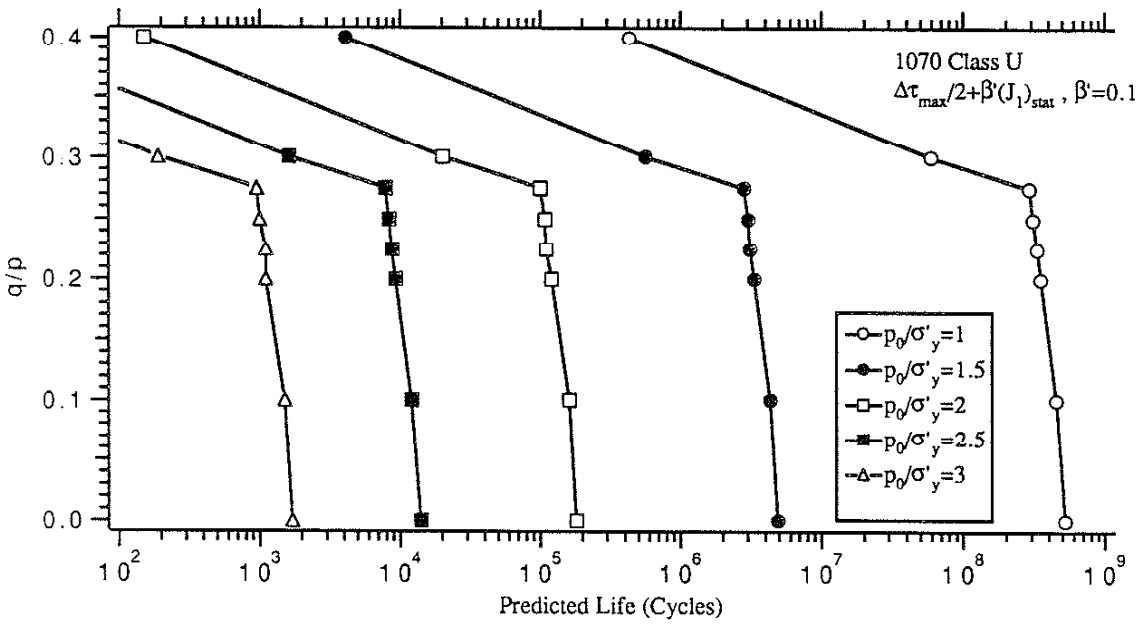

Fig.25 Fatigue Life Prediction Using $\Delta\tau_{max}/2+\beta'(J_1)_{stat}$ Parameter for Class U Material, $\beta'=0.1$

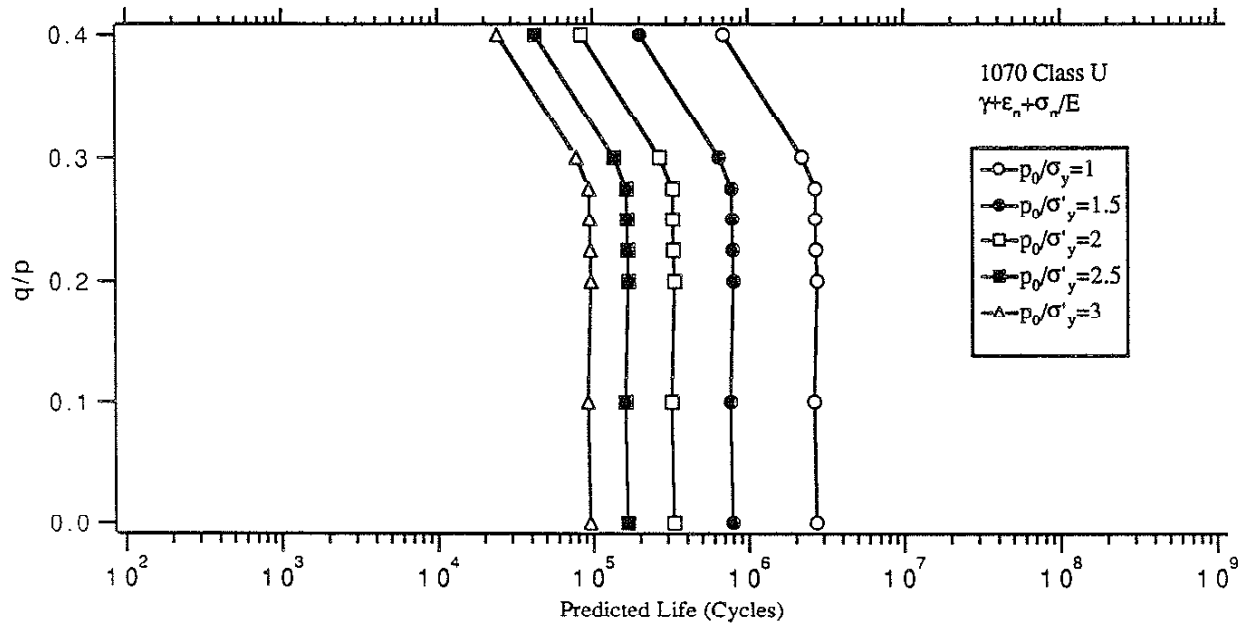

Fig.26 Life Prediction Using $\gamma+\varepsilon_n+\sigma_n/E$ Parameter
for Class U Material

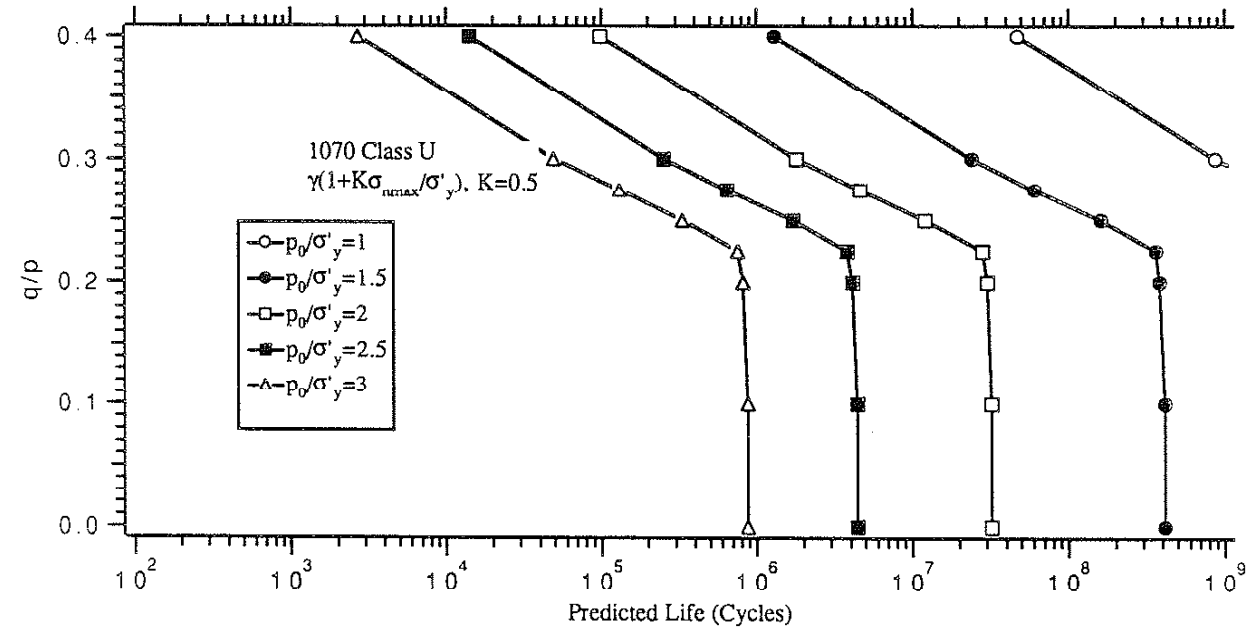

Fig.27 Life Prediction Using $\gamma(1+K\sigma_{nmax}/\sigma'_y)$ Parameter
for Class U Material, K=0.5

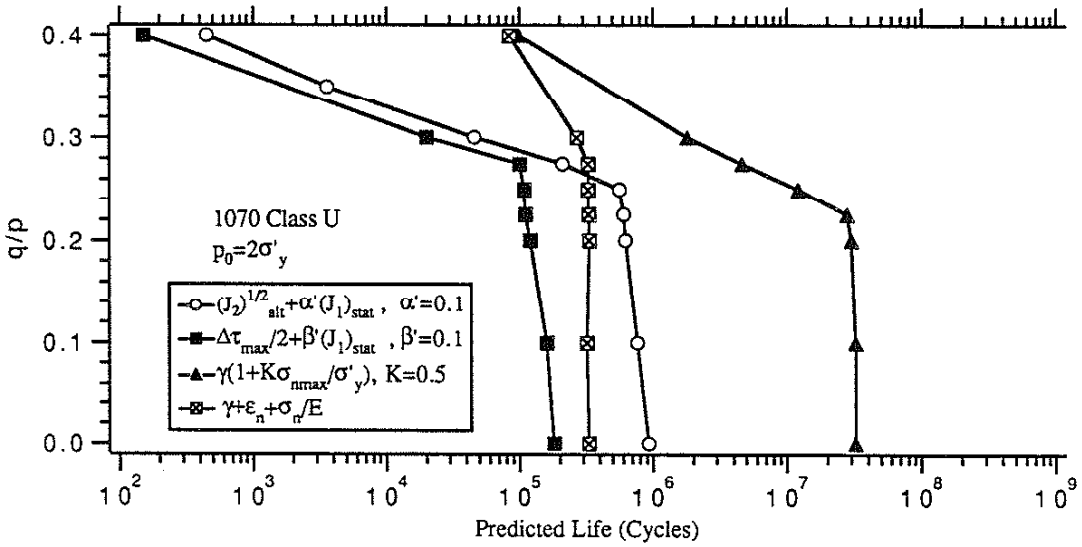

Fig.28 Fatigue Life Prediction with Different Models for Class U Material, $p_0/\sigma'_y=2$

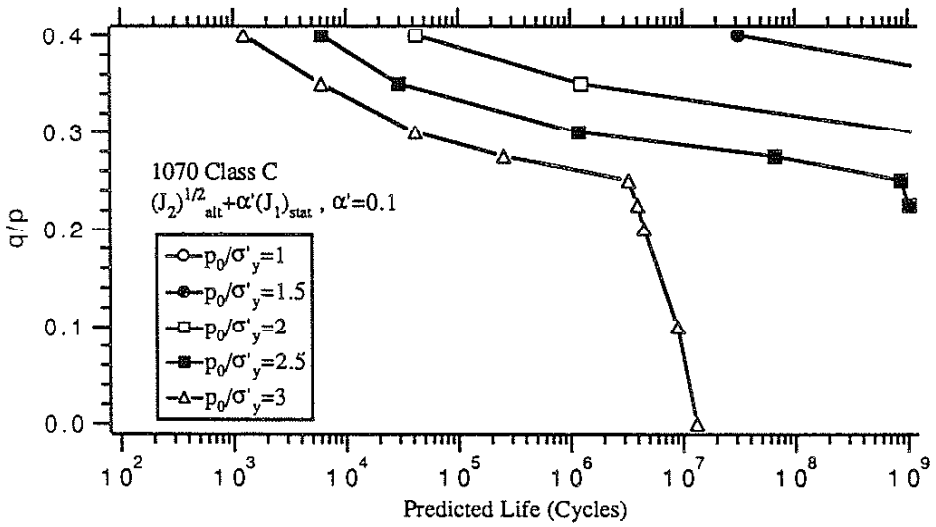

Fig.29 Fatigue Life Prediction Using $(J_2)^{1/2}_{alt}+\alpha'(J_1)_{stat}$ Parameter for Class C Material, $\alpha'=0.1$

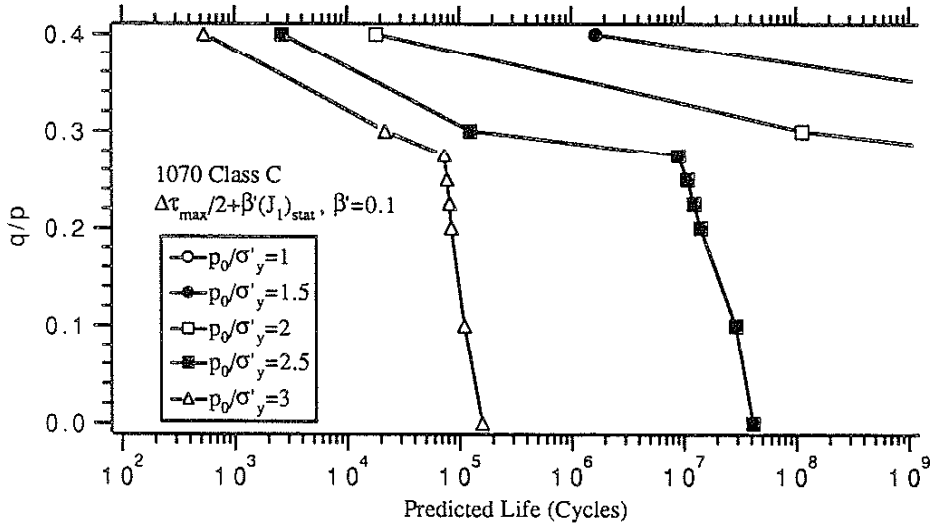

Fig.30 Fatigue Life Prediction Using $\Delta\tau_{max}/2+\beta'(J_1)_{stat}$ Parameter for Class C Material, $\beta'=0.1$

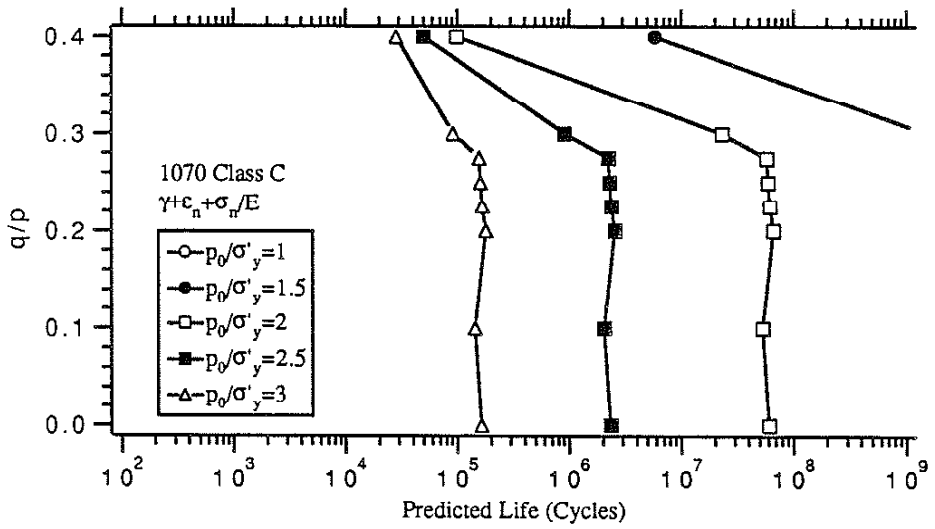

Fig.31 Fatigue Life Prediction Using $\gamma+\varepsilon_n+\sigma_n/E$ Parameter for Class C Material

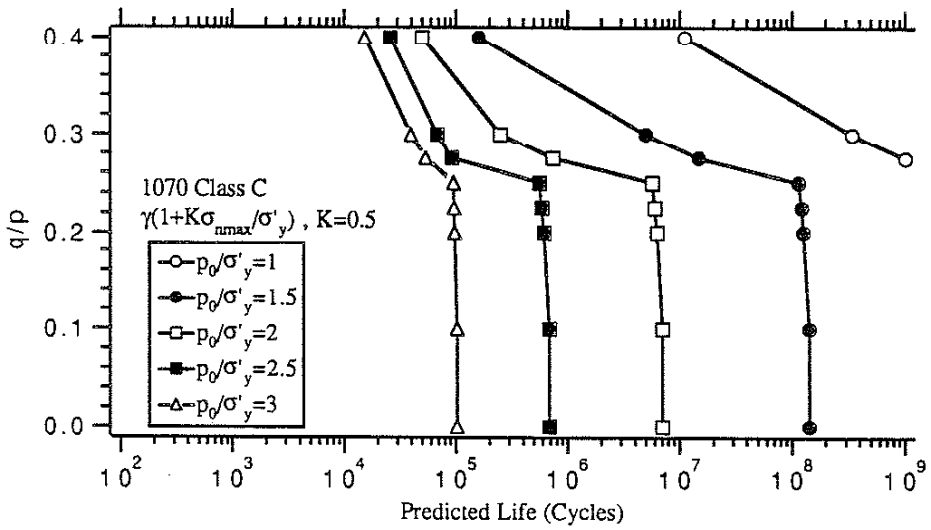

Fig.32 Fatigue Life Prediction Using $\gamma(1+K\sigma_{nmax}/\sigma'_y)$ Parameter for Class C Material, K=0.5

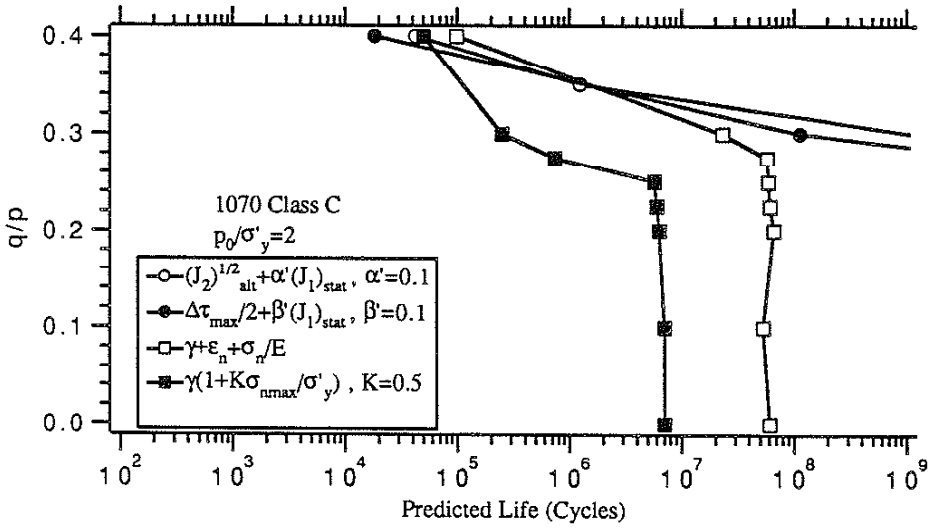

Fig.33 Fatigue Life prediction with Different Models for Class C Material, p_0/σ'_y=2

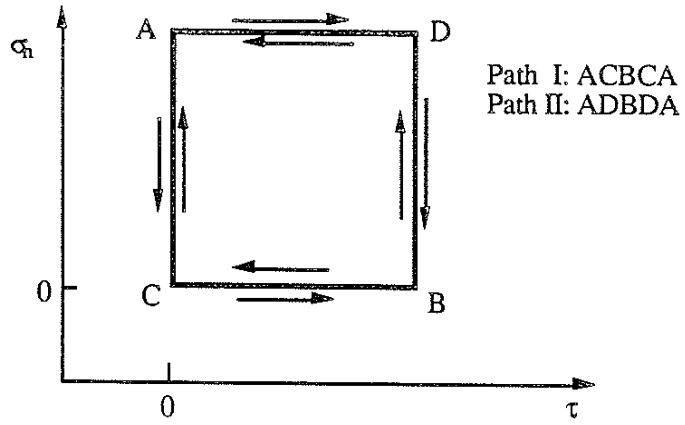

Fig.34 Path Effect: The Limitations of the Models to Handle Non-proportional Loading

Cyclic Stresses for Contact with Different Tangential Load Distributions

Y. Roger Jiang
and
Huseyin Sehitoglu

Report No.2 prepared for
Association of American Railroads

March 1991

Progress Report #2 submitted to Association of American Railroads

Cyclic Stresses for Contact with Different Tangential Load Distributions

Roger Jiang, Research Assistant
Huseyin Sehitoglu, Associate Professor
Department of Mechanical and Industrial Engineering
University of Illinois
Urbana, Il. 61801

Abstract

This study determined the cyclic stresses under line contact for a Hertzian distributed normal force and three different kinds (Type I, II and III) of slip plus stick tangential force distributions. Under slip-stick conditions, the $\Delta\tau_{max}$ location moved to contact surface when the Q/P (Total tangential force/ Total normal force) ratio was as low as 0.1. The magnitude of maximum shear stress range, $\Delta\tau_{max}$, and the orientation of $\Delta\tau_{max}$ plane was established. The variations of shear stress and normal stresses (τ versus σ) on the $\Delta\tau_{max}$ planes changed with different tangential tractions. Slip plus stick conditions were identified for highest maximum shear stress range, $\Delta\tau_{max}$, and highest tensile normal stresses. When Q/P = 0.3, $\Delta\tau_{max}$ reached as high as $0.85p_o$, and the maximum tensile normal stress on the $\Delta\tau_{max}$ plane was as high as $0.7p_o$. The orientation of the planes of $\Delta\sigma_{max}$ and σ_{max} was also established. The $\Delta\sigma_{max}$ and σ_{max} were highest at the contact surface. The $\Delta\sigma_{max}$ was as high as $2.4p_o$ in the Type I, Q/P =0.3 case. We made the important observation that the $\Delta\sigma_{max}$ and $\Delta\tau_{max}$ planes became nearly coincident at increased Q/P levels. The results have direct implications in understanding failure locations, failure planes, fatigue parameters, and designing experiments to study the wheel shelling and spalling phenomena.

Nomenclature

a	Half width of the line contact area
α, β	Angles used to represent the normal to an arbitrary plane
b	Portion of contact width over which stick occurs
$\Delta\tau_{max}$	Maximum shear stress range obtained by surveying all planes
$\Delta\sigma_{max}$	Maximum normal stress range obtained by surveying all planes
f	Friction coefficient between the two bodies in contact
J_1	First stress invariant= $\sigma_1+\sigma_2+\sigma_3$
$(J_1)_{stat}$	Mean value of the first stress invariant
J_2	Second deviatoric stress invariant
$(J_2)^{1/2}_{alt}$	Alternating value of the second deviatoric stress invariant during one cycle
$(J_2)^{1/2}_{max}$	Maximum value of the second deviatoric stress invariant during one cycle
k	Yield stress of the material in simple shear
ξ	The total tangential load Q, divided by the maximum tangential load that the two contacting bodies can support without overall sliding. $Q/fP=\xi$
μ	Poisson's Ratio
p	Hertzian surface pressure on the contact area
p_o	Maximum Hertzian pressure on the contact area
P	Total normal load acting on the contact area
q	Tangential surface traction
q_0	Maximum tangential surface traction
q'_0	Maximum tangential surface traction of the oppositely signed, superimposed, elliptically distributed tangential force
Q	Total tangential load acting on the contact area
σ_{max}	Maximum normal stress obtained by surveying all planes

Introduction

In this study, we examined the variations of the shear stress and normal stress on the plane of maximum shear stress range (the critical plane). We also investigated the $(J_2)^{1/2}_{alt}$, τ_{max}, $(J_2)^{1/2}_{max}$, $(J_1)_{stat}$ and their variation with depth under three tangential traction distributions- Type I, Type II, and Type III. These results were then compared with the Type 0 case, examined in AAR Progress Report #1 [1], where shear tractions were proportional to normal tractions over the entire contact area.

In early studies, Thomas and Hoersch [2], Radzimovsky [3], Smith-Liu [4], Mitsuda [5], and Sackfield and Hills [6-7] determined stresses under contact loading. However, none of these investigators determined the range of maximum shear stress, normal stress range and/or $(J_2)^{1/2}_{alt}$ needed for contact fatigue analysis. In real contact situations, the tangential forces are not proportional to the normal force over the contact area; instead, a combination of slip and stick regions develops. The maximum shear stress ranges and maximum normal stress ranges will be modified under slip- stick conditions compared to the Type 0 case. The report provides a comparison of cyclic stresses for different traction conditions.

Description of the Load Distributions and the Representation of a Plane

When two elastic bodies are rolling, stick could occur between the surfaces within the contact area [8]. Therefore, the contact area could be divided into a region of slip and a 'locked' or stick region of non-slip. In steady rolling, the stick area extends to the edge of the contact where the material is entering the contact. The relative slip occurs after material had passed through the stick area [9]. Three different types of shear traction distributions are shown in Figures 1(a)-1(c), classified as Type I, Type II and Type III, to represent the stick slip conditions observed in reality.

The 'x' direction denotes the rolling direction and the half contact width is 'a'. The shear traction for Type I and Type II cases can be mathematically described as:

$$q=q_0[1-(x/a)^2]^{1/2}-q'_0[1-((x \pm c)/b)^2]^{1/2}$$

where the + sign holds for the Type I distribution and the - sign holds for the Type II distribution. The distribution of tangential force for the Type III case is expressed as:

$$q=q_0[1-(x/a)^2]^{1/2}-q'_0[1-(x/b)^2]^{1/2}$$

The maximum normal pressure is p_0, then $q_0=f \cdot p_0$ where f is the friction coefficient. Q denotes the total tangential load; P is the total normal load, and $Q/P = f \cdot \xi$. Additionally, we define $q_0/q'_0 = a/b$, $f \cdot \xi = Q/P = f[1-(q'_0/q_0)^2]$, and $b = a(1-\xi)^{1/2}$ and $c = a-b= a[1-(1-\xi)^{1/2}]$. In this study, f and ξ were input parameters.

Under dry contact of two bodies undergoing elastic deformation, the normal pressure distribution is elliptical over the contact area [10,11]. The tangential force, however, is described by the Carter-Poritsky distribution [12-14]. Figures 1(a) and 1(b) depict two stick-slip combinations, Type I and II, respectively. The tangential force on a locomotive wheel or a driving wheel under steady rolling conforms to Type I. Type II is, then, the equal and opposite shear distribution transferred to the second body. In Figure 2(a), Type I and Type II coexist in the driving and driven cylinders, respectively. Prior to reaching steady rolling, the tangential force distribution would be of Type III [15] which corresponds to rolling starting from rest. Type I and Type II are generally the cases when rolling is stable [16]. The superposition of two elliptically distributed loadings of opposite sign resulted in these three cases.

The coordinate system is the same as that used in AAR Report #1 [1]. The normal pressure distribution is shown in Figure 3. The orthogonal stress directions, namely σ_x, σ_y, σ_z, τ_{xz}, are labelled on an element cube. The depth is the 'z' direction. First, orthogonal stresses were determined based on Smith and Liu [4] formulas. An arbitrary plane Q' with a normal n was identified through the angles α and β. The normal stress on the arbitrary plane Q' is σ and the shear stress on this plane is τ. The variation of shear stress is

indicated on the plane Q' in Figure 5. The shear stress vector may rotate on the plane Q'. The maximum shear stress range on plane Q' is denoted as $\Delta\tau^{Q'}_{max}$. All possible planes were traced by varying α and β in incremental form and $\Delta\tau^{Q'}_{max}$ was calculated for each plane. By surveying all possible planes, the plane of maximum shear stress range, $\Delta\tau_{max}$, was established. Two orthogonal planes were discovered that experienced $\Delta\tau_{max}$ and were termed the 'critical planes'. One of these planes experienced higher tensile maximum stress and is expected to govern fatigue failure.

The alternating value of the second stress deviator in a cycle was:

$$(J_2)^{1/2}_{alt}=0.5\text{Max}\{[(\Delta S_{xx}-\Delta S_{yy})^2+(\Delta S_{yy}-\Delta S_{zz})^2+(\Delta S_{zz}-\Delta S_{xx})^2 + 6(\Delta S^2_{xy}+\Delta S^2_{yz}+\Delta S^2_{zx})]/6\}^{1/2} \quad .$$

'Max' denotes maximizing the quantity inside the brackets { } with respect to time, and $\Delta S_{ij}=\sigma_{ij}(t_1)-\sigma_{ij}(t_2)$=stress differences, $\sigma_{ij}(t_1)$=stress component at time t_1, $\sigma_{ij}(t_2)$=stress component at time t_2.

Determination of Stresses

For Type I, II and III tangential loadings, the friction coefficient, f, was taken as 0.6 [17] and Poisson's ratio, μ, was 0.3. Calculations were made for Q/P (Total tangential load/Total normal load) ratios of 0.1, 0.2, 0.3 and 0.4. All the stresses and the stress based parameters were normalized with respect peak normal pressure, p_o. All the distances were normalized with respect to the half contact width, a.

Type I Case

Orthogonal stress variations (σ_x, σ_y, σ_z, τ_{xz}) with x (note that x also can represent time) at depths of z/a=0, 0.5 and 1 are given in Figures 6-8 for the Type I case. In these simulations, f=0.6 and Q/P=0.1(ξ=1/6), Q/P=0.2(ξ=1/3) and Q/P=0.3(ξ=0.5). We note in Figure 6(a) that the presence of increased slip in the region -a < x < c-b resulted in an increase in σ_x component approaching

$0.6p_o$. The corresponding principal stresses, σ_1, σ_2, σ_3, are presented in Figures 9-11. Figures 12 through 14 depict the Tresca shear stresses, τ_{max}, Von Mises effective stress, $(J_2)^{1/2}$, and the hydrostatic stresses, $J_1/3$. Note the presence of high compressive hydrostatic stresses at $z/a=0$. The variations of $(J_2)^{1/2}_{alt}$, $(J_2)^{1/2}_{max}$, $(J_1)_{stat}$ and τ_{max} are given as functions of depth in Figures 15(a)-15(d). $(J_1)_{stat}$ represents the mean value of the first stress invariant. A third of $(J_1)_{stat}$ is, then, the mean hydrostatic stress during a single rolling pass.

The variations of the orthogonal shear stress range, $\Delta\tau_{xz}$, as a function of depth, z/a, are provided in Figure 16. The maximum orthogonal shear stress range, $\Delta\tau_{xzmax}$, occured on the surface when $Q/P \geq 0.25$. We may contrast these results with, $\Delta\tau_{max}$, maximum shear stress range obtained by surveying all material planes shown in Figure 17. The magnitude of $\Delta\tau_{max}$ was $0.50p_o$, $0.68p_o$, and $0.82p_o$ for Q/P values of 0.1, 0.2 and 0.3, respectively. The results are summarized in Table III; the orientations of the normal for the planes of maximum shear stress range were $\alpha=0°$, and $\beta = 87°/-3°$, $67°/-23°$ and $66°/-24°$ for Q/P=0.1, 0.2, 0.3, respectively.

The $\alpha=0°$ was a common feature of the critical plane orientation for different Q/P values. Note that this does not imply that all the critical planes had $\alpha=0°$. We provide results in Table II where $\alpha=45°$ when f=0.4.

Type II Case

Orthogonal stress variations (σ_x, σ_y, σ_z, τ_{xz}) with time are given at depths of $z/a=0$, 0.5 and 1 in Figures 18-20. In these simulations, we considered f=0.6 and Q/P=0.1($\xi=1/6$), Q/P=0.2($\xi=1/3$) and Q/P=0.3 ($\xi=1/2$) respectively. We note in Figure 18 (a) that the normal stress σ_x undergoes a subcycle at $x>c$. In contrast to Type I, σ_x remained compressive in Type II. The corresponding principal stresses σ_1, σ_2, σ_3 are presented in Figures 21-23. The Tresca shear stresses τ_{max}, Von Mises effective stress $(J_2)^{1/2}$ and the hydrostatic stresses, $J_1/3$, are given in Figures 24 through 26. The variations of $(J_2)^{1/2}_{alt}$, $(J_2)^{1/2}_{max}$, $(J_1)_{stat}$ and τ_{max} as functions of depth are given in Figure 27(a)-27(d).

The variations of orthogonal shear stress range, $\Delta\tau_{xz}$, as a function of depth, z/a, are provided in Figure 28. We note that $\Delta\tau_{xzmax}$ occured on the surface

when the Q/P ratio was 0.3 and had a magnitude of $0.54p_o$. The variation of $\Delta\tau_{max}$ along the depth is shown in Figure 29. The magnitudes of $\Delta\tau_{max}$ were $0.50p_o$, $0.68p_o$, and $0.82p_o$ for Q/P ratios of 0.1, 0.2 and 0.3, respectively. Table IV summarizes the findings. The $\Delta\tau_{max}$ planes were oriented with normal angles α=0° and, β= 85°/-5°, 23°/-67° and 24°/-66° for Q/P=0.1, 0.2, 0.3, respectively.

Type III Case

Orthogonal stress variations (σ_x, σ_y, σ_z, τ_{xz}) with time are given at depths of z/a=0, 0.5 and 1 in Figures 30-32. In these simulations, we considered f=0.6, Q/P=0.1(ξ=1/6), Q/P=0.2(ξ=1/3) and Q/P=0.3 (ξ=1/2) respectively. Note the presence of two σ_x subcycles in Figures 30-32 for a single rolling pass. The corresponding principal stresses σ_1, σ_2, σ_3 are presented in Figures 33 through 35. We note, in Figures 36-38, the Tresca shear stresses τ_{max}, Von Mises effective stress $(J_2)^{1/2}$ and the hydrostatic stresses, $J_1/3$. The variations of $(J_2)^{1/2}_{alt}$, $(J_2)^{1/2}_{max}$, $(J_1)_{stat}$ and τ_{max} as functions of depth are given in Figures 39(a)-39(d).

The variations of the orthogonal shear stress range, $\Delta\tau_{xz}$, as a function of depth, z/a, is provided in Figure 40. We note that the maximum orthogonal shear stress ranges occured at the subsurface for all the three Q/P ratios. The magnitude of $\Delta\tau_{xzmax}$, $=0.50p_o$, did not increase with increasing Q/P ratio. The variation of maximum shear stress range along the depth is shown in Figure 41. The magnitude of $\Delta\tau_{max}$ was $0.50p_o$, $0.69p_o$, and $0.85p_o$ for Q/P values of 0.1, 0.2 and 0.3 respectively. The results are summarized in Table V. The $\Delta\tau_{max}$ planes are oriented with normal angles α=0° and β= 86.5° /-3.5°, ±45° and ±45° for Q/P=0.1, 0.2, 0.3, respectively.

Variation of Normal Stress and Shear Stress on the Critical ($\Delta\tau_{max}$) Planes

As noted earlier in Figure 5, shear stress in an arbitrary plane is a vector that is represented by its direction and magnitude. Only when α=0°, the shear stress vector is fixed on the plane as shown in Figure 10 in AAR Report #1. In such special cases, the shear stress on the critical plane may be described as a

scalar quantity with positive sign representing one direction and negative sign representing the opposite direction.

Figures 42-44 show the variations of shear stress and normal stress on the critical plane with time (or x/a) on the left hand side of the page. On the right hand side of the page, the relation between the shear stress and the normal stress on the critical plane is available. Figure 42 corresponded to Type I case, Figure 43 corresponded to Type II case and Figure 44 described the Type III case. In Figures 45-47, similar results are shown on the alternate critical planes that lied perpendicular to those in Figures 42-44. The shear stresses and normal stresses, in Figures 42-47, for a given Q/P ratio, were greater than the results given in AAR Report #1 for Type 0 case.

For Type I tangential traction distribution, the maximum shear stress range, $\Delta\tau_{max}$, was $0.82p_o$ when Q/P=0.3. For Type I cases, Q/P=0.2 and 0.3 (Figure 42(b)(c) and Figure 45(b)(c)), when the shear stress was a minimum, the normal stress was a maximum, and when the shear stress was a maximum the normal stress was a minimum. The shear stress-normal stress variation on the critical plane was non-proportional. For Type I, Q/P=0.3 case, the maximum normal stress on the α=0° β=-24° plane was 0.7 p_o which exceeded the maximum normal stress of $0.2p_o$ on the α=0° β=66° plane.

For Type II tangential traction distribution, the maximum shear stress range, $\Delta\tau_{max}$, was $0.82p_o$ when Q/P=0.3. The maximum normal stresses on the 24° and -66° planes were $0.3p_o$ and $0.1p_o$ respectively. The Type II cases for Q/P=0.2 and 0.3 are indicated in Figures 43(b)(c) and 46(b)(c)) respectively. In Figure 43 (b) and (c), the normal stress was a maximum at a small shear stress, and the normal stress was a minimum when the shear stress was zero. The history in Figure 46(b) and 46(c) resembled a bow-tie, and the history was highly non-proportional. The highest shear stress range of the cycle corresponded to a compressive mean normal stress.

For Type III tangential traction distribution, the maximum shear stress range, $\Delta\tau_{max}$, was 0.85 p_o when Q/P=0.3. The maximum normal stress on these planes was $0.4p_o$. In Figure 47(b) and 47(c) note that the maximum of shear stress and normal stress coincided, while the minimum shear stress coincided

with zero normal stress level. In Figures 47(b) and 47(c), it was interesting that for one shear cycle, there were two normal stress cycles - a major cycle and a smaller subcycle. A subcycle with a much lower range existed in Figure 44(b) and 44(c).

Equivalent Normal and Traction Loads for Initial Yielding and for Maximum Shear Stress Range

The results showing the equivalent p_o/k and Q/P levels to initiate first yielding are given in Figure 48. Tresca yield criteria was used, which corresponded to $\tau_{max}/k=1$, and Type 0, I, II and III cases were presented. The Type I, Type II and Type III tangential traction distributions required lower p_o/k and Q/P combinations to reach $\tau_{max}/k=1$ than Type 0 case. The results given in Figure 48 agreed with selected cases investigated by K.L.Johnson [8,16].

The contribution of this study was to establish the p_o/k and Q/P combinations that resulted in a given $\Delta\tau_{max}/k$ ratio. In Figure 49, the p_o/k and Q/P levels are plotted for $\Delta\tau_{max}/k=0.5$. Note that the loads required are far below those to initiate yielding. The p_o/k levels were less than 1 and as low as 0.6, depending on the traction type, to obtain $\Delta\tau_{max}/k=0.5$. The $\Delta\tau_{max}/k=0.5$ value was chosen as this is the shear stress range that would correspond to approximately 10^7 cycles in a uniaxial test. Type I and II resulted in similar levels of p_o/k to achieve $\Delta\tau_{max}/k=0.5$. Corresponding p_o/k values for Type III were lower. The normal stresses corresponding to Types 0, I, II and III differed, therefore; differences in fatigue among these four types are noteworthy.

Variation of Normal Stress and Shear Stress on the Plane of $\Delta\sigma_{max}$

The variation of normal stress and shear stress on the planes of maximum normal stress range are shown in Figures 50 for Type 0 and I and in Figure 51 for Type II and III cases. We note that the maximum normal stress range occured at z/a=0 for Types 0, 1, II and III. It is worth noting the following: (1) the maximum normal stress range in Figure 50(f) is as high as 2.364 p_o for the Type I, Q/P=0.3 case, (2) the normal stresses exhibited an R ratio ($=\sigma_{min}/\sigma_{max}$

) approaching -1 for the Type I and III cases; the Type 0 and Type II resulted in R ratios less than -1, (3) the orientation of the maximum normal stress range plane, β, is in the range 0° to 45°.

The Orientation of $\Delta\sigma_{max}$ planes

We note that the planes of $\Delta\sigma_{max}$, given in Figures 50 and 51, were not inclined 45° to the planes of $\Delta\tau_{max}$, given in Figures 45-47. This behavior has been noted in non-proportional stress cycling conditions and our experiments (see forthcoming Report #3) under compression and torsion confirm this phenomena. To gain further insight into the orientations where $\Delta\sigma_{max}$ and σ_{max} occured, we consider Figures 52- 55 where $\Delta\sigma$, $\Delta\tau$ and σ_{max} were given at $z/a=0$. In Figure 52 $\Delta\tau$, $\Delta\sigma_{max}$ and σ_{max} were plotted versus the angle β for Type 0 case. The maximum value of $\Delta\tau$ occured at $\beta=\pm$ 45° and the plane where σ_{max} was a maximum was $\beta=0°$ plane. For the case $Q/P=0.3$, $\Delta\sigma_{max}$ and $\Delta\tau_{max}$ occured on the surface. The angle between $\Delta\tau_{max}$ and $\Delta\sigma_{max}$ was less than 45°. The results for Type I case are shown in Figure 53. We note that the variation of $\Delta\tau$ with angle β appears small relative to the variation of $\Delta\sigma_{max}$ with β in $Q/P=0.1$ case. When $Q/P=0.2$ and 0.3, the $\Delta\sigma_{max}$ and $\Delta\tau_{max}$ occured on the surface therefore, the curves in 53(b) and 53(c) may be directly compared. The angle between $\Delta\tau_{max}$ and $\Delta\sigma_{max}$ was less than 45°. The results for Type II are shown in Figure 54. The most interesting result here is that, for the $Q/P=0.3$ case, the planes of $\Delta\tau_{max}$ and $\Delta\sigma_{max}$ are practically coincident. The results for Type III are indicated in Figure 55. The planes of $\Delta\tau_{max}$ and $\Delta\sigma_{max}$ planes approached each other as Q/P ratio increased from 0.2 to 0.3. It is worth noting that the plane of σ_{max} coincided with the x-direction ($\beta=0°$, $z/a=0$) for all cases (Types 0, I, II, III) considered.

Discussion of Results

τ_{max} Behavior: When $Q/P\geq0.085$ the maximum shear stress, τ_{max}, occured on the surface for both Type I and Type II tangential tractions. For Type III, the maximum shear stress occured on the surface when $Q/P\geq0.155$. We may compare these results to Table 1 (Type 0 case) where the maximum shear stress occured on surface whenever $Q/P\geq0.25$. Therefore, Types I, II and III

caused the maximum shear stress to occur on the surface at a lower value of Q/P than the Type 0 case. The τ_{max}'s in Type I and Type II tangential loadings were greater than τ_{max} in the Type III and Type 0 cases as noted in Tables I, III-V. In view of the results presented in Figure 48, for the same Q/P ratio, the contact pressure was the smallest at first yield when the tangential loading was Type I or Type II. Type 0 required the highest value of contact pressure, with the Type III curve lying between these two extremes.

$\Delta\tau_{max}$ Behavior: Referring to Tables III-V, the maximum shear stress range was the largest for the Type III case, almost equal for Type I and Type II for the same Q/P ratio. The orientations differed for the planes of maximum shear stress ranges. Furthermore, the normal stresses for Types I-III were very different. Therefore, it is not wise to select the worst case based on $\Delta\tau_{max}$ alone.

The maximum shear stress range, $\Delta\tau_{max}$, occured on the surface when $Q/P \geq 0.13$ for Type I and Type II. When $Q/P \geq 0.105$, $\Delta\tau_{max}$ occured on the surface for Type III tangential loading. It is worth recalling that for Type 0 the maximum shear stress range occured on the surface only when $Q/P \geq 0.225$ [1]. Comparing the results in Figure 48 with those in Figure 49, we find that the contact pressure was much higher for first yield than for $\Delta\tau_{max}/k=0.5$. Furthermore, in Figure 48, the curves for Type I and II are the lower bounds while in Figure 49 the curve for Type III was the lower bound. It is clear from these results that τ_{max} and $\Delta\tau_{max}$ behaviors differed. Nevertheless, for both the first yield and $\Delta\tau_{max}/k$=constant, Type 0, the proportional tangential loading type, required the highest contact pressure for the same Q/P ratio.

$\Delta\sigma_{max}$ and σ_{max} Behavior : When tangential load/ normal load ratios were 0.2 and 0.3 (Type I, II and III), the planes of $\Delta\tau_{max}$, $\Delta\sigma_{max}$ were inclined at an angle far less than 45° relative to each other. However, the planes of tensile σ_{max} were near 0° for all cases considered. Only careful experiments that produce similar variations in shear stress and normal stress will show precisely which planes will be most prone to fatigue damage. These experiments are currently underway.

Fatigue and Failure Locations: The variations of $(J_2)^{1/2}_{alt}$ were similar to those of the maximum shear stress ranges, $\Delta\tau_{max}$. This suggested that the two forms

of Sines' criterion ($(J_2)^{1/2}_{alt}$ versus $\Delta\tau_{max}$) discussed in AAR Report #1[1] were nearly identical. Type 0 produced the largest compressive hydrostatic stress, which was $-0.43p_0$ on the surface (Refer to Figure 3(e) in AAR Report #1 [1]). The Q/P ratio had very little influence on the mean value of the hydrostatic stress for all types of tangential loadings. For Types I- III, the maximum hydrostatic stresses within a cycle occured at z = 0.06a, and ranged from $-0.35p_0$ to $-0.41p_0$ for the Q/P ratios between 0.1 and 0.3.

For Types I-III when Q/P ratio increased above 0.11, the $\Delta\tau_{xzmax}$ location moved to the surface and the $\Delta\tau_{xzmax}$ value increased with increasing Q/P ratio. When Q/P was less than 0.11, the type of tractions, Types 0-III, influenced τ_{xzmax} and τ_{xzmin}, but the $\Delta\tau_{xzmax}$ was the same for these cases. When $\Delta\tau_{xzmax}$ occured at z=0.54a, it had a value of $0.5p_0$ irrespective of type of tangential tractions.

The tangential loading type and the Q/P ratio had little influence on the stresses for z≥a. When Q/P≥ 0.1, the possible main controlling parameters of fatigue such as the τ_{max}, $\Delta\tau_{max}$, $(J_2)^{1/2}_{max}$ and $(J_2)^{1/2}_{alt}$ all occured on the contact surface (z/a=0). From Figures 17, 29 and 41, the maximum shear stress ranges had very large gradients within z/a< 0.1. This suggested that in a finite element analysis element size should be about a/50~a/100 in z-direction to account correctly for the stresses and strains in the depth direction. Unfortunately, this was not considered in the finite element analyses published in literature [18-20].

The existence of a tangential force caused the stresses to vary sharply with time on the surface. The peaks in the shear stress and normal stress plots are clearly visible in Figures 42(b)(c)-47(b)(c). These peaks are easily missed if care is not taken in their calculation in finite element studies. To avoid problems, the translation of the roller (wheel) should be chosen over extremely small elements (element size should be about a/50~a/100 in x-direction).

The $\Delta\tau_{max}$ occured on the surface when Q/P≥0.13 for Type I and Type II tangential loadings, and Q/P≥0.105 for Type III tangential loading (f=0.6, μ=0.3). The most damaging stress states occured in a very thin layer below and including the contact surface when Q/P≥ 0.13 and 0.105. When Q/P was less

than these limiting values, the location of initial plastic deformation was subsurface while the location of $\Delta\tau_{max}$ and normal stress range that result in fatigue damage was still at the surface. Residual stresses will form at subsurface when Q/P=0.2 (Type 0), as reported by Hahn and his co-workers [18-20]. Without going into elastic-plastic analysis, it was easy to see that for Type I, II or III residual stresses would be highest on the surface.

Due to the tangential tractions, the maximum normal stress on the critical plane was always tensile within the thin affected layer. The thickness of this layer was 0.1a. Beyond this layer, the maximum normal stress on any plane was zero or compressive. We further note that the maximum normal stress was always zero in Figures 42(a)-45(a) when the maximum shear stress range occured near z=0.5a. Therefore, the critical plane parameter, $\gamma(1+K\sigma_{nmax}/\sigma_y)$ would not be discriminating in these cases, since when σ_{nmax} was zero, the parameter was reduced to γ. Then, the fatigue lives, according to this parameter, should be the same as that obtained in a pure shear experiment. Unfortunately, the real life situation is far more complicated, and the quest for finding the correct fatigue parameter for compressive loading regime continues.

Actual tangential loads experienced by railroad wheels are a combination of three types shown in Figure 1. The locomotive wheels are subjected to Type I tangential loading, and the car wheels experience Type II. Type III develops when a train starts from rest. Type III tangential forces caused larger shear stress ranges than Type I and Type II. The stresses produced by the combined loads could complicate our analysis and are not examined at this time.

Summary

1) As Q/P ratio was increased above 0.1 for Type I, II and III cases, the critical location moved to the surface and $\Delta\tau_{max}$ was a strong function of Q/P ratio. The results proved that the maximum normal stress on the critical planes for Type I, II and III were tensile and their magnitude approached p_o.

2) The maximum shear stress range was similar for Type I and Type II tangential traction distributions, and higher for Type III tangential traction

distribution. However, the maximum normal stress was the highest for Type I. Our experiments on 1070 steel under compression-torsion exhibited great sensitivity to maximum tensile stresses, therefore the damage levels in Type I could exceed Type II and III. Moreover, Types I, II and III resulted in significantly higher shear stress ranges and maximum normal stresses compared to Type 0 case.

3) For the Type III case, on the $\Delta\tau_{max}$ plane, we discovered two normal stress cycles - a major cycle and a subcycle under a single rolling pass. The subcycle was in compression and coincided with zero shear stress. The damage accumulation rate is expected to increase when subcycles interact with the major cycle.

4) There were two planes where $\Delta\tau_{max}$ was a maximum for all types of tractions considered. In Type 0, I, II and III one of these planes of $\Delta\tau_{max}$ experienced higher maximum stress and higher stress range than the other.

5) The planes of $\Delta\tau_{max}$ and $\Delta\sigma_{max}$ were no longer inclined 45° to each other at $z/a=0$ and when Q/P ratio was 0.2 and 0.3. This suggested that the most damaging plane where $\Delta\tau_{max}$, $\Delta\sigma_{max}$ occured may coincide, such as in Type II, $Q/P=0.2$ and 0.3 case. Only experiments can reveal the plane most conducive to fatigue damage under these conditions.

6) When Q/P was larger than about 0.1, the high cyclic stresses developed at the contact surface for the three types of tangential loadings. The stress gradients in z-direction were very large; therefore, in a finite element analysis, the mesh size should be fine enough to reveal these stress gradients.

7) Actual tangential loads between car wheels, locomotive wheels and the rail are a combination of the three types shown in Figure 1. These combined stresses would be considered in future work.

8) Experiments on tubular specimens of 1070 steel are currently underway that are aimed at understanding the role of compressive stresses in combined shear-normal stress cycling conditions. The results will be discussed in the forthcoming AAR Report #3.

Acknowledgements

This research was supported by Association of American Railroads, Technical Center, Chicago, Illinois. The cooperation of Dr. Dan Stone and Mr. Michael Fec is appreciated. Discussions with Dr. Gerald Moyar were valuable. Mr. Mark Balzer, Research Assistant, helped with the preparation of the manuscript.

References

1. Sehitoglu, H., and Jiang, R., 'Contact Fatigue Life Prediction Methods', Report #1 prepared for AAR, November 1990

2. Thomas, H.R. and Hoersch, V.A., "Stresses due to the Pressure of One Elastic Solid upon Another", Engineering Experiment Station Bulletin 212, University of Illinois at Urbana-Champaingn, College of Engineering, July, 1930

3. Radzimovsky, E.I."Stress Distribution and Strength Condition of Two Rolling Cylinders Pressed Together", Engineering Experiment Station Bulletin 408, University of Illinois at Urbana-Champaign, College of Engineering, 1953

4. Smith, J.O. and Liu, C.K., "Stresses Due to Tangential and Normal Loads on an Elastic Solid with Application to Some Contact Stress Problems", ASME, J.Appl.Mech., Vol.20, 1953, pp.157-166

5. Mitsuda, T., "An Investigation of Pitting and Shelling Failures in Rolling Contact", Engineering Experiment Station Bulletin 286, University of Illinois at Urbana-Champaingn, College of Engineering, Sept., 1965

6. Sackfield, A. and Hills, D.A., "Some Useful Results in the Classical Hertz Contact Problem", J. Strain Anal., Vol.18, No.2, 1983, pp.101-105

7. Sackfield, A. and Hills, D.A., "Some Useful Results in the Tangentially Loaded Hertzian Contact Problem", J. Strain Anal., Vol.18, No.2, 1983, pp.107-110

8. Johnson, K.L., "Tangential Tractions and Micro-slip in Rolling Contact", in *Rolling Contact Phenomena*, Bidwell, J.B., Ed., Elsevier Pub. Company, 1962, pp.6-25

9. Cain, B.S., Discussion, J.Appl.Mech., Trans.ASME, Dec., 1950, p.465

10. Bentall, R.H. and Johnson, K.L., "Slip in the Rolling Contact of Two Dissimilar Elastic Rollers", Inter.J.Mech.Sci., Vol.9, 1967, pp.389-404

11. Hunter, S.C., "The Rolling Contact of a Rigid Cylinder with a Viscoelastic Half Space", J.Appl.Mech., Trans.ASME, Dec., 1961, pp.611-617

12. Carter, F.W., "On the Action of a Locomotive Driving Wheel", Proc., Royal Society, A112, 1926, pp.151-157

13. Poritsky, H., "Stresses and Deflections of Cylindrical Bodies in Contact with Application to Contact of Gears and Locomotive Wheels", Trans ASME, J.Appl.Mech., Dec., 1950, pp.191-201

14. Kalker, J.J., "Transient Phenomena in Two Elastic Cylinders Rolling over each other with Dry Friction", Trans ASME, J.Appl.Mech., Sept.1970, pp.677-688

15. Poritsky, H., Discussion, J.Appl.Mech., Trans.ASME, Dec.,1950, pp.466-468

16. Johnson, K.L. *Contact Mechanics*, Cambridge University Press, 1987

17. Suh, Nam P., Chapter 3, in *Tribophysics*, Prentice-Hall, Inc., New Jersey, 1986.

18. Bhargava, V., Hahn, G.T., and Rubin, C.A., "An Elastic-Plastic Finite Element Model of Rolling Contact, Part 1: Analysis of Single Contacts", J.Appl.Mech., Trans. ASME, Vol.52, March 1985, pp.67-74

19. Bhargava, V., Hahn, G.T., and Rubin, C.A., "An Elastic-Plastic Finite Element Model of Rolling Contact, Part 2: Analysis of Repeated Contacts", J.Appl.Mech., Trans. ASME, Vol.52, March 1985, pp.75-82

20. Ham, G., Rubin, C.A., Hahn, G.T., and Bhargava, V., "Elasto-Plastic Finite Element Analysis of Repeated, Two-Dimensional Rolling-Sliding Contacts", J. Tribology, Trans ASME, Vol.110, pp.44-49

Table I Summary of Calculated Results

f=0.3 , ξ=1, μ=0.3 ,Proportional Tangential Force, Type 0

Q/P			Maximum Orthogonal Shear Stress Range $\Delta\tau_{xzmax}/p_o$	Maximum Shear Stress τ_{max}/p_o	$(J2)^{1/2}_{max}/p_o$	Maximum Shear Stress Range $\Delta\tau_{max}/p_o$	$(J2)^{1/2}_{alt}/p_o$
0	Magnitude		0.5000	0.3003	0.3219	0.5000	0.2500
	Location, z/a		0.504	0.792	0.708	0.500	0.504
	Orien-	α°	0	0	-	0	-
	tation	β°	0, 90	±45	-	0, 90	-
0.1	Magnitude		0.5000	0.3049	0.3265	0.5016	0.2508
	Location, z/a		0.504	0.744	0.672	0.490	0.492
	Orien-	α°	0	0	-	0	-
	tation	β°	0, 90	31.1, -58.9	-	-3.5, 86.5	-
0.2	Magnitude		0.5000	0.319	0.3406	0.5069	0.2537
	Location, z/a		0.504	0.600	0.564	0.465	0.468
	Orien-	α°	0	0	-	0	-
	tation	β°	0, 90	16.4, -73.6	-	-8, 82	-
0.3	Magnitude		0.5000	0.3595	0.3855	0.600	0.3159
	Location, z/a		0.504	0	0	0	0
	Orien-	α°	0	51.7,128.3	-	0	-
	tation	β°	0, 90	25.7, -25.7	-	±45	-
0.4	Magnitude		0.5000	0.415	0.4716	0.7985	0.4146
	Location, z/a		0.504	0	0	0	0
	Orien-	α°	0	50.6,129.4	-	0	-
	tation	β°	0, 90	23.8,-23.8	-	±45	-

The normal load is elliptically distributed.
a is the half width of the contact area.
f is the friction coefficient.
Q/P=ξf , where Q is the total tangential load and P is the total normal load acting on the surface.
p_0 is the maximum Hertzian normal pressure acting on the contact area.
μ is the Poisson's ratio of the material.
See the text for the definitions of $\Delta\tau_{max}$, $(J_2)^{1/2}_{alt}$, and $(J_2)^{1/2}_{max}$

Table II Summary of Calculated Results

f=0.4,μ=0.3, Type I Tangential Force

Q/P			Maximum Orthogonal Shear Stress Range $\Delta\tau_{xzmax}/p_o$	Maximum Shear Stress τ_{max}/p_o	$(J2)^{1/2}_{max}/p_o$	Maximum Shear Stress Range $\Delta\tau_{max}/p_o$	$(J2)^{1/2}_{alt}/p_o$
0.1	Magnitude		0.5003	0.3210	0.3283	0.5018	0.2672
	Location, z/a		0.5400	0	0.	0.540	0.
	Orien-	α°	0	46.0,134	-	0	-
	tation	β°	0,90	10.5,-10.5	-	86.5,-3.5	-
0.2	Magnitude		0.4954	0.3787	0.4314	0.5333	0.3085
	Location, z/a		0.5880	0.	0.	0.	0.
	Orien-	α°	0	52.4,127.6	-	⊥45.0	-
	tation	β°	0,90	26.8,-26.8	-	0.	-
0.3	Magnitude		0.4934	0.4638	0.5261	0.6909	0.3907
	Location, z/a		0.5880	0	0	0	0
	Orien-	α°	0	49.6,130.4	-	0	-
	tation	β°	0,90	21.8,-21.8	-	62.5,-27.5	-
0.4	Magnitude		0.5000	0.415	0.4716	0.7985	0.4146
	Location, z/a		0.5040	0	0	0	0
	Orien-	α°	0	50.6,129.4	-	0	-
	tation	β°	0, 90	23.8,-23.8	-	±45	-

The normal load is elliptically distributed.
a is the half width of the contact area.
f is the friction coefficient.

Q/P=ξf , where Q is the total tangential load and P is the total normal load acting on the surface.
p_0 is the maximum Hertzian normal pressure acting on the contact area.

μ is the Poisson's ratio of the material.

See the text for the definitions of $\Delta\tau_{max}$, $(J_2)^{1/2}_{alt}$, and $(J_2)^{1/2}_{max}$

Table III Summary of Calculated Results

f=0.6,μ=0.3, Type I Tangential Force

Q/P		Maximum Orthogonal Shear Stress Range $\Delta\tau_{xzmax}/p_0$	Maximum Shear Stress τ_{max}/p_0	$(J_2)^{1/2}_{max}/p_0$	Maximum Shear Stress Range $\Delta\tau_{max}/p_0$	$(J_2)^{1/2}_{alt}/p_0$
0.1	Magnitude	0.5012	0.3422	0.3787	0.5025	0.3280
	Location, z/a	0.540	0.	0.	0.54	0.
	Orien- α°	0	0	-	0	-
	tation β°	0,90	3.9, -86.1	-	87,-3	-
0.2	Magnitude	0.5005	0.4560	0.4890	0.6822	0.4223
	Location, z/a	0.588	0.	0.	0.	0.
	Orien- α°	0	0	-	0	-
	tation β°	0,90	0,90	-	66.5.-23.5	-
0.3	Magnitude	0.5431	0.5525	0.5994	0.8212	0.4384
	Location, z/a	0	0	0	0	0
	Orien- α°	0	0	-	0	-
	tation β°	0,90	5.3,-84.7	-	65.8,-24.2	-
0.4	Magnitude	0.5907	0.6123	0.6694	0.9539	0.5188
	Location, z/a	0	0	0	0	0
	Orien- α°	0	0	-	0	-
	tation β°	0,90	7.6,-82.4	-	62.5,-27.5	-

The normal load is elliptically distributed.
a is the half width of the contact area.
f is the friction coefficient.

Q/P=ξf , where Q is the tangential load and P is the normal load acting on the surface.

p_0 is the maximum Hertzian normal pressure acting on the contact area.

μ is the Poisson's ratio of the material.

See the text about the definitions of $\Delta\tau_{max}$, $(J_2)^{1/2}_{alt}$, and $(J_2)^{1/2}_{max}$

Table IV Summary of Calculated Results

f=0.6,μ=0.3, Type II Tangential Force

Q/P		Maximum Orthogonal Shear Stress Range $\Delta\tau_{xzmax}/p_o$	Maximum Shear Stress τ_{max}/p_o	$(J2)^{1/2}_{max}/p_o$	Maximum Shear Stress Range $\Delta\tau_{max}/p_o$	$(J2)^{1/2}_{alt}/p_o$
0.1	Magnitude	0.5014	0.3248	0.3533	0.5040	0.2520
	Location, z/a	0.444	0.	0.	0.435	0.432
	Orien- α°	0	0	-	0	-
	tation β°	0,90	83.3,-6.7	-	85,-5	-
0.2	Magnitude	0.5190	0.4561	0.4879	0.6821	0.3265
	Location, z/a	0.336	0.	0.	0.	0.
	Orien- α°	0	0	-	0	-
	tation β°	0,90	0,90	-	23.5,-66.5	-
0.3	Magnitude	0.5431	0.5525	0.5828	0.8211	0.4006
	Location, z/a	0	0	0	0	0
	Orien- α°	0	0	-	0	-
	tation β°	0,90	5.3,-84.7	-	24.3,-65.7	-
0.4	Magnitude	0.5907	0.6123	0.6411	0.9538	0.4775
	Location, z/a	0	0	0	0	0
	Orien- α°	0	0	-	0	-
	tation β°	0,90	7.6,-82.4	-	27.5,-62.5	-

The normal load is elliptically distributed.
a is the half width of the contact area.
f is the friction coefficient.

Q/P=ξf , where Q is the total tangential load and P is the total normal load acting on the surface.
p_o is the maximum Hertzian normal pressure acting on the contact area.

μ is the Poisson's ratio of the material.

See the text for the definitions of $\Delta\tau_{max}$, $(J_2)^{1/2}_{alt}$, and $(J_2)^{1/2}_{max}$

Table V Summary of Calculated Results

f=0.6,μ=0.3, Type III Tangential Force

Q/P			Maximum Orthogonal Shear Stress Range $\Delta\tau_{xzmax}/p_o$	Maximum Shear Stress τ_{max}/p_o	$(J2)^{1/2}_{max}/p_o$	Maximum Shear Stress Range $\Delta\tau_{max}/p_o$	$(J2)^{1/2}_{alt}/p_o$
0.1	Magnitude		0.5000	0.3209	0.3430	0.5012	0.2872
	Location, z/a		0.504	0.	0.	0.495	0
	Orien-	α°	0	45.3,134.7	-	0	-
	tation	β°	0,90	5.8, -5.8	-	86.5,-3.5	-
0.2	Magnitude		0.5000	0.3464	0.3797	0.6926	0.3554
	Location, z/a		0.504	0.	0.	0.	0.
	Orien-	α°	0	0	-	0	-
	tation	β°	0,90	78,-12	-	±45	-
0.3	Magnitude		0.5008	0.4243	0.4650	0.8483	0.4358
	Location, z/a		0.5040	0	0	0	0
	Orien-	α°	0	0	-	0	-
	tation	β°	0,90	58,-32	-	±45	-
0.4	Magnitude		0.5040	0.4898	0.5370	0.9796	0.5041
	Location, z/a		0.5014	0	0	0	0
	Orien-	α°	0	0	-	0	-
	tation	β°	0,90	28.9,-61.3	-	±45	-

The normal load is elliptically distributed.
a is the half width of the contact area.
f is the friction coefficient.

$Q/P=\xi f$, where Q is the total tangential load and P is the total normal load acting on the surface.

p_o is the maximum Hertzian normal pressure acting on the contact area.

μ is the Poisson's ratio of the material.

See the text for the definitions of $\Delta\tau_{max}$, $(J_2)^{1/2}_{alt}$, and $(J_2)^{1/2}_{max}$

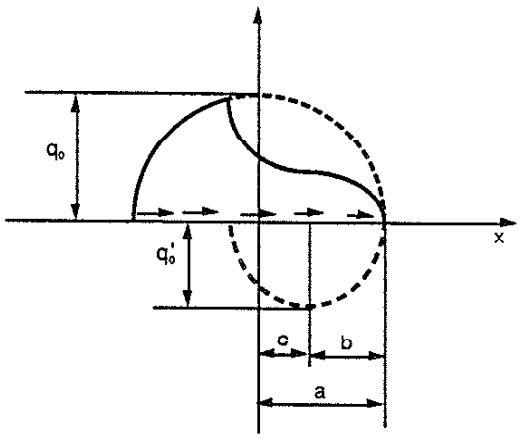

(a) Type I

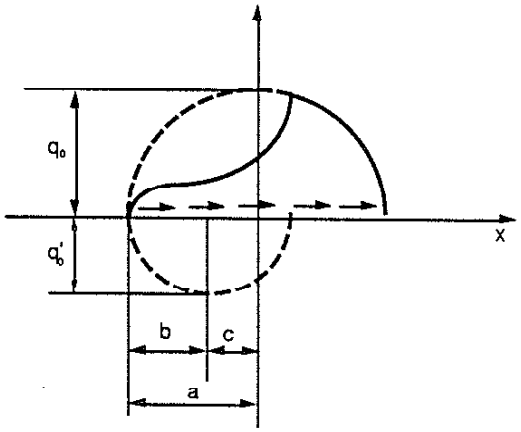

(b) Type II

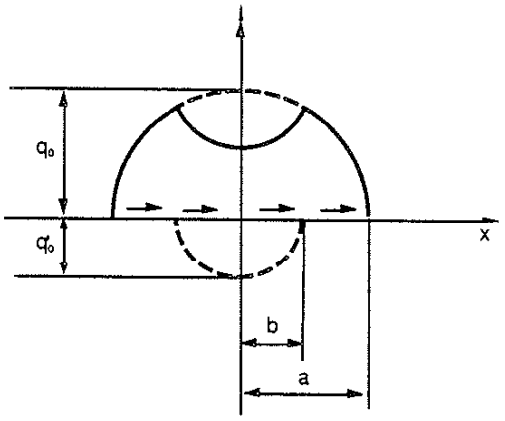

(c) Type III

Fig.1 Tangential Traction Distribution

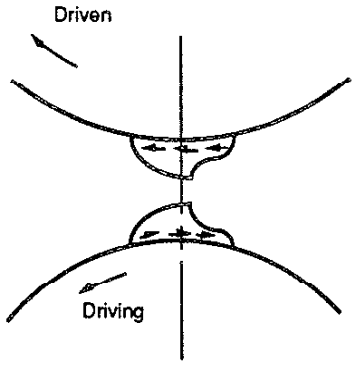

(a) Tangential Forces Acting on the Two Cylinders in Contact

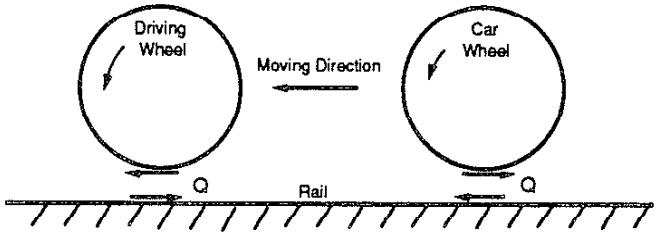

(b) Tangential Force Directions of a Driving Wheel and a Car Wheel

Fig.2 Directions of Tangential Traction Forces

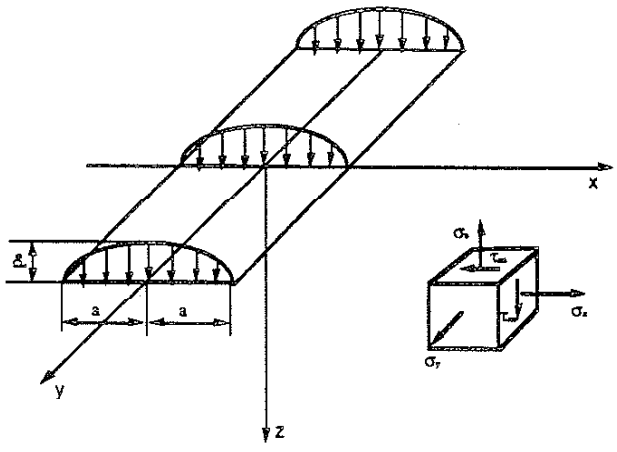

Fig.3 Line Contact, Coordinates System, Normal Load Distribution, and Orthogonal Stresses

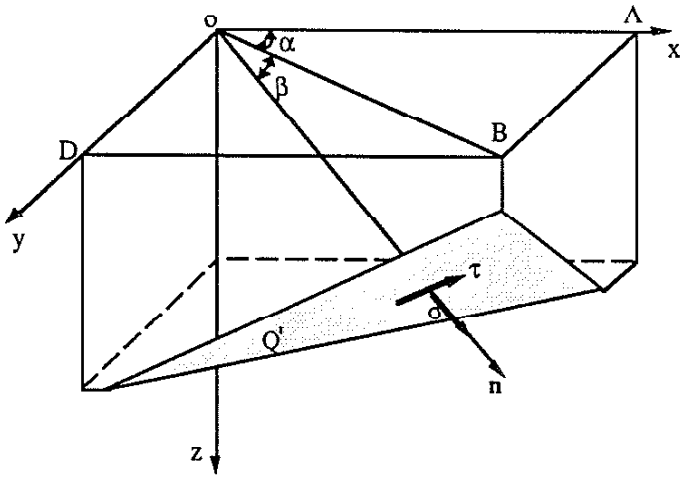

Representation of an arbitary plane Q' by its unit normal n
$n = i\cos\alpha\cos\beta + j\sin\alpha\cos\beta + k\sin\beta$

σ and τ are normal stress and shear stress, respectively, on plane Q'.

Fig.4 Representation of a Plane by Its Normal

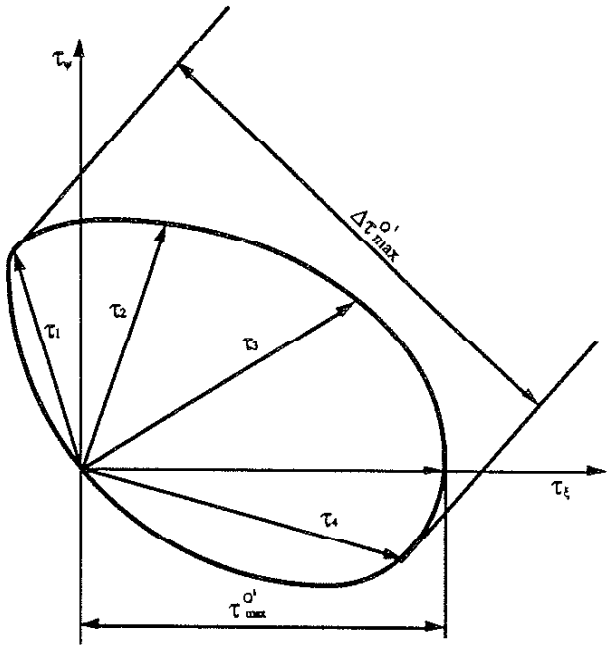

τ_1, τ_2, τ_3, and τ_4 are shear stresses at time 1,2,3, and 4, respectively. $\tau^{o'}_{max}$ is the maximum shear stress on this plane. $\Delta\tau^{o'}_{max}$ is the maximum shear stress range on the plane Q'

τ_ξ is the direction of maximum shear stress and τ_w is the direction perpendicular to it

$\Delta\tau^{o'}_{max} = \tau_4 - \tau_1$

Fig.5 A Schematic Illustration of Shear Stress Variation (Direction and Magnitude) on an Arbitrary Plane, Q'

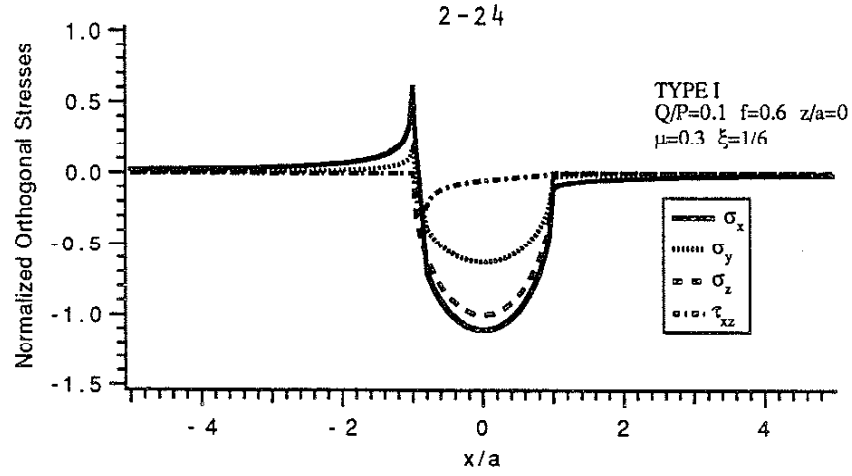

(a) z/a=0, Q/P=0.1, f=0.6

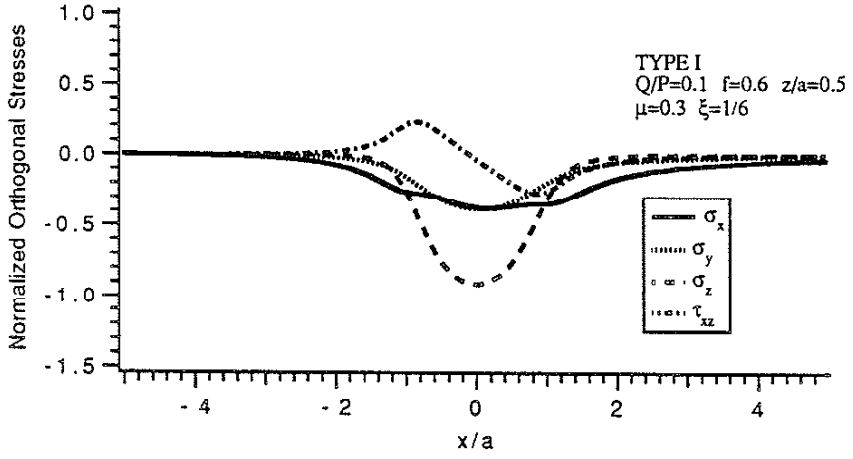

(b) z/a=0.5, Q/P=0.1, f=0.6

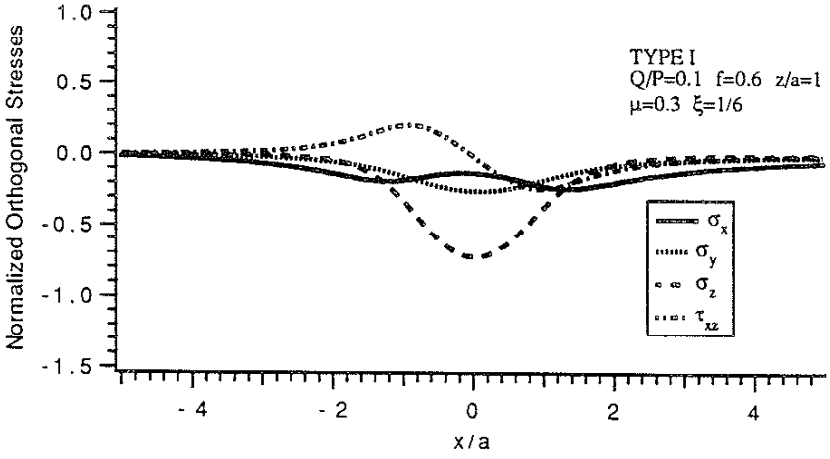

(c) z/a=1, Q/P=0.1, f=0.6

Fig.6 Variations of Orthogonal Stresses(Q/P=0.1, f=0.6, μ=0.3, TYPE I)

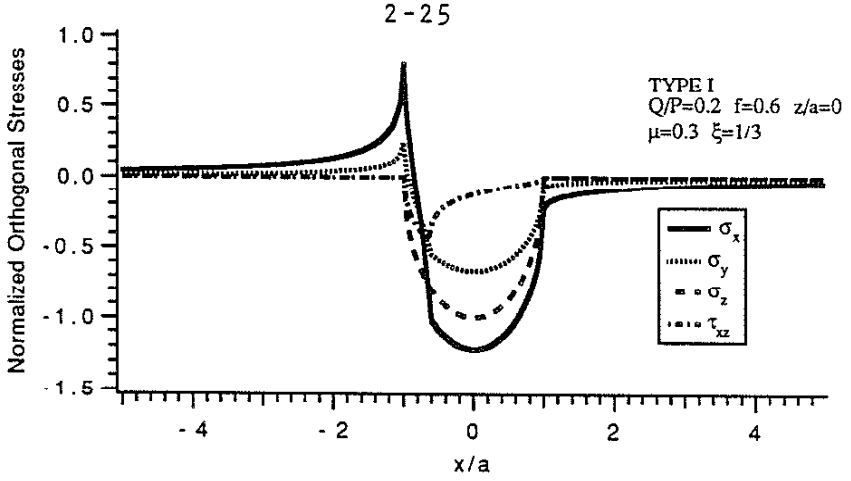

(a) z/a=0, Q/P=0.2, f=0.6

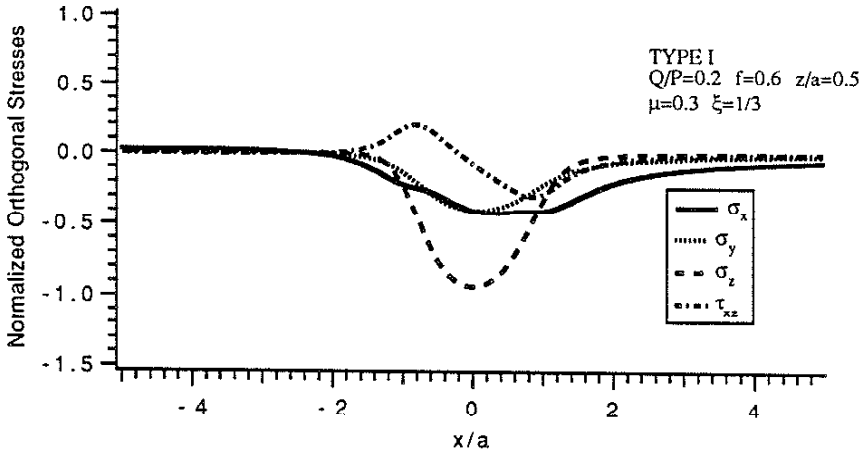

(b) z/a=0.5, Q/P=0.2, f=0.6

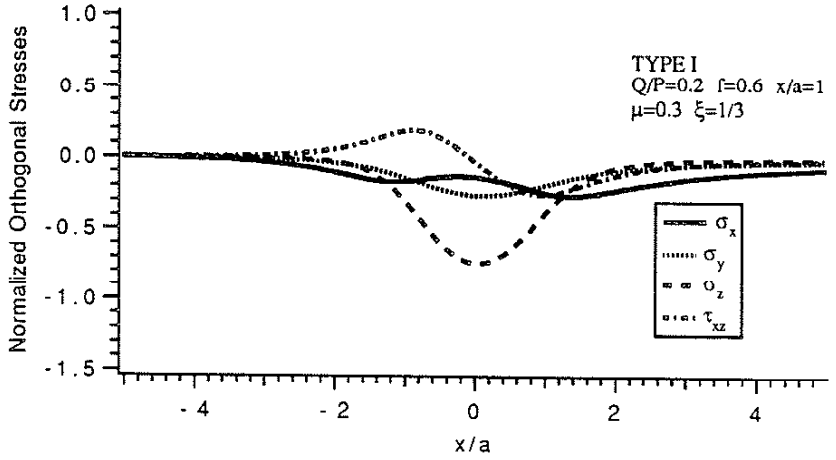

(c) z/a=1, Q/P=0.2, f=0.6

Fig.7 Variations of Orthogonal Stresses(Q/P=0.2, f=0.6, μ=0.3, TYPE I)

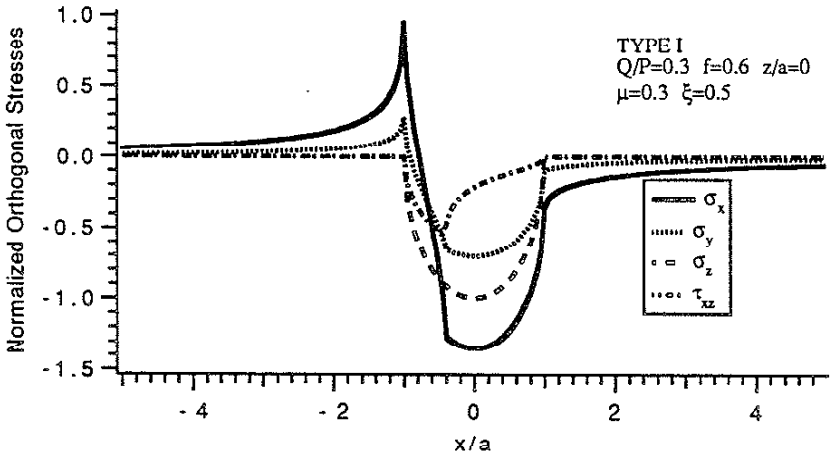

(a) z/a=0, Q/P=0.3, f=0.6

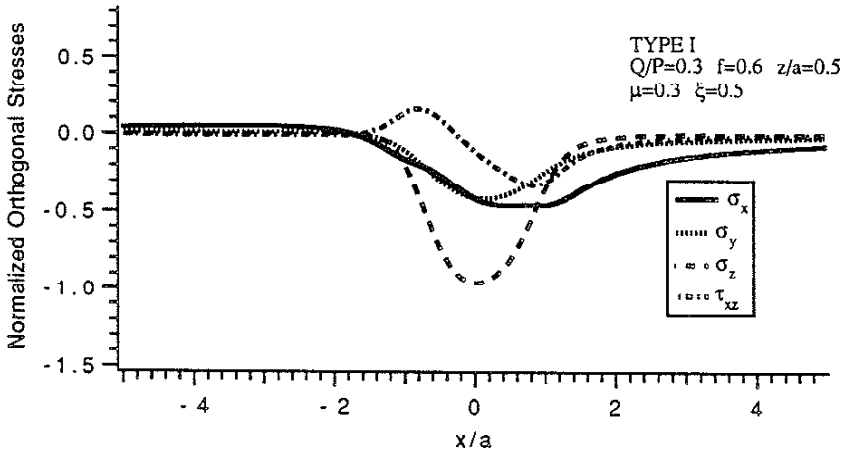

(b) z/a=0.5, Q/P=0.3, f=0.6

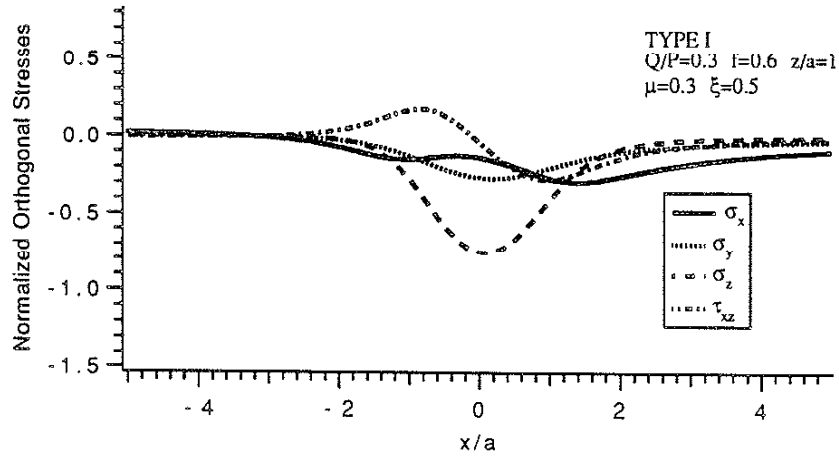

(c) z/a=1, Q/P=0.3, f=0.6

Fig.8 Variations of Orthogonal Stresses(Q/P=0.3, f=0.6, μ=0.3, TYPE I)

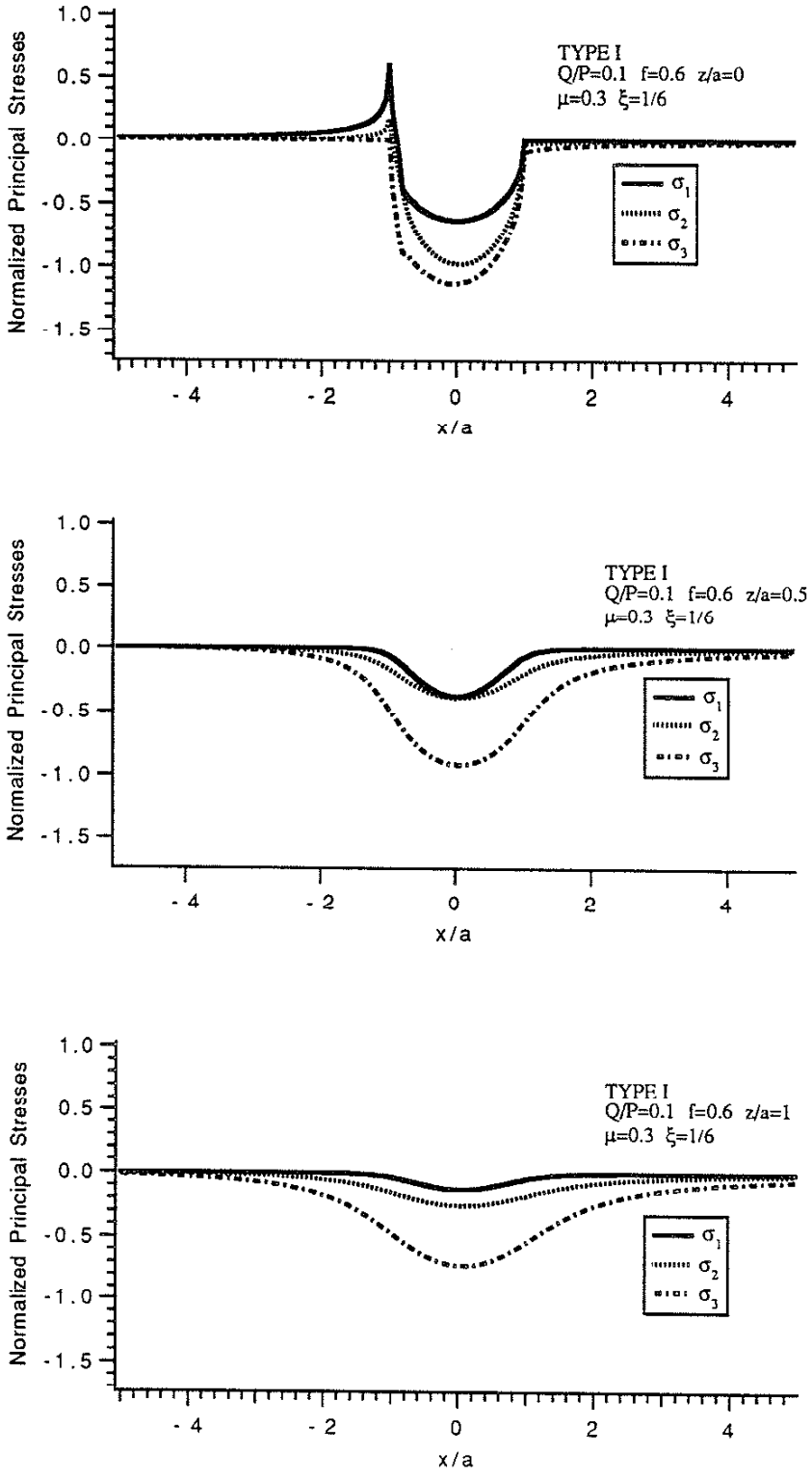

Fig.9 Variations of Principal Stresses (Q/P=0.1, f=0.6, μ=0.3, TYPE I)

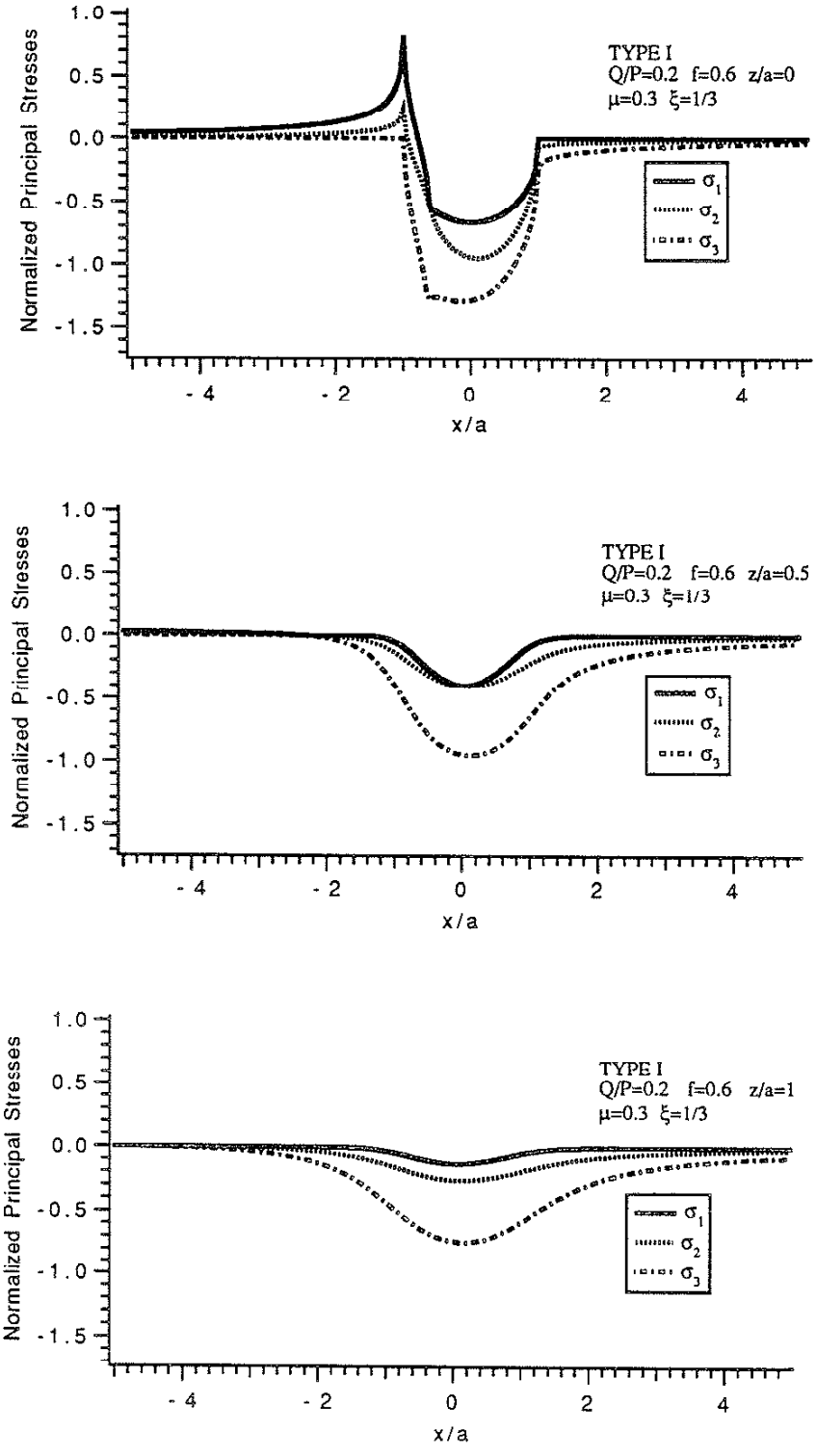

Fig.10 Variations of Principal Stresses (Q/P=0.2, f=0.6, μ=0.3, TYPE I)

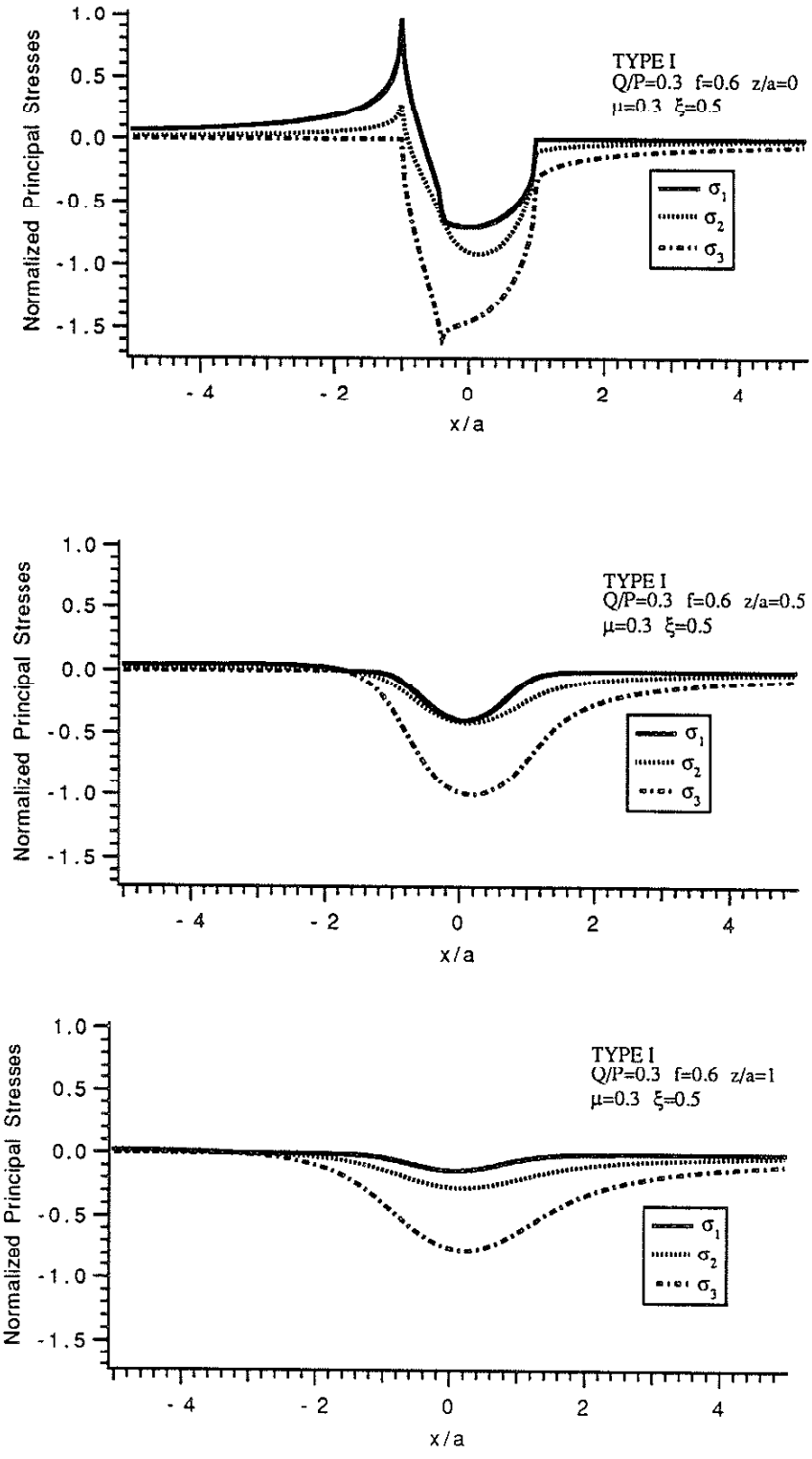

Fig.11 Variations of Principal Stresses (Q/P=0.3, f=0.6, μ=0.3, TYPE I)

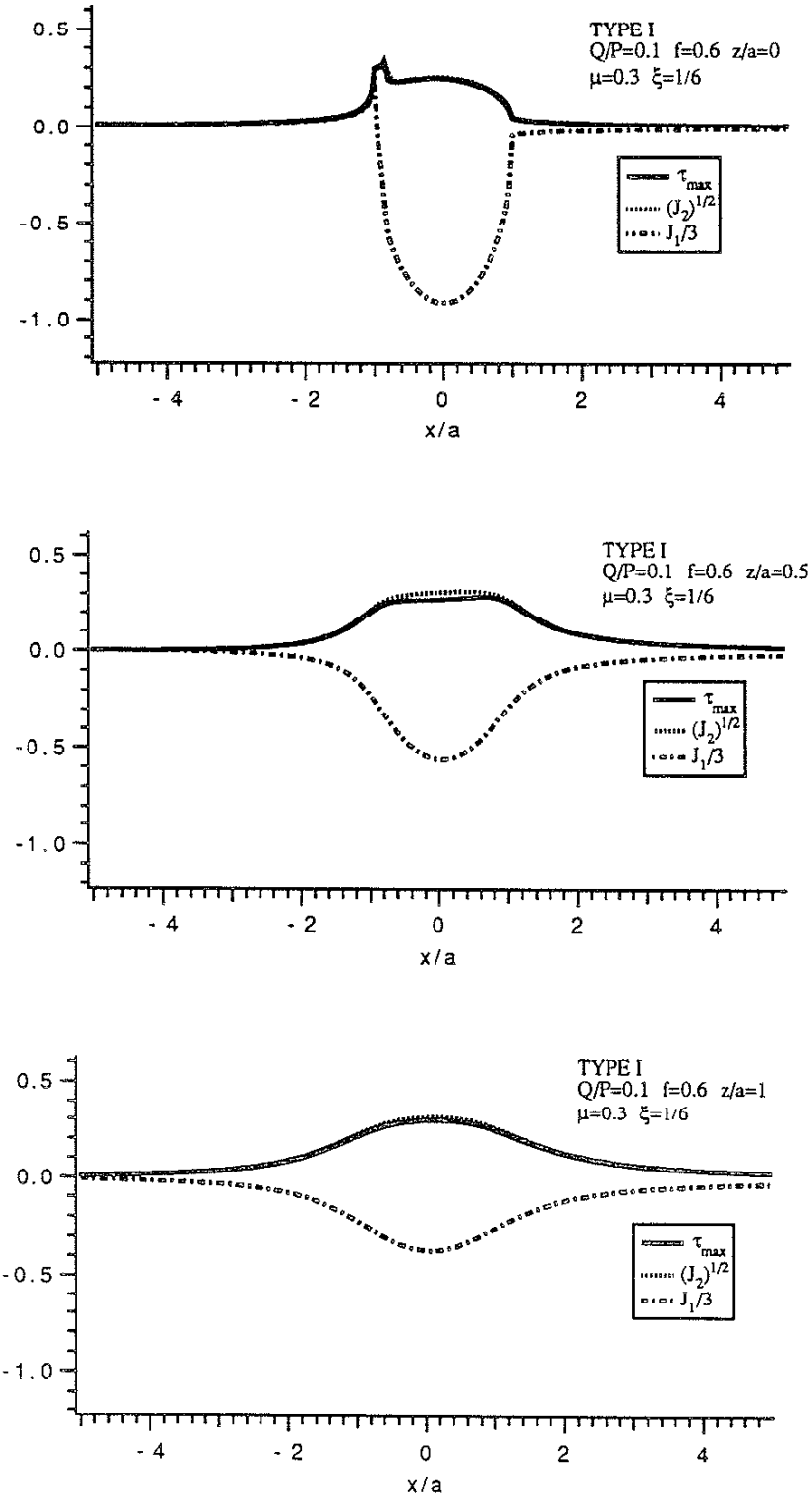

Fig.12 Variations of Tresca Shear Stress, Von Misses Stress, and Hydrostatic Stress(Q/P=0.1, f=0.6, μ=0.3,TYPE I)

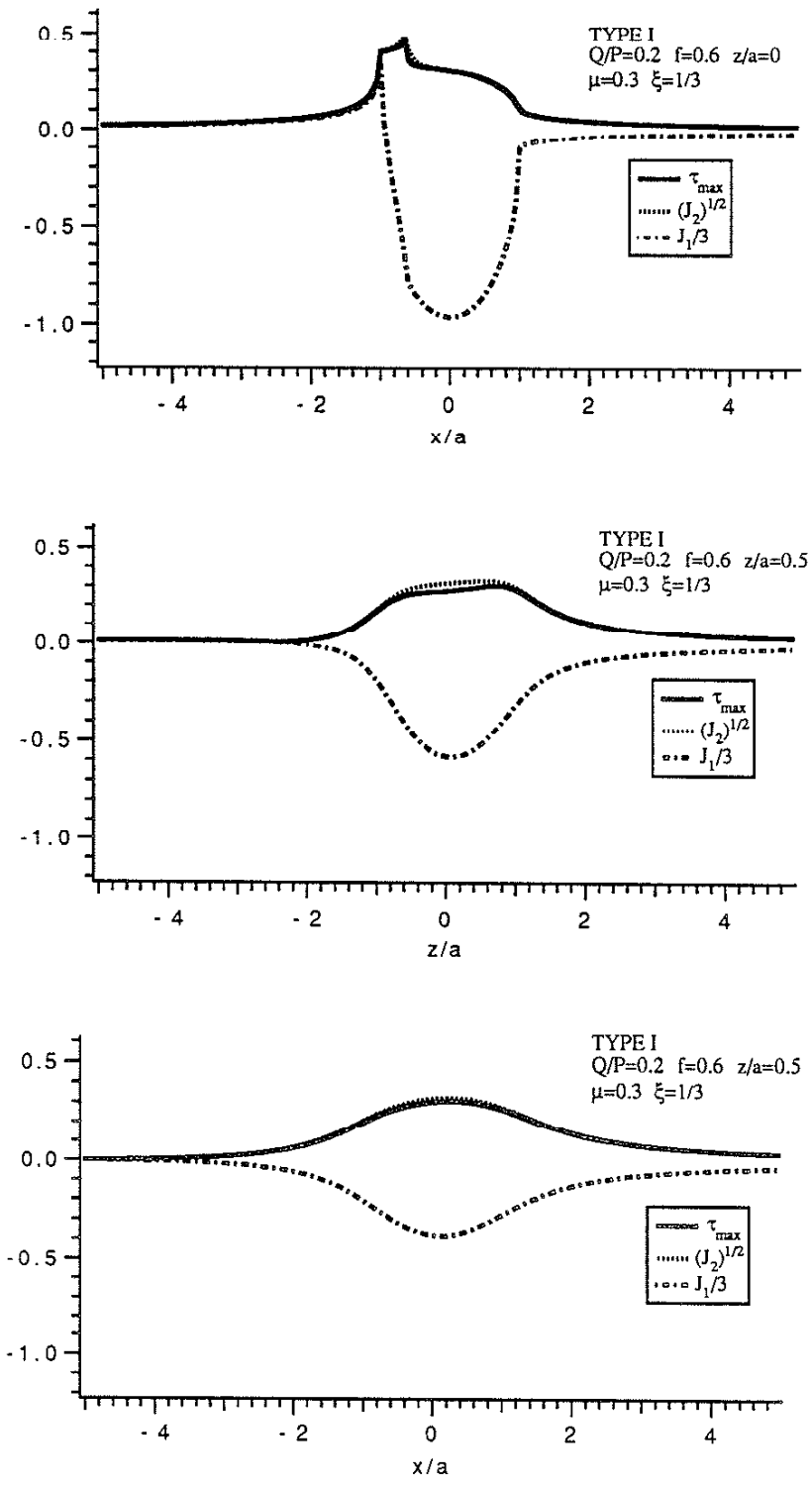

Fig.13 Variations of Tresca Shear Stress, Von Misses Stress, and Hydrostatic Stress(Q/P=0.2, f=0.6, μ=0.3,TYPE I)

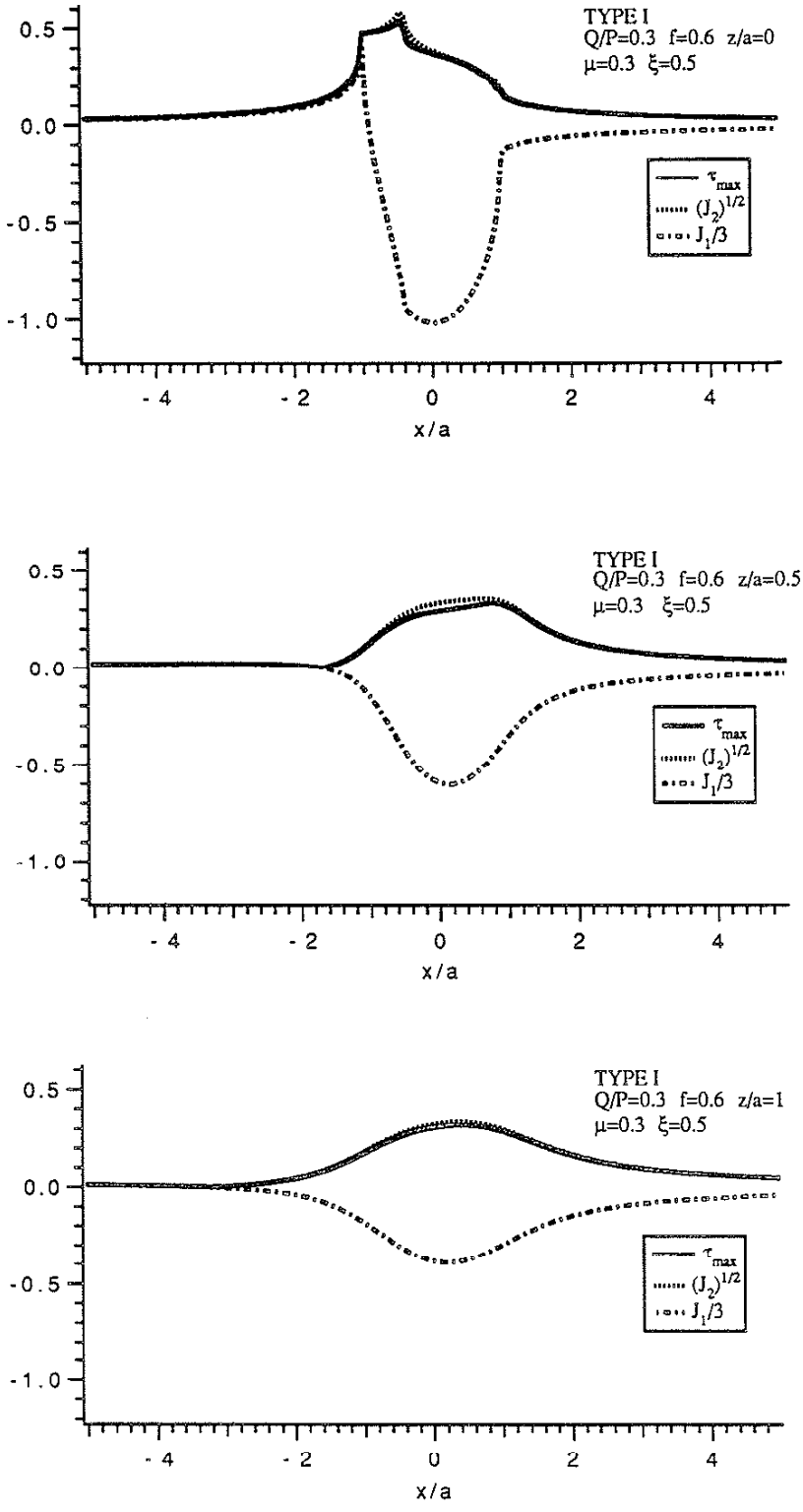

Fig.14 Variations of Tresca Shear Stress, Von Misses Stress, and Hydrostatic Stress(Q/P=0.3, f=0.6, μ=0.3,TYPE I)

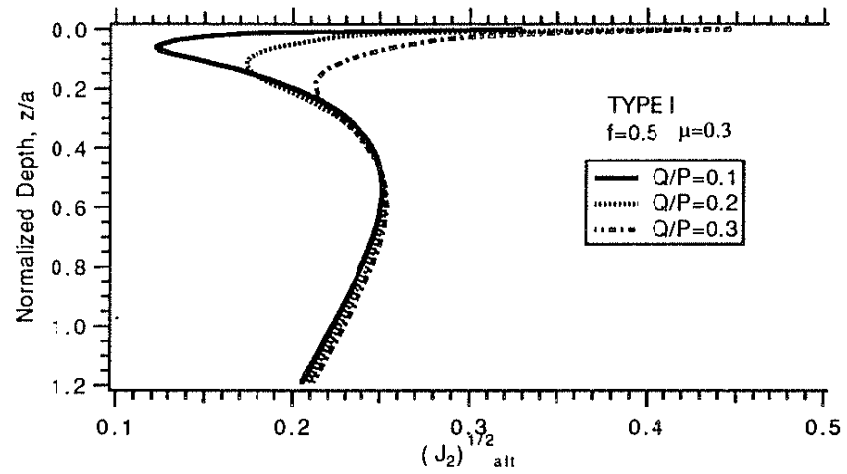

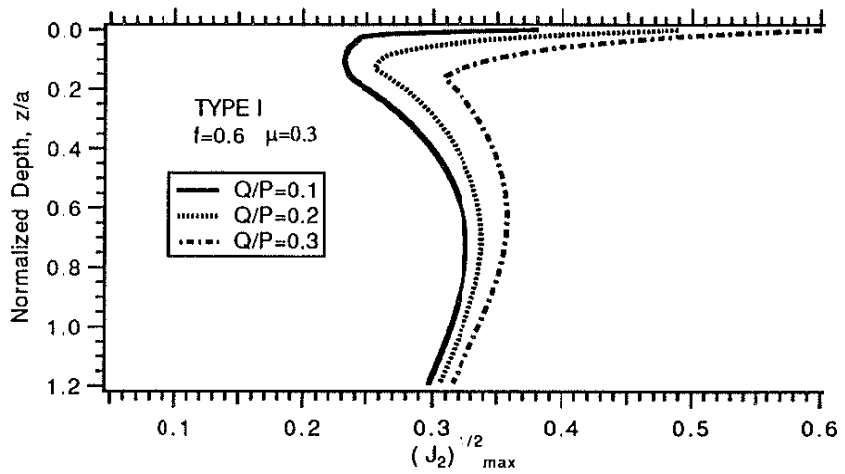

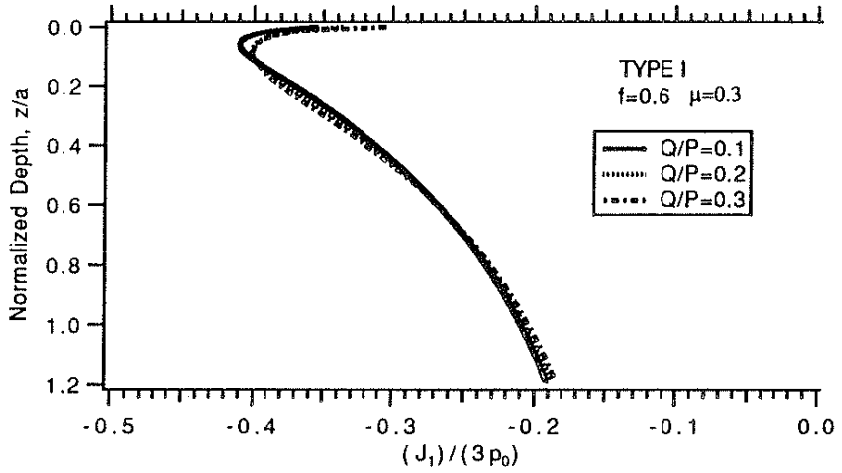

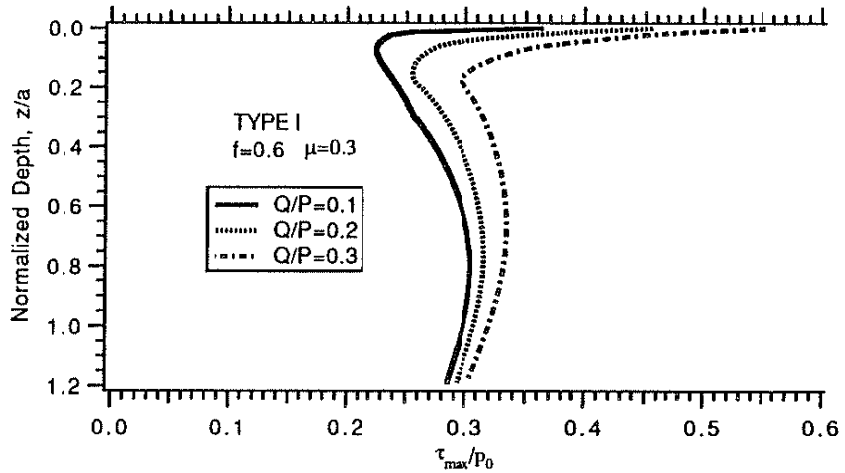

Fig.15 Variations of $(J_2)^{1/2}_{alt}$, $(J_2)^{1/2}_{max}$, $(J_1)_{stat}$, and τ_{max} along z-axis(f=0.6 μ=0.3, TYPE I)

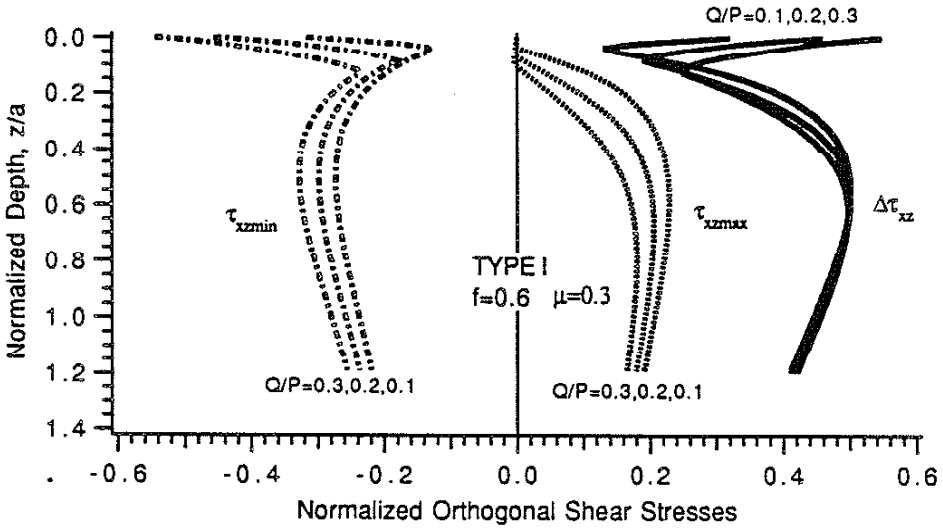

Fig.16 Variations of Orthogonal Shear Stresses along z-axis with Different Q/P Ratios (f=0.6, μ=0.3, TYPE I)

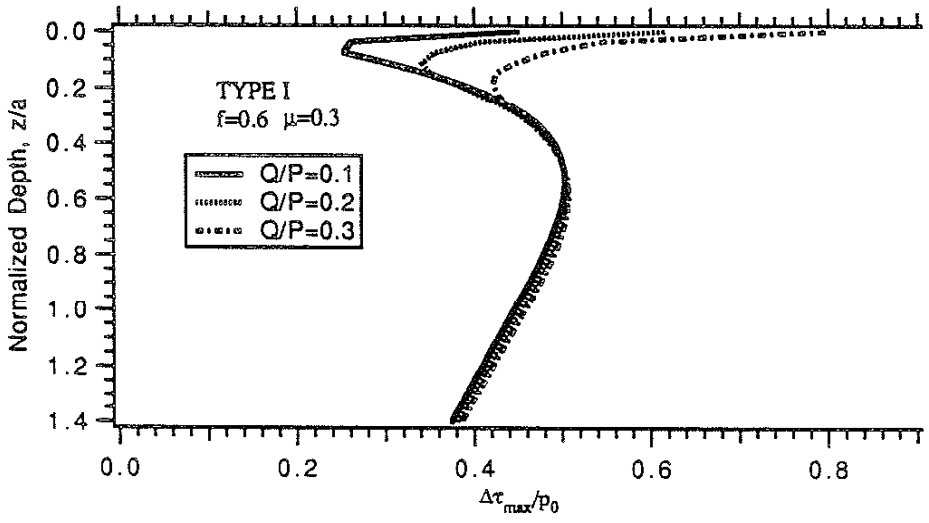

Fig.17 Variation of Maximum Shear Stress Range along z-axis(f=0.6, μ=0.3, TYPE I)

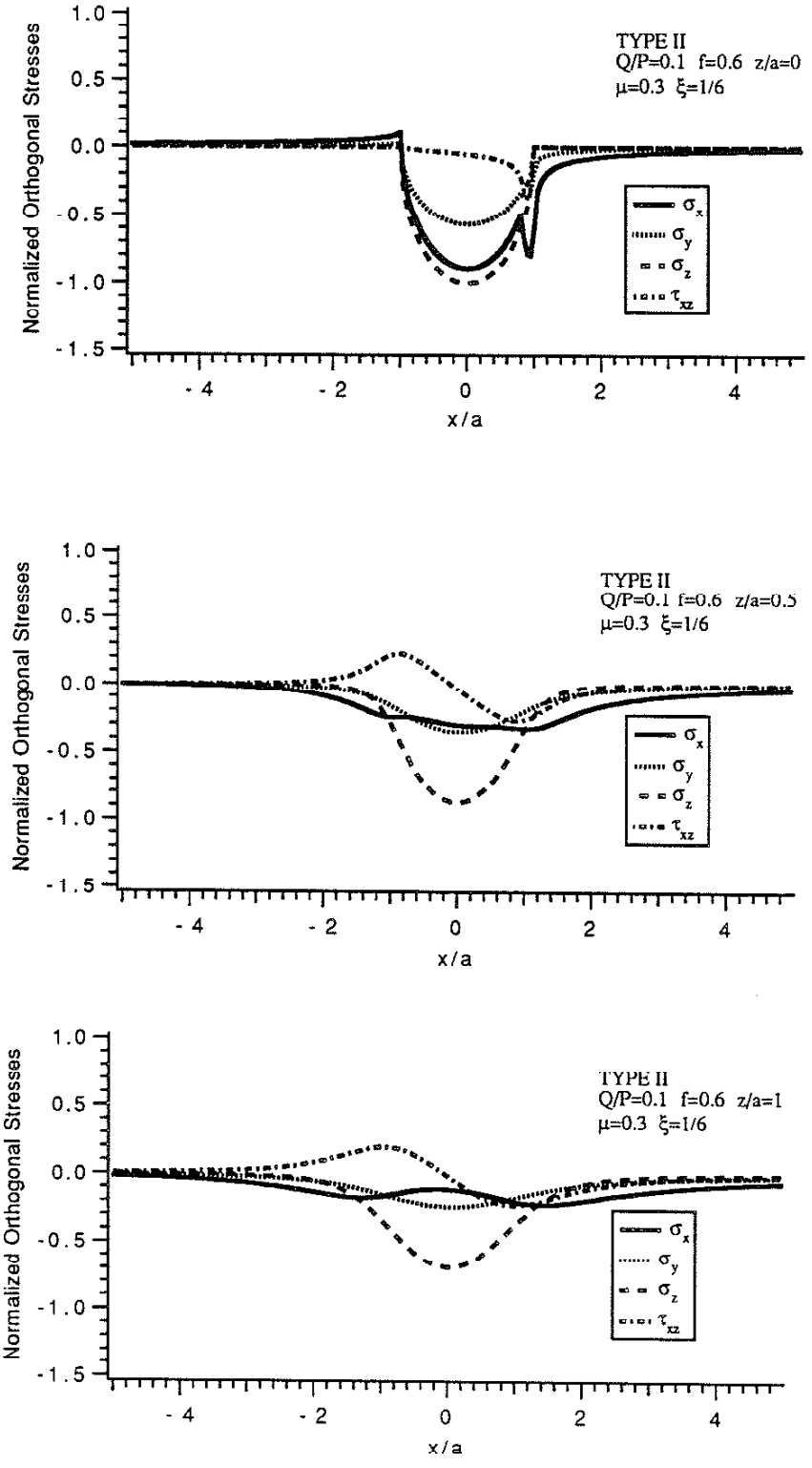

Fig.18 Variations of Orthogonal Stresses (Q/P=0.1, f=0.6, μ=0.3, TYPE II)

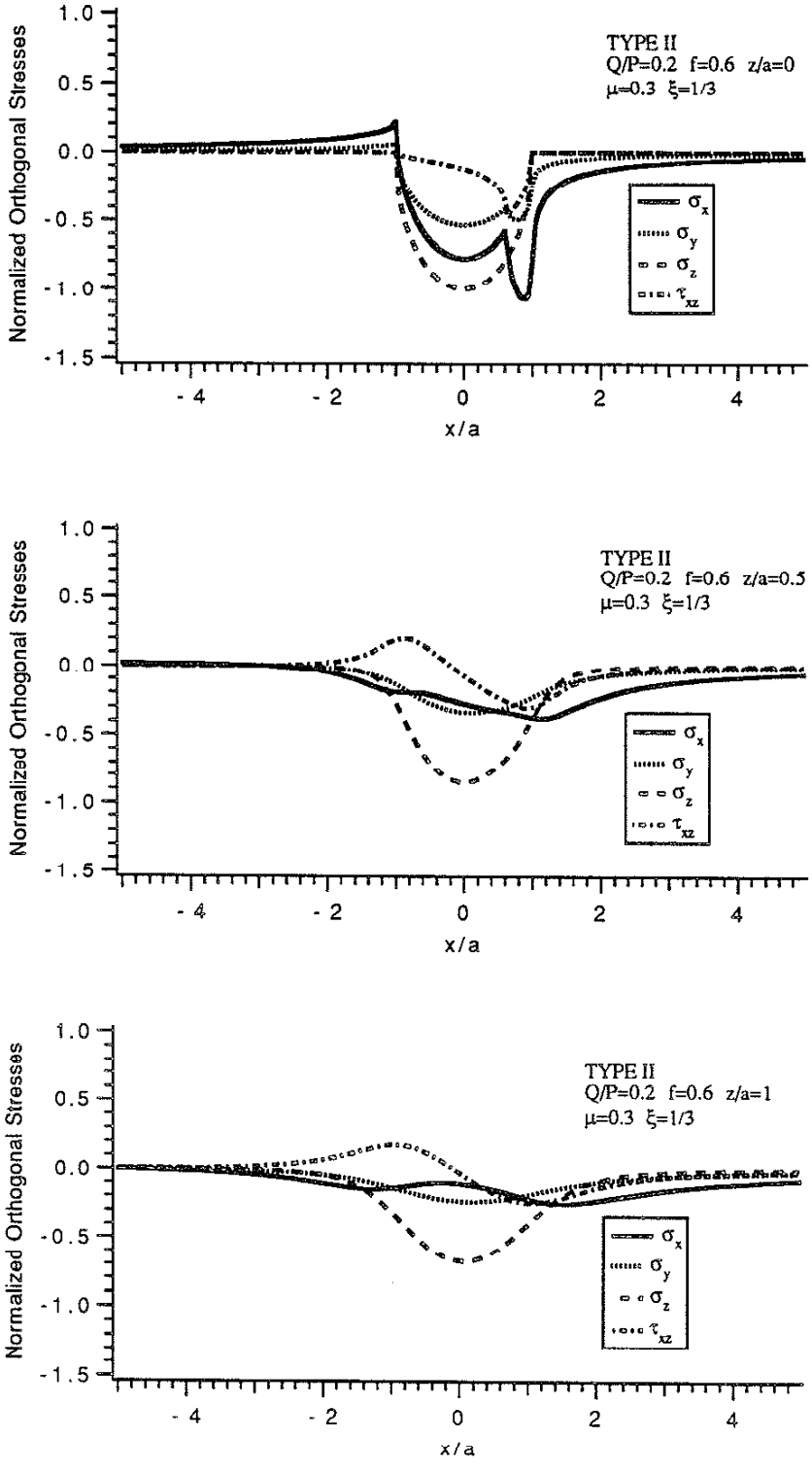

Fig.19 Variations of Orthogonal Stresses (Q/P=0.2, f=0.6, μ=0.3, TYPE II)

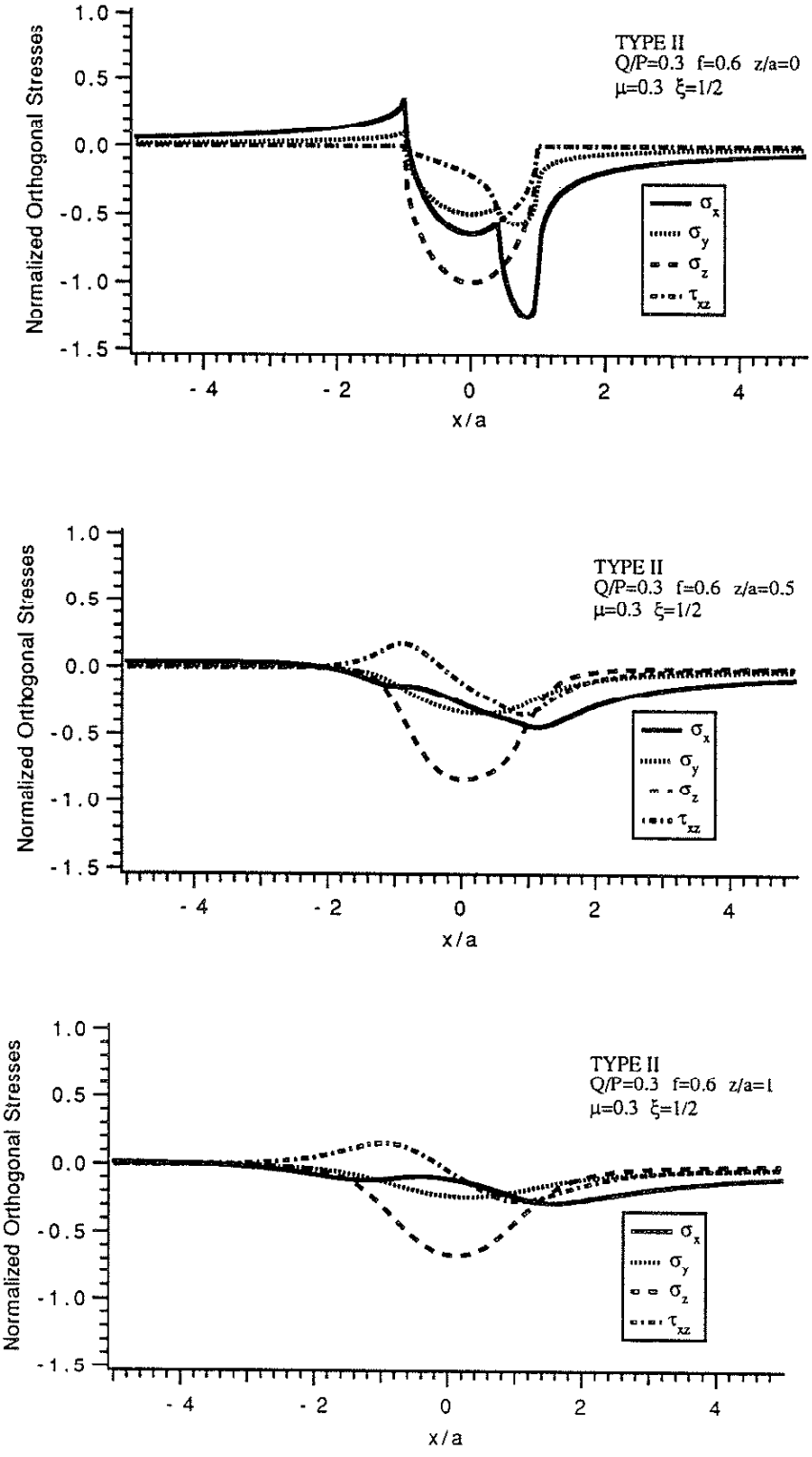

Fig.20 Variations of Orthogonal Stresses (Q/P=0.3, f=0.6, μ=0.3, TYPE II)

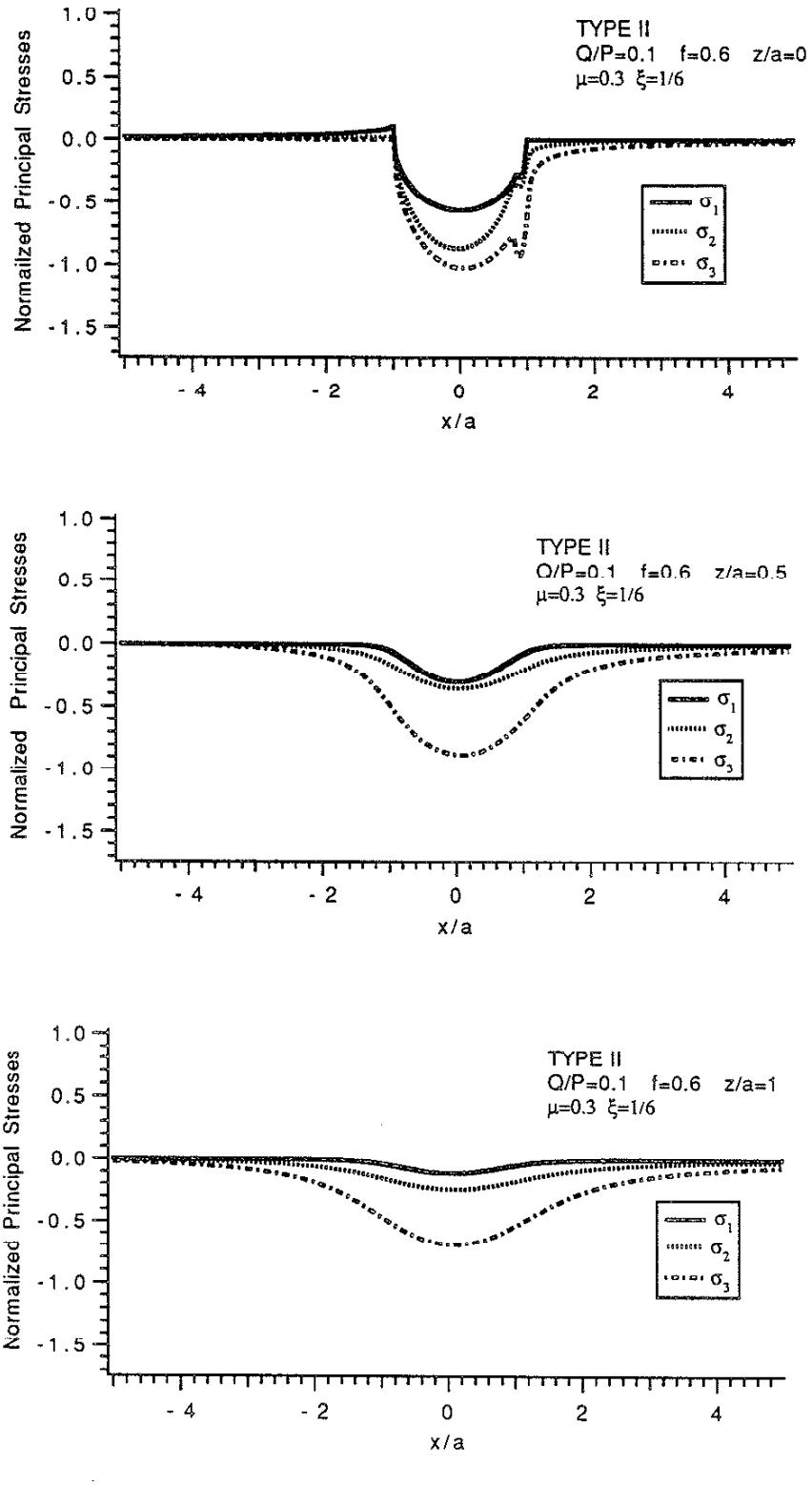

Fig.21 Variations of Principal Stresses(Q/P=0.1, f=0.6, μ=0.3,TYPE II)

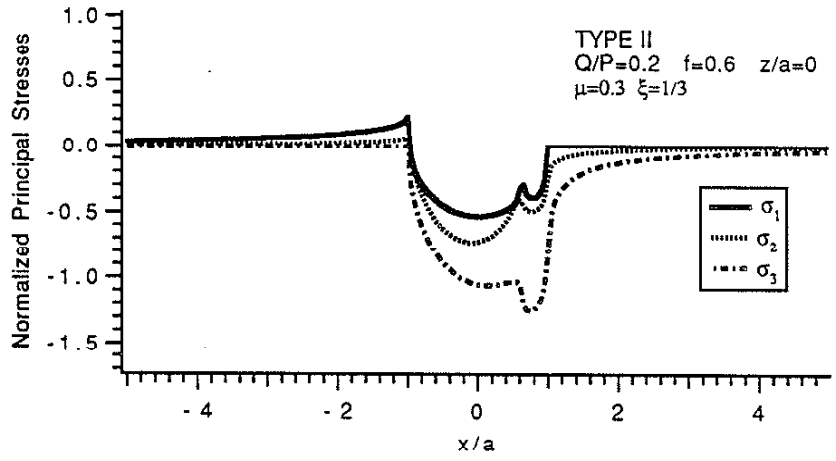

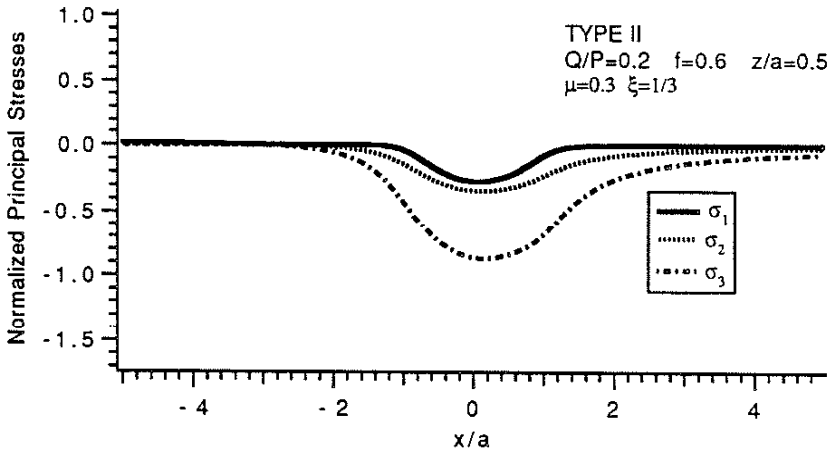

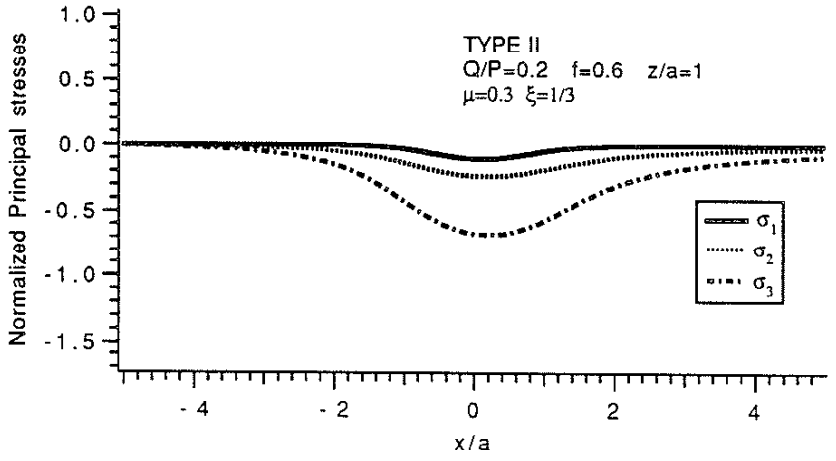

Fig.22 Variations of Principal Stresses(Q/P=0.2, f=0.6, μ=0.3,TYPE II)

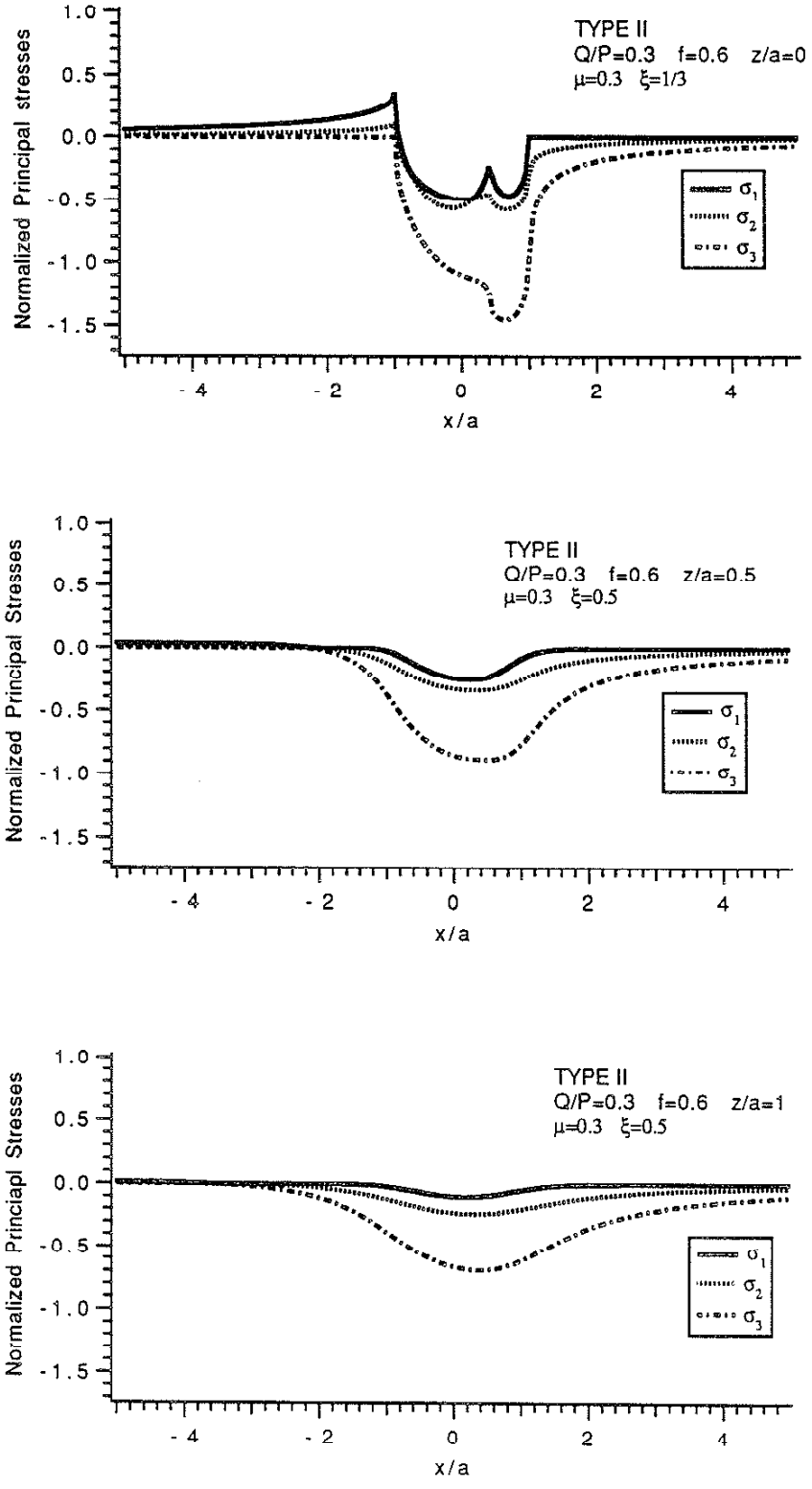

Fig.23 Variations of Principal Stresses(Q/P=0.3, f=0.6, μ=0.3,TYPE II)

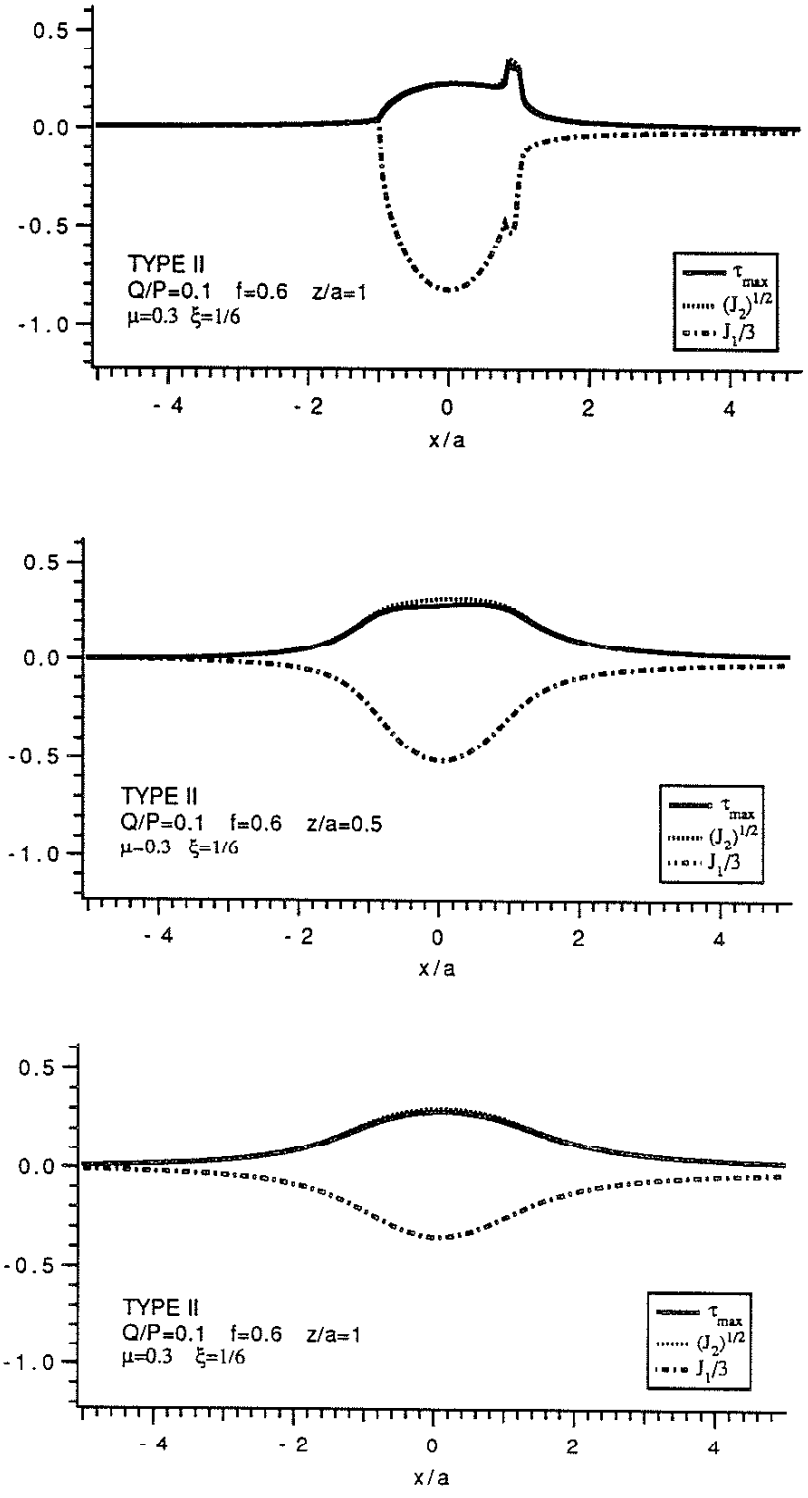

Fig.24 Variations of Tresca Shear Stress, Von Mises Shear Stress, and Hydrostatic Stress(f=0.6, Q/P=0.1, μ=0.3, TYPE II)

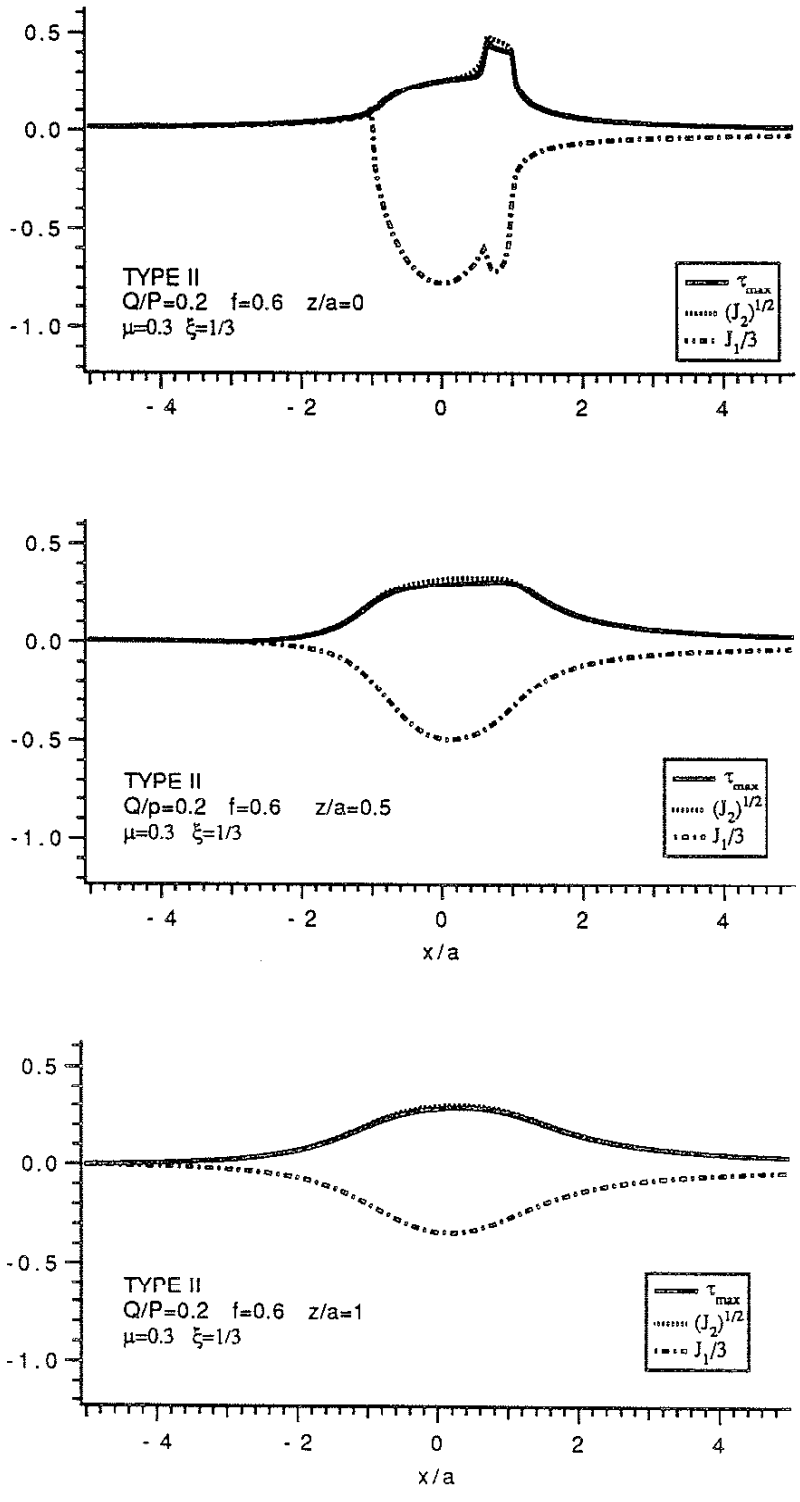

Fig.25 Variations of Tresca Shear Stress, Von Mises Shear Stress, and Hydrostatic Stress (Q/P=0.2,f=0.6, μ=0.3, TYPE II)

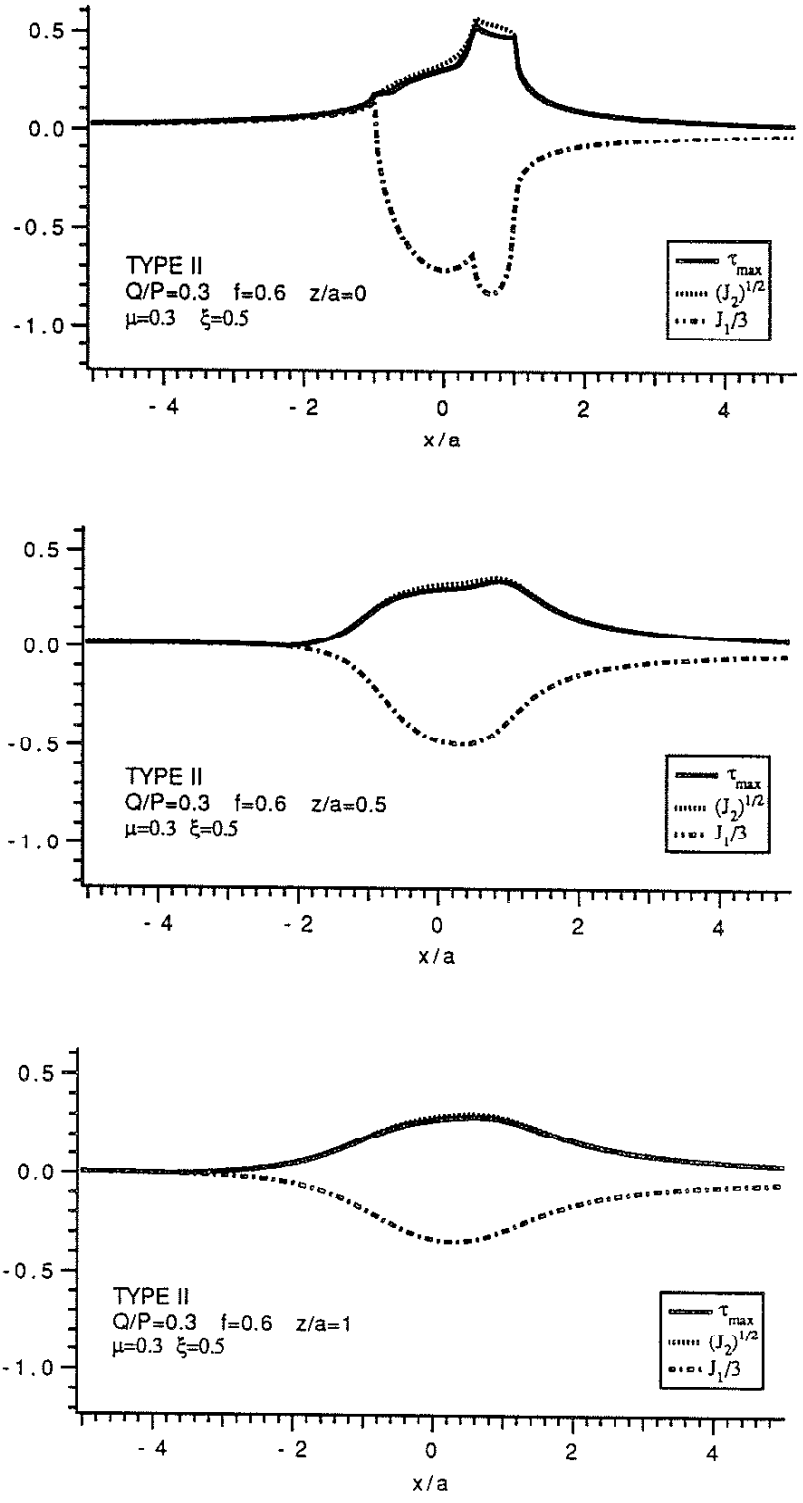

Fig.26 Variations of Tresca Shear Stress, Von Mises Shear Stress, and Hydrostatic Stress (Q/P=0.3, f=0.6, μ=0.3, TYPE II)

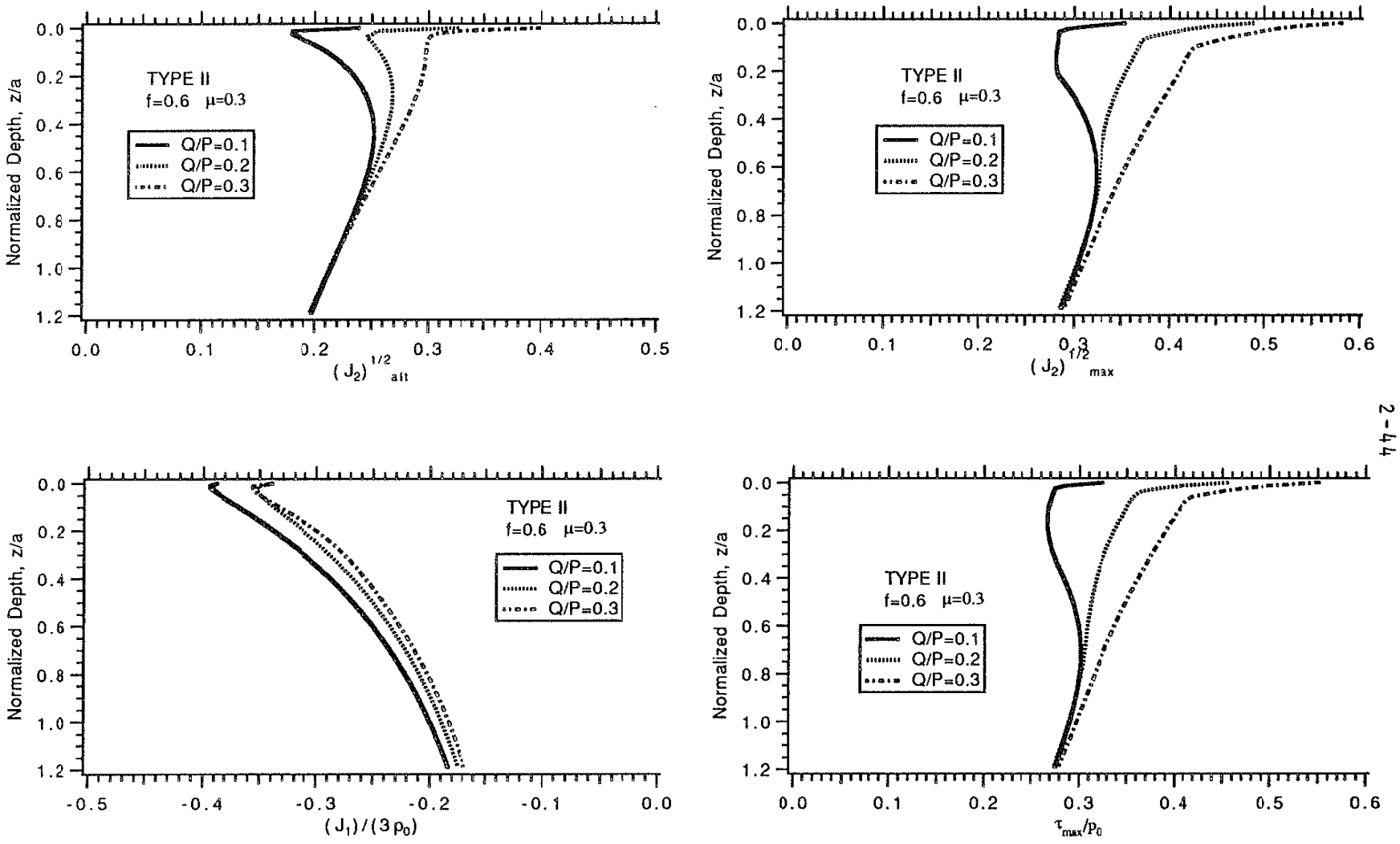

Fig.27 Variations of $(J_2)^{1/2}_{alt}$, $(J_2)^{1/2}_{max}$, $(J_1)_{stat}$, and τ_{max} along z-axis(f=0.6, μ=0.3, TYPE II)

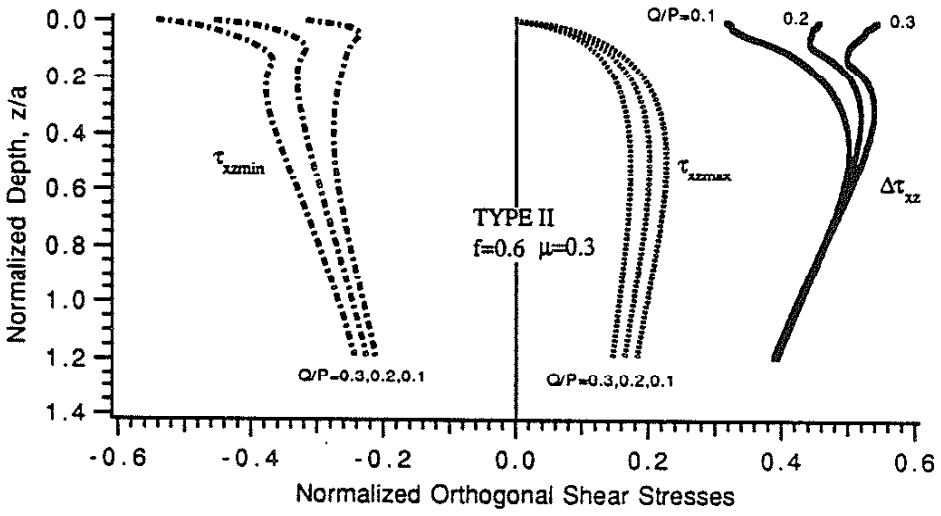

Fig.28 Variations of Orthogonal Shear Stresses along z-axis with Different Q/P Ratios(f=0.6, μ=0.3, TYPE II)

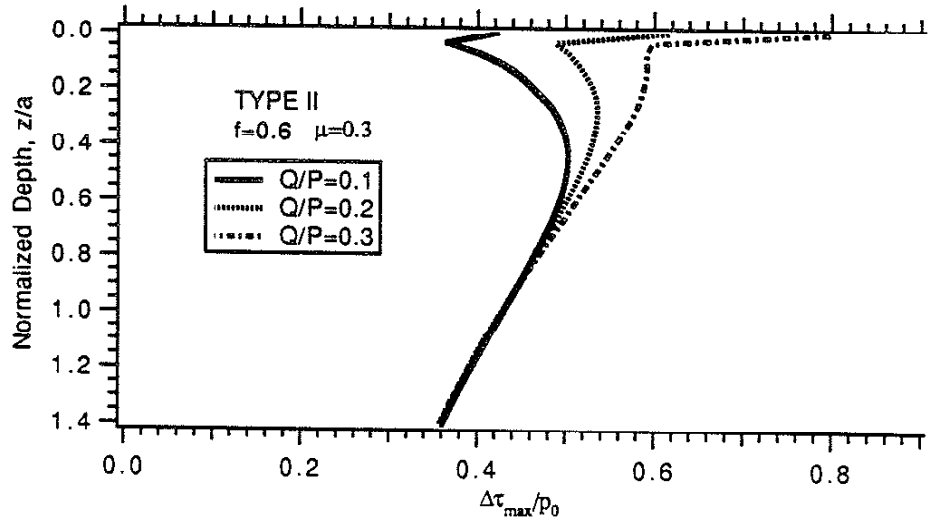

Fig.29 Variation of Maximum Shear Stress Range along z-axis(f=0.6, μ=0.3, TYPE II)

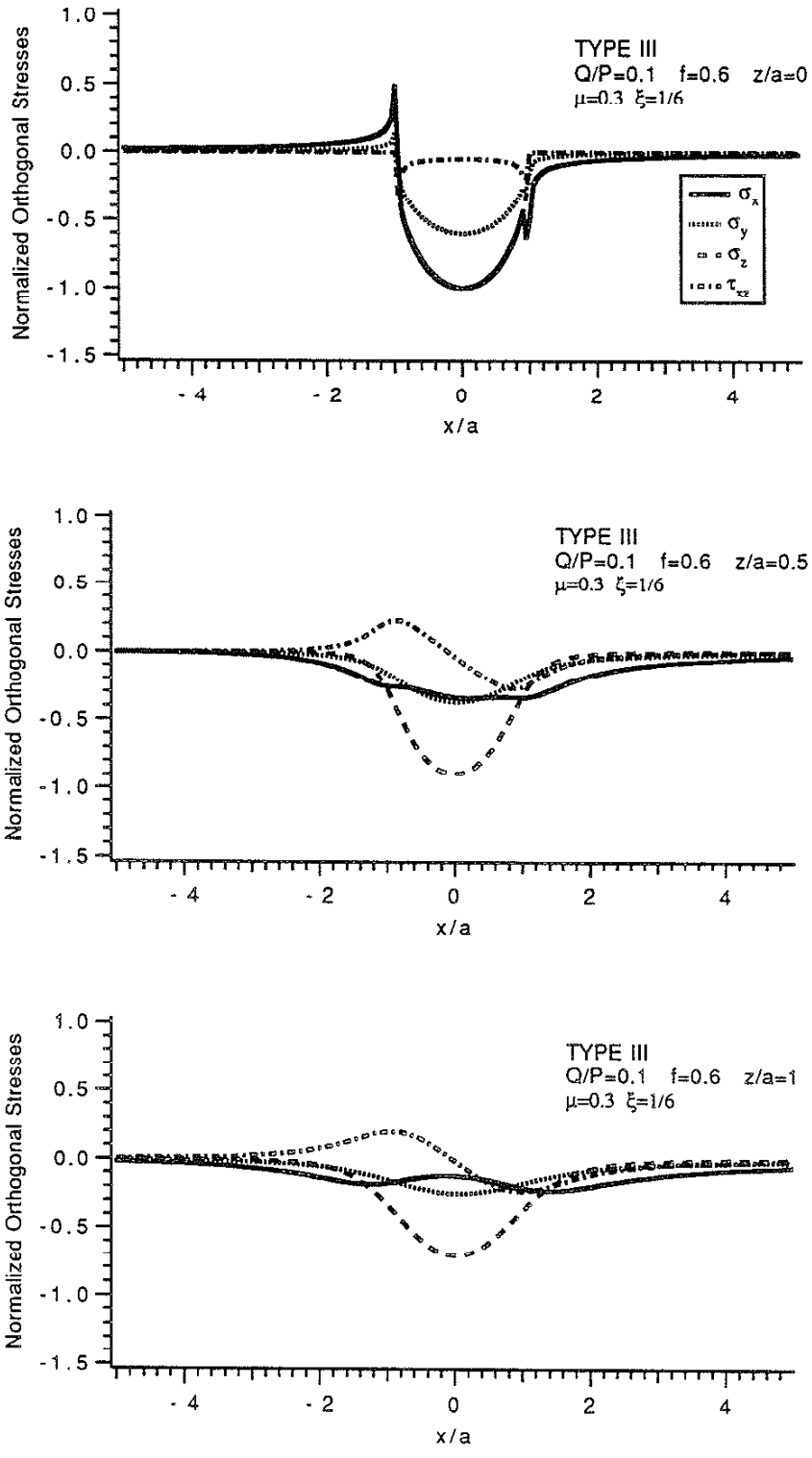

Fig.30 Variations of Orthogonal Stresses(Q/P=0.1, f=0.6, μ=0.3, TYPE III)

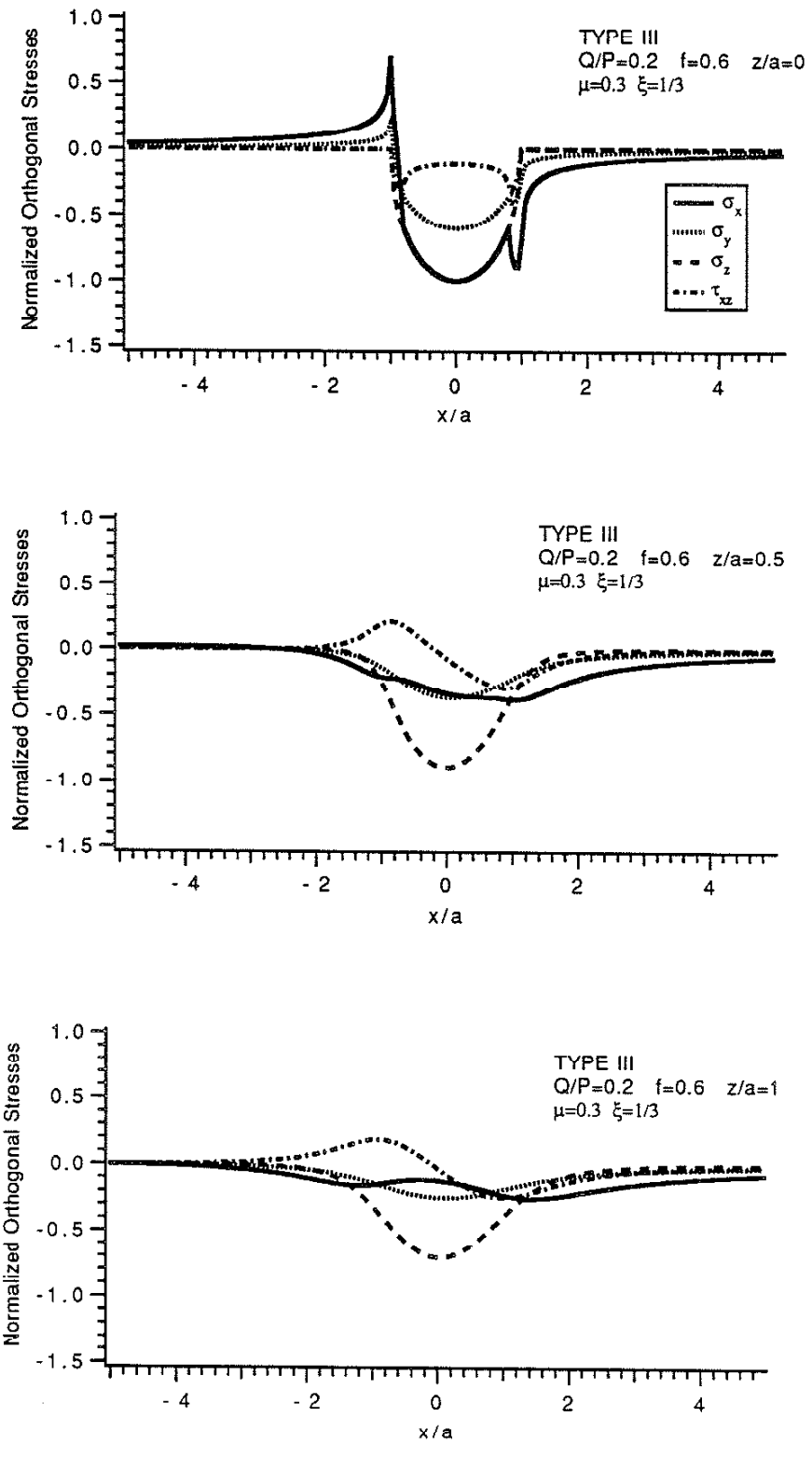

Fig.31 Variations of Orthogonal Stresses(Q/P=0.2, f=0.6, μ=0.3, TYPE III)

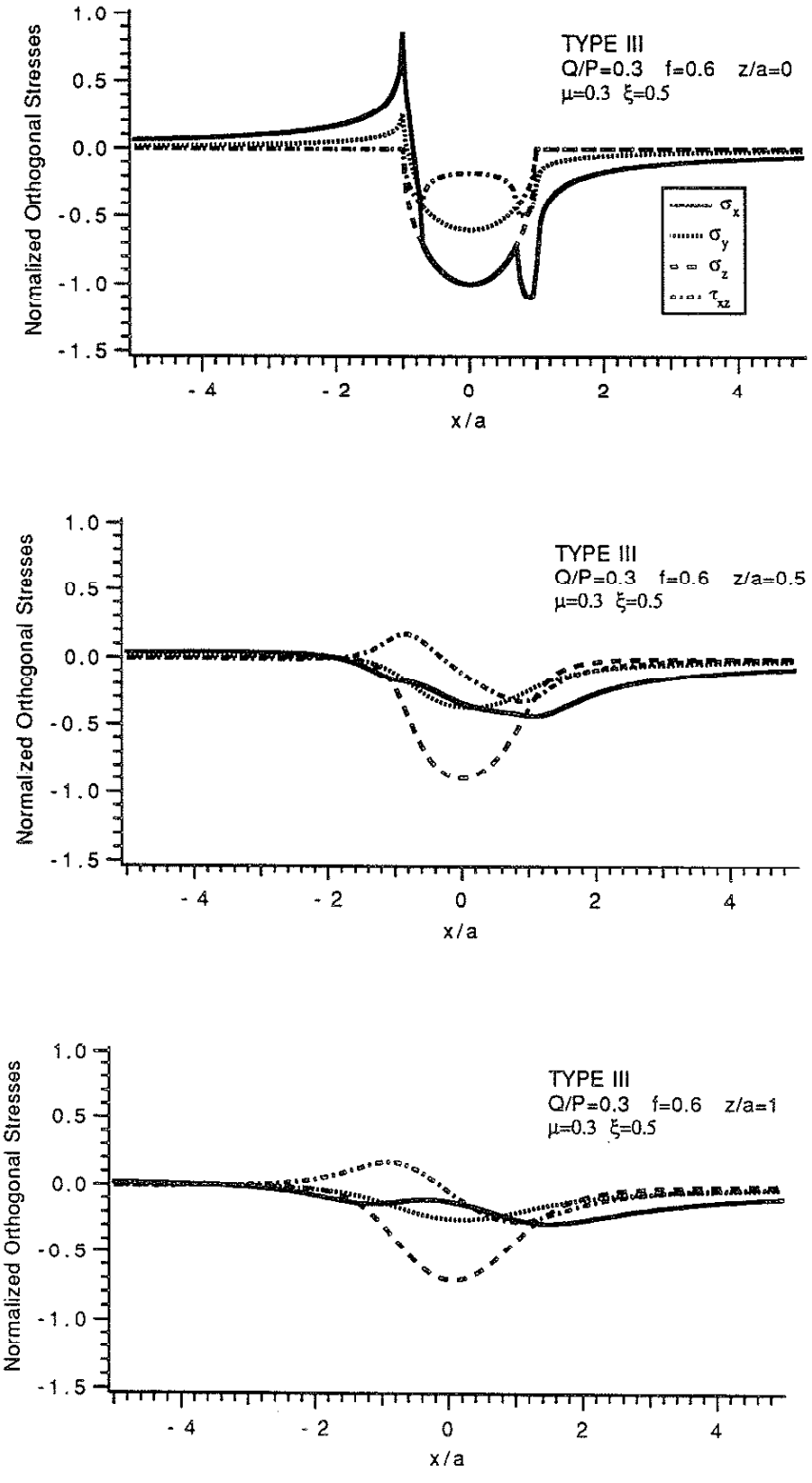

Fig.32 Variations of Orthogonal Stresses(Q/P=0.3, f=0.6, μ=0.3, TYPE III)

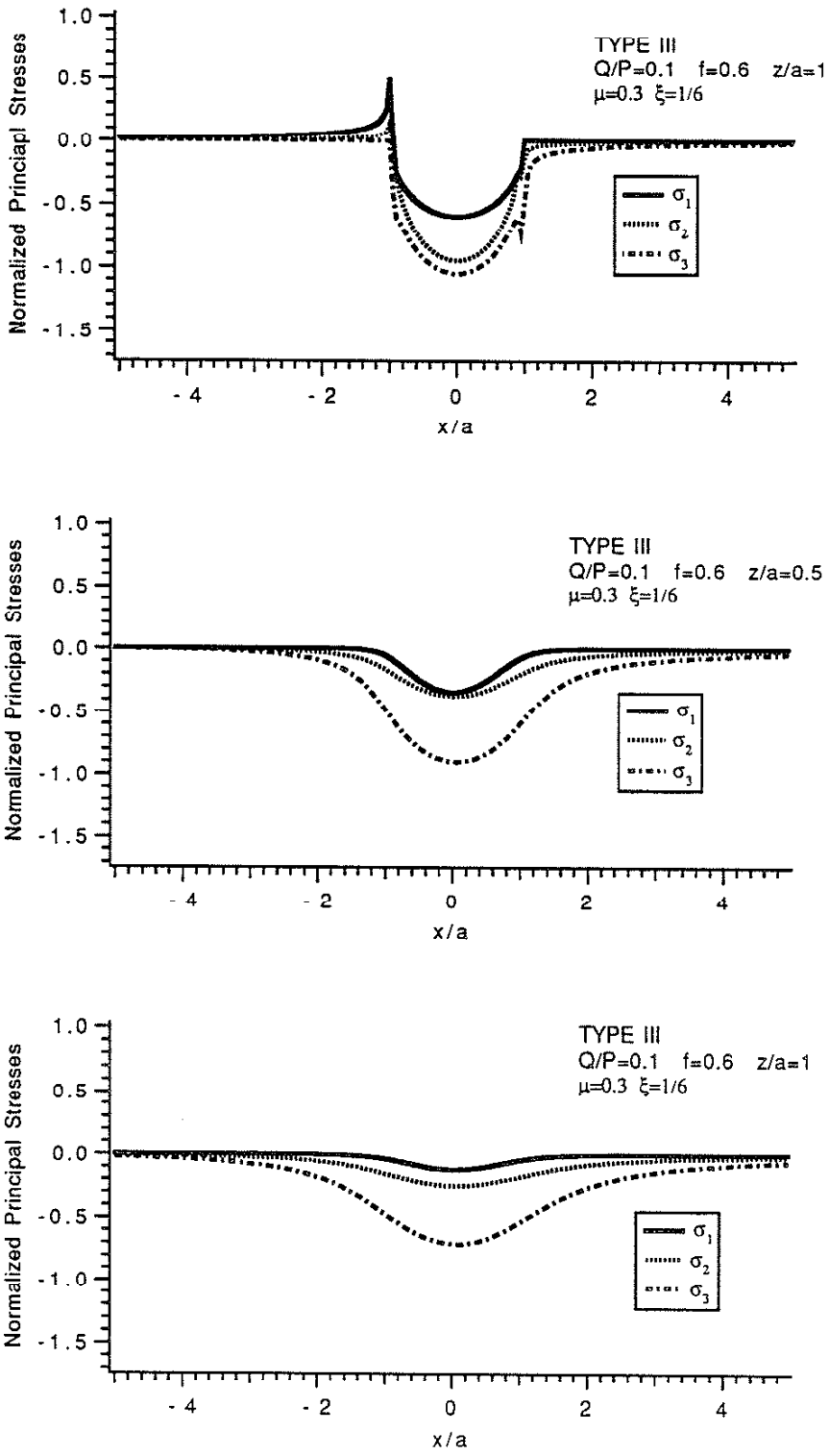

Fig.33 Variations of Principal Stresses(Q/P=0.1, f=0.6, μ=0.3, TYPE III)

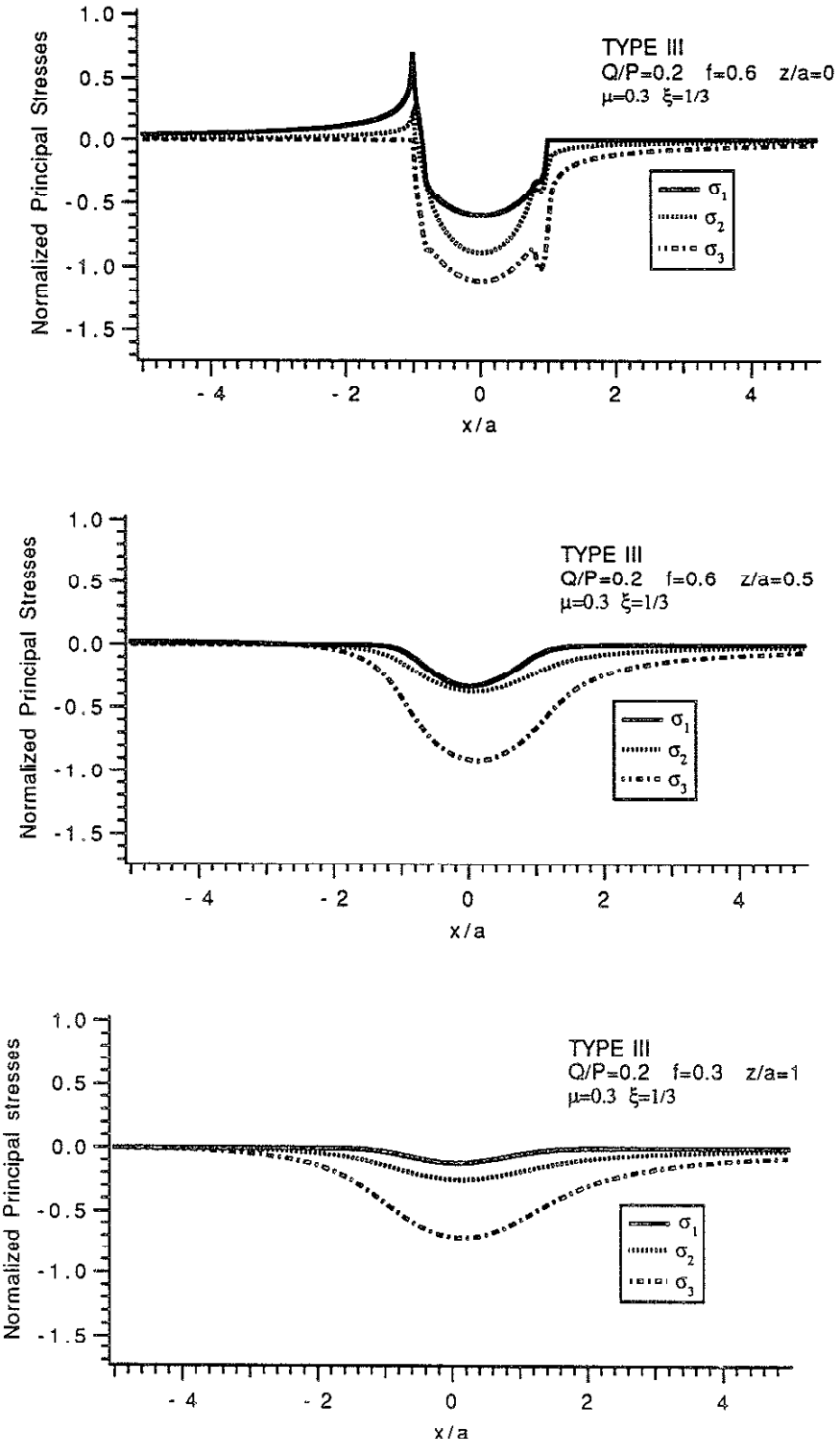

Fig.34 Variations of Principal Stresses(Q/P=0.2, f=0.6, μ=0.3, TYPE III)

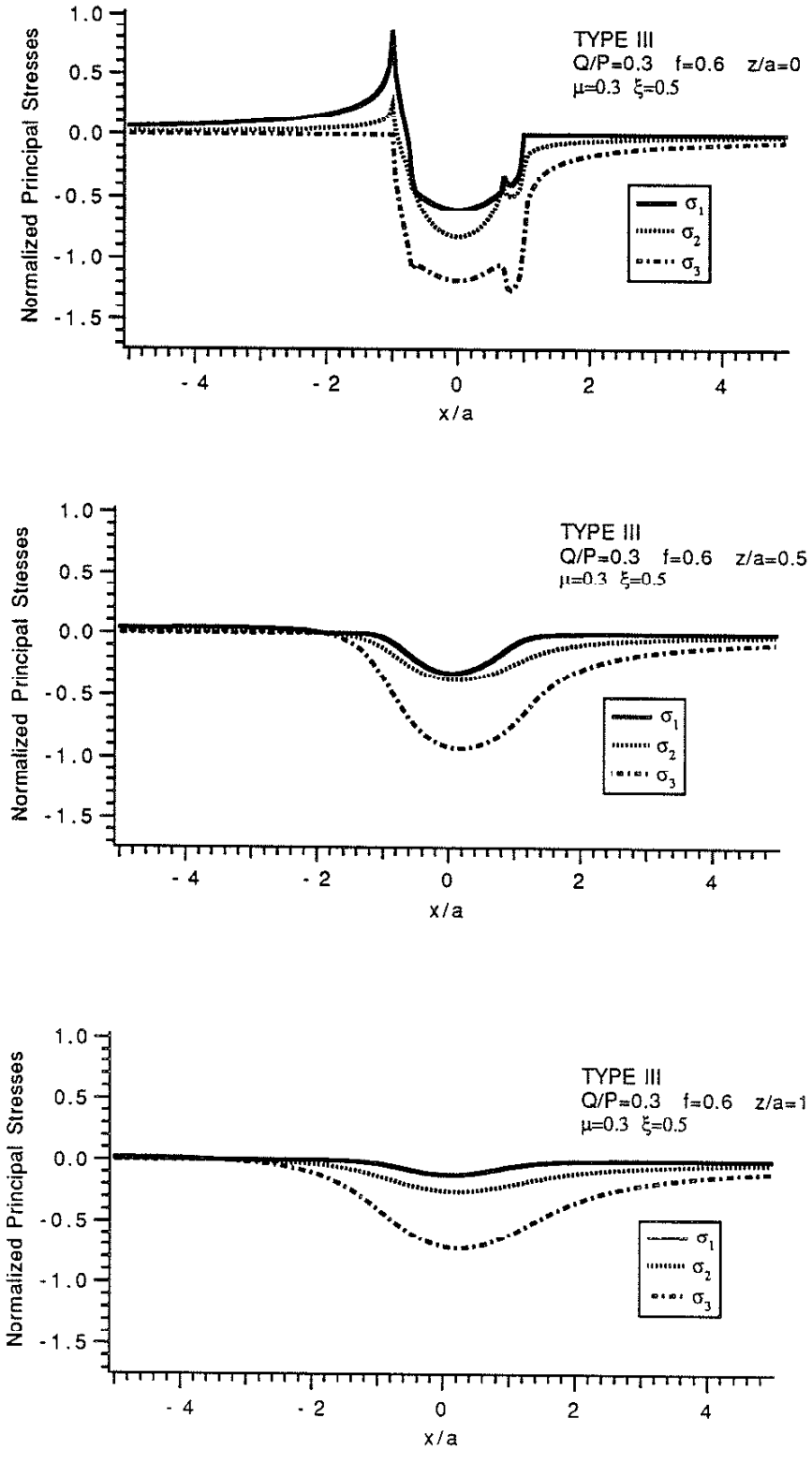

Fig.35 Variations of Principal Stresses(Q/P=0.3, f=0.6, μ=0.3, TYPE III)

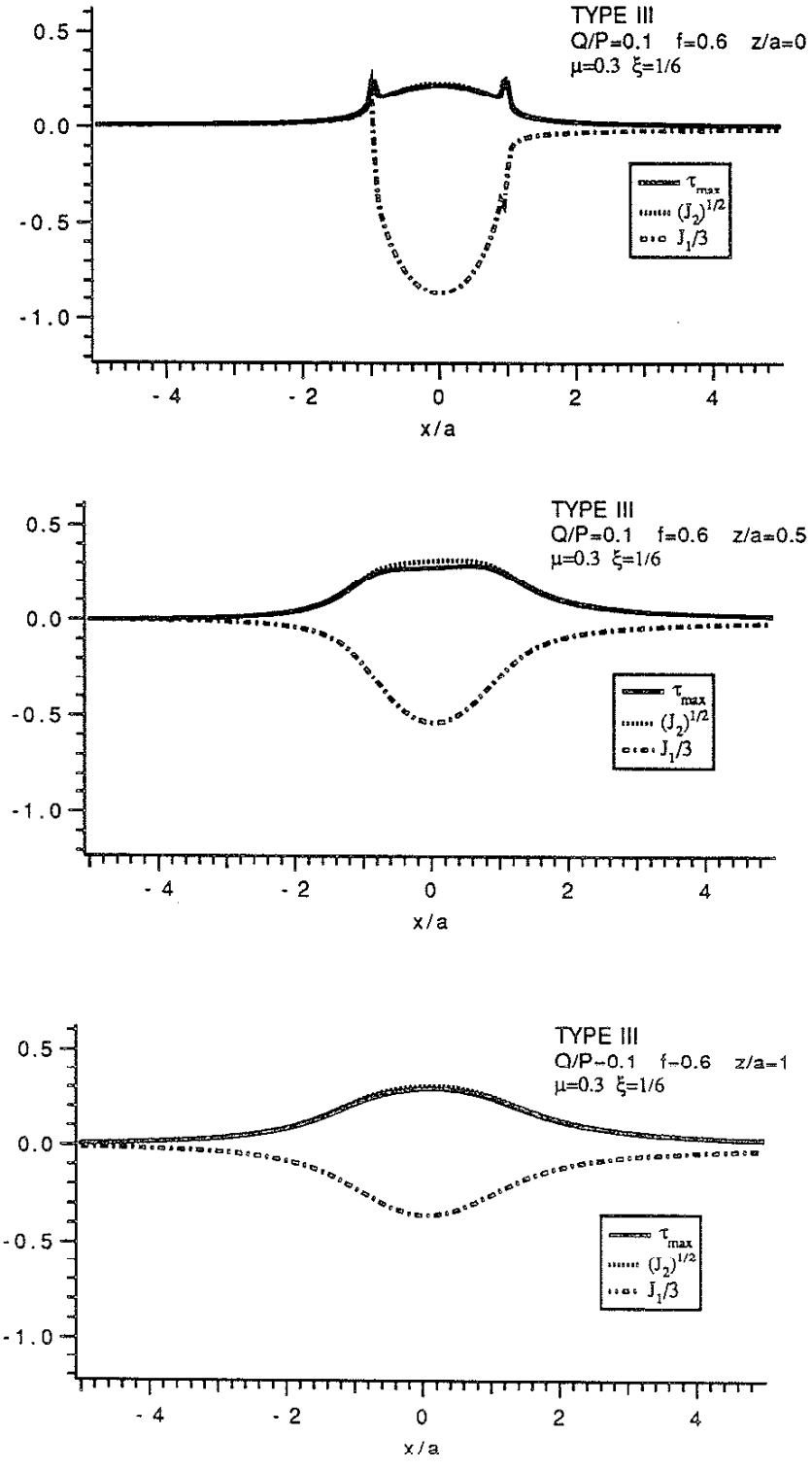

Fig.36 Variations of Tresca Shear Stress, Von Mises Shear Stress, and Hydrostatic Stress(Q/P=0.1, f=0.6, μ=0.3, TYPE III)

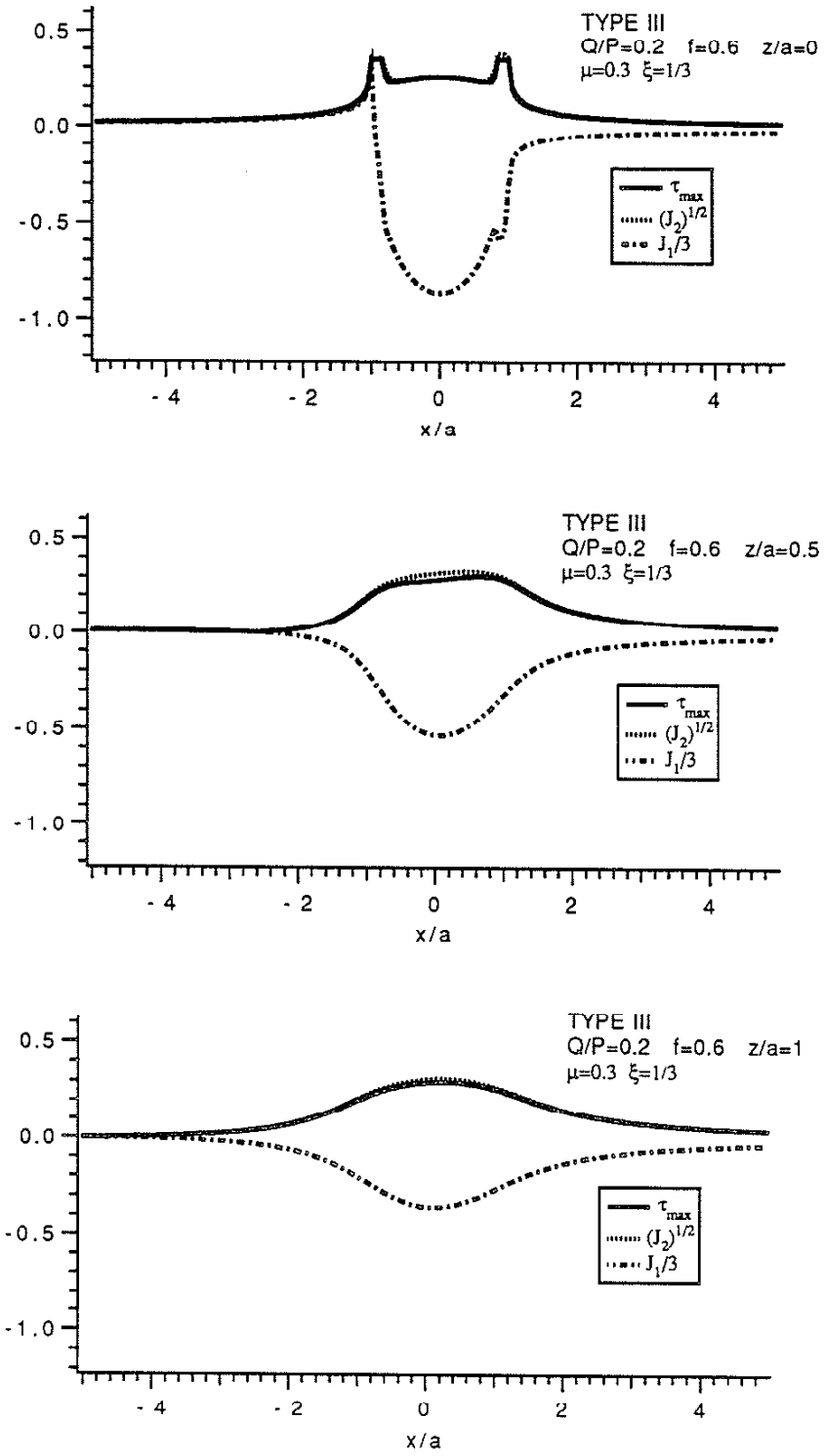

Fig.37 Variations of Tresca Shear Stress, Von Mises Shear Stress, and Hydrostatic Stress(Q/P=0.2, f=0.6, μ=0.3, TYPE III)

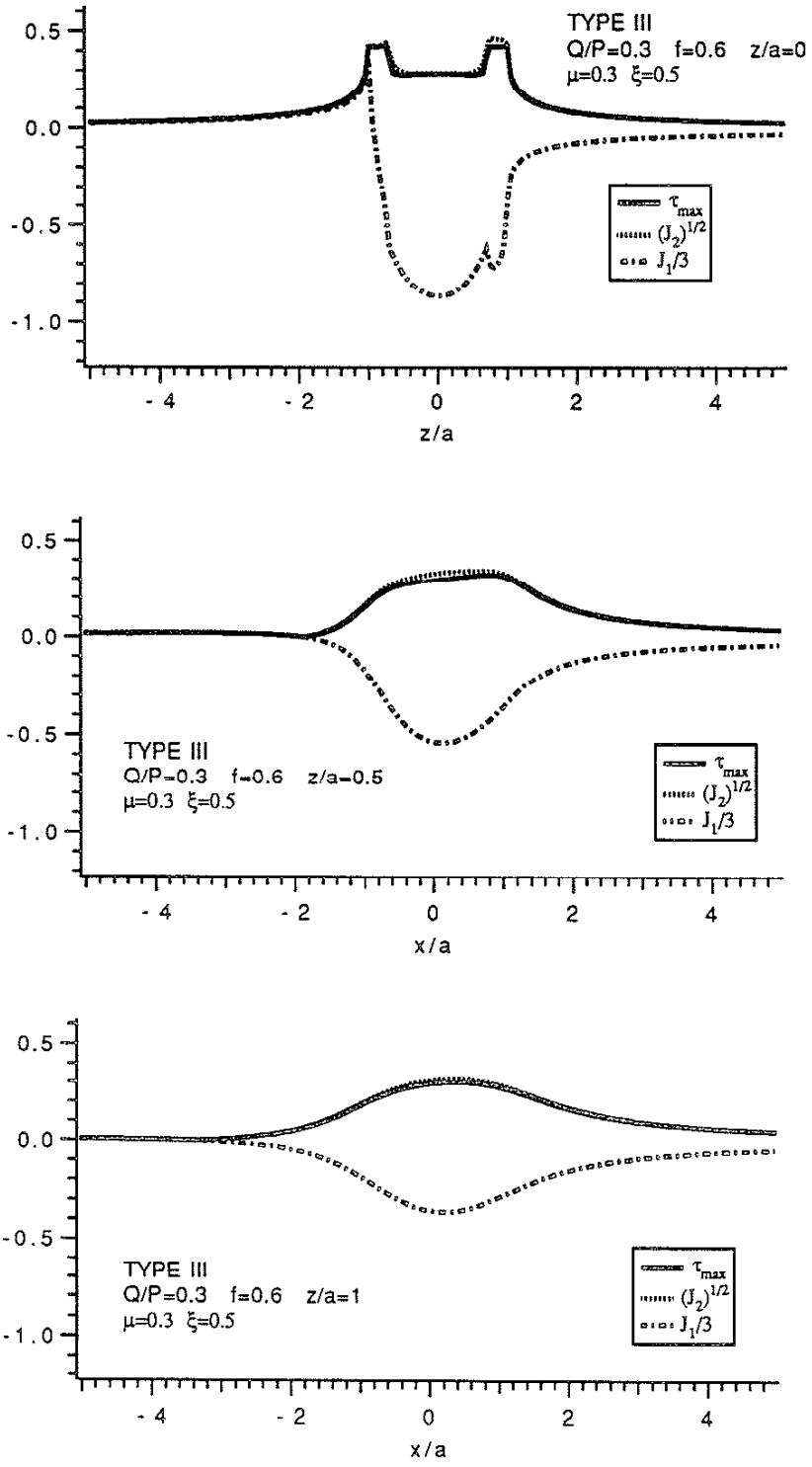

Fig.38 Variations of Tresca Shear Stress, Von Mises Shear Stress, and Hydrostatic Stress(Q/P=0.3, f=0.6, μ=0.3, TYPE III)

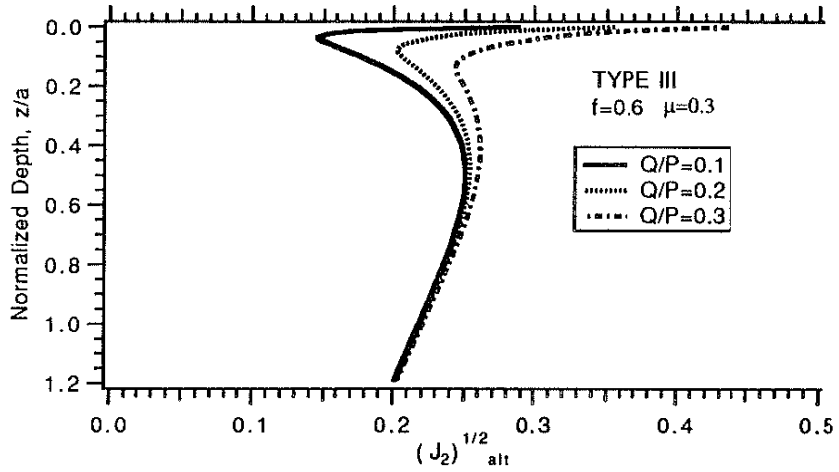

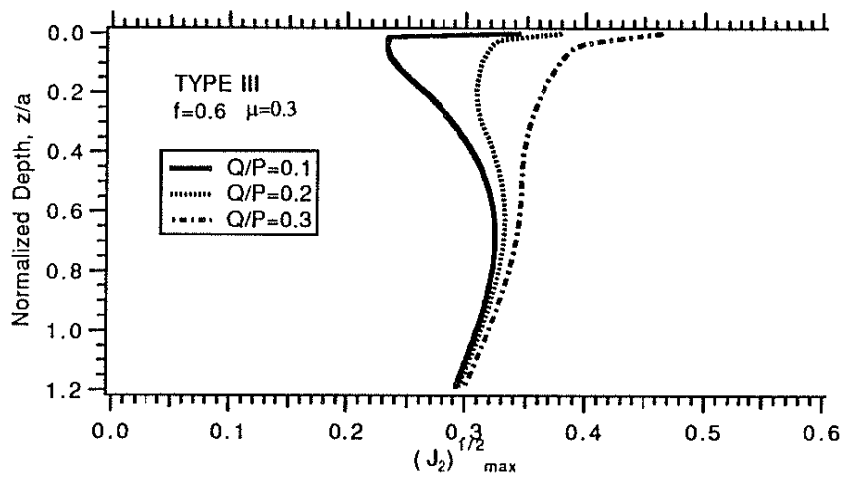

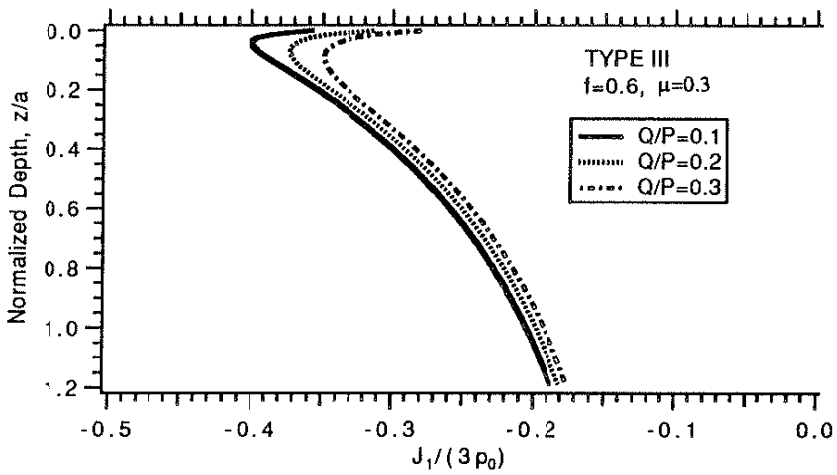

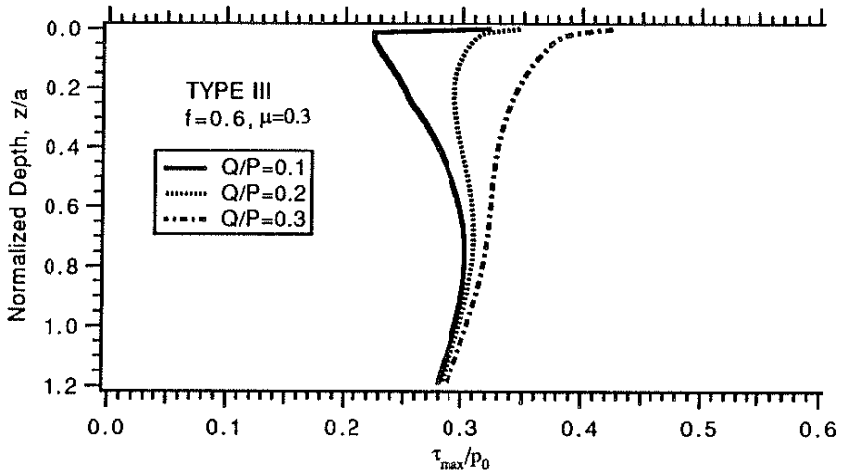

Fig.39 Variations of $(J_2)^{1/2}_{alt}$, $(J_2)^{1/2}_{max}$, $(J_1)_{stat}$, and τ_{max} along z-axis(f=0.6, μ=0.3, TYPE III)

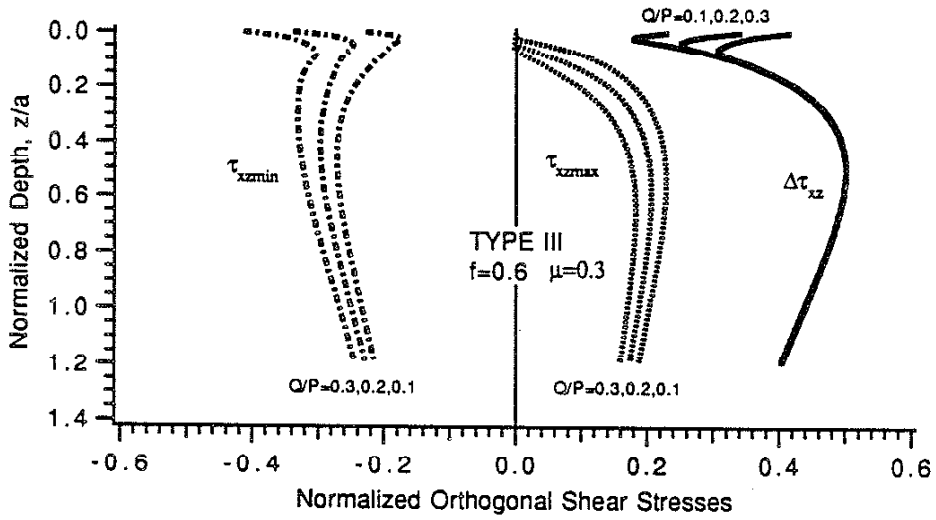

Fig.40 Variations of Orthogonal Shear Stresses along z-axe with Different Q/P Ratios (f=0.6, μ=0.3, TYPE III)

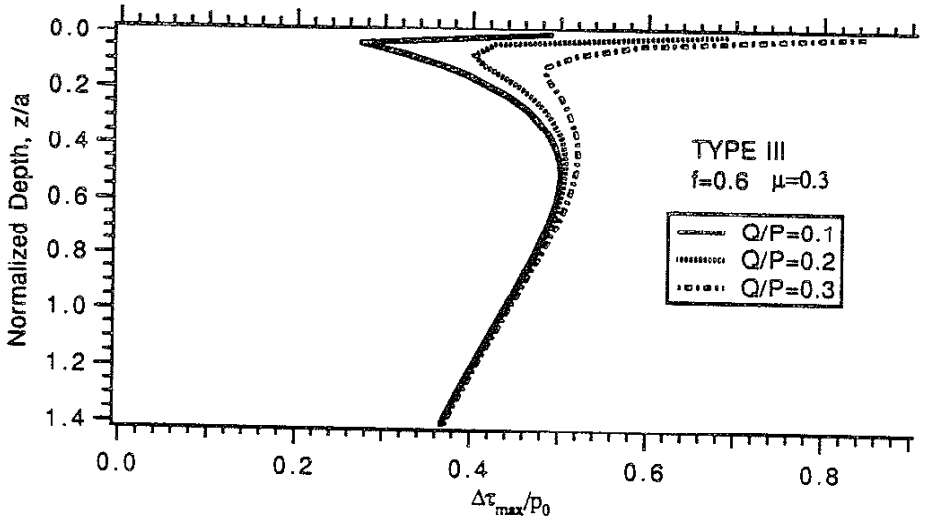

Fig.41 Variation of Maximum Shear Stress Range along z-axis(f=0.6, μ=0.3, TYPE III)

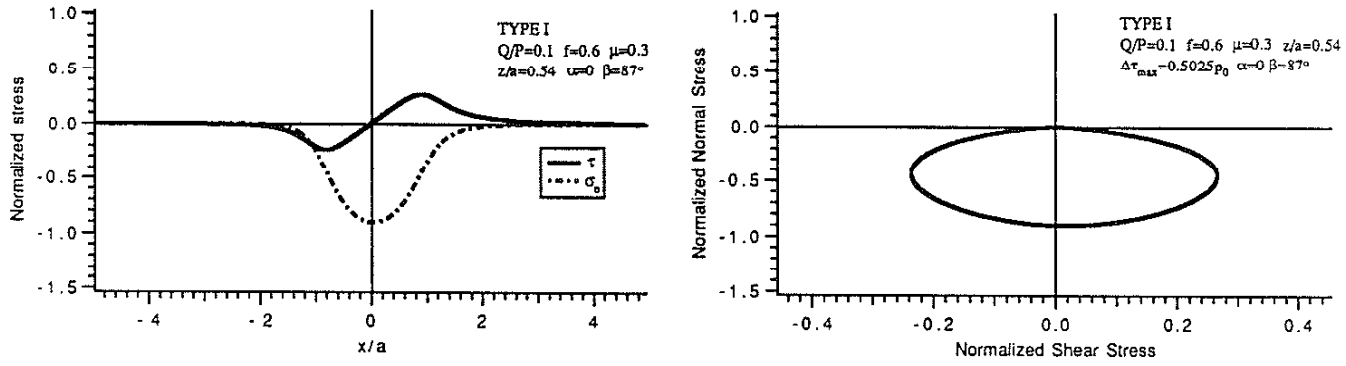

(a) Q/p=0.1 f=0.6 μ=0.3

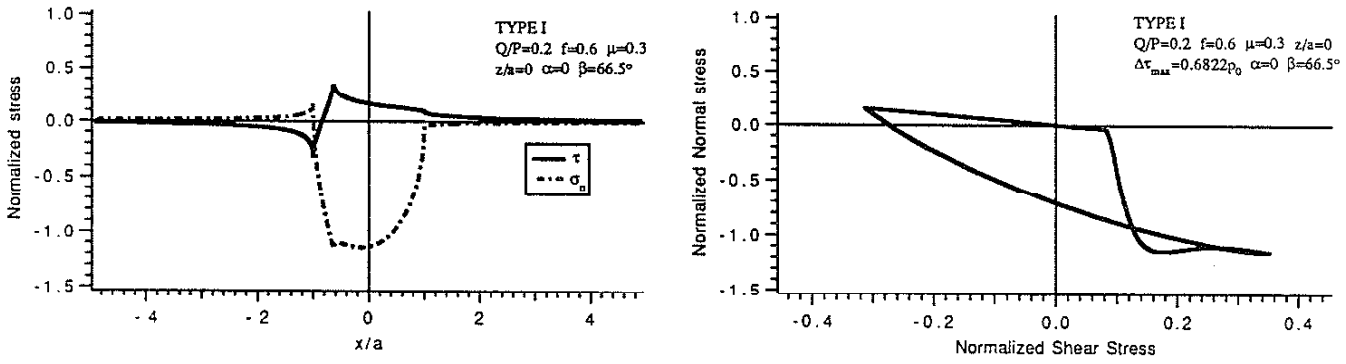

(b) Q/p=0.2 f=0.6 μ=0.3

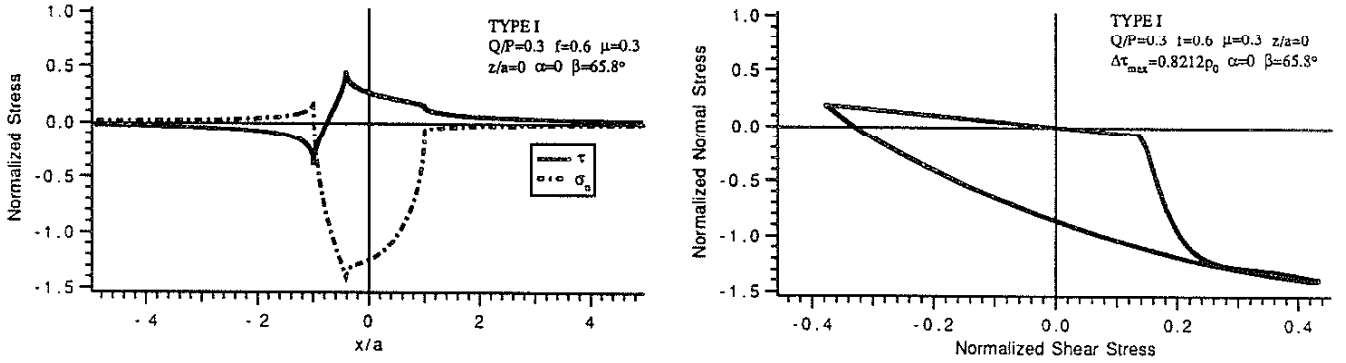

(c) Q/p=0.3 f=0.6 μ=0.3

Shear Stress and Normal Stress Variations with Time on the Plane of Maximum Shear Stress Range

Normal Stress vs Shear Stress on the plane of Maximum Shear Stress Range

Fig.42 Stress Variations on the Plane of Maximum Shear Stress Range(Critical Plane)(f=0.6, μ=0.3, TYPE I)

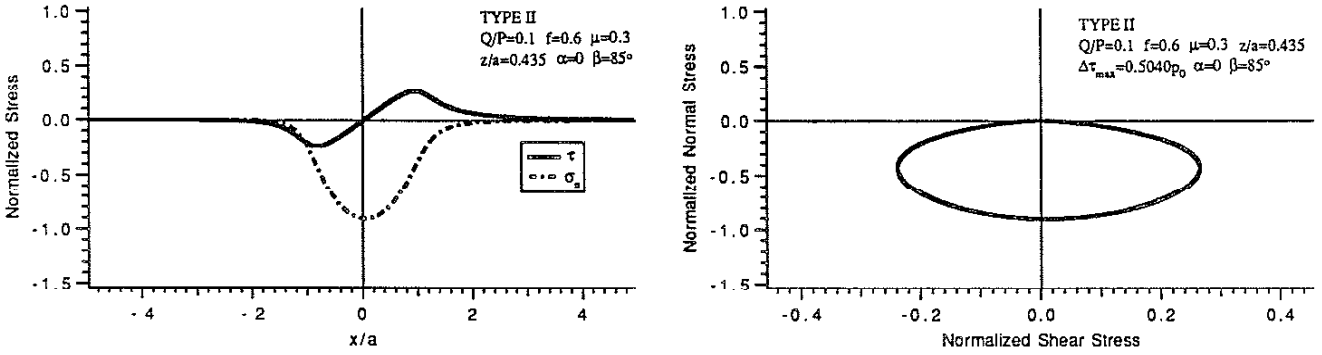

(a) Q/p=0.1 f=0.6 μ=0.3

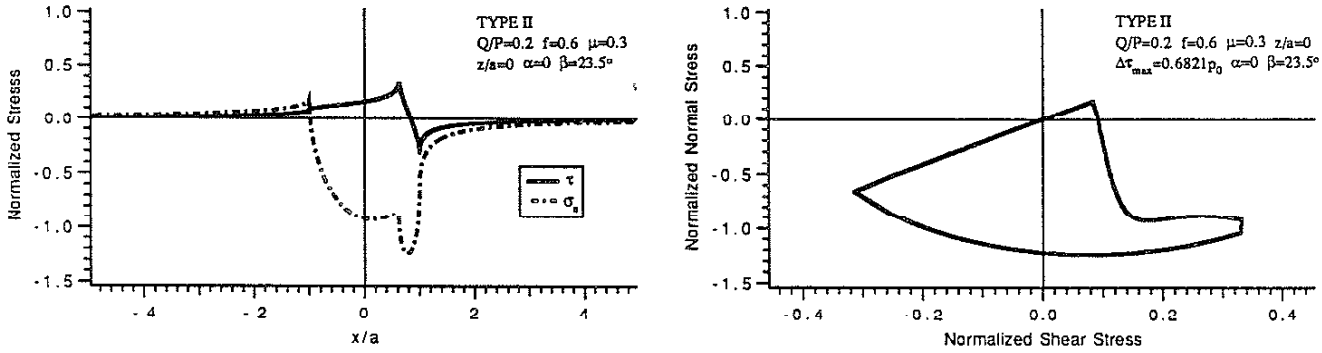

(b) Q/p=0.2 f=0.6 μ=0.3

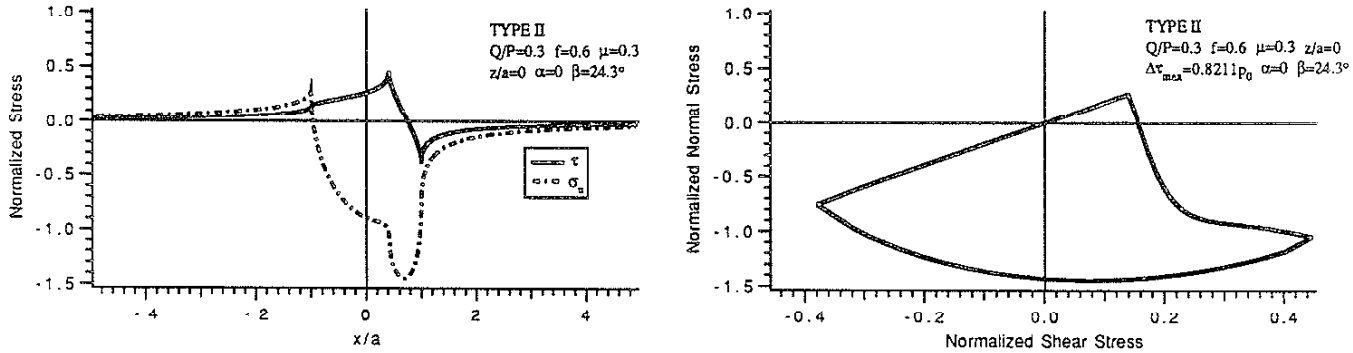

(c) Q/p=0.3 f=0.6 μ=0.3

Shear Stress and Normal Stress Variations with Time on the Plane of Maximum Shear Stress Range

Normal Stress vs Shear Stress on the plane of Maximum Shear Stress Range

Fig.43 Stress Variations on the Plane of Maximum Shear Stress Range(Critical Plane)(f=0.6, μ=0.3, TYPE II)

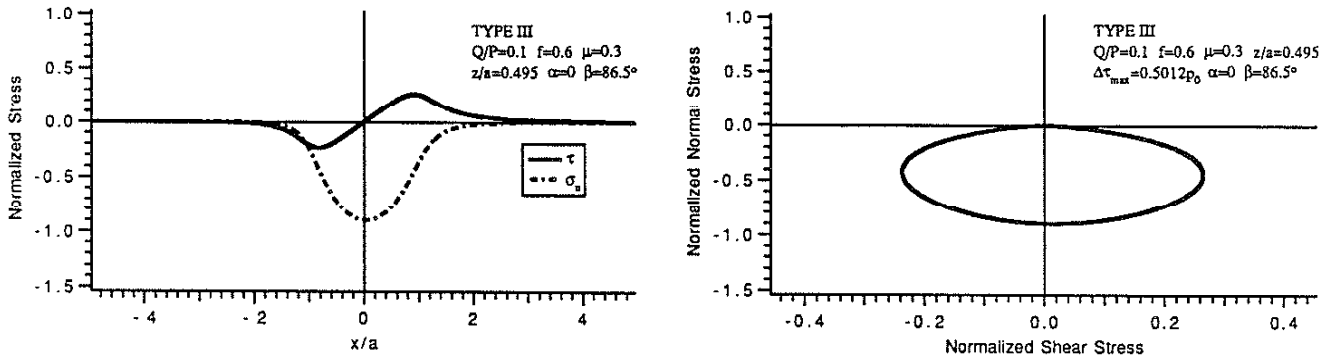

(a) Q/p=0.1 f=0.6 μ=0.3

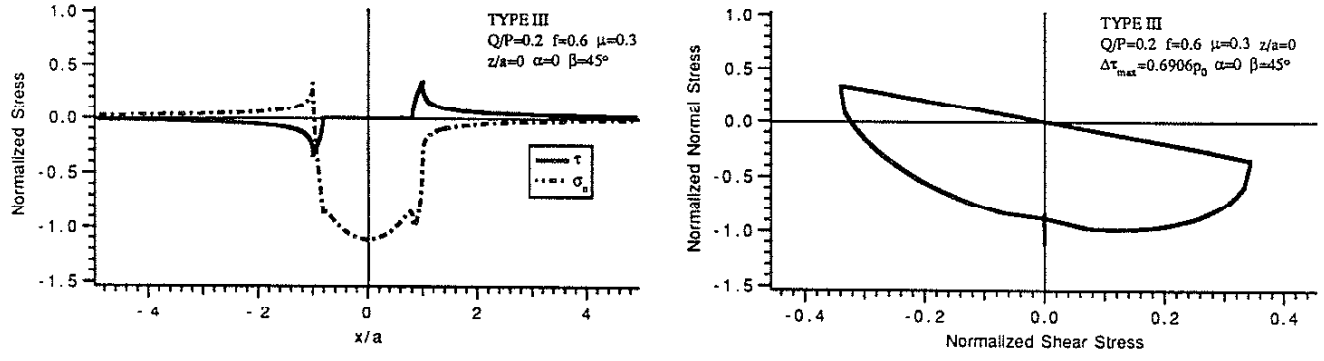

(b) Q/p=0.2 f=0.6 μ=0.3

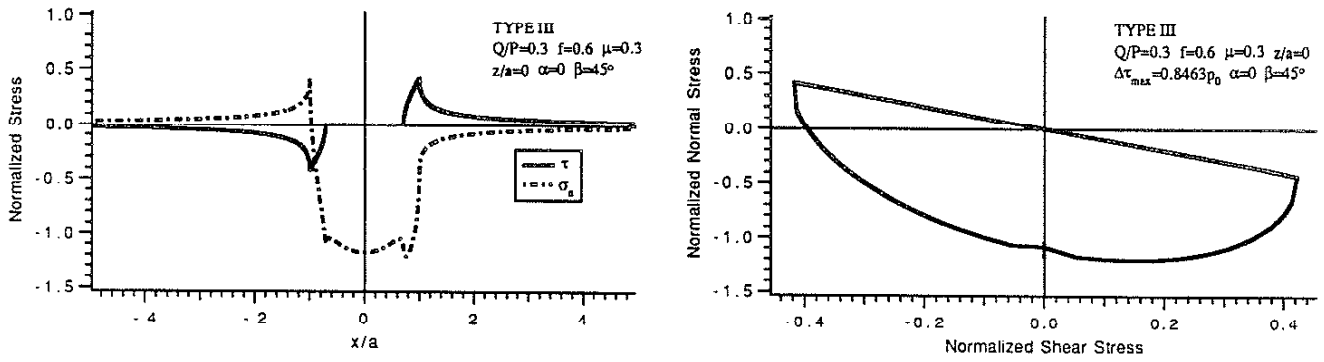

(c) Q/p=0.3 f=0.6 μ=0.3

Shear Stress and Normal Stress Variations with Time on the Plane of Maximum Shear Stress Range

Normal Stress vs Shear Stress on the plane of Maximum Shear Stress Range

Fig.44 Stress Variations on the Plane of Maximum Shear Stress Range(Critical Plane)(f=0.6, μ=0.3, TYPE III)

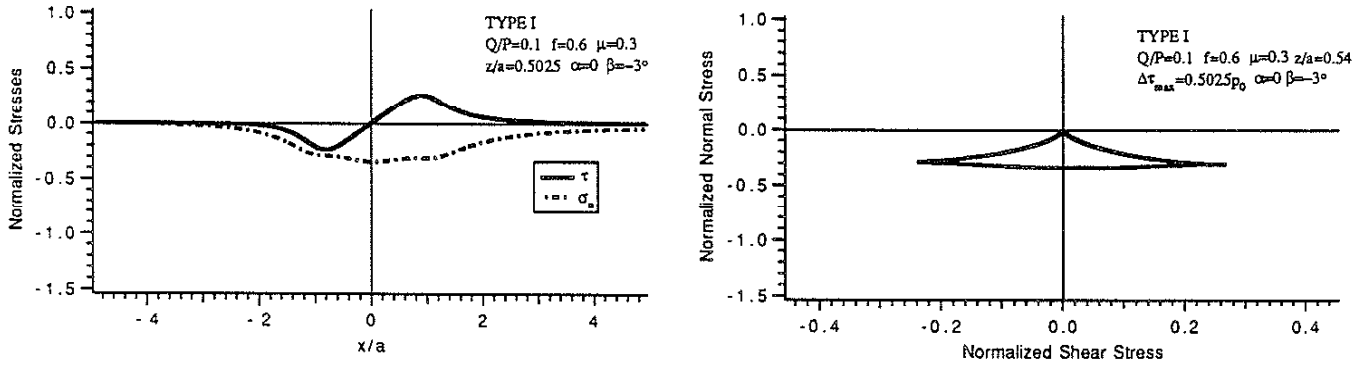

(a) Q/P=0.1 f=0.6 μ=0.3

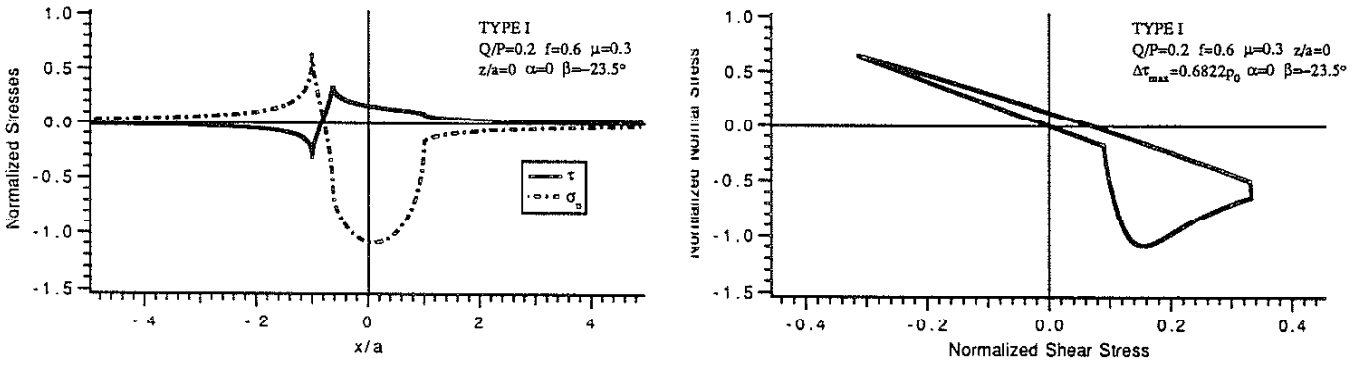

(b) Q/P=0.2 f=0.6 μ=0.3

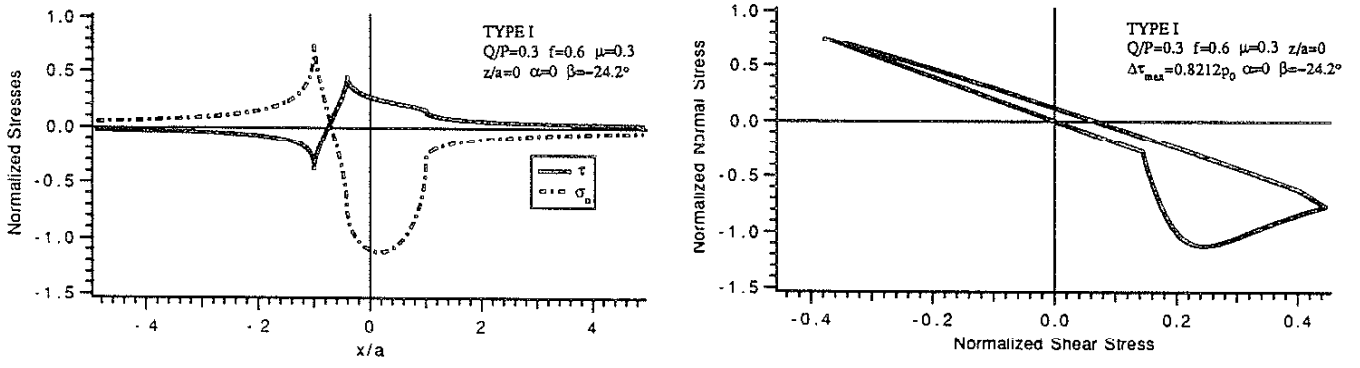

(c) Q/P=0.3 f=0.6 μ=0.3

Shear Stress and Normal Stress Variations with Time on the Plane of Maximum Shear Stress Range

Normal Stress vs Shear Stress on the Plane of Maximum Shear Stress Range

Fig.45 Stress Variations on the Plane of Maximum Shear Stress Range(Critical Plane)(f=0.6, μ=0.3,TYPE I)

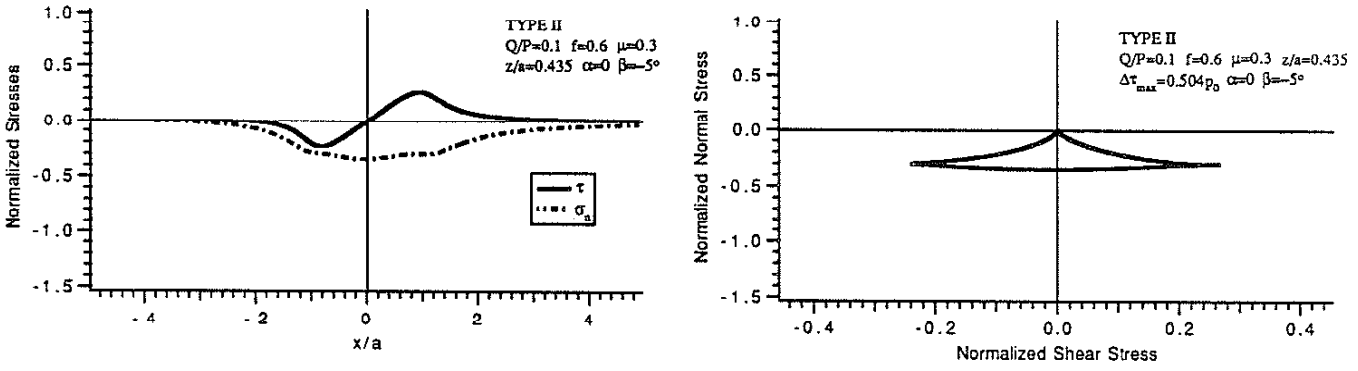

(a) Q/P=0.1 f=0.6 μ=0.3

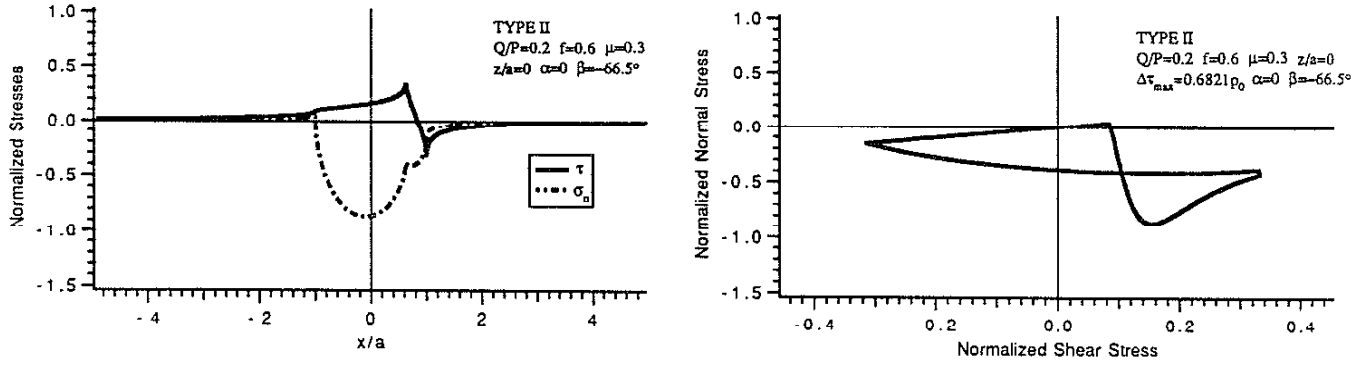

(b) Q/P=0.2 f=0.6 μ=0.3

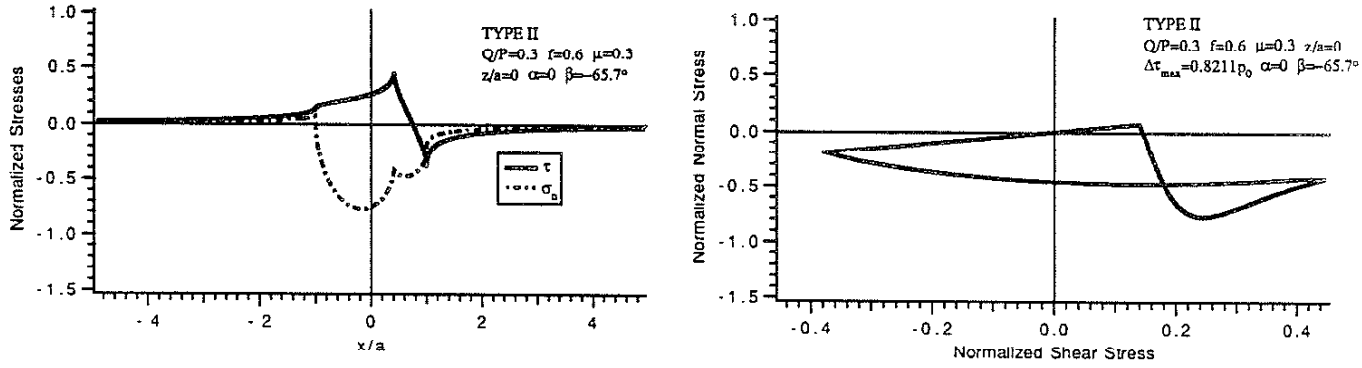

(c) Q/P=0.3 f=0.6 μ=0.3

Shear Stress and Normal Stress Variations with Time on the Plane of Maximum Shear Stress Range

Normal Stress vs Shear Stress on the Plane of Maximum Shear Stress Range

Fig.46 Stress Variations on the Plane of maximum Shear Stress Range(Critical Plane)(f=0.6, μ=0.3, TYPE II)

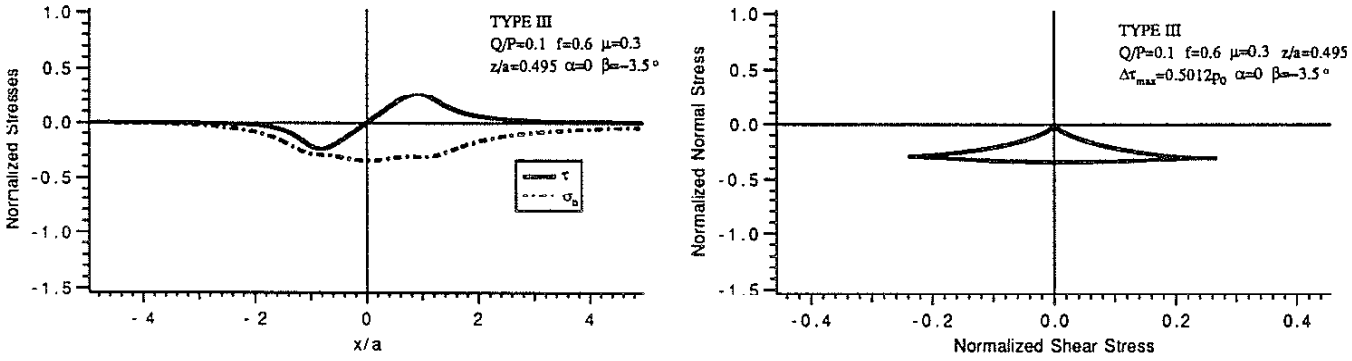

(a) Q/P=0.1 f=0.6 μ=0.3

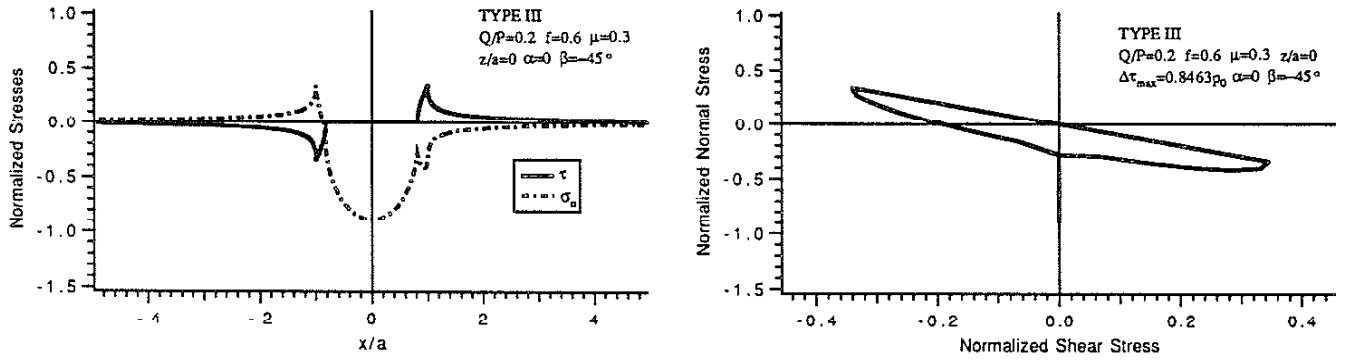

(b) Q/P=0.2 f=0.6 μ=0.3

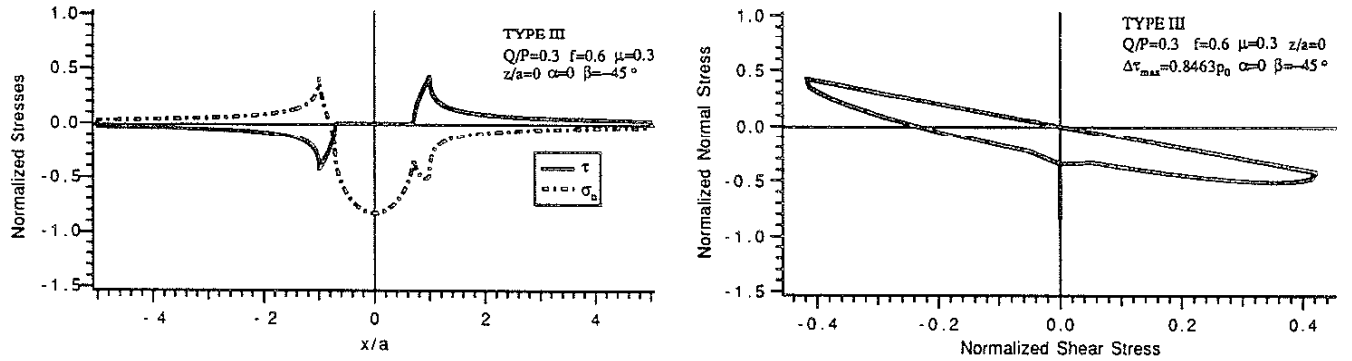

(c) Q/P=0.3 f=0.6 μ=0.3

Shear Stress and Normal Stress Variations with Time on the Plane of Maximum Shear Stress Range

Normal Stress vs Shear Stress on the Plane of Maximum Shear Stress Range

Fig.47 Stress Variations on the Plane of Maximum Shear Stress Range(Critical Plane)(f=0.6μ=0.3, TYPE III)

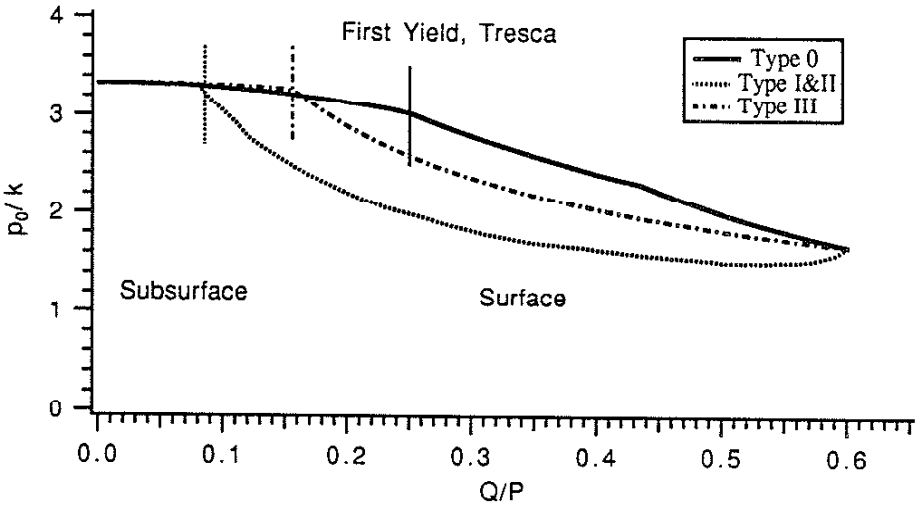

Fig.48 Effect of Q/P Ratio and Type of Tangential Loading on the Contact Pressure for First Yield

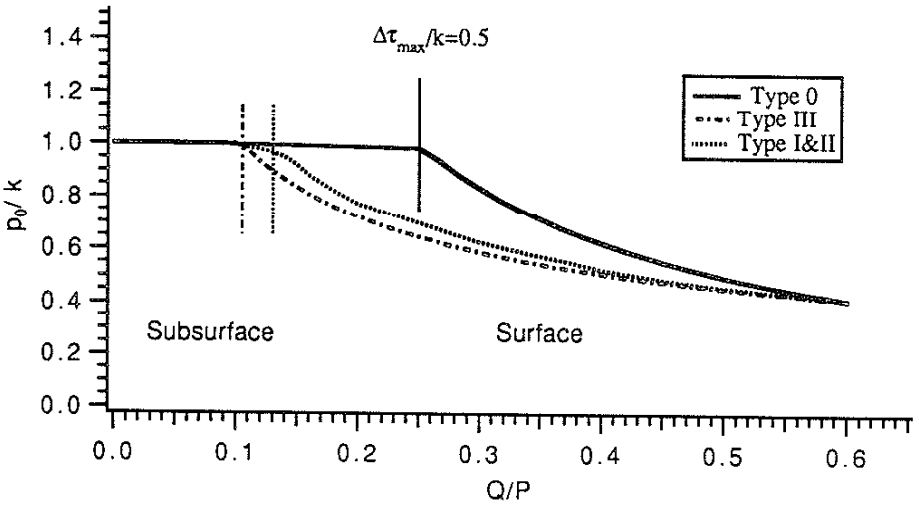

Fig.49 Effect of Q/P Ratio and Type of Tangential Loading on the Contact Pressure for $\Delta\tau_{max}/k=0.5$

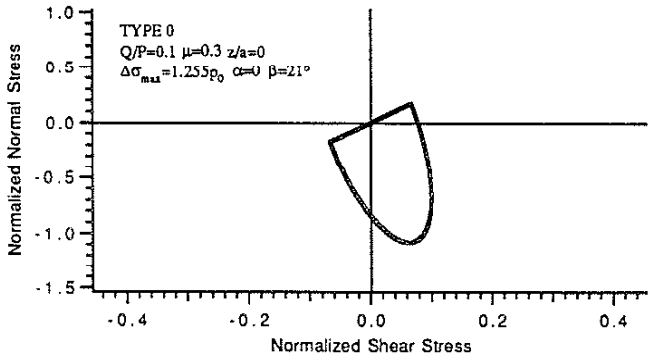

(a) TYPE 0, Q/P=0.1

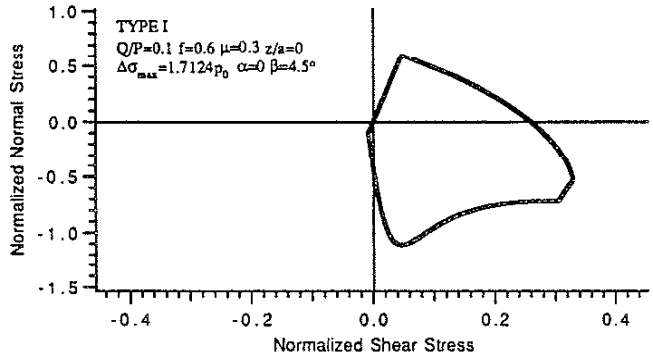

(d) TYPE I, Q/P=0.1, f=0.6

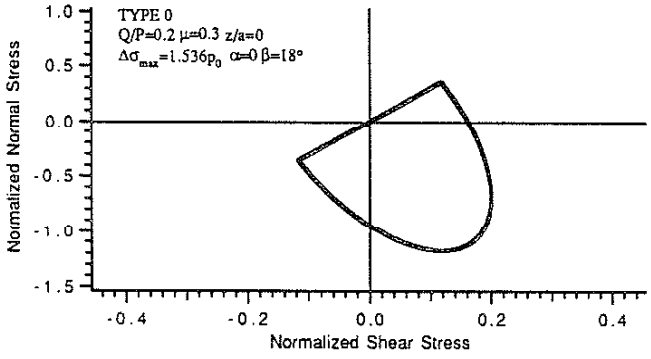

(b) TYPE 0, Q/P=0.2

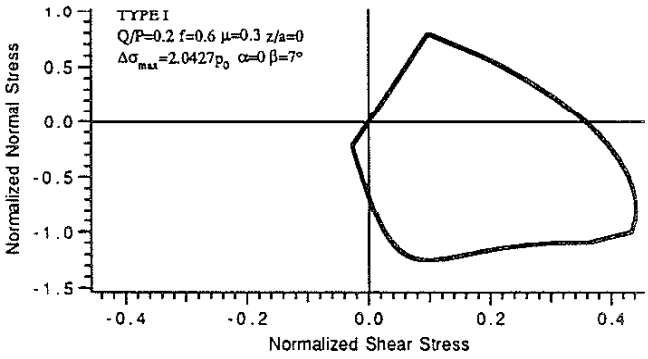

(e) TYPE I, Q/P=0.2, f=0.6

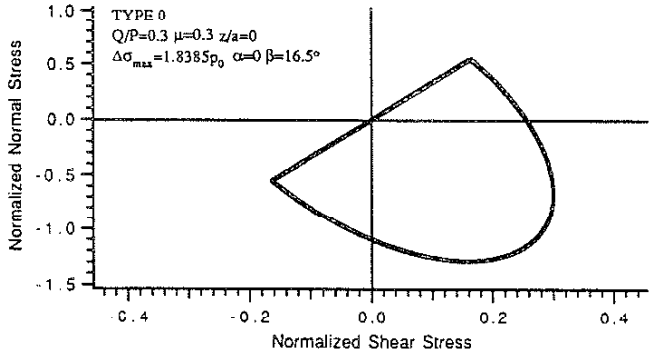

(a) TYPE 0, Q/P=0.3

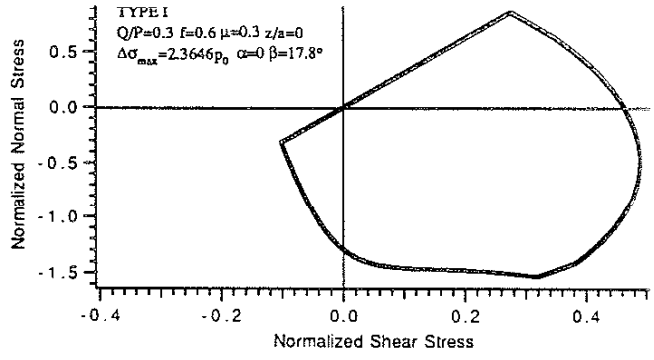

(f) TYPE I, Q/P=0.3, f=0.6

Fig.50 Stress Variations on the Plane of Maximum Normal Stress Range(μ=0.3, TYPE 0 and TYPE I)

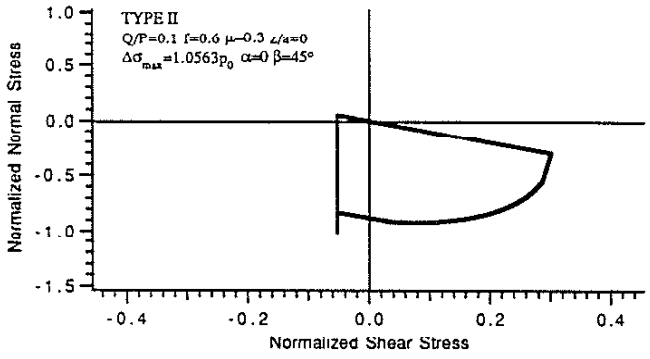

(a)TYPE II, Q/P=0.1, f=0.6

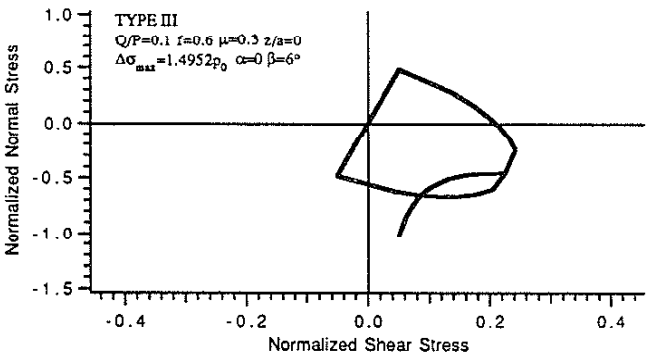

(d)TYPE III, Q/P=0.1, f=0.6

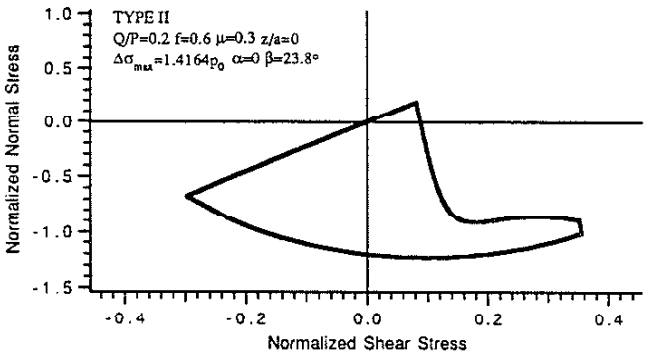

(b)TYPE II, Q/P=0.2, f=0.6

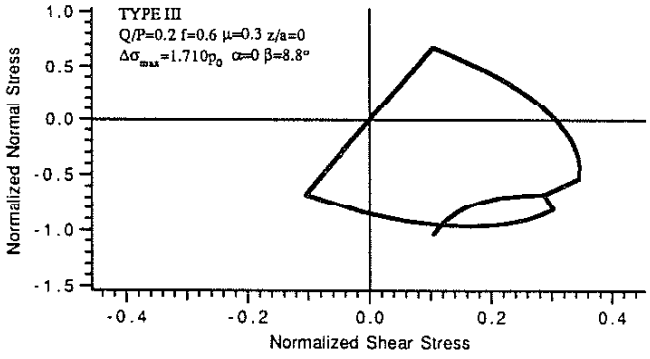

(e)TYPE III, Q/P=0.2, f=0.6

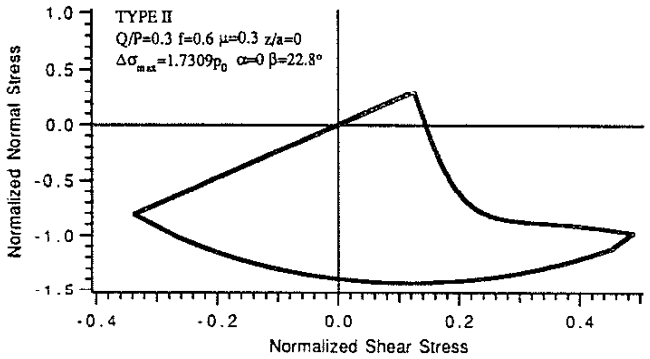

(c)TYPE II, Q/P=0.3, f=0.6

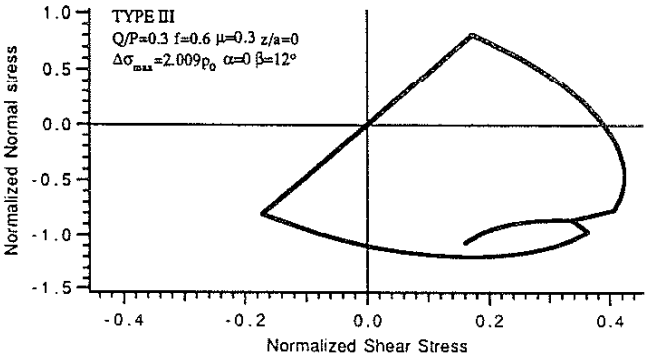

(f)TYPE III, Q/P=0.1, f=0.6

Fig.51 Stress Variations on the Plane of Maximum Normal Stress Range(f=0.6, μ=0.3, TYPE II and TYPE III)

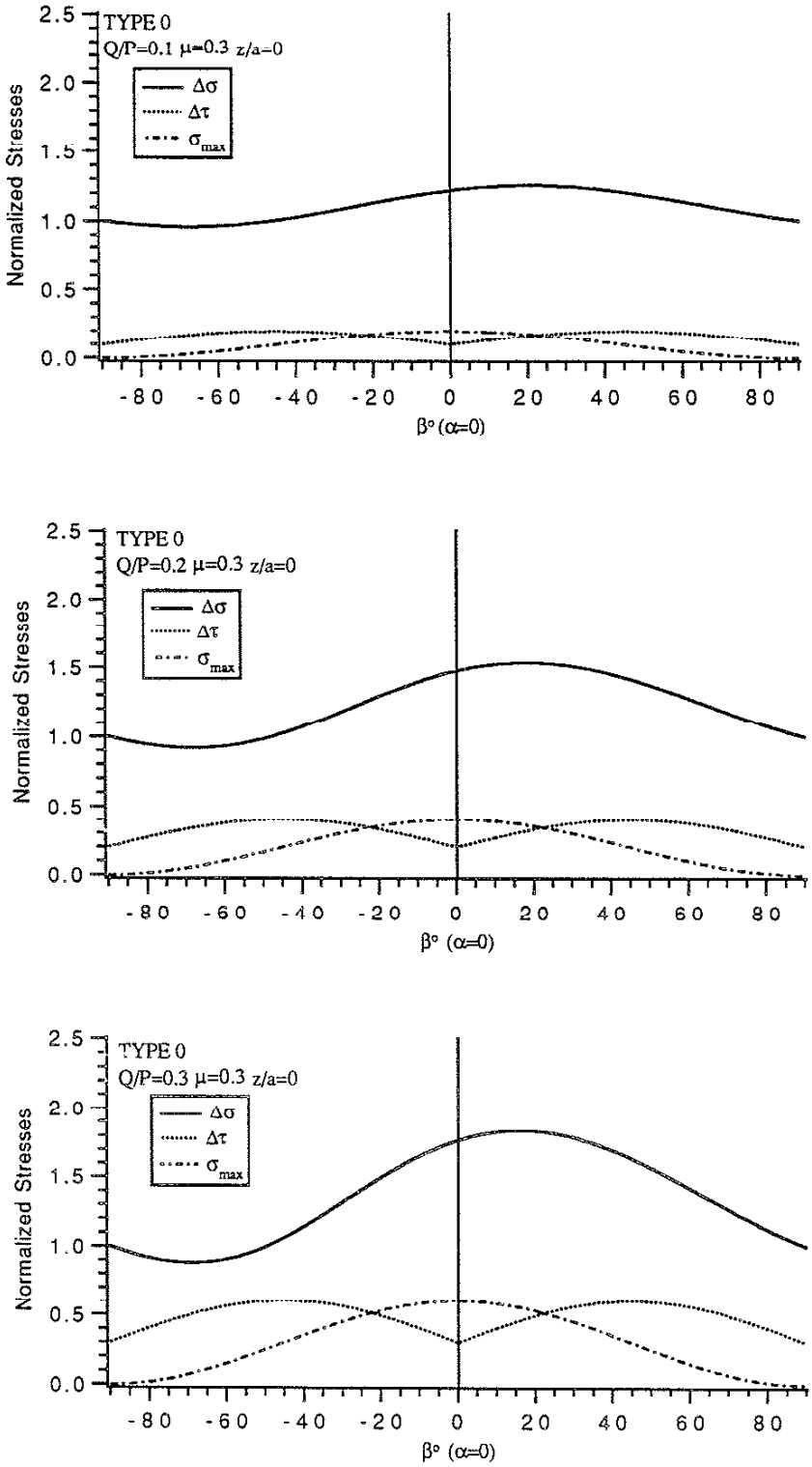

Fig.52 Variations of Shear Stress Range, Normal Stress Range, and Maximum Normal Stress on the Planes perpendicular to xoz Plane(α=0)(z=0, μ=0.3, TYPE 0)

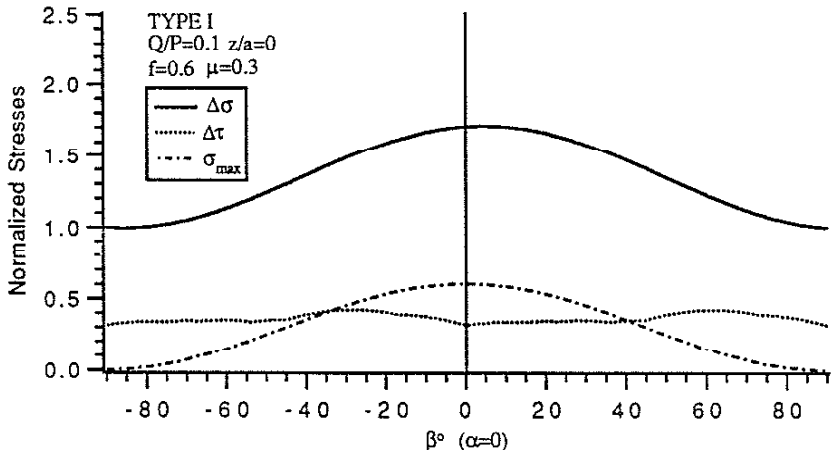

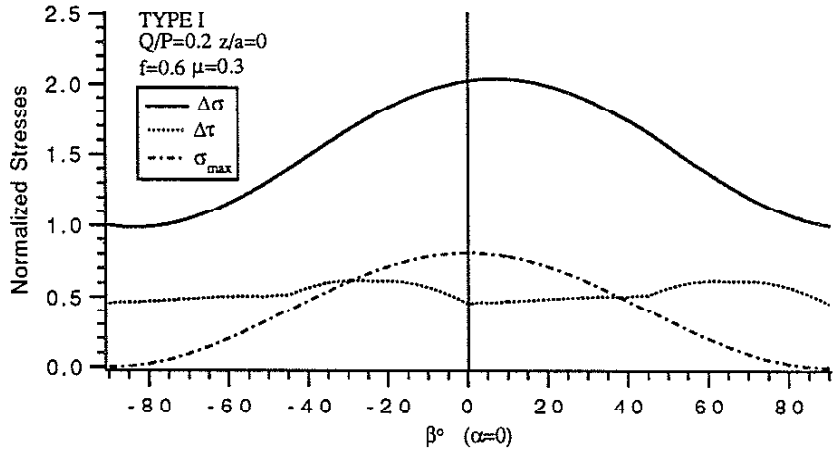

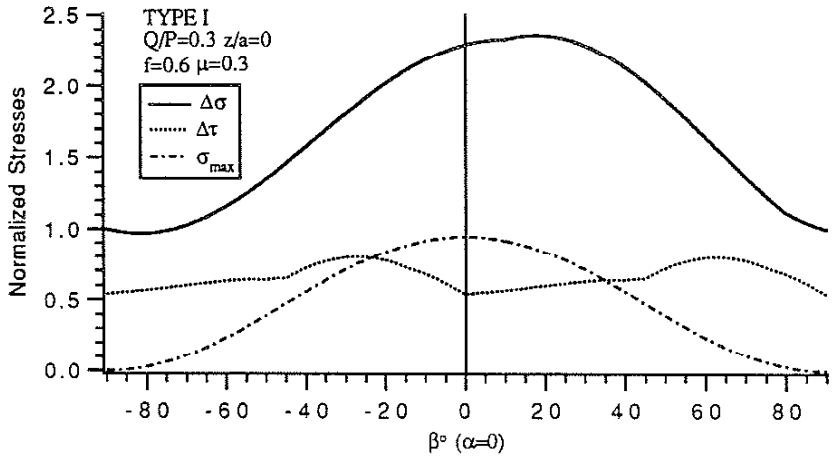

Fig.53 Variations of Shear Stress Range, Normal Stress Range, and Maximum Normal Stress on the Planes perpendicular to xoz Plane(α=0)(z=0, f=0.6,μ=0.3,TYPE I)

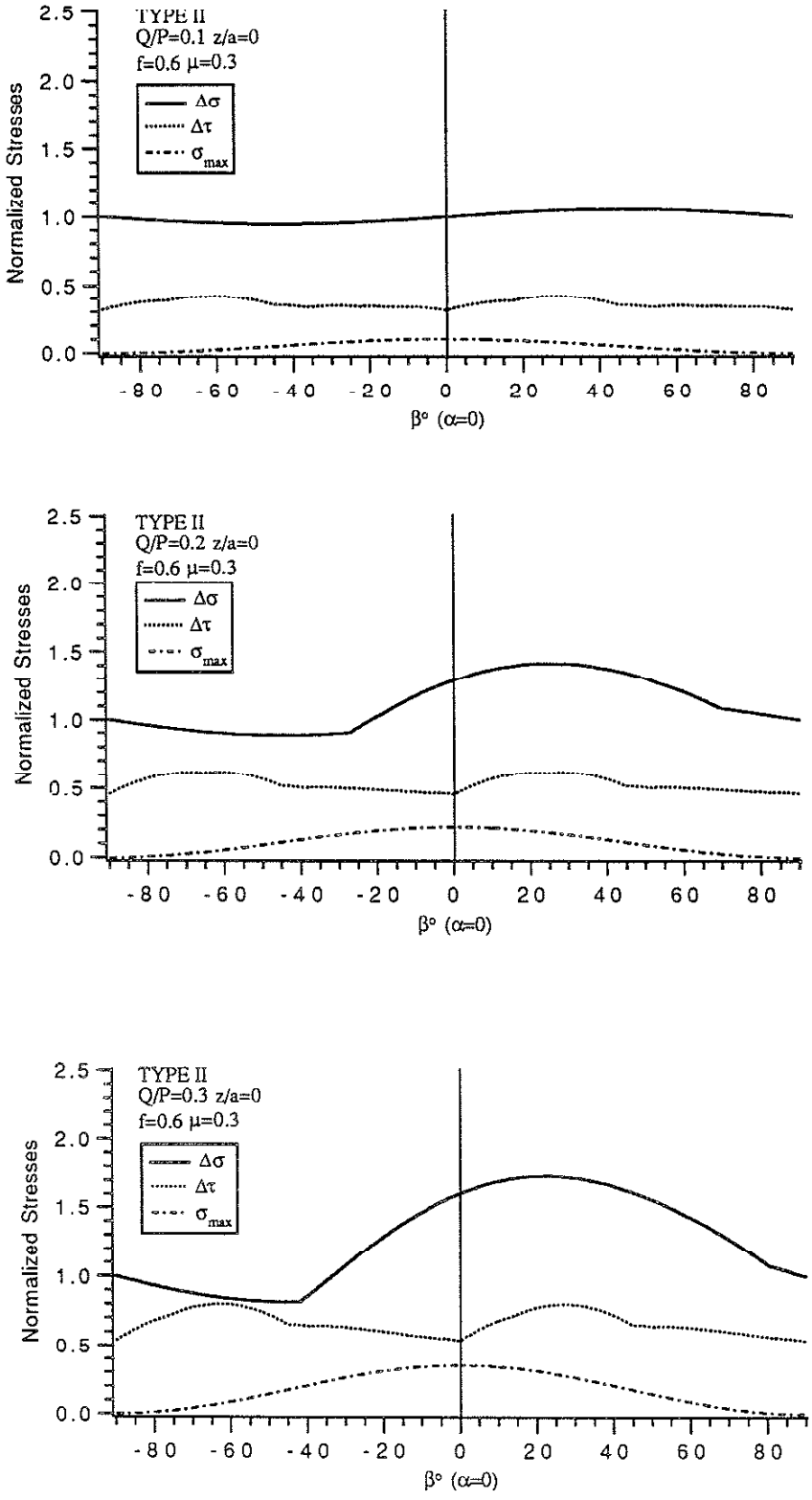

Fig.54 Variations of Shear Stress Range, Normal Stress Range, and Maximum Normal Stress on the Planes perpendicular to xoz Plane(α=0)(z=0, f=0.6,μ=0.3,TYPE II)

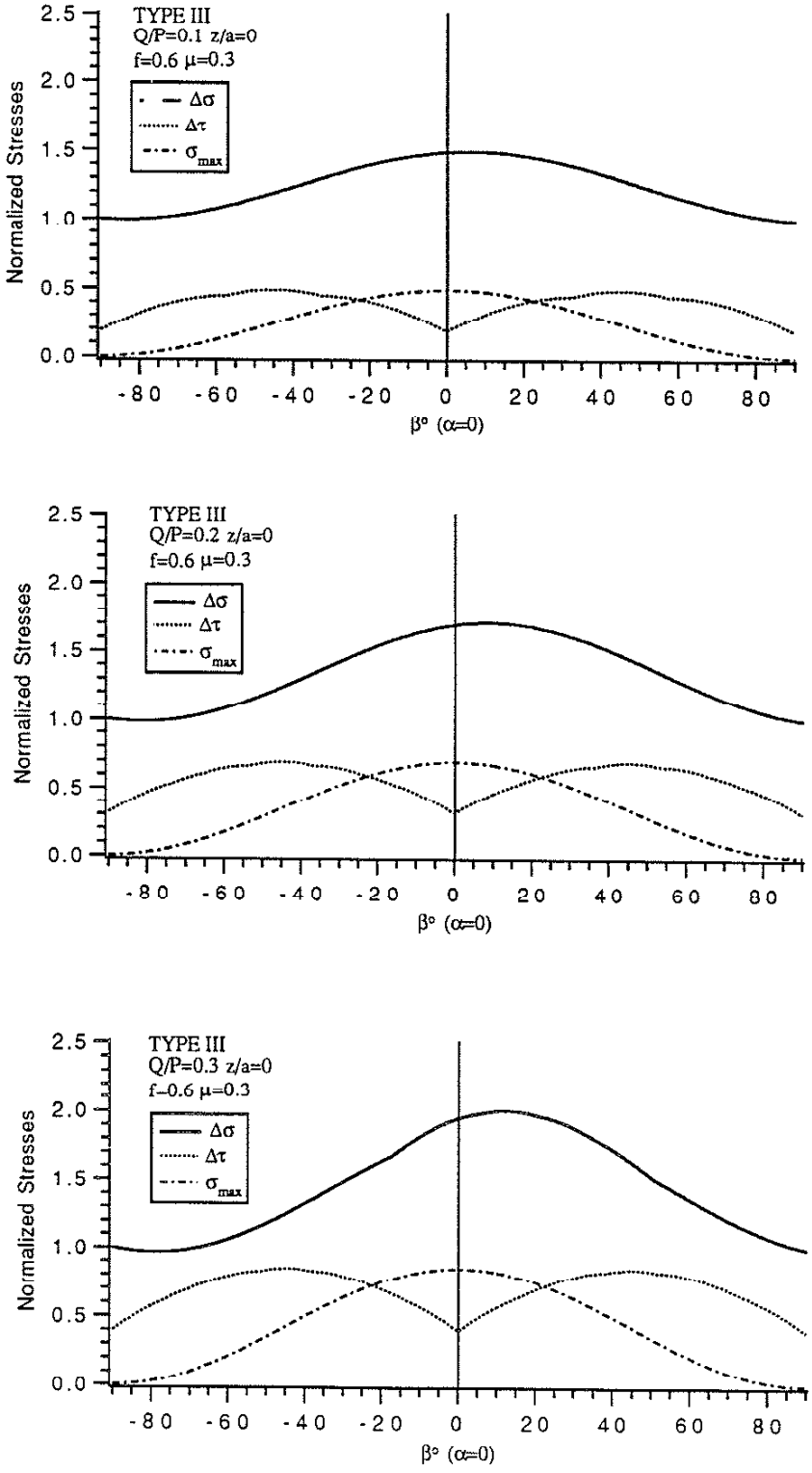

Fig.55 Variations of Shear Stress Range, Normal Stress Range, and Maximum Normal Stress on the Planes perpendicular to xoz Plane(α=0)(z=0, f=0.6,μ=0.3,TYPE II)

Multiaxial Fatigue of 1070 Steel under Proportional and Non-Proportional Loading

Y. Roger Jiang
and
Huseyin Sehitoglu

Report No.3 prepared for
Association of American Railroads

July 1991

Multiaxial Fatigue of 1070 Steel under Proportional and Non-Proportional Loading

Huseyin Sehitoglu, Associate Professor
Y. Roger Jiang, Research Assistant

Department of Mechanical and Industrial Engineering
University of Illinois at Urbana-Champaign
Urbana, IL 61801

Abstract

In view of the need to develop fatigue models for stress states encountered in contact loading situations, which were extensively documented in AAR Report #1 '90, and AAR Report #2 '91, proportional and non-proportional compression-shear loading experiments are conducted on 1070 Steel. The normal stress-strain behavior and shear stress-strain behavior are evaluated on the specimen coordinate planes and later resolved on material planes including the principal stress range planes and the planes of maximum shear strain range. Macroscopic crack growth directions coincided with the planes of maximum principal stress range for most cases. Several fatigue life prediction parameters are employed to correlate the experimental results; critical plane models which utilized the maximum shear strain, and principal stress amplitudes, and two bulk parameters which are the effective stress amplitude modified by the hydrostatic stress, and the plastic strain energy approach. Despite the occurrence of crack growth on maximum principal stress amplitude planes, the predictions based on shear strain range parameters exhibited better agreement with the experimental results compared to the principal stress amplitude. The predictions based on the effective stress amplitude underpredicted the fatigue damage particularly at long lives, while the predictions based on the plastic strain energy density parameter agreed well with the experiments. A new multiaxial fatigue parameter is forwarded which combines the shear and the principal stress-strain terms and whose maximum value, obtained by surveying all planes, dictates the multiaxial fatigue damage.

Nomenclature

α	Constant in effective stress parameter
$f(N_f)$	Function of N_f, fatigue life
G	Shear Modulus
J_1	First stress invariant= $\sigma_1+\sigma_2+\sigma_3 = \sigma_x+\sigma_y+\sigma_z$
$(J_1)_{stat}$	Mean value of the first stress invariant
J_2	Second deviatoric stress invariant
$(J_2)^{1/2}_{alt}$	Alternating value of the second deviatoric stress invariant in one cycle
$(J_2)^{1/2}_{max}$	Maximum value of the second deviatoric stress invariant in one cycle
K	Material constant in the shear based critical plane parameter
K'	Material constant in the proposed critical plane parameter
N_f	Fatigue life, cycles to failure
γ	shear strain amplitude on the plane $\theta°$
μ	Combined elastic-plastic Poisson's ratio
$\bar{\sigma}_{eq}$	Equivalent stress amplitude
$\bar{\varepsilon}_{eq}$	Equivalent strain amplitude
σ_{max}	Maximum stress on the plane $\theta°$
σ_{nmax}	Maximum normal stress on the plane $\theta°$
σ_{na}	Stress amplitude on the plane $\theta°$
σ_{nmean}	Mean stress on the plane $\theta°$
σ_y	Yield strength
$\bar{\varepsilon}^p_{eq}$	Equivalent plastic strain amplitude
ε_n	Normal strain amplitude on the plane $\theta°$
$\Delta\varepsilon$	Normal strain range on the plane $\theta°$
$\theta°$	Angle between the axial direction and the normal to an arbitrary plane
ΔW^p	Plastic strain energy density per cycle

Background

When the surfaces of two rolling solid bodies are forced into contact, the resultant stress state is highly complicated from both a deformation and a damage standpoint.

From the deformation standpoint, the stress state in the vicinity of the contact is triaxial, displaying compressive hydrostatic stresses whose magnitudes could reach several times the monotonic strength of the material. Moreover, the loading is non-proportional, i.e. the directions of the principal stresses rotate during a rolling cycle, exposing a large number of material planes to extreme stress ranges.

From the damage standpoint, the behavior of materials under high superimposed compressive mean stresses has been examined in only a few studies, since it is almost impossible to impose the aforementioned stress states on laboratory specimens. In non-proportional loading, the planes of maximum stress and the maximum strain are not synonymous; furthermore, the stress and strain maxima in a cycle do not coincide, unlike the uniaxial loading case for stable materials.

In this study, we attempt to bridge the gap between our understanding of 1070 material behavior under uniaxial loading, which is well characterized, and biaxial compression-shear loading, including non-proportional paths, which is not. The objectives of this research are: (i) to evaluate several of the promising multiaxial fatigue criteria for combined compression-torsion loading, (ii) to experimentally determine the orientation of the crack plane or the critical plane, and (iii) to forward new models, if necessary, to explain the multiaxial fatigue data trends.

Multiaxial Fatigue Models

There have been numerous multiaxial fatigue life prediction methods proposed over near a century of research, but no universally accepted multiaxial fatigue theory exists. Most previous multiaxial fatigue experiments have been conducted under proportional loading, and considerable emphasis has been placed on the tensile mean stress effect. Tensile stresses on the crack (critical) plane facilitate shear growth by providing a Mode I type opening hence decreasing the asperity contact of crack surfaces. Although some multiaxial theories are successful for one

material or another under a given set of loading conditions, the applicability of these theories to contact fatigue situations remains an unresolved problem.

In order to meet these objectives, thin-walled tubular specimens were tested under strain-controlled proportional and non-proportional axial-torsion loading, with the controlled axial strain and torsional strain in the compressive regime in order to produce as high of a compressive mean stress as possible. Uniaxial tests have been conducted to establish the base line data for comparison and to determine the material constants in the multiaxial fatigue criteria evaluated.

In certain class of materials, crack nucleation and growth is confined to well defined planes called the 'critical plane'. The critical plane approaches have been based on the early work of Gough '35, '37 and Guest '37, '40 on combined loading. The critical plane defined by Stulen-Cummins '54 and Findley '56, '59 is the plane where the linear combination of shear stress and normal stress reaches a maximum value. The shear stress based critical plane models have been used extensively by McDiarmid '81, and the shear strain based models have been adopted by Brown-Miller '73, and Socie and coworkers '84, '88. The latter researchers defined the critical plane as the plane of maximum shear strain range. On the other hand, models have been developed with shear stress range and normal stress range averaged over all the planes in the material. The models proposed by Crossland '56, '70 and Sines '55, '81, and other equivalent stress approaches (ASME Code) fall into this category and are designated as bulk damage models. Two overviews of multiaxial fatigue literature by Garud '81 and Krempl '74 describe some of these models.

Despite the variety in the forms, all the available multiaxial fatigue theories can be classified into two categories; the plane-orientation-dependent approaches and the plane-orientation-independent approaches. The plane-orientation-dependent approaches are those so called critical plane criteria, while the plane-orientation-independent approaches include equivalent stress/strain approaches with hydrostatic stress modification and the energy approaches. The plane-orientation-dependent criteria predict that the plane with maximum fatigue damage accumulation will be the plane of crack initiation or/and propagation. On the other hand, the plane-orientation-independent approaches assume that fatigue damage is uniformly distributed on all planes and a bulk, direction independent parameter characterizes the

fatigue damage. The latter approach considers fatigue damage to be a scalar at a material point while the premise of plane-orientation-dependent approaches is that fatigue damage at a material point is a tensor. Noting this difference, it is possible to critically determine which category of fatigue criteria is physically valid by testing specimens along selected loading paths, followed by microscopic examination of samples cut from the specimens.

Inconel 718 and 1045 steel, considered by Sehitoglu '88, Fash '85, Hua '84 and Fatemi et al. '88, obeyed maximum shear strain range governed crack initiation and crack growth. In pure shear experiments, long macroscopic cracks were observed along the specimen axis (θ=0°). The preferred crack orientation in 1045 steel was influenced by the longitudinal stringer type inclusions making the interpretation of the results somewhat difficult. In a low carbon steel (Berard '90), the shear strain range governed crack direction and growth in proportional tests; however, in non-proportional experiments the preferred crack orientation was not observed, and the crack orientations were more evenly distributed.

In this report, we examined five multiaxial fatigue criteria that fall into two categories. They are: (i) the two critical plane approaches utilizing shear based parameters, principal stress/strain parameters, and (ii) the bulk approach that includes the effective stress modified by hydrostatic stress, and the plastic strain energy approach. The three criteria under (i) are the plane-orientation-dependent approaches, and the last two, under (ii), fall into the plane-orientation-independent category. Finally, a new multiaxial fatigue criteria is proposed that has the positive attributes of shear and principal stress-stain based critical plane approaches.

The two critical plane approaches can be expressed mathematically [Socie, et al. '89, Fatemi, et al. '88]as;

$$\gamma+\varepsilon_n+\sigma_{nmean}/E=f(N_f) \tag{1}$$

and

$$\gamma(1+K\sigma_{nmax}/\sigma_y)=f(N_f) \tag{2}$$

where γ is the shear strain amplitude on the critical plane, ε_n is the normal strain amplitude to the critical plane, σ_{nmean} is the mean normal stress on the critical plane, σ_{nmax} is the maximum normal stress on the critical plane,

K is a material constant, E is elastic modulus, N_f is the fatigue life, and $f(N_f)$ is a function of fatigue life. The above two critical plane criteria were proposed for materials where cracks propagated on the planes with the maximum shear strain or stress ranges [Fatemi, et al. '88, Socie, et al. '88]. As discussed in AAR Reports #1 '90 and #2 '91, the determination of the critical plane position and orientation requires surveying all material planes and this could be computationally intensive when the stress state changes with position and time. Furthermore, the non-coincidence of maximum stresses and maximum plastic strains within a cycle should be noted for non-proportional loading. Therefore, one should also consider the plane where the parameters (Equation (1) L.H.S, Equation (2) L.H.S) are a maximum. Between the two equations, Equation (2) incorporates the constant K which is a weighting factor on the maximum stress. We note that Equation (1) does not include a constant. Equation (1) predicts the same life in a pure shear test and in a uniaxial test, and this is unrealistic in the long life regime as pointed out by Sines '55.

The Smith et al. '70 model (SWT) applied to multiaxial loading usually results in good fatigue life predictions for conditions conducive to tensile cracking [Socie '87]. This model is;

$$\Delta\varepsilon\sigma_{max}=f(N_f) \tag{3}$$

where $\Delta\varepsilon$ is the maximum principal strain range while σ_{max} is the maximum normal stress on the plane of maximum principal strain range.

The effective stress amplitude modified by the hydrostatic stresses is often referred to as Sines' model and is expressed [Sines '55] as,

$$(J_2)^{1/2}_{alt}+\alpha(J_1)_{stat}=f(N_f). \tag{4}$$

In Equation (4) $(J_2)^{1/2}_{alt}$ is the alternating value of the second stress deviator in a cycle which is defined as;

$$(J_2)^{1/2}_{alt}=0.5Max\{[(\Delta S_{xx}-\Delta S_{yy})^2+(\Delta S_{yy}-\Delta S_{zz})^2+(\Delta S_{zz}-\Delta S_{xx})^2+6(\Delta S^2_{xy}+\Delta S^2_{yz}+\Delta S^2_{zx})]/6\}^{1/2}$$

where Max { } denotes maximizing the quantity inside the brackets with respect to time, and where $\Delta S_{ij}=\sigma_{ij}(t_1)-\sigma_{ij}(t_2)$ are the stress differences with $\sigma_{ij}(t_1)$ being the stress component at time t_1, and $\sigma_{ij}(t_2)$ being the stress component at time t_2. $(J_1)_{stat}$ is the mean value of the first stress invariant and α is a material constant depending on life which describes the sensitivity of the material to hydrostatic stress.

The last criterion examined is the plastic strain energy density approach which can be generally expressed as;

$$\Delta W^P=f(N_f) \tag{5}$$

where ΔW^P, is the plastic strain energy density per cycle, is determined by integrating Equation (5) below,

$$\Delta W^P=\oint \sigma_{ij}\, d\varepsilon^P_{ij} \tag{6}$$

where σ_{ij} and $d\varepsilon^P_{ij}$ are stress and plastic strain rate tensors, respectively.

The plastic strain energy density per cycle, ΔW^P, is the product of stress and plastic strain rate integrated over the fatigue cycle [Garud '81, Golos-Ellyin '88, Ellyin '82]. Only the plastic strain energy portion has been used as a measure of fatigue damage, although this becomes difficult to compute in the long life regime where the strains are predominantly elastic. The criticism of the plastic work approach has been the lack of hydrostatic stress dependence, and the sensitivity of results on plastic strain rate predictive capability, ie. constitutive equations, under non-proportional loading.

SWT parameter and plastic strain energy have the same dimensions; both have the units of stress. For a material cracking on the principal stress planes under uniaxial reversed loading, SWT uses the resolved normal stresses and strains on the principal plane and represents the tensile total hysteresis energy. In proportional loading, there is an approximate linear relationship between plastic strain energy density and the SWT parameter. However, under non-proportional multiaxial loading, such a linear relationship between the SWT parameter and the plastic strain energy density cannot be expected. Besides, plastic strain energy density is a plane-

orientation-independent parameter, hence a scalar, while the SWT parameter is dependent on the plane orientation.

Previous fatigue criteria have usually been based on experiments conducted with low to moderate tensile mean stress, and the compressive stresses were ignored. The validity and applicability of the available criteria to contact fatigue situations require further examination. A series of uniaxial and mutiaxial fatigue experiments are conducted in an attempt to reveal material behaviors with compressive mean stresses.

Experiments and Test Results

Uniaxial Tests

Uniaxial tests were conducted on smooth specimens of 1070 steel to compute the material constants and to generate the data base for comparison with mutiaxial fatigue results. The specimens were machined from hot rolled bars that have been heat treated at 800° C for 4 hours followed by air-cooling. The diameter of the specimen was 7.62mm (0.3 in). Both strain- and stress-controlled tests were conducted. The strain ratios were $R_\varepsilon=\varepsilon_{min}/\varepsilon_{max}$ = -1, 2, and -∞, respectively. Stress ratios of -1 and -2 were employed in stress-controlled tests. Failure was defined as a 10% load drop in strain-controlled tests and a 50% increase in maximum strain in stress-controlled tests. The stress-strain response for the tests nearly stabilized at half life and the stress quantities used in life calculations corresponded to half-life.

The 1070 steel has a monotonic yield strength of 449 MPa, an ultimate strength of 825 MPa, and a reduction in area of 30%. Based on the uniaxial fatigue tests conducted, a material coefficient α=0.15 was selected for the $(J_2)^{1/2}_{alt}+\alpha(J_1)_{stat}$ model. The material constant K in the critical plane parameter Equation (2) was found to be 0.5.

Compression-Torsion Tests

Thin-walled tubular specimen (Figure 1(a)) was used in compression-torsion tests. The specimen had a 25.4mm (1.0 inch) internal diameter and a wall thickness of 2.54mm (0.1 in). Thin-walled tubular specimens were machined from hot rolled bars that have been heat treated under the same conditions as the uniaxial smooth bars. The specimen surface was polished to about 1 micron surface finish.

An MTS model 809 tension-torsion servohydraulic load frame (50 kip axial- 20 kip-in torsional load capacity) with an MTS model 463 processor/interface was used. A PDP 11/23 computer controlled the strains via an external axial- shear extensometer. The cyclic data including axial and torsional deformations and axial force and torque were recorded at logarithmic cycle intervals. A total of 200 data points was recorded per cycle.

The tubular specimens were subjected to compression and torsion under both proportional and non-proportional loadings. All the tests were strain-controlled. The proportional tests employed a shear strain/axial strain ratio of 1.732, where the axial strains were in the compressive regime. Non-proportional paths were butterfly shaped, with all the controlled strain parameters being negative, in order to obtain compressive mean normal stresses on the critical plane(s). The multiaxial paths considered are given in Figures 1(b) and 1(c). The path in Figure 1(b) is proportional and the path in Figure 1(c) is non-proportional. The stress-strain response for the tests in the first eight cycles and at half life will be reported here. Failure or fatigue life was defined as a 10% drop of the stable axial stress.

Before presenting the details of the experimental results, it is worth noting the difficulties encountered in obtaining data in the compressive stress regime. When combined axial-torsional paths under axial strain control are conducted, failure will not necessarily occur on the plane that experiences the compressive stresses, but rather on a plane that undergoes zero or tensile mean stress. This must be kept in mind when designing loading paths for fatigue testing. Another factor is the gradual (sometimes rapid) relaxation of mean stresses even when small plastic strains develop in the cycle. The butterfly path was chosen to delay the mean stress relaxation by reducing the plastic strain range.

Stress-Strain Behavior under Compression-Torsion Loading

The stress and strain states of an element on the surface of a tubular specimen are indicated in Figure 2(a). The x direction is the axial direction and the y direction is the circumferential direction of the tube and z is the thickness direction. The normal stresses in the y and z directions are zero, while the strains in the y and z directions are $-\mu\varepsilon_x$ where μ is the Poisson's ratio. The normal stress, the normal strain and the shear stress and shear

strain at an arbitrary plane measured θ° from the x axis is denoted in Figure 2(b).

The stress and strain responses for the first 8 cycles under proportional strain-controlled loading condition for specimen TUS03 are shown in Figures 3(a)-3(d). Note that Figure 3(c) is the controlled path 1-2-1-2..... We observe the gradual mean stress relaxation in Figure 3(a). Although the shear strain and axial strain were enforced to be proportional, we find that the shear stress and axial stress (Figure 3(d)) were not entirely proportional. For the same experiment, the plots in Figure 4 indicate the variations of stress and strain parameters with the plane orientation, θ°, at half life. The top figure denotes the normal and shear strains. The shear strain amplitude is a maximum at θ°= -19.5° and 70.5°. The middle figure denotes the shear stress amplitude, normal stress amplitude, and the mean stress. We note that the planes -35° < θ < 80° undergo compressive mean stresses. It is noted that under this proportional loading, there are two planes that have the same maximum shear strain range and also two planes that have the same maximum shear stress range. But, there is only one plane that is subjected to maximum normal stress range. The three parameters $\gamma+\varepsilon_n+\sigma_{nmean}/E$, $\gamma(1+K\sigma_{nmax}/\sigma_y)$, and $\Delta\varepsilon\sigma_{max}/\sigma_y$ are plotted against plane orientation on the bottom figure. In order to plot the three parameters in the same coordinates, the SWT parameter was normalized by σ_y, the yield strength. We note that each of the maximum values of the three parameters occurs on planes, which differ from maximum shear strain range plane or maximum shear stress range plane. For example, the $\gamma+\varepsilon_n+\sigma_{nmean}/E$, $\gamma(1+K\sigma_{nmax}/\sigma_y)$ reach their peaks at 59° and -17° respectively while the planes of maximum shear strain range were 70.5°and -19.5°. We note that these planes differ considerably from the observed crack plane of 32°.

To gain further understanding of the material behavior, the variation between normal stress and shear stress on the planes of maximum shear strain range (θ= -19.5° and 70.5°) is indicated in Figure 5 for the specimen TUS03 at half life. Among these two planes that have the same shear strain range, the shear stress ranges are also similar. Note that the normal stress range is larger on -19.5° plane than that on the 70.5° plane. In Figure 6, the relation is shown between normal stress and shear stress on the observed crack plane, θ= 32°. We find that for specimen TUS03 under proportional strain-controlled condition the crack plane, θ= 32°, does not coincide with the

planes of maximum shear strain range, θ= -19.5° and 70.5°. The shear stress range and shear strain range are much smaller on the observed crack plane than those on the planes of maximum shear strain range and maximum shear stress range; however, the normal stress range is much higher on the observed crack plane. The crack plane, θ=32°, is near the plane of maximum normal stress range, θ=23°, in Figure 4(b). We note that the mean compressive stress on the crack plane is approximately one-fourth the normal stress amplitude.

Figures 7 through 10 show the results for Specimen TUS11 that was tested under non-proportional strain-controlled loading condition. The controlled strain path is shown in Figure 7(c). In the first reversal, the specimen is strained to point 1, followed by point 2, point 3, point 4, then point 1 and so on. The other plots in Figure 7 show the stress-strain responses corresponding to this loading path for the first 8 cycles. We note that there are two shear cycles in a single normal cycle. This phenomenon is also reflected in the plots in Figure 8 where the stress and strain parameters are plotted against material plane orientation. Upon comparing with Figure 4 for proportional loading, the variations of shear stress range and shear strain range with the plane orientation are much flatter under this non-proportional loading. Theoretically, if the controlled strain path has strictly followed the desired path, there will be four planes which have the same maximum shear strain range. Due to mechanical hysteresis in the system, it is almost impossible to follow the designed strain path exactly. We can observe from the top two plots in Figure 8 that there are four θ values where the shear strain range and shear stress range are high, but only at two θ values the maximum levels are reached. The orientations for the planes of maximum shear strain range were -22° and 68°. The orientations for the planes of maximum shear stress range were -68° and 22°. These results clearly demonstrate that under this non-proportional loading the orientation of the planes of maximum shear strain range differ from the planes of maximum shear stress range.

Figures 9 and 10 show the normal stress and shear stress on the planes of maximum shear strain range and the observed crack plane, respectively. We note in Figure 9 that the material plane θ = -21° undergoes the same shear stress range as the θ = 69° plane, however the normal stress range on the θ = -21° plane is almost a factor of three higher than on the θ = 69° plane. The

experimentally observed crack plane is $\theta = -10°$ in this case. Once again, the crack plane does not coincide with the planes of maximum shear strain range.

Crack Growth Directions

The observed crack growth directions and the orientations of some planes of interest are shown in Figure 11 for selected specimens. Table I summarizes the orientations of observed crack planes for each tested specimen and the orientations of other planes of interest. We find in Figure 11(a) that the planes of maximum shear strain range are inclined 45° to the plane of maximum normal stress range for the case of proportional loading. This does not hold for the cases under non-proportional loading shown in Figures 11(b)-11(d) where the planes of $\Delta\sigma_{nmax}$ and $\Delta\gamma_{max}$ are inclined less than 45° to each other. Another observation is concerned with the planes of maximum shear strain range and planes of maximum shear stress range being identical in Figures 11(a) and 11(b), while in Figures 11(c) and 11(d), those two shear planes are far from each other. We note in Figure 11(c) that for specimen TUS09, under non-proportional loading, the plane of maximum normal stress range is near one of the planes of maximum shear stress range. Also, in Figure 11(d), for Specimen TUS11, the plane of maximum normal stress range is almost identical to one of the planes of maximum shear strain range.

Of those planes of maximum shear strain range, maximum shear stress range, and maximum normal stress range, the observed crack planes nearly coincided with the plane of maximum normal stress range.

Fatigue Life Results and Correlations

Fatigue life correlation and prediction have been made for the proportional and non-proportional 1070 steel tests based on different criteria. Figure 12(a) shows the predictions based on the parameter $\gamma_+\varepsilon_n+\sigma_{nmean}/E$. The solid line is the uniaxial data and the symbol "⋈" denotes the non-proportional tests while " o" denotes the proportional tests. The observed life is plotted versus the predicted life in Figure 12(b). The predictions based on the uniaxial tests are somewhat conservative; however, most of the test results lie within the factor of two bounds.

Figure 13 shows the fatigue life correlation and prediction based on the parameter $\gamma(1+K\sigma_{nmax}/\sigma_y)$. From the two plots in Figure 13, it is found that the critical parameter $\gamma(1+K\sigma_{nmax}/\sigma_y)$ correlates the test data very well and is slightly non-conservative for the non-proportional loading cases.

Figure 14 shows the correlation and prediction based on SWT parameter $\Delta\varepsilon\sigma_{max}$. It is interesting to note that most crack planes of the 11 tested specimens are nearly consistent with the planes of maximum principal stress range, nevertheless, the parameter resulted in highly non-conservative predictions for this material.

Figure 15 shows the fatigue life correlation and prediction based on the parameter $(J_2)^{1/2}_{alt}+\alpha(J_1)_{stat}$. This criterion also results in highly non-conservative life predictions at long lives.

The results were predicted based on the plastic energy density per cycle, ΔW^P and are given in Figure 16. The energy approach predicted the data within a factor of two for most cases.

Multiaxial Cyclic Stress-Strain Behavior for 1070 Steel

The equivalent stress amplitude versus equivalent plastic strain amplitude at the first half cycle and at the half fatigue lives are given in Figures 17 and 18, respectively. The equivalent stress amplitude is defined as

$$\bar{\sigma}_{eq}=\sqrt{3}\,(J_2)^{1/2}_{alt} \tag{7}$$

where $(J_2)^{1/2}_{alt}$ is the alternating value of the second stress deviator in a cycle defined in Equation (4). The equivalent plastic strain amplitude is obtained using the equivalent plastic strain increment and is defined analogous to $(J_2)^{1/2}_{alt}$ as

$$\bar{\varepsilon}^P_{eq}=\frac{1}{\sqrt{6}}\mathrm{Max}\{[\varepsilon^P_x(t_1)-\varepsilon^P_x(t_2)]^2+[\varepsilon^P_y(t_1)-\varepsilon^P_y(t_2)]^2+[\varepsilon^P_z(t_1)-\varepsilon^P_z(t_2)]^2+$$
$$2[\gamma^P_{xy}(t_1)-\gamma^P_{xy}(t_2)]^2+2[\gamma^P_{xy}(t_1)-\gamma^P_{xy}(t_2)]^2+2[\gamma^P_{xy}(t_1)-\gamma^P_{xy}(t_2)]^2\}^{1/2} \tag{8}$$

where Max { } denotes maximizing the quantity inside the brackets with respect to time. The plastic strain components are defined as follows,

$$d\varepsilon^{p}_{ij} = d\varepsilon_{ij} - \frac{1}{2G}\{ d\sigma_{ij} - \frac{\mu}{(1+\mu)}\delta ij\, d\sigma_{kk} \} \qquad (9)$$

where ε_x, ε_y, ε_z, $\gamma_{xy}= 2\varepsilon_{xy}$, $\gamma_{yz}= 2\varepsilon_{yz}$, and $\gamma_{zx}= 2\varepsilon_{zx}$ are the total strain components, σ_x, σ_y, σ_z, τ_{xy}, τ_{yz}, and τ_{zx} are the stress components, E is the elastic modulus, and G is the shear modulus .

We note in Figure 17 that for the first reversal in uniaxial case there is a distinct yield point, while for the multiaxial case gradual plastic deformation is detected at very low stress levels. The $\bar{\sigma}_{eq}$ versus $\bar{\varepsilon}^{p}_{eq}$ curves at the half lives (Figure 18) indicate hardening compared to the first reversal particularly when plastic strains exceeded 0.002.

The stress-strain behavior for the uniaxial experiments is shown in Figures 19(a) through 19(c). The first 100 cycles are shown in Figure 19(a) and cycles 1000-47000 are indicated in Figure 19(b). The experimental loops for fatigue tests under the same stress range, 687 MPa, with compressive mean stress are shown in Figure 19(c). We note that the plastic strain range in the cycle is lower in R=-2 case compared to R=-1 cycling. Gradual ratcheting of strain in the compressive direction is noted. The specimen did not fail after 5,000,000 cycles in this case.

The $(\Delta\varepsilon\sigma_{max}+K'\Delta\gamma\Delta\tau)_{max}$ Parameter

Material planes that undergo maximum strain amplitude also undergo considerable shear strain amplitude and shear stresses (Figure 8). The previous parameters proposed do not account for the shear stress and shear strain effect on the principal strain planes. A model is proposed that accounts for the presence of the shear and normal stress -strain values on any arbitrary plane. The results could be correlated with the $(\Delta\varepsilon\sigma_{max}+K'\Delta\gamma\Delta\tau)_{max}$ parameter (K'=0.3). Multiaxial damage is calculated on the plane where this parameter is a maximum. Typical results for the specimens TUS03 and TUS11 are presented in Figure 20(a) and 20(b). We note that the parameter predicts the crack plane location accurately for TUS03 case while the previously proposed parameters, incorporating shear terms, did not predict the crack plane closely (Figure 4). The crack plane (θ=10°) is not predicted exactly for the TUS11 specimen, but lies between the two peaks observed in Figure 20(b).

The life predictions with this parameter are shown in Figure 21. The predictions are within a factor of two of the experimental results for most cases.

Discussion of Results

Critical Plane

The basis of the critical plane approaches is that the fatigue damage accumulation on the "critical" plane is highest among all possible planes. The results on Table I indicate that critical plane (crack plane) is not necessarily the plane of maximum shear strain range or the plane of maximum shear stress range. It occured on a plane near the maximum principal (normal) stress range. For this material, we could postulate that the critical plane appears to be strongly influenced by the principal stresses, with shear stresses and mean normal stresses having a modifying effect. The proposed multiaxial parameter has the correct form to capture the synergism between the shear and principal stress components and the potential to predict the orientation of the critical plane.

The results show that the principal stress directions are not coincident with the principal strain directions. Also, the plane at which the maximum shear stress range occurs is not the same plane as that of the maximum shear strain range. This is characteristic of non-proportional loading as noted in Table I. Considering Table I and Figure 8, we can find that in most cases the planes of maximum shear strain range are only several degrees from the planes of maximum shear stress range; while in other cases the orientations of the two planes could be 30° apart. Having recognized this subtle distinction, one should specify the critical plane as being principal stress or strain based or shear stress or strain based or a plane where the combination of these parameters is a maximum.

Comparison of Multiaxial Fatigue Criteria

The two shear based critical plane criteria, Equations (1) and (2), performed equally well in correlating and predicting the test data of 1070 steel under proportional and non-proportional loadings with compressive mean stresses on the crack planes. The problem was that the crack directions were not consistent with the planes of maximum shear strain range, as explicitly

assumed in these criteria. As we have noted, the observed crack directions nearly coincided with the planes of maximum normal stress ranges for most cases. SWT parameter has been shown to be able to correlate such tensile cracks (Socie' 88) well; but, as shown in Figure 14, this parameter did not correlate the experimental data satisfactory. Sines' model underpredicted the lifetimes in the long life regime. The stress based models, when correlating the strain controlled experiments, are very sensitive to the constitutive response of the material, particularly under mutiaxial loading conditions. For example, in Figure 18, the stress amplitude in multiaxial loading is lower than the uniaxial case at small plastic strains. Therefore, predictions based on stress quantities (SWT parameter and the Sines type models) yielded longer lives for the multiaxial case compared to the uniaxial case.

We note that an equation with an experimentally determined constant does not necessarily guarantee better predictions. The first critical plane criterion, Equation (1), includes no 'material' constants while the second critical plane criterion, Equation (2), includes one constant. Sines' model has one "material" constant α, while the SWT parameter and energy parameter involve no such constants. The proposed parameter has one constant, K'=0.3.

Critical Evaluation of Multiaxial Fatigue Criteria

Selected experimental results cannot guarantee which multiaxial fatigue criterion is physically valid or invalid. The difficulties lie mainly in the following three factors related to the multiaxial fatigue experiments: (1) fatigue data scatter, say a factor of two, (2) limited stress/strain state and loading paths, and (3) the interrelationship between the parameters.

The combination of the above three factors makes the evaluation somewhat ambiguous. Little can be done in eliminating the fatigue data scatter, nor is it wise to try every possible stress/strain state and loading path. Emphasis should be placed on finding special but simple loading paths for which different criteria will predict detectably different fatigue lives. The proposed experiments using external pressure will provide considerable insight into the capabilities of these models under high compressive stresses.

Item (3) requires further explanation. We note that although the underlying basis of the models presented differ, there is implicit coupling between the models through the stress and strain quantities used. For example, under uniaxial loading the ratio of shear strain amplitude to the

principal strain amplitude is constant. For axial-torsion loading paths that are proportional in the $\gamma-\varepsilon$ space the ratio $1+\mu < \gamma_{max}/\varepsilon_{max} < 2$ holds. This relation implies that the data trends could be correlated using shear strain or normal strain without introducing any significant errors. Similarly, a comparison of $\gamma+\varepsilon_n$ and $\bar{\varepsilon}_{eq}$ parameters for axial-torsional loading yields, $1.732 < \gamma+\varepsilon_n/\bar{\varepsilon}_{eq} < 1.9$. Therefore, the laboratory tests are severely limited in their ability to discriminate between the different models. Non-proportional tests, similar to the paths examined here, are more discriminatory, yet they also suffer from the coupling between the parameters. Many of the parameters have been developed based on tubular specimen testing where plane stress conditions prevail, i.e. $\sigma_3=0$. As documented earlier (AAR Report #1 '90 and #2 '91), the stress state in contact has a high hydrostatic stress component and the determination of the critical planes require surveying three dimensional coordinate space.

The question of whether the fatigue damage, under the multiaxial loadings, can be expressed as a tensorial quantity at a material point or as a scalar quantity has implications in predicting a locomotive wheel life. Let us say that the fatigue life of a locomotive wheel set is N_f when running in one direction only, and that after the locomotive has run $0.95N_f$ in one direction, we change the running direction of the locomotive or change the right wheel with the left wheel. From the critical plane point of view, the locomotive wheel set will run nearly another N_f, because the critical plane is no longer the same as that before the wheel change. If the damage accumulation were uniform on all neighboring planes, then a scalar description of damage would be applicable. In this case, if the locomotive direction is reversed the remaining life will be near (not exactly) $0.05N_f$.

Future Work

Development of a fatigue criteria should be considered concurrently with the contact stress analysis, since fatigue criterion to be used in the contact fatigue analysis will determine which aspects of the stress analysis should be emphasized and vice versa. For example, once the criteria for the critical plane is established for this material, the stress/strain at every plane should be traced in order to find the critical plane orientation and the depth of greatest fatigue damage. The numerical stress analysis should make use of

a suitable yielding criterion and a flow rule consistent with the biaxial stress-strain behavior observed experimentally.

The determination of residual stresses in contact loading should be part of a contact fatigue model and we are currently making progress in this area. Previous attempts by Merwin and Johnson '62, Hearle and Johnson '87, Bower and Johnson '89, and McDowell and Moyar '90 have concentrated on ratcheting under repeated rolling and sliding conditions. From a contact fatigue analysis view point, accurate determination of stress-strain components, including residual stresses in x-y directions, is needed. Our initial calculations (Roger Jiang) show that the choice of the constitutive model (multiple surface versus single flow surfaces) and the elastic constraint assumptions have a paramount influence on the residual stresses. The results of stresses, including residual stresses, for various normal to traction ratios will be available in Report #4. Since plastic deformation is confined to an infinitesimally small region in the vicinity of the contact, which grows with increasing p_o/k ratio, the use of finite elements (Bhargava, Hahn, et al. '83 '90) is rather crude in capturing the details of the stress-strain gradients and the residual stress.

To gain an understanding of 1070 material in the compressive regime specimens will be subjected to high external pressure loading conditions. Through suitable, simultaneous control of the fluid pressure and the axial load/strain, we will conduct tests that impose on the specimens cyclic stresses with large compressive hydrostatic stress components. Previous attempts at axial fatigue testing with controlled tensile or compressive mean stresses were not successful due to a) rapid mean stress relaxation in strain controlled testing, or b) ratcheting in stress controlled testing. In previous work, necking and barrelling of specimens have occured, often with no evidence of fatigue failure, under stress controlled testing with a high mean stress. Using pressurized tubular specimens, Morrow '88 was able to obtain fatigue failures at tensile mean stress levels without experiencing the above mentioned problems, however his tests created a biaxial tensile mean stress, rather than a triaxial states of stress. External pressurization of a solid test specimen will allow a true triaxial stress state to be developed, and ensure that the specimens will fail in fatigue. The results of our future research will provide new data with which to assess the validity of the various multiaxial fatigue life prediction models.

We are also performing finite element calculations to simulate the rail chill effect on the wheel and comparing our results with the calculations made by Moyar and Stone, '90. We developed a technique for imposing remote displacement boundary conditions in the FEM model so that a small portion of the body in contact may be analyzed, allowing sufficient mesh refinements at the regions of interest. The results are forthcoming in Progress Report #5.

Summary

1. The planes of maximum shear strain range and the planes of maximum shear stress range are not coincident. The difference in orientation of these planes is most evident in non-proportional loading.
2. In non-proportional loading, the planes of maximum shear stress range and the planes of maximum normal stress range are not inclined 45° to each other.
3. Experimental crack growth directions nearly coincided with the plane of maximum principal stress range for most cases. The SWT parameter, which was designed to predict crack growth on principal (tensile) stress planes, resulted in highly non-conservative life predictions.
4. Although the crack plane did not occur on the plane where maximum shear strain range is a maximum, the two shear based critical plane parameters correlated the experimental data well.
5. Effective stress amplitude modified by the hydrostatic stresses resulted in highly non-conservative life predictions at long lives.
6. The fatigue life predictions based on the plastic strain energy density parameter agreed with the experimental results.
7. The lack of success of $\bar{\sigma}_{eq}$ and σ_{max} based multiaxial fatigue parameters is due to the lower stress levels (early yielding) for the same strain in multiaxial loading case compared to the uniaxial loading.
8. The proposed parameter has the advantage of incorporating the modifying influence of shear stress-strain effect on the principal plane and vice versa. The predictions based on this parameter were very satisfactory.

Acknowledgements

Discussions with Dr. Dan Stone and Mr. Michael C. Fec of AAR and Dr. Gerald Moyar, consultant of Moyar Technical Services, are acknowledged. Dr. Peter Kurath, Research Engineer, MERL, University of Illinois, is thanked for his time and assistance throughout the testing program. Mr. Mark Balzer helped with the preparation of this manuscript.

References

Berard, J.A., " A Micro-mechanical approach to Biaxial Low Cycle Fatigue", PhD Thesis, Georgia Institute of Technology, 1990.

Bhagava, V., Hahn, G. T., and Rubin, C. A., "An Elastic-Plastic Finite Element Model of Rolling Contact. Part I: Single Contacts, Part II: Repeated Contacts," *J. Applied Mechanics, Trans. ASME*, Vol. 52, 1983, pp. 66-74, pp.75-82.

Bhagava, V., Hahn, G. T., Ham, G., Kulkarni, S., and Rubin, C. A., "Influence of Kinematic Hardening on Rolling Contact Deformation," 3rd Inter. Symp. on Contact Mechanics and Wear of Rail/Wheel Systems, Cambridge, U.K., June 1990.

Bower, A. F., and Johnson, K. L., "The Influence of Strain Hardening on Cumulative Plastic Deformation in Rolling and Sliding Line Contact," *J. Mech. Phys. Solids*, Vol. 37, No. 4, 1989, pp. 471-493.

Bower, A. F., and Johnson, K. L., "Plastic Flow and Shakedown of the Rail Surface in Repeated Wheel-Rail Contact," 3rd Inter. Symp. on Contact Mechanics and Wear of Rail/Wheel Systems, Cambridge, U.K., June 1990.

Brown, M. W., and Miller, K. J., "A Theory for Fatigue Failure under Multiaxial Stress-Strain Conditions," *Proc. Instn. Mech. Engrs*, Vol. 187, 1973, pp. 745-755.

Crossland, B.,"Effect of Large Hydrostatic Pressures on the Torsional Fatigue Strength of an Alloy Steel," *Proc. Inter. Conf. on Fatigue*, London, 1956, pp. 138-149.

Crossland, B.,"The Effect of Pressure on Fatigue of Metals," Chapter 7 in *The Mechanical Behavior of Materials under Pressure*, H.L.P.D. Pugh, Ed., Elsevier Publishing Company, Limited, 1970

Fash, J., " An Evaluation of Damage Development During Multiaxial Fatigue of Smooth and Notched Specimens", PhD Thesis, University of Illinois, 1985.

Fatemi, A., and Socie, D. F., "A Critical Plane Approach to Multiaxial Fatigue Damage Including Out-of-Phase Loading," *Fatigue and Fracture of Materials and Structures*, Vol. 11, No. 3, 1988, pp. 149-165.

Findley, W. N., Coleman, J. J., and Hanley, B. C., "Theory for Combined Bending and Torsion Fatigue with Data for SAE 4340 Steel," *Proc. of the Inter. Conf. on Fatigue of Metals, Instn Mech Engr*, London, 1956, pp. 150-157.

Findley, W. N., "A Theory for the Effect of Mean Stress on Fatigue of Metals under Combined Torsion and Axial Load or Bending," *Journal of Engineering for Industry, Trans. ASME*, Nov. 1959, pp. 302-305.

Garud, Y. S., "Multiaxial Fatigue: A Survey of the State of the Art," *Journal of Testing and Evaluation, JTEVA*, Vol. 9, No. 3, May 1981, pp. 165-178.

Golos, K., and Ellyin, F., "A Total Strain Energy Density Theory for Cumulative Fatigue Damage," *Journal of Engineering Materials and Technology, Trans. ASME*, Vol. 110, Feb. 1988, pp. 36-41.

Gough, H. J., and Pollard, H. V., "The Strength of Metals under Combined Alternating Stress," *Proceedings of the Institution of Mechanical Engineers*, Vol. 131, No. 3, Nov. 1935, pp. 3-54.

Gough, H. J., and Pollard, H. V., "Properties of Some Materials for Cast Crankshafts, with Special Reference to Combined Stresses," *Proceedings, Institution of Automobile Engineers*, Vol. 31, March 1937, pp. 821-893.

Gough, H. J., "Engineering Steels under Combined Cyclic and Static Stresses," *Journal of Applied Mechanics*, Series E, Trans ASME, Vol. 72, June 1950, pp. 113-125.

Guest, J., "Combined Stress, A Criticism of the Gough and Pollard Law," *The Automobile Engineer*, Sept. 1937, pp. 326-332.

Guest, J., "Recent Research on Combined Stress", *Proc. Instn. of Automobile Engineer*, Vol. 35, Dec. 1940, pp. 33-72.

Hearle, A. D., and Johnson, K. L., "Cumulative Plastic Flow in Rolling and Sliding Line Contact," *J. Applied Mechanics*, Vol. 54, March 1987, pp. 1-7.

Hua, C.T. "Fatigue Damage and Small Crack Growth During Biaxial Loading", PhD Thesis, University of Illinois, 1984

Lefebre, D., and Ellyin, F., "Cyclic Response and Inelastic Strain Energy in Low Cycle Fatigue," *Int. J. of Fatigue*, Vol. 6, No. 9, 1984, pp. 9-15.

Krempl, E., "The Influence of State of Stress on Low-Cycle Fatigue of Structural Materials: A Literature Survey and Interpretive Report," STP 549, American Society for Testing and Materials, Philadephia, 1974.

McDiarmid, D. L.,"Fatigue Behavior Under Out-of-Phase Bending and Torsion," *Aeronautical Journal*, March 1981, pp. 118-122.

Merwin, J. E., and Johnson, K. L., "An Analysis of Plastic Deformation in Rolling Contact," *Proc. Inst. Mech. Engrs.*, Vol. 177, No. 25, 1963, pp. 676-685.

McDowell, D. L., and Moyar, G. J., "Parametric Study of Cyclic Plastic Deformation in Rolling and Sliding Line Contact with Realistic Nonlinear Material Behavior," *3rd Inter. Symp. on Contact Mechanics and Wear of Rail/Wheel Systems*, Cambridge, U.K., June 1990.

Moyar, G.J., and Stone D.H., " An Analysis of the Thermal Contributions to Railway Wheel Shelling", 3rd. International Symposium on Contact Mechanics and Wear of Rail/Wheel Systems, Cambridge, 1990

Morrow, D., " Biaxial Tension of Inconel 718", PhD Thesis, University of Illinois, 1988.

Sehitoglu, H., D.F.Socie, D. Worthem, " Crack Growth Studies in Biaxial Fatigue", ASTM STP 924, 1988, pp. 120-135

Sehitoglu, H., Jiang Y., AAR Report #1, Contact Fatigue Life Prediction Methods, 1990

Sehitoglu, H., Jiang Y., AAR Report #2, "Cyclic Stresses for Contact with Different Tangential Load Distributions", 1991

Sines, G., "Failure of Materials under Combined Repeated Stresses with Superimposed Static Stresses," Technical Note 3495, National Advisory Council for Aeronautics, Washington, D.C., 1955.

Sines, G., and Ohgi, G., "Fatigue Criteria Under Combined Stresses or Strains," *Journal of Engineering Materials and Technology, Trans. ASME*, April 1981, Vol. 103, pp. 82-90.

Smith, R. N., Watson, P., and Topper, T. H., "A Stress Strain Function for the Fatigue of Metals," *Journal of Materials, JMLSA*, Vol. 5, No. 4, 1970, pp. 767-778.

Socie, D. F., Kurath, P., and Koch, J., "A Multiaxial Fatigue Damage Parameter," *Biaxial and Multiaxial Fatigue, ECF3*, Brown, M. W. and Miller, K.J., Eds., Mechanical Engineering Publications, London, 1989, pp. 535-550.

Socie, D. F., "Multiaxial Fatigue Damage Models," *Journal of Engineering Materials and Technology, Trans. ASME*, Vol. 109, 1987, pp. 293-298.

Socie, D. F., and Shield, T. W., "Mean Stress Effects in Biaxial Fatigue of Inconel 718," *Journal of Engineering Materials and Technology, Trans. ASME*, Vol. 106, July 1984, pp. 227-232.

Socie, D. F., and Bannantine, J., "Bulk Deformation Fatigue Damage Models," *Materials Science and Engineering*, A103, 1988, pp. 3-13.

Stulen, F. B., and Cummings, H. N., "A Failure Criterion for Multiaxial Fatigue Stresses," *Proceedings American Society for Testing and Materials*, Vol. 54, Philadelphia, 1954, pp. 822-835.

Table I Crack Plane and Planes of Some Maximum Parameters

Specimen No. and Loading Type	Crack Plane (°)	Plane of Maximum Shear Strain Range (°)	Plane of Maximum Shear Stress Range (°)	Plane of Maximum Normal Stress Range (°)	Plane of Maximum Critical Plane Parameter $\gamma+\varepsilon_n+\sigma_{nmean}/E$ (°)	Plane of Maximum Critical Plane Parameter $\gamma(1+K\sigma_{nmax}/\sigma_y)$ K=0.5 (°)	Fatigue Life Cycles to Faiulre
TUS02, N*	16	-18, 72	-71, 19	10	18	17	150,000
TUS03, P**	30	-19, 71	-23, 67	23	59	-17	250,000
TUS04, N	6	-22, 68	-24, 66	17	20.5	-21	65,000
TUS05, N	20	-22, 68	-24, 66	20	-23	-22	60,000
TUS06, N	12	-21, 69	-24, 66	14	19	17	280,000
TUS07, N	-22, 18	-22, 68	-23, 67	20	-22	-22	40,000
TUS08, N	-2~-15	-72, 18	-71, 19	0	20	17	600,000
TUS09, N	10	-18, 72	-72, 18	10	18	16	70,000
TUS10, N	-10	-17, 73	-72, 18	5	19	17	80,000
TUS11, N	-10	-22, 68	-68, 22	-20	-21	-21	4,100
TUS14, P	28	-20, 70	-24, 66	23	57	-16	25,000

* N stands for *Non-proportional Loading*

** P stands for *Proportionl Loading*

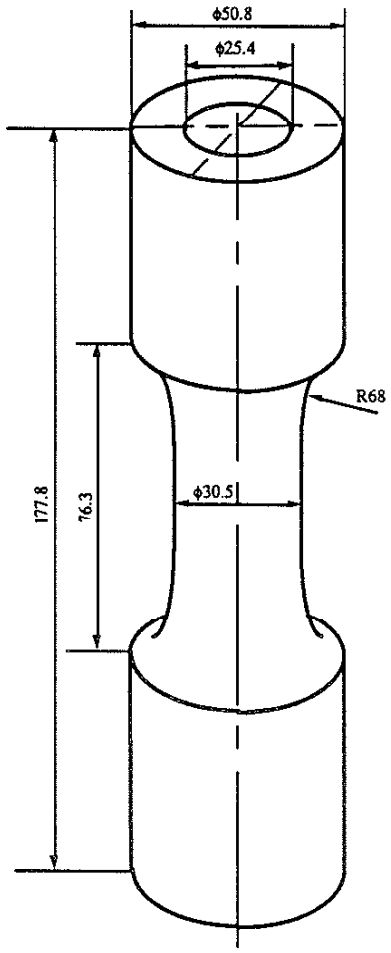

Fig. 1(a) Tubular Specimen (Dimensions in mm)

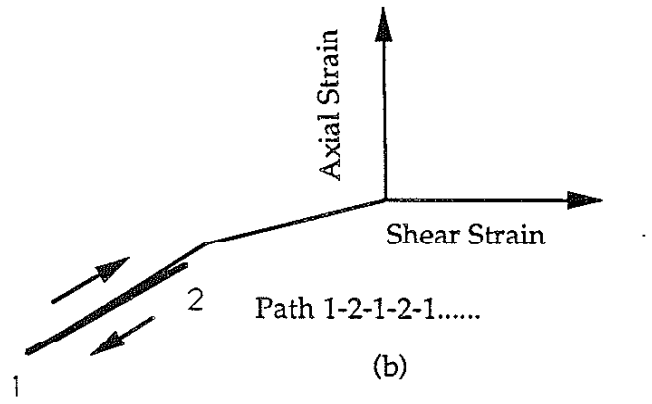

(b)

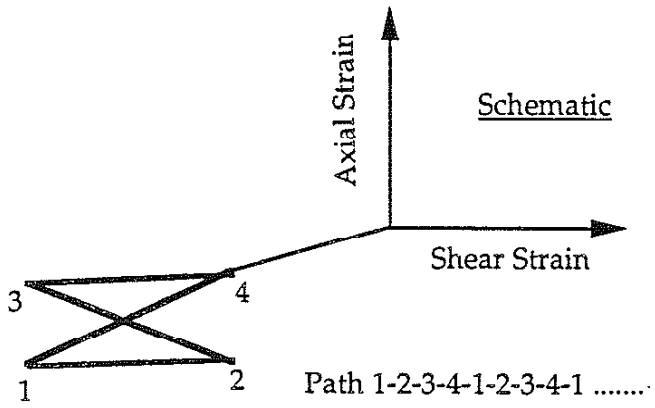

(c)

Figure 1(b)-(c) Schematic of axial strain shear strain paths considered in this study

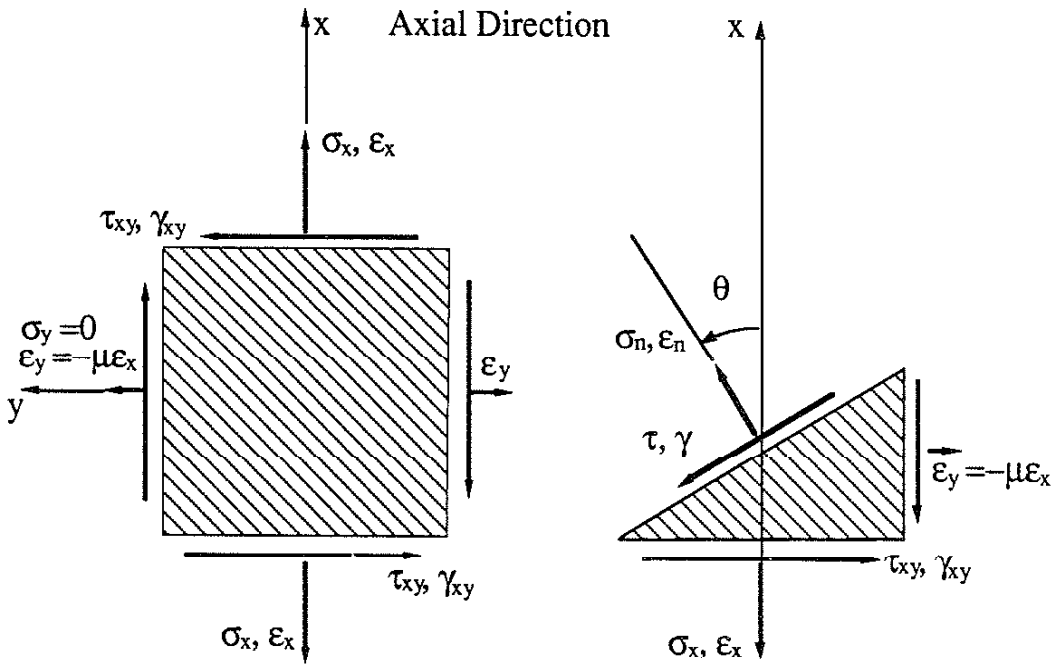

(a) Orthogonal Stresses and Strains

(b) Stresses and Strains on the Plane θ Degrees to Axial Direction

Fig.2 Stress and Strain States of an Elememt on the Surface of a Tubular Specimen (μ is the combined elastic-plastic Poisson's ratio)

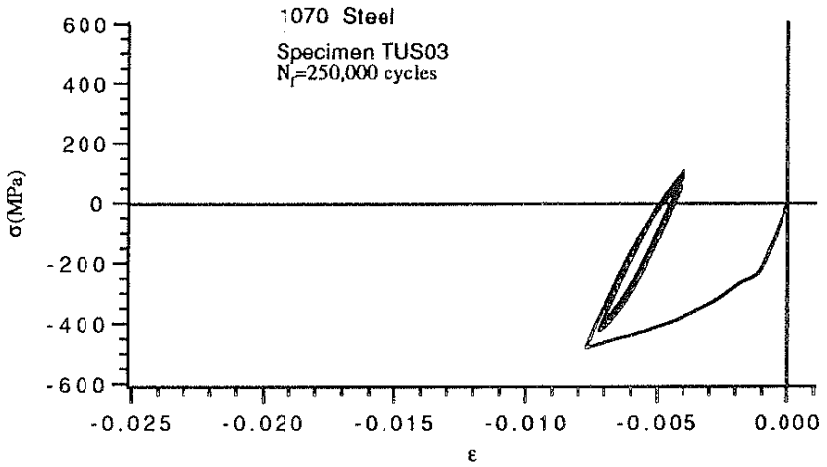

(a) Axial Stress vs Axial Strain

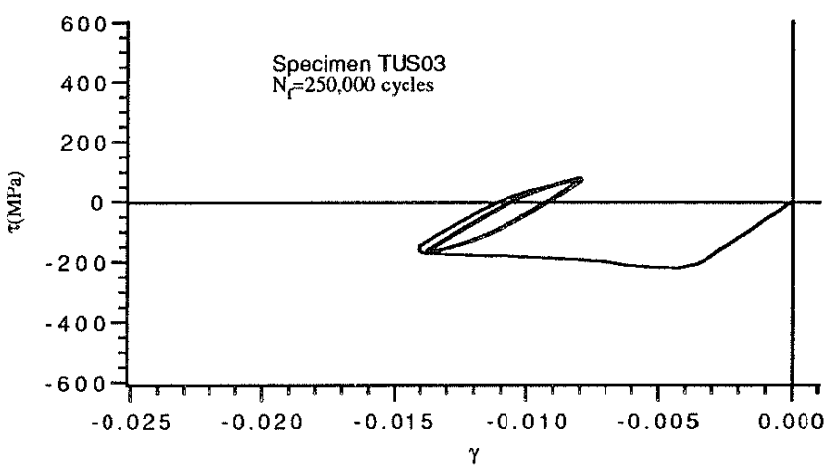

(b) Shear Stress vs Shear Strain

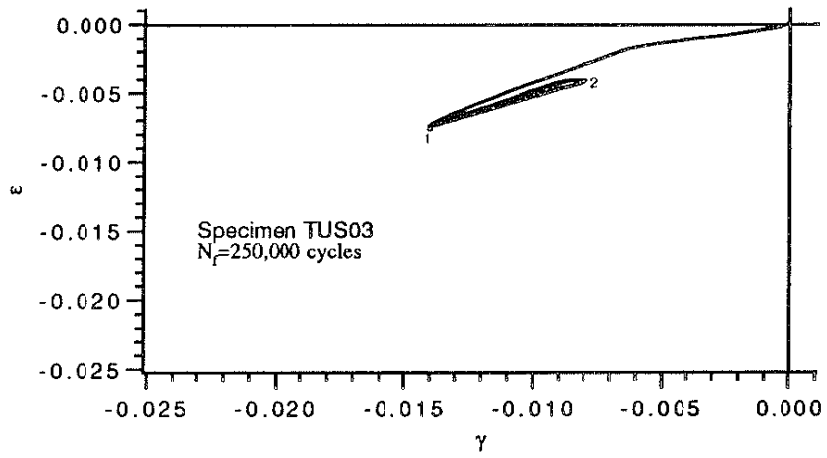

(c) Axial Strain vs Shear Strain, the Controlled Loading Path

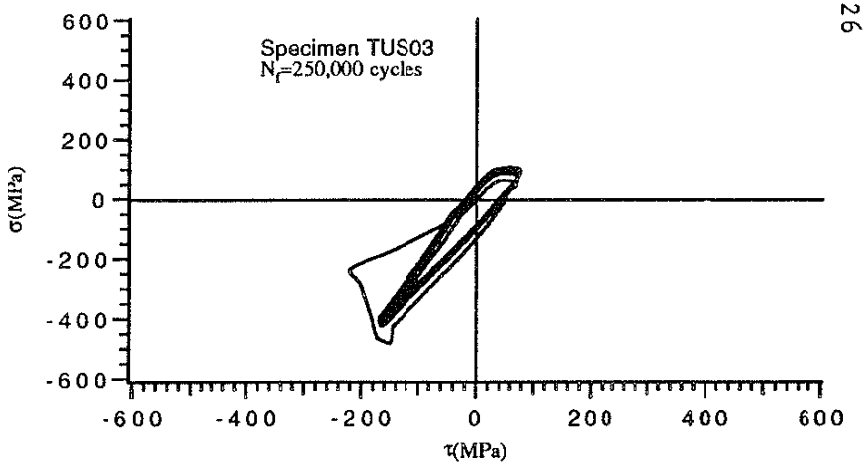

(d) Axial Stress vs Shear Stress

Fig.3 Stress and Strain Responses at First 8 Cycles(Specimen TUS03, Proportional Strain-Controlled, N_f=250,000 cycles)

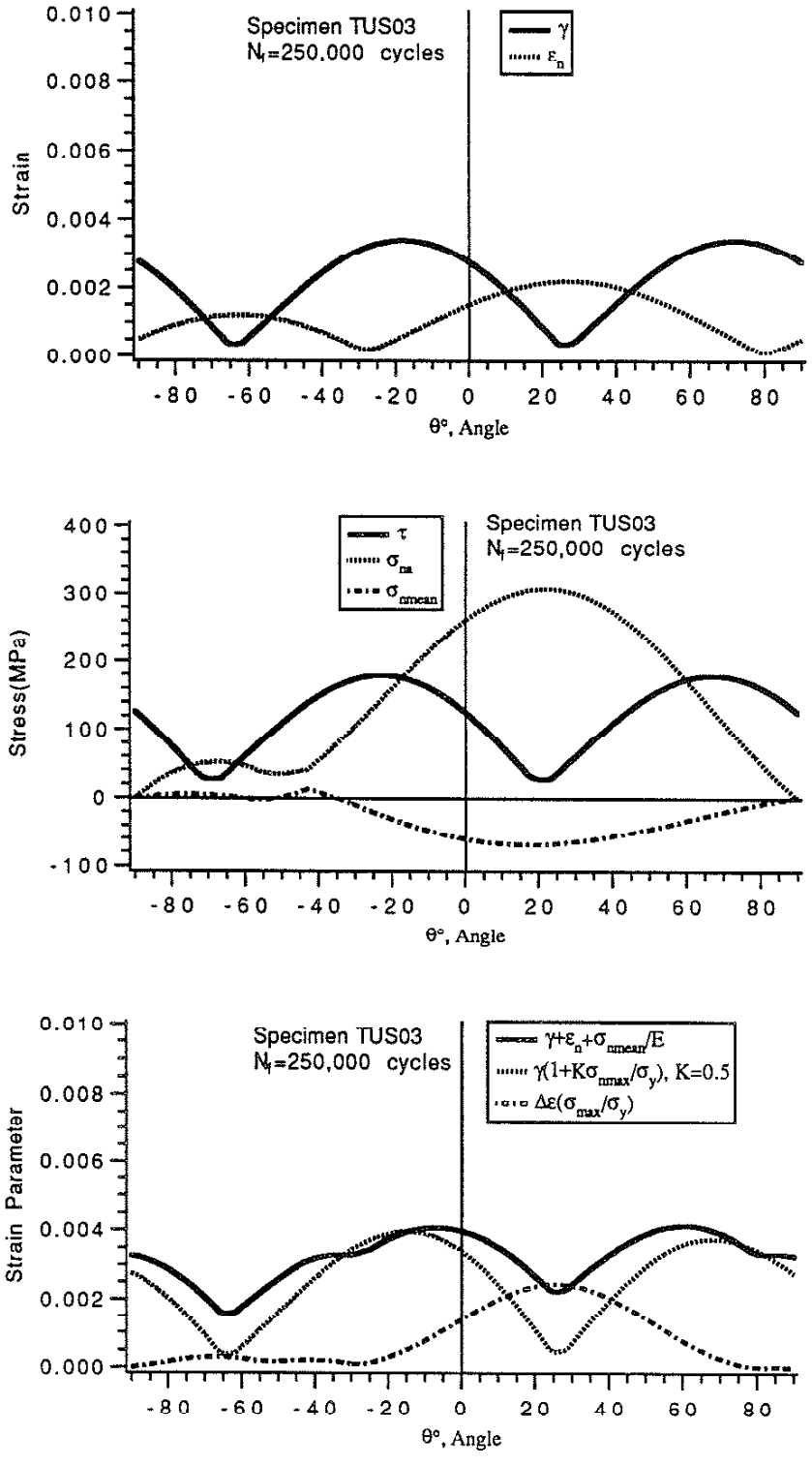

Fig.4 Variations of Stress and Strain Parameters with the Orientation of Plane at Half Fatigue Life (Specimen TUS03, Proportional Strain-Controlled, N_f=250,000 cycles)

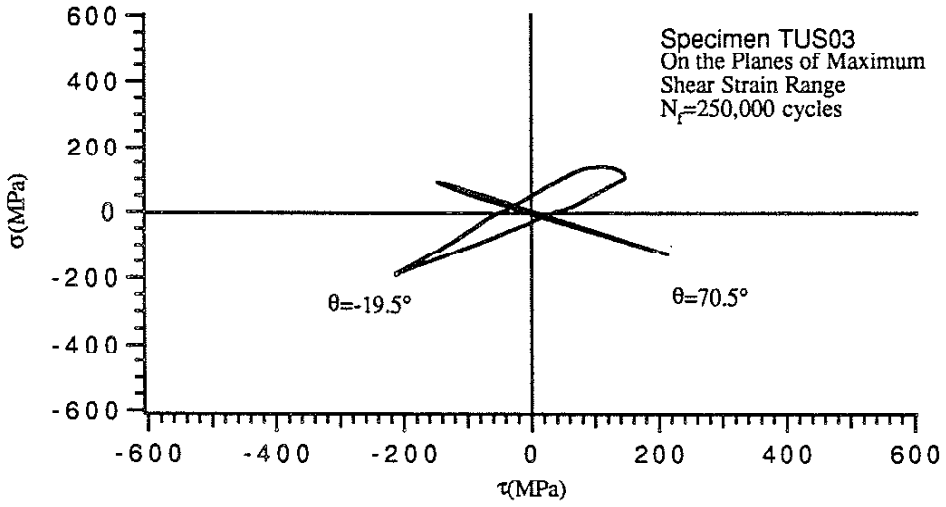

Fig. 5 Relation between Normal Stress and Shear Stress on the Plane of Maximum Shear Strain Range(Specimen TUS3, Proportional Strain-Controlled,N_f=250,000 cycles)

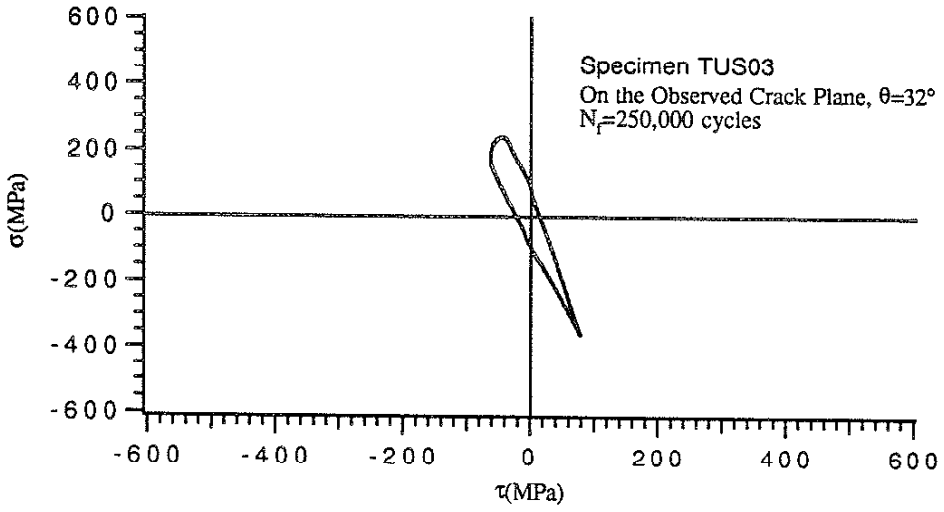

Fig.6 Relation between Normal Stress and Shear Stress on the Observed Crack Plane (Specimen TUS03, Proportional Strain-Controlled,N_f=250,000 cycles)

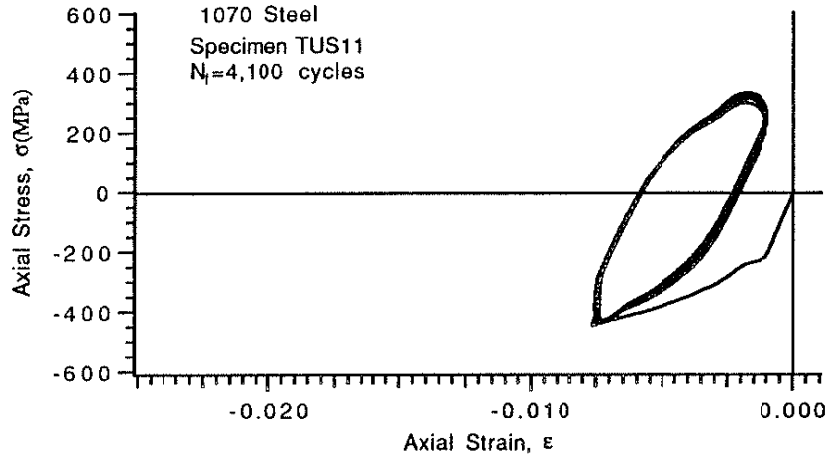

(a) Axial Stress vs Axial Strain

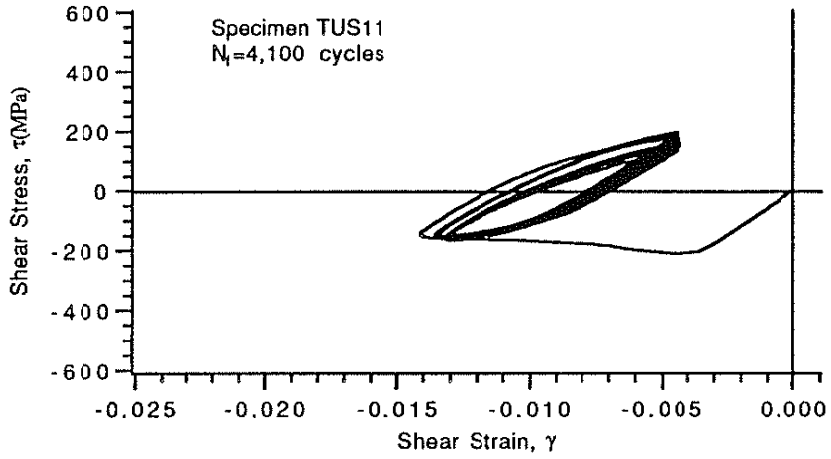

(b) Shear Stress vs Shear Strain

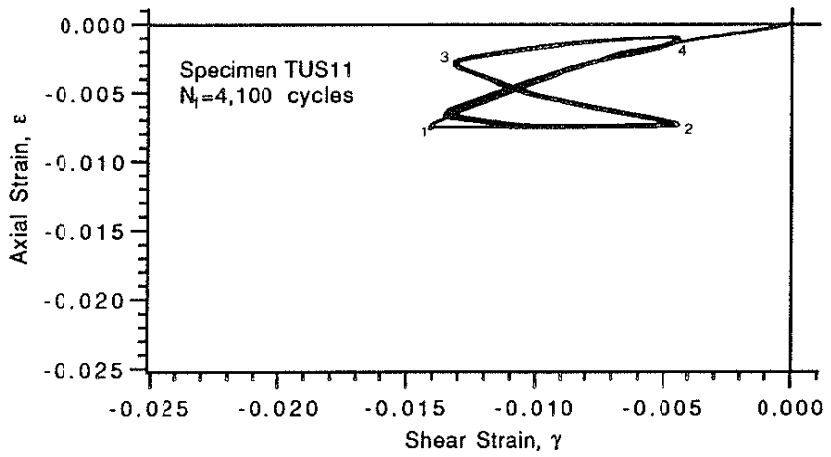

(c) Axial Strain vs Shear Strain, the Controlled Loading Path

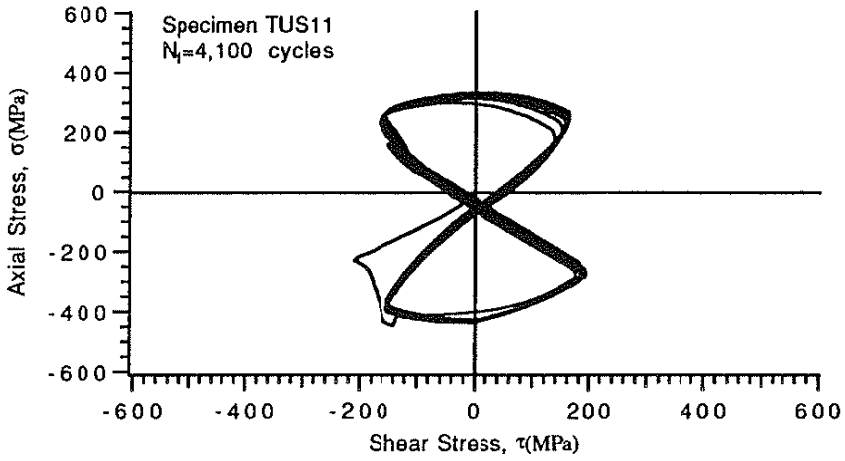

(d) Axial Stress vs Shear Stress

Fig.7 Stress and Strain Responses at First 8 Cycles(Specimen TUS11, Non-Proportional Strain-Controlled, N_f=4,100 cycles)

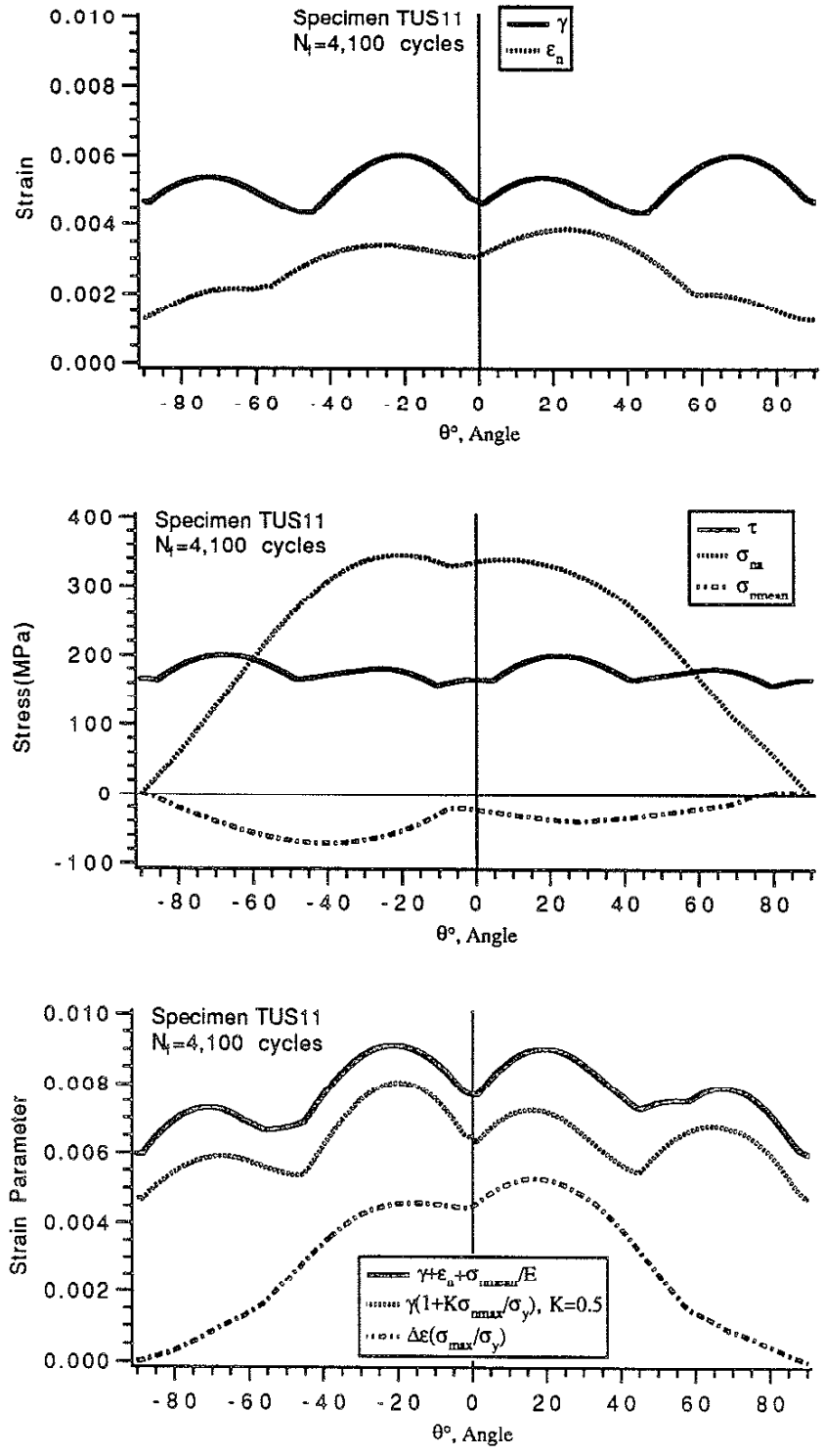

Fig.8 Variations of Stress and Strain Parameters with the Orientation of Plane at Half Fatigue Life (Specimen TUS11, Non-Proportioanl Strain-Controlled, N_f=4,100 cycles)

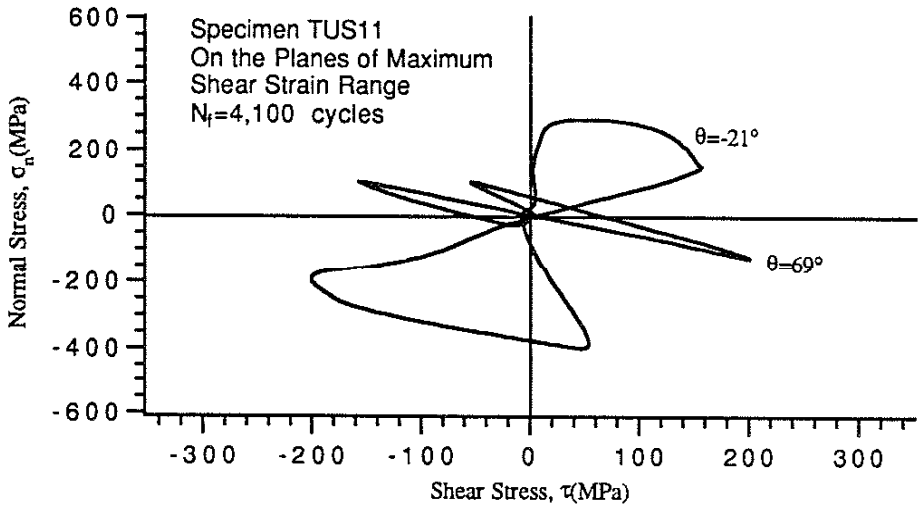

Fig.9 Relation between Normal Stress and Shear Stress on the Planes of Maximum Shear Strain Range(Specimen TUS11, Non-Proportional Strain-Controlled, N_f=4,100 cycles)

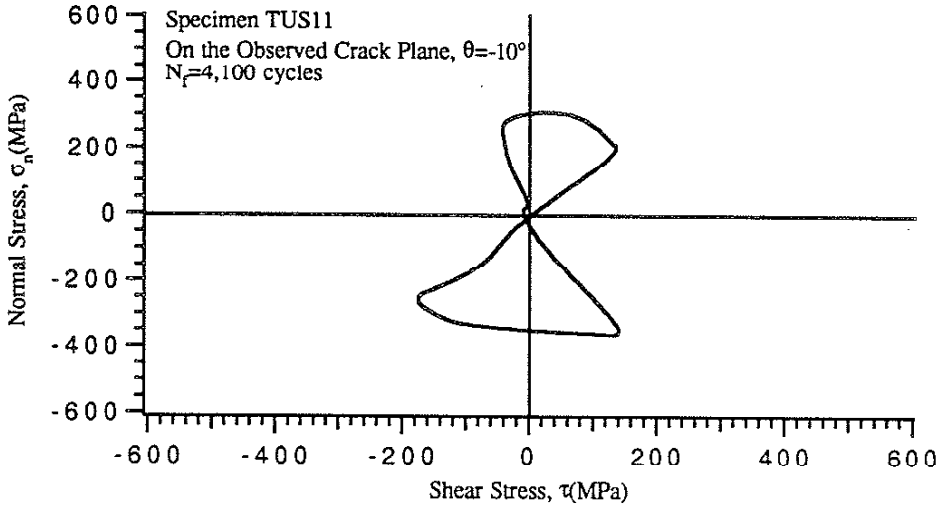

Fig.10 Relation Between Normal Stress and Shear Stress on the Observed Crack Plane (Specimen TUS11, Non-Proportional Strain-controlled, N_f=4,100 cycles)

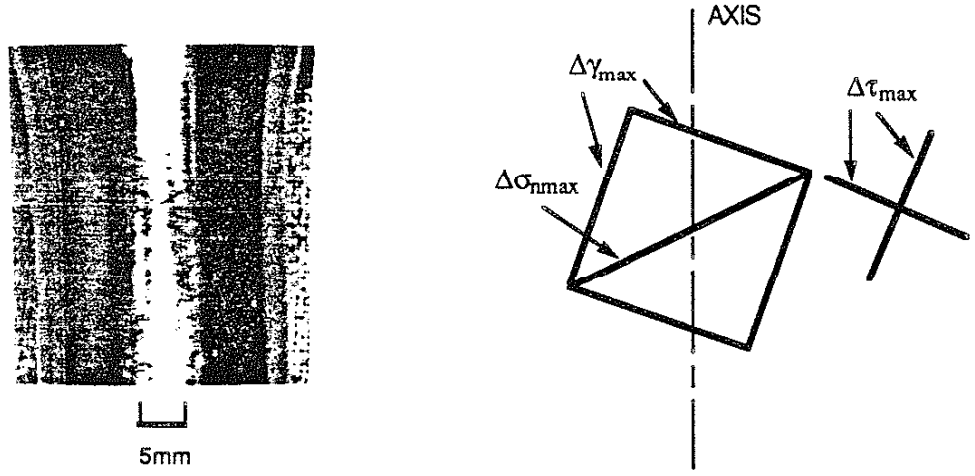

(a) Specimen TUS03, Proportional Strain-Controlled, N_f=250,000 cycles

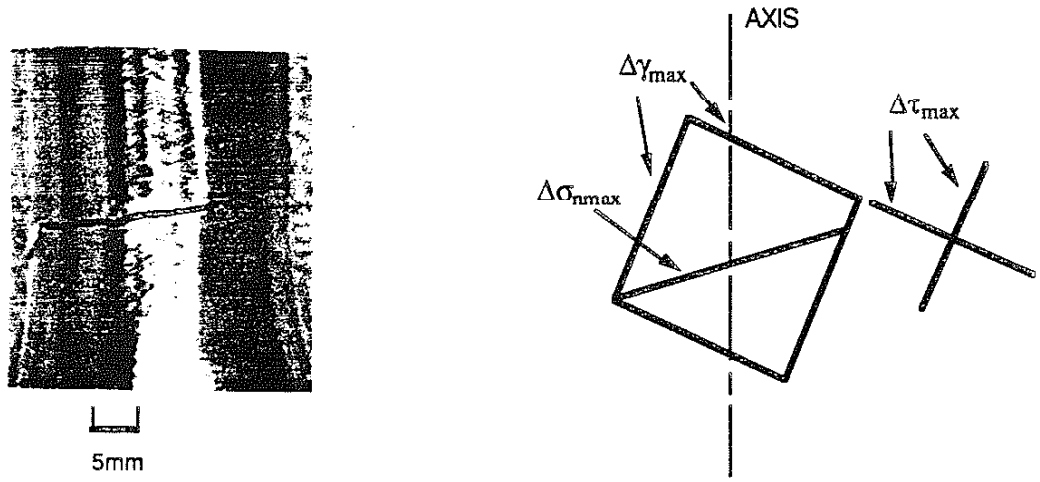

(b) Specimen TUS04, Non-Proportional Strain-Controlled, N_f=65,000 cycles

Fig.11 Fatigue Crack Growth Direction

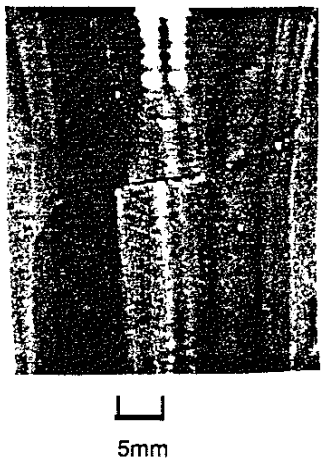

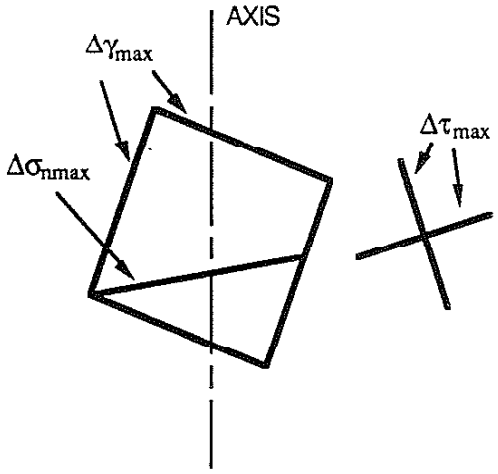

(d) Specimen TUS09, Non-Proportional Strain-Controlled, N_f=70,000 cycles

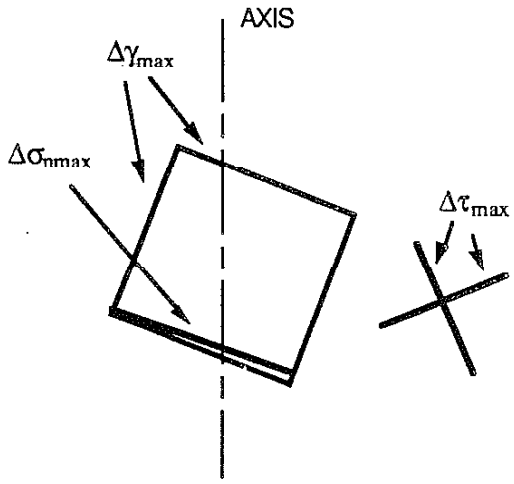

(d) Specimen TUS11, Non-Proportional Strain-Controlled, N_f=4,100 cycles

Fig.11(Cont'd) Fatigue Crack Growth Direction

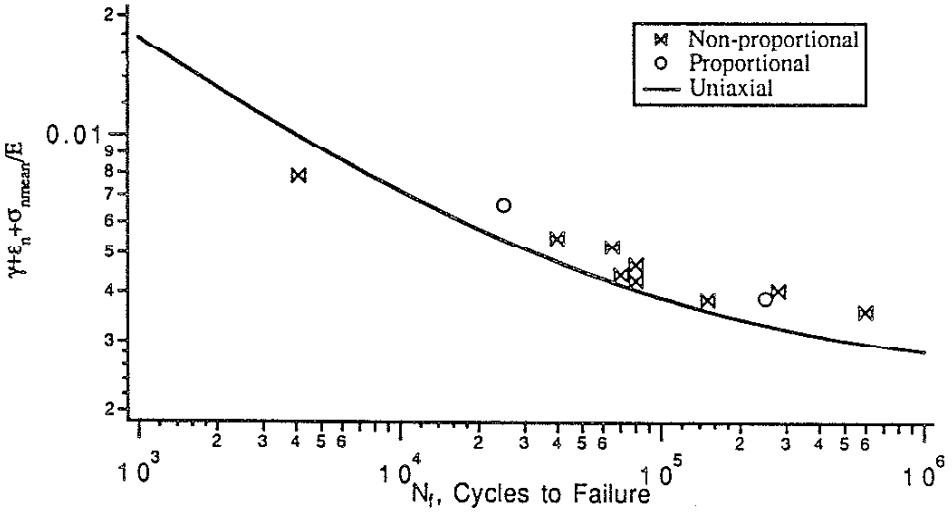

(a) Parameter $\gamma+\varepsilon_n+\sigma_{nmean}/E$ vs. N_f, Cycles to Failure

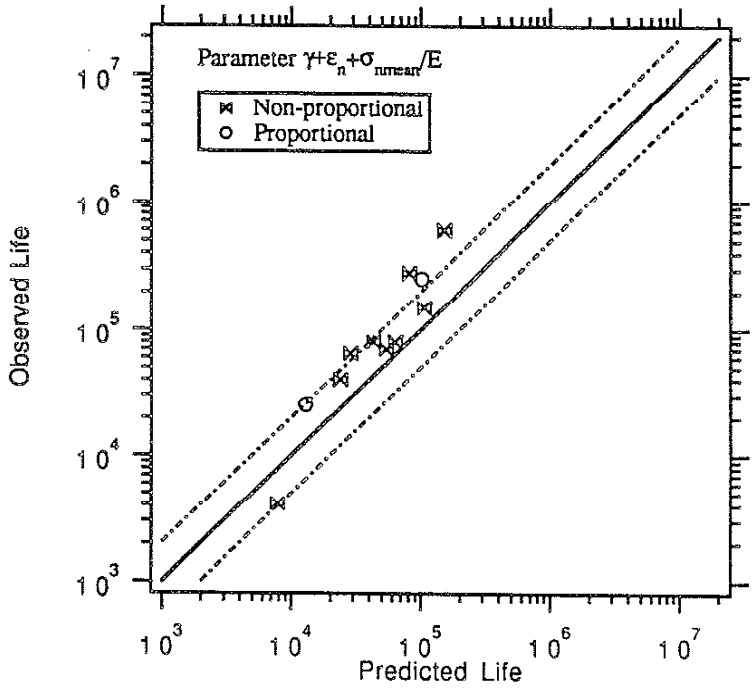

(b) Observed Life vs. Predicted Life

Fig.12 Fatigue Life Correlation and Predictions for Proportional and Non-Proportional 1070 Steel Tests Based on Critical Plane Parameter $\gamma+\varepsilon_n+\sigma_{nmean}/E$

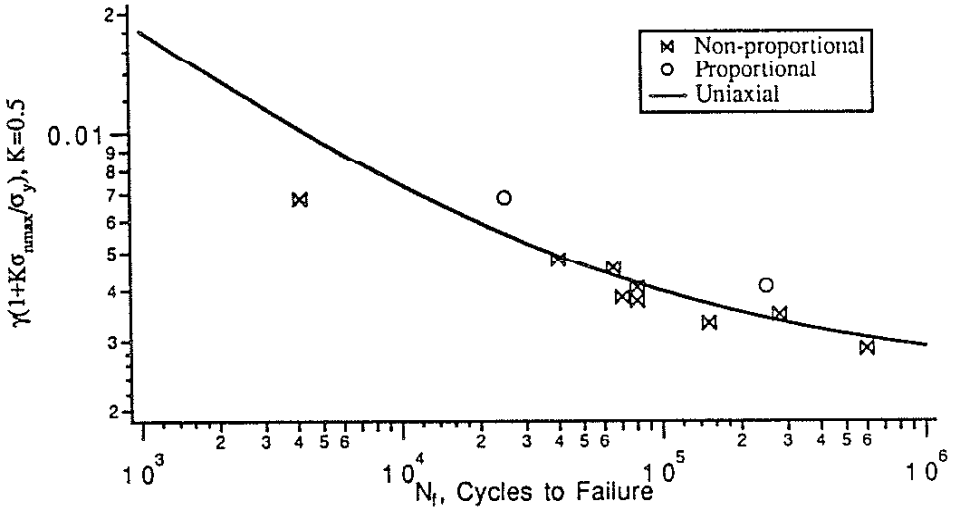

(a) Parameter $\gamma(1+K\sigma_{nmax}/\sigma_y)$, K=0.5, vs. N_f, Cycles to Failure

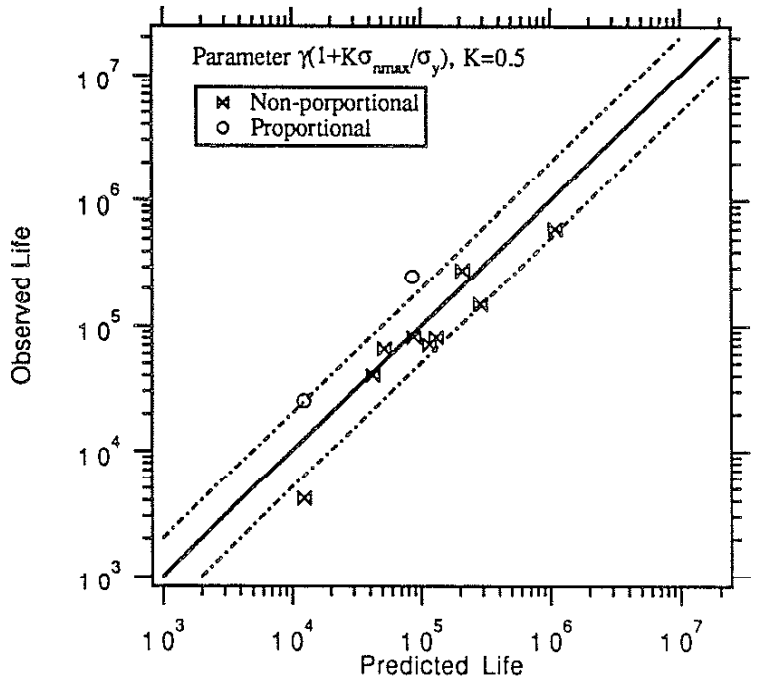

(b) Observed Life vs. Predicted Life

Fig.13 Fatigue Life Correlation and Predictions for Proportional and Non-Proportional 1070 Steel Tests Based on Critical Plane Parameter $\gamma(1+K\sigma_{nmax}/\sigma_y)$, K=0.5

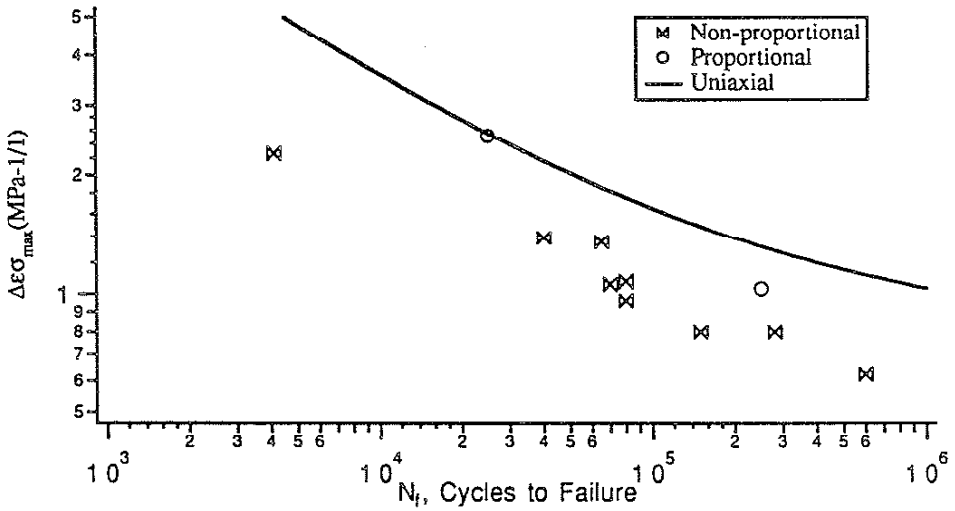

(a) Parameter $\Delta\varepsilon\sigma_{max}$ vs. N_f, Cycles to Failure

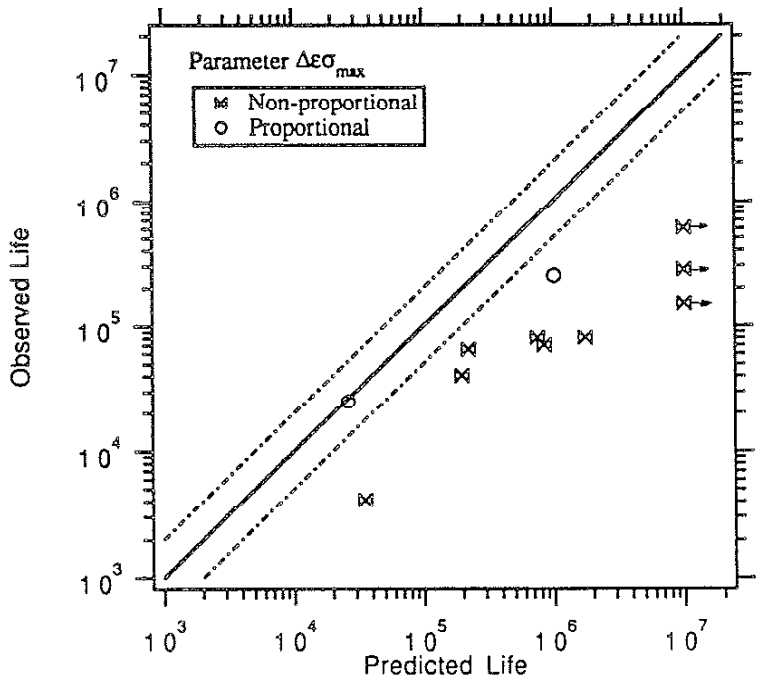

(b) Observed Life vs. Predicted Life

Fig.14 Fatigue Life Correlation and Predictions for Proportional and Non-Proportional1070 Steel Tests Based on Parameter $\Delta\varepsilon\sigma_{max}$

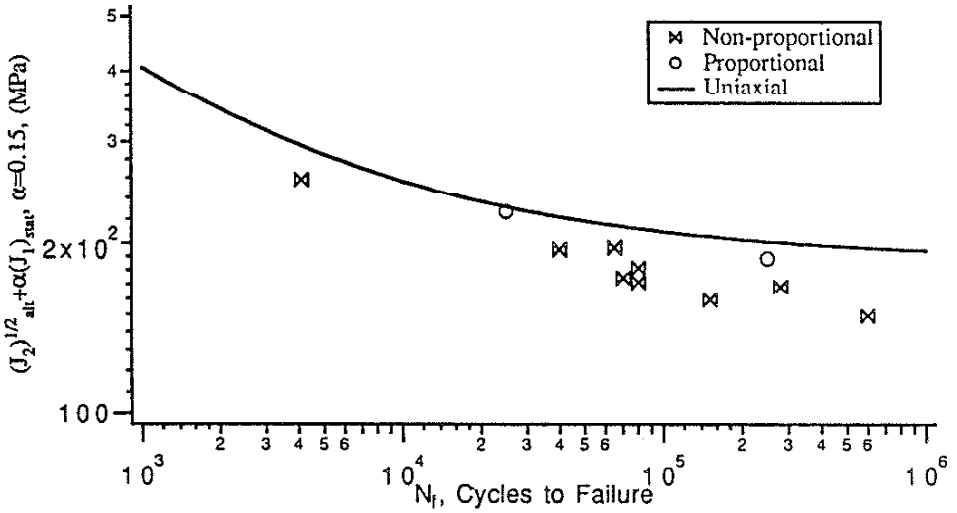

(a) Parameter $(J_2)^{1/2}_{alt}+\alpha(J_1)_{stat}$, α=0.15, vs N_f, Cycles to Failure

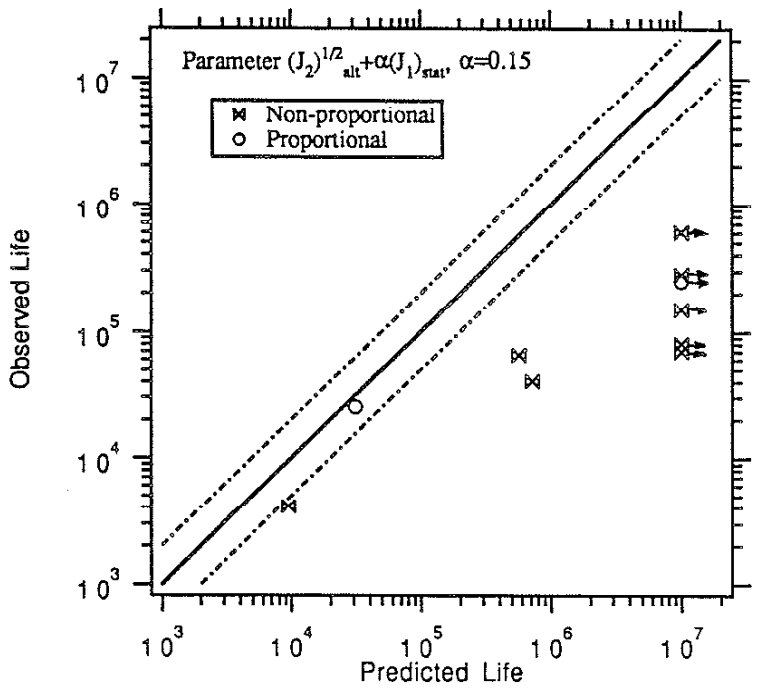

(b) Observed Life vs. Predicted Life

Fig.15 Fatigue Life Correlation and Predictions for Proportional and Non-Proportional 1070 Steel Tests Based on Sines' Parameter $(J_2)^{1/2}_{alt}+\alpha(J_1)_{stat}$, α=0.15

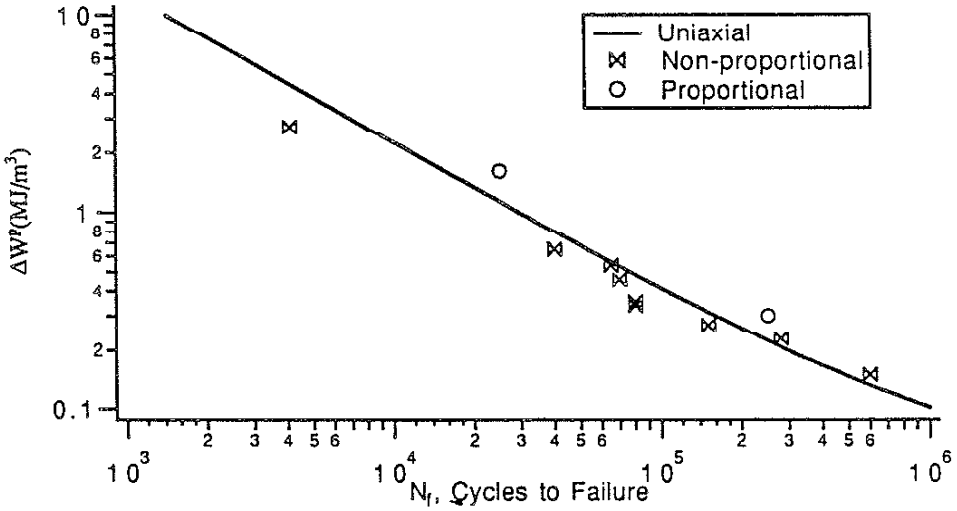

(a) Parameter ΔW^P vs. N_f, Cycles to Failure

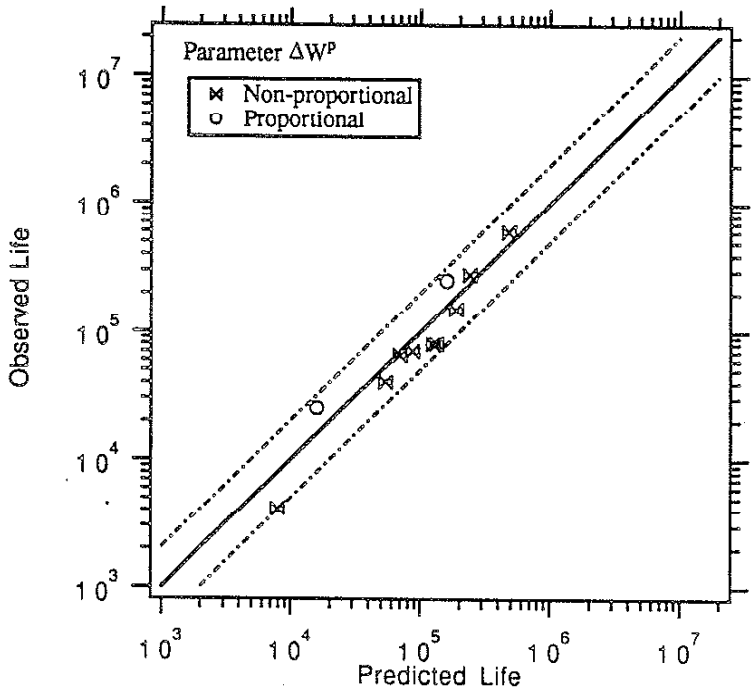

(b) Observed Life vs. Predicted Life

Fig.16 Fatigue Life Correlation and Predictions for Proportional and Non-Proportional1070 Steel Tests Based on Parameter ΔW^P

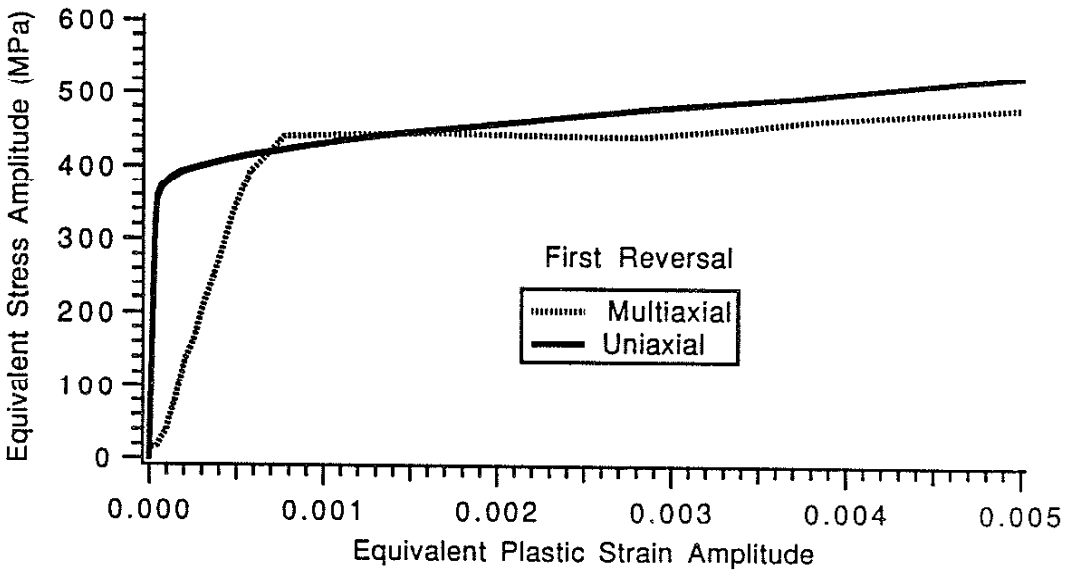

Fig.17 Equivalent Stress versus Equivalent Plastic Strain at First Reversal

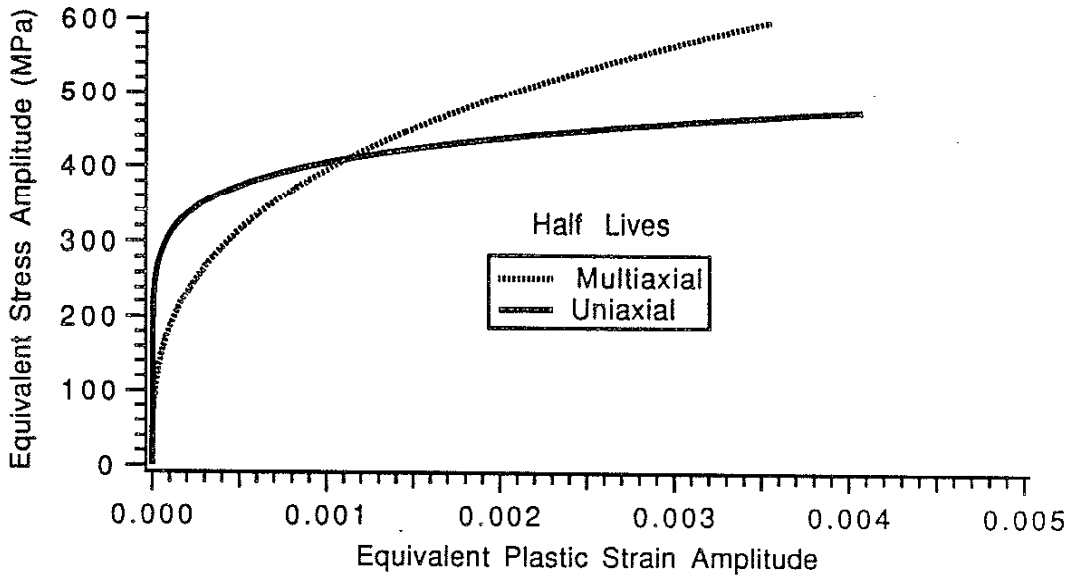

Fig.18 Equivalent Stress versus Equivalent Plastic Strain at Half Fatigue Lives

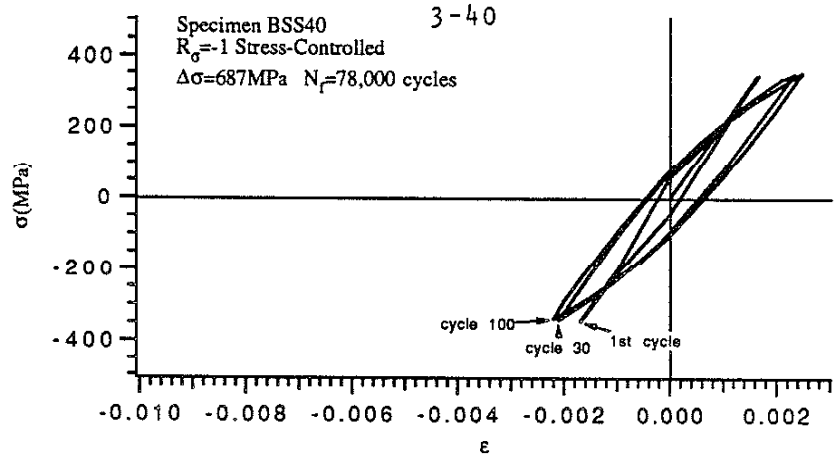

(a) Specimen BSS40 without Mean Stress

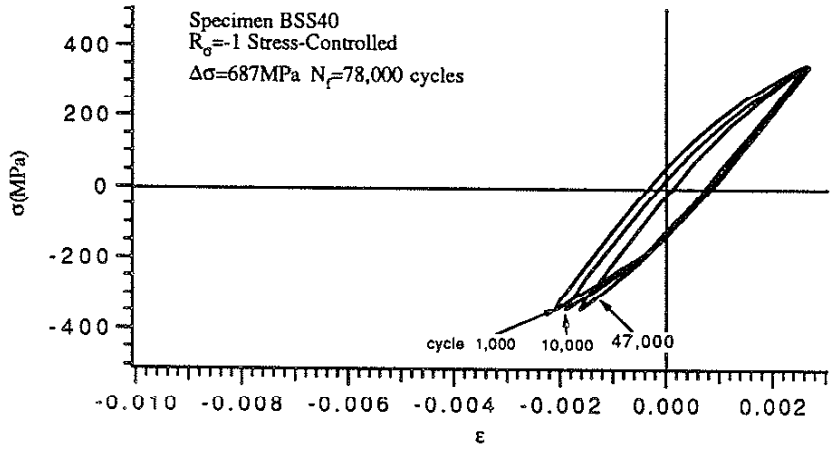

(b) Specimen BSS40 without Mean Stress

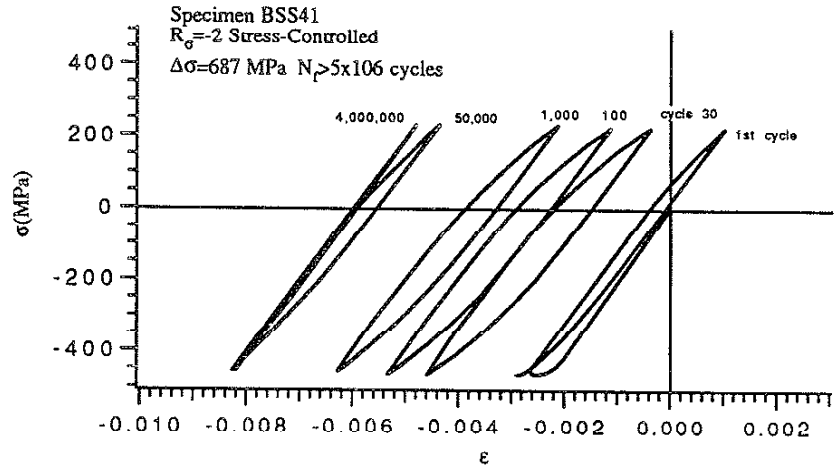

(c) Specimen BSS41 with Compressive Mean Stress

Fig.19 Cyclic Loops under Uniaxial Stress-Controlled Loadings

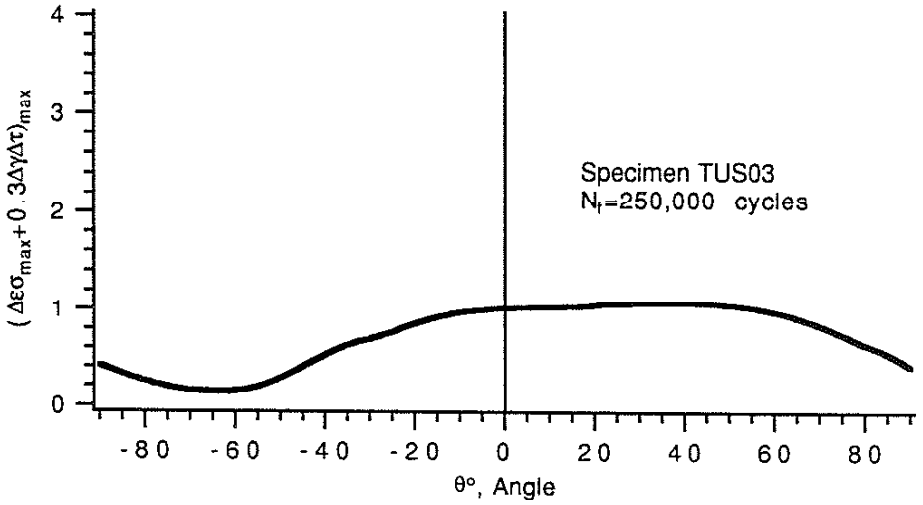

Figure 20(a)Variation of Proposed Parameter with the Orientation of Plane at Half Fatigue Life (Specimen TUS03, Proportional, N_f = 250,000 cycles)

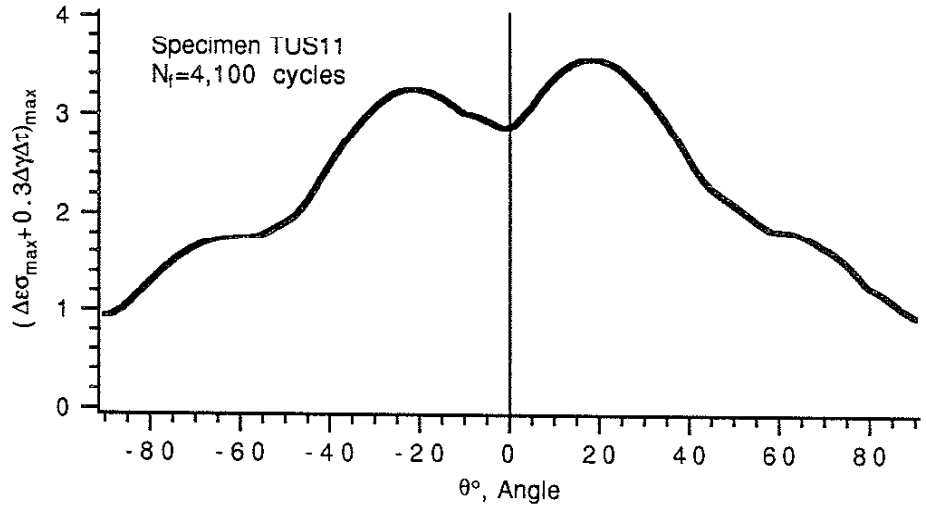

Figure 20(b) Variation of Proposed Parameter with the Orientation of the Plane at Half Life(Specimen TUS11, Non-proportional, N_f= 4,100 cycles)

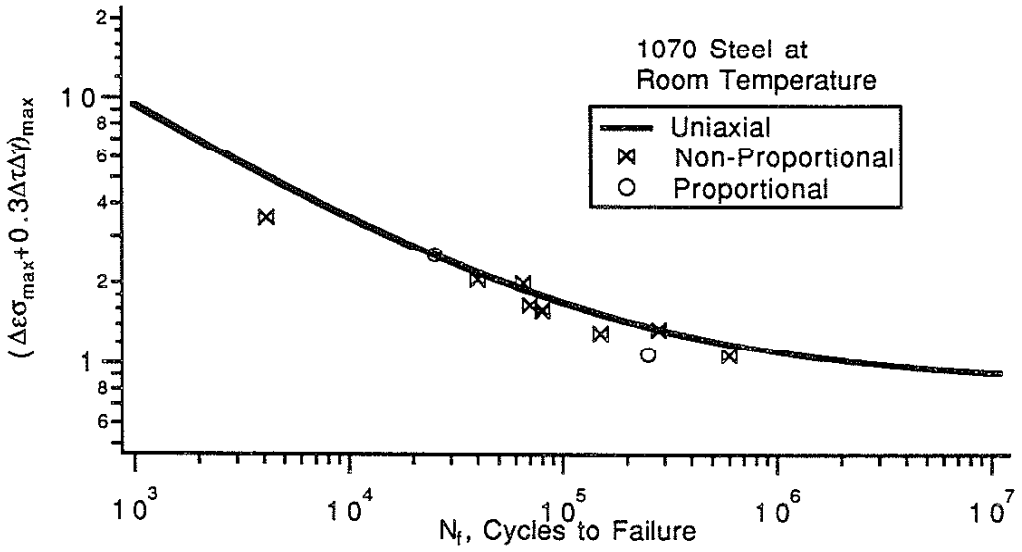

(a) Parameter $(\Delta\varepsilon\sigma_{max}+K'\Delta\gamma\Delta\tau)_{max}$, K'=0.3, vs N_f, Cycles to Ffailure

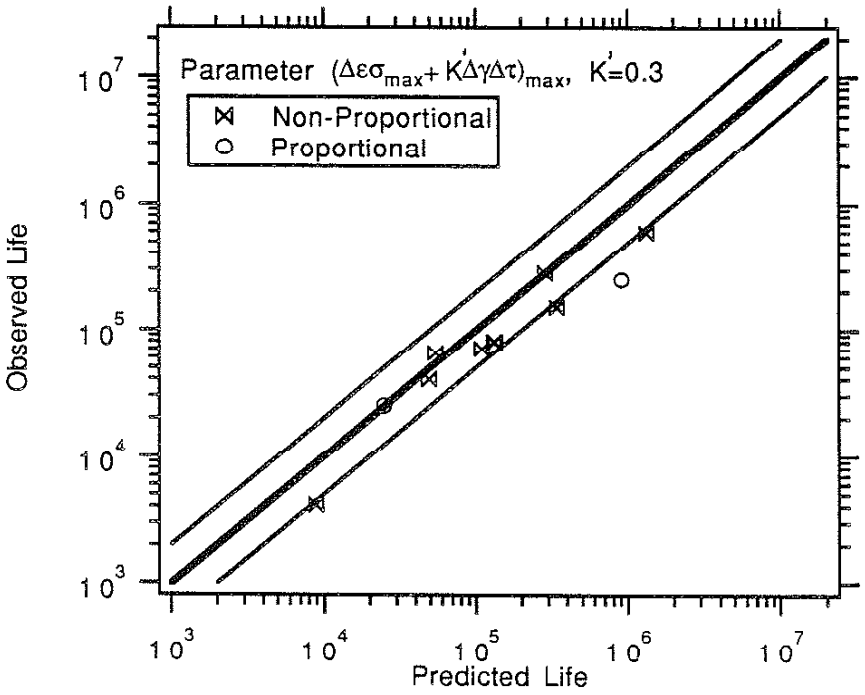

(b) Observed Life vs. Predicted Life

Fig. 21 Fatigue Life Correlation and Predictions for Proportional and Non-Proportional 1070 Steel Tests Based on Parameter $(\Delta\varepsilon\sigma_{max}+K'\Delta\gamma\Delta\tau)_{max}$, K'=0.3

An Analytical Approach for Elastic-Plastic Stress Analysis of Rolling Contact

Y. Roger Jiang
and
Huseyin Sehitoglu

Report No.4 prepared for
Association of American Railroads

November 1991

An Analytical Approach for Elastic-Plastic Stress Analysis of Rolling Contact

Huseyin Sehitoglu, Associate Professor
Y. Roger Jiang, Research Assistant

Department of Mechanical and Industrial Engineering
University of Illinois at Urbana-Champaign
Urbana, Illinois 61801

Abstract:

An analytical approach, based on a stress invariant assumption and a stress/strain relaxation procedure, is developed for determination of residual stresses and strains in rolling contact. For line contact problems, the proposed method provides residual stress results comparable to published results obtained using the finite element method. Upon comparison of residual stress results with Merwin-Johnson's method, McDowell-Moyar's method, the proposed approach provided closest agreement with the finite element method.

The proposed approach is applied to the calculation of contact stresses and displacements under normal and tangential tractions using 1070 wheel steel properties. The study shows that a driven wheel undergoes higher plastic shear strains, hence higher fatigue damage, compared to the driving wheel. Single surface, two-surface and multiple surface yield theories are employed, and the results (stresses, displacements) depended strongly on the details of the plasticity relations.

1. Introduction

In rolling contact of railroad wheels, residual stresses will develop when the loading results in shakedown, cyclic plasticity or ratchetting conditions. Under repeated rolling, outside the shakedown limit, plastic deformation and incremental surface displacement results in progressive degradation of the material. A rational fatigue analysis requires that the stress/strain history, including the stress states and gradients, be determined.

Due to the three dimensional stress/strain state and complex stress gradients involved in the rolling contact problem, a closed form elastic-plastic stress solution is not possible. Merwin-Johnson [1][2] studied the plastic deformation in rolling contact by assuming that the strain cycle remains identical with the elastic strain cycle. They predicted cumulative surface displacements, using elastic-perfectly plastic model, in agreement with the experimental data [3]. Later studies using finite elements [4][5] confirmed the validity of the Merwin-Johnson approach. Since the predicted surface displacement rates were smaller than FEM, Hearle and Johnson [4] forwarded an alternate method using the orthogonal shear strain component as the only plastic strain occurring throughout the cycle. Later, Bower and Johnson [6], noting the difference between subsurface surface plastic flow, assumed stress invariance at the surface, yet maintained the Hearle-Johnson's concept of subsurface flow. The demarcation of 'surface', 'subsurface', and 'near surface' was not defined, and continuity cannot be guaranteed. Neverthless, they employed a nonlinear kinematic hardening rule described by Bower [7-9], and obtained surface displacement rates in agreement with experiments.

McDowell and Moyar [10][11] calculated residual stresses and strains in rolling line contact by assuming that the orthogonal shear stress and radial stress are identical to the elastic solutions and that the strain rates in the rolling (x) and axial (y) directions are

always zero. These conditions allow all the stress components to be determined from the elastic solutions. Their work emphasized the need for more sophisticated plasticity relations, capable of handling the non-proportional histories observed in rolling contact.

Hahn and co-workers[5][12-15] conducted elastic-plastic analyses of rolling contact using the finite element method. They considered elastic-perfectly plastic and susequently bilinear material properties, and used the Prager-Ziegler hardening rules. Their results indicated that the strain hardening of a material behavior has a profound influence on the residual stress magnitudes and cumulative shear strain under rolling contact. In view of the sensitivity of the results to the plasticity relations, the need for using constitutive representations geared towards the non-proprtional loading is apparent.

The determinations of residual stress/strain and stress/strain histories remain a fundamental problem in contact fatigue analysis. In the analytical models, the compatibility and the equilibrium conditions are not strictly satisfied. Currently, the agreement between the results of available analytical methods and those of finite element analyses is not satisfactory. Development of an approximate analytical method for elastic-plastic stress analysis of contact is desirable and is the subject of this study. The balance of the work emphasizes the sensitivity of the results on plasticity relations, and in particular the translation rules for stress surfaces.

2. The Analytical Approach

We require that the stress cycle during elastic-plastic rolling contact is equal to that for the purely elastic case. Expressing this assumption mathematically,

$$\sigma_{ij}=\sigma_{ij}^{el} \tag{1}$$

where σ_{ij} is the stress tensor and *el* denotes elastic solutions. The stresses and strains at a point are relaxed proportionally at the end of the rolling pass to meet the residual stress and strain conditions.

The rolling line contact is considered in Figure 1 where the coordinate system moves with the load. The stress components at point A are determined using Smith and Liu's formula [16] based on elasticity theory. For repeated rolling, when x is larger than about 10a, the stress state is elastic. As the load moves rightward and x approaches zero, plastic deformation will occur subsurface and/or on the surface depending on the tangential force [17]. As the load moves further to the right and x takes large negative values the stress state will be elastic again. Generally, at the end of the rolling pass, the stress and strain components are nonzero. In order to meet the correct residual stress and strain conditions, the stresses and strains are relaxed proportionally. After the relaxation procedure, the residual stresses and strains are obtained. At this time, one passage of the load is completed. The same routine is repeated for the second and subsequent passages of the load using the previous residual stresses as the initial stresses for the next passage of the load.

When applying the proposed method to the rolling line contact problem Equation (1) becomes,

$$\sigma_x=\sigma_x^{el}\ ;\quad \sigma_z=\sigma_z^{el}\ ;\quad \tau_{xz}=\tau_{xz}^{el} \tag{2}$$

where σ_x^{el}, σ_z^{el}, τ_{xz}^{el} represent the elastic solution. The plane strain condition requires,

$$\dot{\varepsilon}_y = 0 \tag{3}$$

In the elastic region the above equation results in,

$$\dot{\sigma}_y = \mu(\dot{\sigma}_x + \dot{\sigma}_z) \tag{4}$$

where μ is the Poisson's ratio. When the deformation is elastic-plastic, the stress increment $\dot{\sigma}_y$ can be expressed as,

$$\dot{\sigma}_y = \frac{(\mu - \frac{E}{h}n_x n_y)\dot{\sigma}_x + (\mu - \frac{E}{h}n_y n_z)\dot{\sigma}_z - \frac{2E}{h}n_y n_{xz}\dot{\tau}_{xz}}{1 + \frac{E}{h}n_y^2} \tag{5}$$

where E is the elasticity modulus, h is the plastic modulus function, and n_{ij} represents the unit normal on the yield surface. The plastic strain rates are given as,

$$\dot{\varepsilon}_{ij}^p = \frac{1}{h}\langle \dot{S}_{kl} n_{kl} \rangle n_{ij} \tag{6}$$

where $v=\langle u \rangle$ denotes $v=u$ if $u \geq 0$ (plastic loading) and $v=0$ if $u<0$(elastic unloading). $\dot{S}_{ij}$ in Equation (6) is the deviatoric stress tensor. In Equation (5) and Equation (6) n_{ij} is the unit normal in the plastic strain rate direction on the yield surface, which is expressed as,

$$n_{ij}=\frac{S_{ij}-\alpha_{ij}}{\sqrt{2}k}, \tag{7}$$

where α_{ij} is the deviatoric back stress tensor and k is the yield stress in shear. The yield surface is defined as,

$$f=\frac{1}{2}(S_{ij}-\alpha_{ij})(S_{ij}-\alpha_{ij})-k^2=0 \tag{8}$$

The method of determining the increment of the deviatoric back stress depends on the hardening rule used. Prager-Ziegler hardening rule can be expressed as:

$$\dot{\alpha}_{ij}=\dot{S}_{kl}n_{kl}n_{ij} \tag{9}$$

According to Merwin & Johnson [1], the residual stress and strain conditions in line contact problems are,

$$\begin{aligned} (\varepsilon_x)_r &= 0 & (\sigma_x)_r &= f_1(z) \\ (\varepsilon_y)_r &= 0 & (\sigma_y)_r &= f_2(z) \\ (\varepsilon_z)_r &= f_3(z) & (\sigma_z)_r &= 0 \\ (\gamma_{xz})_r &= f_4(z) & (\tau_{xz})_r &= 0 \end{aligned} \tag{10}$$

where f(z) means that f is a function of z only.

The stress and strain components at a point are generally nonzero at the end of the rolling pass. Denote the stress and strain components as $(\sigma_x)_b$, $(\varepsilon_x)_b$, $(\gamma_{xz})_b$, $(\tau_{xz})_b$, etc., and set M steps from the beginning of the relaxation to the end. According to Equation (10), the following stress and strain increments can be obtained,

$$d\varepsilon_x=(\varepsilon_x)_b/M$$
$$d\varepsilon_y=0$$
$$d\sigma_z=(\sigma_z)_b/M \qquad (11)$$
$$d\tau_{xz}=(\tau_{xz})_b/M$$

Knowing the above four increments, the increments of σ_x, σ_y, ε_z, and γ_{xz} can be calculated. When the deformation is elastic-plastic, $d\sigma_x$ and $d\sigma_y$ can be obtained by solving the following equation family,

$$(1+\frac{En_x^2}{h})d\sigma_x+(\frac{En_xn_y}{h})d\sigma_y=Ed\varepsilon_x+(\mu-\frac{En_xn_z}{h})d\sigma_z-\frac{2En_xn_{xz}}{h})d\tau_{xz}$$

(12)

$$(\frac{En_xn_y}{h})d\sigma_x+(1+\frac{En_y^2}{h})d\sigma_y=(\mu-\frac{En_yn_z}{h})d\sigma_z-\frac{2En_yn_{xz}}{h})d\tau_{xz}$$

And then, $d\varepsilon_x$ and $d\gamma_{xz}$ follow,

$$d\varepsilon_x=\frac{d\sigma_z-\mu(d\sigma_x+d\sigma_y)}{E}+\frac{n_z}{h}(n_xd\sigma_x+n_yd\sigma_y+n_zd\sigma_z+2n_{xz}d\tau_{xz}) \qquad (13)$$

$$d\gamma_{xz}=\frac{d\tau_{xz}}{G}+\frac{2n_{xz}}{h}(n_xd\sigma_x+n_yd\sigma_y+n_zd\sigma_z+2n_{xz}d\tau_{xz}) \qquad (14)$$

Note that $d\varepsilon_x$, $d\varepsilon_y$, $d\sigma_z$, $d\tau_{xz}$ are determined according to Equation (11). The components of the normal to the yield surface n_x, n_y, n_z, and n_{xz} are calculated from Equation (7). Therefore, $d\sigma_x$ and $d\sigma_y$ can be solved from Equation (12). Substituting $d\sigma_x$ and $d\sigma_y$ into Equation (13) and Equation (14), $d\varepsilon_x$ and $d\gamma_{xz}$ can be obtained.

A Two Surface Plasticity Model

An illustration of the two surface model is shown in Figure 2. The flow rule, yield surface equation, and normal to the yield surface are expressed in Equation (6), Equation (8), and Equation (7),

respectively. In the two surface model, the increment of deviatoric back stress is expressed as [18][19],

$$\dot{\alpha}_{ij}=\frac{\dot{S}_{kl}n_{kl}}{v_{mn}n_{mn}}v_{ij} \tag{15}$$

where

$$v_{ij}=S^{*}_{ij}-S_{ij} \tag{16}$$

and

$$S^{*}_{ij}=\frac{R_{max}}{R}(S_{ij}-\alpha_{ij}) \tag{17}$$

Here, S^{*}_{ij} is a point on the bounding surface f* defined by

$$f^{*}=\frac{3}{2}S^{*}_{ij}S^{*}_{ij}-R^{2}_{max}=0 \tag{18}$$

where R_{max} is the bounding surface radius given by,

$$R_{max}=\begin{cases} R^{*} \text{ if } \max[\sqrt{\frac{3}{2}S_{ij}S_{ij}}]\leq R^{*} \\ \max[\sqrt{\frac{3}{2}S_{ij}S_{ij}}] \text{ if } \max[\sqrt{\frac{3}{2}S_{ij}S_{ij}}]>R^{*} \end{cases} \tag{19}$$

For the sake of simplicity, in the two surface model and Prager-Ziegler Rule, the plastic modulus function suggested by Drucker [20] is used,

$$h=\frac{2}{3}H=\frac{W}{(\sqrt{J_2}/k)^{b}} \tag{20}$$

where W and b are constants and J_2 is the second stress invariant, h is the plastic modulus function, and H is the plastic modulus in uniaxial tension-compression. For 1070 steel the cyclic stress-strain parameters are as following,

G=80GPa, m=0.3, k=139MPa

$$\frac{H}{G}=\frac{4.11}{(\sqrt{J_2}/k)^{2.1}}, \quad R^*=4R$$

Garud Hardening Rule

Garud used stress surfaces 'geometrically' similar to the initial yield surface each having a constant plastic modulus. This concept was introduced by Mroz [18][19]. Garud realized the possible inconsistencies when Mroz hardening rule is used, and introduced a new hardening rule. Referring to Figure 3, the direction of the center of ith surface is given by the vector joining its center o_i and o'_i where o'_i is the center of the ith surface if the stress increment $\Delta\mathbf{S}$ were so large such that it reached the point p' where ith surface and (i+1)th surface were tangential. The magnitude of the translation is given by the consistency condition according to which the current state of stress should remain on the surface(s) if plastic flow occurs. Detailed description of Garud hardening rule can be found in Reference [21].

Except for Garud rule, in all the previously referenced rules that involve translation of the yield surface in stress space, the magnitude and direction of translation is independent of the direction of stress increment. In general, as pointed out by Garud [21][22], the consistency condition is not satisfied in the case where the stress increment is finite. Here the inconsistency is avoided by employing the following procedure. A hardening rule specifies the direction of the translation of yield surface. Assume that the unit vector of this direction in the deviotoric plane is $\mathbf{n}^\alpha$, then the magnitude of the back stress increment can be expressed as,

$$\Delta\alpha=p\mathbf{n}^\alpha \qquad (21)$$

where p is the smaller positive root of the following quadratic polynomial equation with respect to p,

$$f(\mathbf{S}+\Delta\mathbf{S},\alpha+p\mathbf{n}^{\alpha}) = 0 \qquad (22)$$

where f represents the yielding surface, or a surface in the multiple surface model, which is in the form as Equation (8). Obviously, Equation (22) is the consistency condition that requires the incremented stress state to remain on the yield surface.

We note that, contrary to common presumptions, the number of surfaces used in Mroz or Garud rules will influence the directions of surface translation which will change the calculated results. This will be discussed later.

3. Analytical Results

Hahn and his colleages [5][12-15] have conducted a number of finite element elastic-plastic stress analyses of rolling line contact problems. Their results are reproduced here and compared with those obtained using Merwin-Johnson's method, McDowell-Moyar method, and the proposed method. All the results are summarized in Figures 4-7 Stresses and Hertzian pressure are normalized with respect to the yield shear stress, k. Plastic modulus is normalized with respect to elasticity modulus in shear, G. All distances are normalized with respect to a, the half width of the contact area.

In the comparisons shown in Figure 4 through Figure 7, FEM analyses [12-15], and the analytical approaches use the Prager-Ziegler hardening rule combined with a bilinear stress-strain relation. The residual stresses after the 11th passage of the load are taken to be the steady state for the Merwin-Johnson and the proposed methods. More passages of the load are usually necessary

to reach a steady state when McDowell-Moyar's method is used and 21st passage of the load is taken to be the steady state in this case. In Figure 4, results from Kumar et al.'s [14] FEM analyses are reproduced and compared with the analytical approaches. Both residual stresses in the rolling direction, $(\sigma_x)_r$, and the axial direction, $(\sigma_y)_r$, are shown. The material properties of a bearing steel are used, which has a yield strength in shear, k, of 606MPa and the plastic modulus, H, of 25.7G. The results depict the case of a driven wheel or the rail when a locomotive (driving) wheel is passing over.

Merwin-Johnson method underestimates the residual stress in the rolling (x) direction. In the first two cases in Figure 4, the locations of maximum residual stress in the rolling (x) direction is about 0.5a beneath the contact surface according to Merwin-Johnson's method while the FEM predicts the value to be about 1.0a. McDowell-Moyar's method requires that $(\sigma_x)_r=(\sigma_y)_r$. For all the three cases in Figure 4, according to McDowell-Moyar's method, the maximum residual stresses in both the rolling (x) and axial (y) directions are on the contact surface; while the FEM and the other two methods predict those maximum locations to be subsurface. We note that the apparent rapid changes in residual stress with McDowell-Moyar's method is not a numerical or a model problem, it is a consequence of overlapping residual stress fields from previous cycles. When the load is $p_0/k=6$, Figure 4(c), both Merwin-Johnson and McDowell -Moyar's predictions of residual stress in the rolling (x) direction display significant deviations in both magnitude and distribution pattern from the FEM results.

The proposed method provides good quantitative residual stress results in both the rolling (x) and the axial (y) directions compared with the FEM results. Moreover, the locations of the maximum residual stress and the size of the residual stress zone are predicted accurately. When the load is small, the residual stresses predicted by the proposed method are practically identical to the FEM results. When the load is $p_0/k=6$, the results from the

proposed method display deviations from the FEM results; nevertheless, the agreement is satisfactory.

To illustrate the capabilities of the proposed method further, we consider in Figure 5 two pure rolling cases with steady state residual stresses predicted by the FEM [13], Merwin-Johnson method, and the proposed method. Merwin-Johnson's method underestimates the residual stresses while the proposed method provides good agreement with the FEM results.

FEM results [15] using rail steel properties are illustrated in Figure 6. The yield stress in shear, k, is 139MPa and the plastic modulus, H, is 1.64G, where G is the elasticity modulus in shear. Merwin-Johnson's method predicts smaller residual stress in both the rolling (x) and axial (y) directions compared to FEM. The results from the proposed method are in good agreement with the FEM predictions of residual stresses in both the rolling (x) and the axial (y) directions. More comparisons are shown in Figure 7. The material properties of a similar steel are used, which has a yield stress in shear of 139MPa and a slightly lower plastic modulus of 1.3G. Similar conclusions can be drawn from those cases. Because in Reference [12] the residual stress in the axial (y) direction was not available, only the residual stresses in the rolling (x) direction are shown in Figure 7. Compared with the previous cases shown in Figure 2-4, the larger deviation between the result of the proposed method and that of the FEM results is due to the smaller plastic moduli used.

The following results, in Figures 8-10, are obtained from the proposed analytical approach using the two-surface plasticity model with 1070 steel properties. Shown in Figure 8 are the build-up of residual stresses and residual strains with repeated rolling passes. Pure rolling with $p_o/k=5$ is considered here. The steady state is taken to be that after the 11th passage of the load. It can be seen from Figure 8 that the residual stress in the rolling (x) direction and the residual stress in the axial (y) direction differ. In this case the residual stress in the rolling (x) direction (Figure 8(a)) on the

surface is zero while the residual stress in the axial (y) direction on the surface is slightly compressive (Figure 8(b)). Figure 8(c) shows the variation of the transient radial residual strain, $\Delta(\varepsilon_z)_r$. In the steady state, the increment of radial strain is nearly zero. Because at $p_0/k=5$, the shakedown limit is exceeded, there will be a cumulative surface displacement which is related to $\Delta(\gamma_{xz})_r$ as,

$$\delta=\int_0^{\infty} \Delta(\gamma_{xz})_r dz \tag{23}$$

where δ is the surface displacement rate. A positive δ implies a forward surface displacement and a negative δ corresponds to a backward surface displacement. In Figure 8(d), the steady state residual strain increment, $\Delta(\gamma_{xz})_r$, is much smaller than that of the first cycle. Because the plastic zone in contact problem is generally small, the upper limit in integration Equation (23) can be limited to approximately 3a.

The influence of the normal load on the variations of steady state residual stresses and residual strain is shown in Figure 9. Figure 9(a) shows the influence of the normal load on the residual stress in the rolling (x) direction, $(\sigma_x)_r$. Under the pure rolling condition the peak value of residual stress is located at z/a=0.7-1.0 depending on the p_o/k ratio. It is clear that under pure rolling the residual stress in the rolling (x) direction is compressive below the contact surface and zero on the contact surface.

The influence of the normal load on the residual stresses in axial (y) direction is shown in Figure 9(b). The location of the peak value of the residual stress in the axial (y) direction, $(\sigma_y)_r$, is about z/a=0.6 and is independent of the p_o/k ratio. When the normal load is $p_o/k=4.0$, the axial residual stress, $(\sigma_y)_r$, is zero on the surface. When the normal load is larger, the axial residual stress, $(\sigma_y)_r$, is compressive on the surface. At small p_o/k ratios under pure rolling,

residual stress in the axial (y) direction, $(\sigma_y)_r$, is slightly smaller than that in the rolling direction, $(\sigma_x)_r$. When the p_o/k ratio becomes large, residual stress in axial direction, $(\sigma_y)_r$, is larger than that in the rolling direction, $(\sigma_x)_r$.

Figure 9(c) shows the influence of normal load on the residual shear strain rate, $\Delta(\gamma_{xz})_r$. At $p_o/k=4.0$, there is no cumulative residual strain accumulation, which is in agreement with Johnson's shakedown prediction [23]. Under pure rolling, the residual shear strain, $\Delta(\gamma_{xz})_r$, is always positive, which corresponds to a forward surface flow according to Equation (23).

The influence of tangential force on the steady state residual stresses and residual shear strain rate are shown in Figure 10. The normal load, p_o/k, is taken to be 4.5 and the tangential force, Q/P, changes from -0.2 to +0.2. A positive Q/P ratio corresponds to the loading situation in a driving wheel (or a wheel undergoing braking) and a negative Q/P ratio simulates a driven wheel.

The tangential force has an influence on residual stresses in both axial and rolling directions, but this influence is small as compared with the influence of the normal load. A significant result is that, except in the very thin layer of about 0.2a-0.3a, the tangential force has no practical influence on the depth of the residual stress zone size. When the normal load is the same, Figure 10(a) and Figure 10(b) show that a negative tangential force creates larger residual stresses than a positive tangential force with the same magnitude does, though the differences are not very significant.

The influence of the tangential force on the residual shear strain rate is shown in Figure 10(c). Both negative and positive residual shear strain rates depend on the Q/P ratio. The residual shear strain rate is always positive, which corresponds to a forward surface displacement rate, when Q/P is zero (pure rolling) or negative (driven wheel). When Q/P ratio is larger than a positive

value, the residual shear strain rate becomes negative, which will result in a backward surface displacement rate according to Equation (23). Note the different dimensions used in Figure 9(c) and Figure 10(c) for the residual shear strain rate, $\Delta(\gamma_{xz})_r$. In Figure 10(c), a negative Q/P ratio will create a larger residual shear strain rate compared to the positive Q/P ratio. Because the residual shear strain rate, $\Delta(\gamma_{xz})_r$, is a measure of plastic deformation, a driven wheel is predicted to be inferior in fatigue life to a driving wheel. This prediction is in agreement with the experimental observations [24].

In order to visualize the plastic deformation predicted by the proposed method, a deformed mesh is plotted with the undeformed mesh background in Figure 11 for $p_0/k=4.5$ and three Q/P ratios 0.1, 0., and -0.1. The deformed dimensions are magnified by the same factor. When Q/P=0.1, the surface displacement is opposite to the rolling direction, i.e., backward surface displacement. When Q/P=0 and Q/P=-0.1, the surface displacements are in the rolling direction, i.e., forward displacement. The predicted deformations shown in Figure 11 are qualitatively in agreement with the experimental observations [3][24].

The prediction of the steady state surface displacement rate predicted by the proposed method for 1070 steel is shown in Figure 12. Figure 12 shows that under pure rolling the surface displacement rate is relatively small compared with that due to rolling with a tangential force. A driving wheel or a wheel in braking will have a backward surface displacement; and a driven wheel will have a forward surface displacement. Under pure rolling there will be a forward surface displacement.

The surface displacement rate results predicted by Merwin-Johnson's method, McDowell-Moyar's method, and the proposed method are compared in Figure 13. The same direction of the displacement is predicted with Merwin-Johnson method and the proposed method; however, the proposed method predicts a larger

surface displacement rate. At the same Q/P values both the Merwin-Johnson and the proposed method predict that a driven wheel experiences greater surface displacement rate than the driving wheel. McDowell-Moyar model predicts the opposite trend. All three models predict similar trends for the pure rolling case.

Figure 14 shows the influence of plasticity theories on residual stresses and strains. The three models used are the Prager-Ziegler kinematic hardening, Mroz type hardening rule using two surfaces, and Garud hardening rule using multiple surfaces. The differences between the results predicted by the Prager-Ziegler kinematic hardening and by the two surface model are not significant; however results obtained using Garud multiple surfaces hardening rule display significant deviations. To illustrate this, consider the loading path in the deviatoric space under pure rolling. Shown in Figures 15 and 16, at point z/a=0.35 the $(J_2)^{1/2}$ is nearly constant between points A and point B. The individual stress components change between A and B, but the stress point remains on the yield surface. Whether elastic unloading or elastic-plastic loading occurs between B and C depends on the direction of the stress tensor and the location of the yield surface in stress space. In Figure 15, two possible positions of the yield surface are indicated. Point A in Figure 15 and Figure 16 represents the first yielding point, which is common to both yield surfaces. When the loading path reaches point B, the yield surface 1, which is obtained according to one hardening rule, and yield surface 2, which is obtained according to another hardening rule, occupy the positions shown in Figure 16. After point B, the material unloads elastically for yield surface 2, but elastic-plastic loading occurs for yield surface 1. For the first yield surface, the elastic-plastic loading will continue until point C. Clearly, there will be larger plastic deformation corresponding to yield surface 1 than yield surface 2, and the resulting residual stresses would differ for the two cases.

4. Discussion of Results

The FEM results, Figures 4 through 7, show that (i) the residual stress magnitudes decrease with increasing plastic modulus, and (ii) the residual stress in the rolling (x) direction differs from the residual stress in the axial (y) direction. The residual stress in the axial (y) direction is always compressive or zero for all the cases presented in Figure 4 through Figure 7. When the plastic modulus is large and the normal load is small such as in the first two cases in Figure 4 and the case in Figure 5(b), the residual stress in the rolling (x) direction on the surface is approximately zero; while the residual stress in the axial (y) direction on the surface is compressive. When the normal load is large and a tangential force is applied, as the case shown in Figure 4(c), there will be a thin layer beneath and including the contact surface where the residual stress is tensile in the rolling (x) direction and compressive in the axial (y) direction. As shown in Figure 4 the residual stress results from McDowell-Moyar's method, especially in the rolling direction, differs from the FEM predictions both in the distribution pattern and the size of the residual stress zone.

The FEM results show that the material properties used have a profound influence on the residual stresses predicted. Therefore, the material properties used in the FEM analyses and the analytical methods must be similar for a fair comparison. The movement of the yield surface has a significant influence on the residual stress and strain results. The Prager-Ziegler type translation rules and the Mroz or Garud translation rules produce different results under highly non-proportional loading paths which is not detected in simple loading cases.

Meshes fine enough to reveal the desired gradients may require excessive computational time. The finite element analysis conducted by Bhargava et al. [12-15] considered the state after the second passage of the load as the steady state. This may not be consistent

with the experimental observations. The number of passes of the load after which the stress state reaches steady state is dependent on the material behavior. As mentioned earlier, the use of plasticity models suitable for non-proportional loading is desired in FEM analyses.

Naturally, there will be differences between the results predicted by the proposed method and the residual stresses measured in wheel/rails. These include the differences between actual contact patches and the idealized contact used. The actual contact load distribution is three dimensional and is idealized as plane strain. In the contact between rail and wheel, normal load and the tangential force distributions are more complex than those used in computational and analytical models.

The proposed theory is limited to small plastic deformations because only under small plastic deformations the stresses in the plastic zone can be approximated by elastic solutions. The agreement of the plastic zone sizes obtained from the proposed method and FEM is excellent. These agreements in Figure 4 through Figure 7 provide strong positive support for the proposed model. In view of the high cycle fatigue (HCF) problems in contact loading, where plastic strains are small, the proposed method will find applicability.

We illustrated the influence of the translation rule on the subsequent unloading or reloading behaviour with a simple example. The precise form of the translation rule has a major effect on residual stresses, and in view of many rolling cycles the deviation of results, depending on the translation rule, is expected to increase. Intersection of yield surfaces when multiple surfaces are used, the apparent violation of consistency condition, and the discontinuities in translation direction for certain non-proportional paths are three fundamental problems encountered in implementing plasticity theorems. Many of these problems are never encountered in paths considered in laboratory testing. We paid special attention to

circumvent these difficulties, but a word of caution needs to be made for future researchers.

The results indicate that residual stress state in the vicinity of the contact is triaxial, displaying compressive hydrostatic stresses exceeding the monotonic strength of the material. Moreover, the loading is non-proportional, i.e., the directions of the principal stresses rotate during a rolling cycle, exposing a large number of material planes to extreme stress ranges. It is possible to impose the contact induced stress states on laboratory specimens with a specialized high pressure experimental set up. These proposed experiments (currently being set up), along with the analytical methods of stress determination examined here, will allow development of realistic contact fatigue models.

5. Conclusions

1. Based on the assumption of elastic stresses and the employment of a stress and strain relaxation procedure, an analytical approach has been developed for approximate determination of residual stresses and strains in rolling contact problems. For line contact problems, the proposed method provides residual stress results comparable to the finite element method predictions. The agreement with FEM is superior compared to Merwin-Johnson and McDowell-Moyar analytical models.

2. When calculating the residual stress/strain for line contact with the proposed method, the results obtained using the kinematic hardening rule differ somewhat from those obtained using the two surface model; however results obtained using Garud's hardening rule deviated significantly from the other two models.

3. The proposed method predicts that a driven wheel experiences greater plastic deformation than the driving wheel does, therefore

the driven wheel is inferior to the driving wheel in fatigue life. This prediction agrees with the experimental observations.

4. Tangential force mainly influences the residual stresses in the 0.3a thick layer beneath the contact surface, and has little influence on the residual stresses beyond this thin layer. It is the normal load that primarily determines the subsurface residual stresses and the size of the subsurface plastic zone.

5. Under pure rolling (Q/P=0) the residual shear strain rate, $\Delta(\gamma_{xz})_r$, which determines the cumulative surface displacement rate, is relatively small. It is the tangential force that has significant influence on the surface displacement rate.

6. Acknowledgements

This research was supported by Association of American Railroads, Technical Center, Chicago, Illinois. The cooperation of Dr. Dan Stone, Executive Director and Mr.Michael Fec, Senior Engineer, of AAR is appreciated. Stimulating discussions were held with Dr. Gerald Moyar, Moyar Technical Services and Dr. Roger Steele, AAR. Mr.Mark Balzer aided in preparation of the manuscript.

7. References

1. Merwin, J.E. and Johnson, K.L., "An Analysis of Plastic Deformation in Rolling Contact", Proc.Inst.Mech.Engrs., Vol.177, No.25, 1963, pp.676-685

2. Johnson, K.L. and Jefferis, M.A., "Plastic Flow and Residual Stresses in Rolling and Sliding Contact", Proceedings of the Smposium on Fatigue in Rolling Contact, March 1963, Paper5, pp.54-65

3. Hamilton, G.M., "Plastic Flow in Rollers Loaded above the Yield Point", Proc Instn Mech Engrs, Vol.177, No.25, 1963, pp.667-675

4. Hearle, A.D. and Johnson, K.L., "Cumulative Plastic Flow in Rolling and Sliding Line Contact", J.Applied Mechanics, Vol.54, March 1987, pp.1-7

5. Bhagava, V., Hahn, G.T., and Rubin, C.A., "An Elastic-Plastic Finite Element Model of Rolling Contact. Part I: Single Contacts, Part II: Repeated Contacts", J. Applied Mechanics, Trans. ASME, Vol.52, 1983, pp.66-74, pp.75-82

6. Bower, A.F. and Johnson, K.L., "The Influence of Strain Hardening on Cumulative Plastic Deformation in Rolling and Sliding Line Contact", J.Mech.Phys.Solids, Vol.37, No.4, 1989, pp.471-493

7. Bower, A.F. and Johnson, K.L., "Plastic Flow and Shakedown of the Rail Surface in Repeated Wheel-Rail Contact", 3rd Inter. Symp. on Contact Mechanics and Wear of Rail/Wheel Systems, Cambridge, U.K., June 1990

8. Bower, A.F., "Cyclic Hardening Properties of Hard-Drawn Copper and Rail Steel", J.Mech.Phys.Solids, Vol.37, No.4, 1989, pp.455-470

9. Bower, A.F., "Some Aspects of Plastic Flow, Residual Stress and Fatigue Cracks due to Rolling and Sliding Contact", Ph.D Dissertation, Emmanuel College, University of Cambridge, Nov.1987

10. McDowell, D.L. and Moyar, G.J., "A More Realistic Model of Nonlinear Material Response--Application to Elastic-Plastic Rolling Contact", 2nd Inter. Symp. on Contact Mechanics and Wear of Rail/Wheel Systems, U. Rhode Island, Kingston, RI, July 1986

11 McDowell, D.L. and Moyar, G.J., "Parametric Study of Cyclic Plastic Deformation in Rolling and Sliding Line Contact with Realistic Nonlinear Material Behavior", 3rd Inter. Symp. on Contact Mechanics and Wear of Rail/Wheel Systems, Cambridge, U.K., June 1990

12. Bhagava, V., Hahn, G.T., Ham, G., Kulkarni, S., and Rubin, C.A., "Influence of Kinematic Hardening on Rolling Contact Deformation", 2nd Inter. Symp. on Contact Mechanics and Wear of Rail/Wheel Systems, Cambridge, U.K., July 1986

13. Hahn, G.T., Bhargava, V., Rubin, C.A., Chen, Q., and Kim, K., "Analysis of the Rolling Contact Residual Stresses and Cyclic plastic Deformation of SAE52100 Steel Ball Bearings", Journal of Tribology, Trans. ASME, Vol.109, Oct.1987, pp.618-626

14. Kumar, A.M., Hahn, G.T., Bhargava, V., and Rubin, C, "Elasto-Plastic Finite Analyses of Two-Dimensional Rolling and Sliding Contact Deformation of Bearing Steel", Journal of Tribology, Trans ASME, Vol.111, April 1989, pp.309-314

15. Ham, G.L., Hahn, G.T., Rubin, C.A., and Bhargava, V. , "Finite Element Analysis of the Influence of Kinematic Hardening in Two-Dimensional, Repeated, Rolling-Sliding Contact", Tribology Transactions, Vol.32, No.3, 1989, pp.311-316

16. Smith, J.O. and Liu, C.K., " Stresses due to Tangential and Normal Loads on an Elastic Solid with Application to Some Contact Stress Problems", Journal Applied Mechanics, Vol.20, June 1953, pp.157-166

17. Sehitoglu, H. and Jiang, Y. Roger, "Cyclic Stresses for Contact with Different Tangential Load Distributions", Report No.2 Prepared for Association of American Railroads, March, 1991

18. Mroz, Z., "On the Description of Anisotropic Workhardening", J.of the Mech. and Phy. of Solids, Vol.15, No.3, May 1967, pp.163-175

19. Mroz, Z., "An Attempt to Describe the Behavior of Metals under Cyclic Loads Using a More General Workhardening Model", Acta Mechanica, Vol.7, No.2-3, 1969, pp.199-212

20. Drucker, D.C. and Palgen, L., "On Stress-Strain Relations Suitable for Cyclic and Other Loading", Journal of Applied Mechanics, Trans.ASME, Vol.48, Sept.,1981, pp.479-485

21. Garud, Y.S., "Multiaxial Fatigue of Metals", Ph.D Dissertation, Mechanical Engineering, Stanford University, April 1981

22. Garud, Y.S., "A New Approach to the Evaluation of Fatigue under Multiaxial Loadings", Journal of Engineering Materials and Technology, Trans ASME, Vol.103, April 1981, pp.118-125

23. Johnson, K.L., "A Shakedown Limit in Rolling Contact", Proceedings, 4th US National Congress of Applied Mechanics, Berkeley, 1962

24. Shima, Masayuki, and Okada, Kazumi, " Measurements of Subsurface Plastic Flow in Rolling Contact", Journal of JSLE Int. Ed., No,2, April 1981, pp.75-80

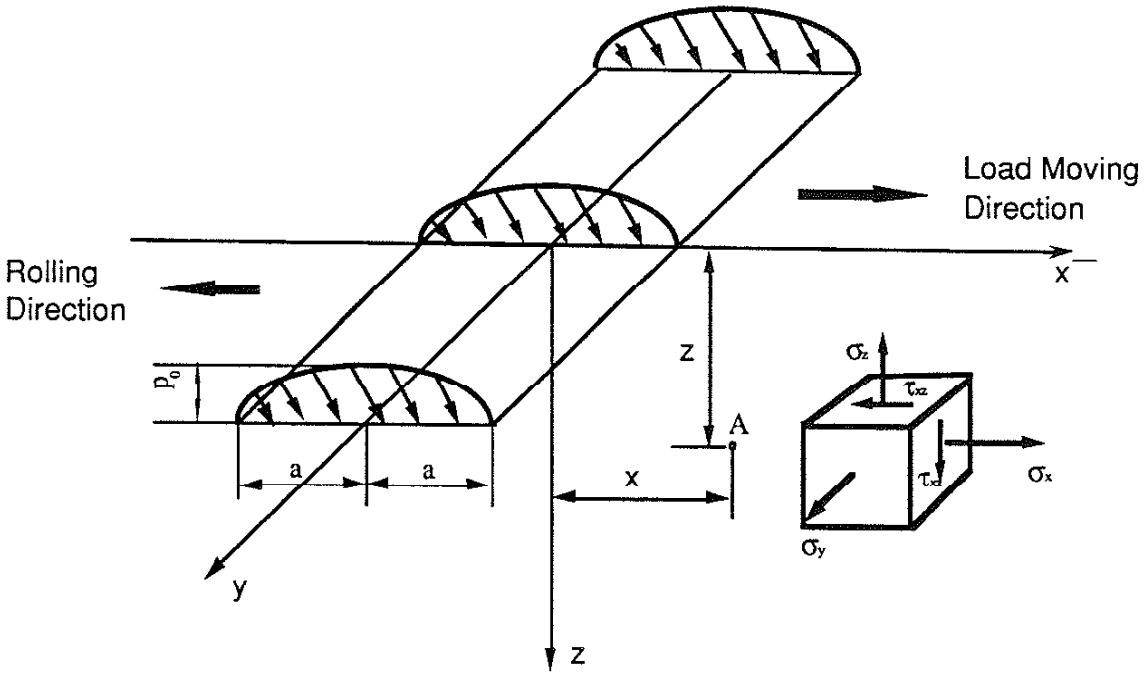

Fig.1 Line Contact, Coordinate System, and Orthogonal Stresses
(Note that the Coordinate System Moves with the Load)

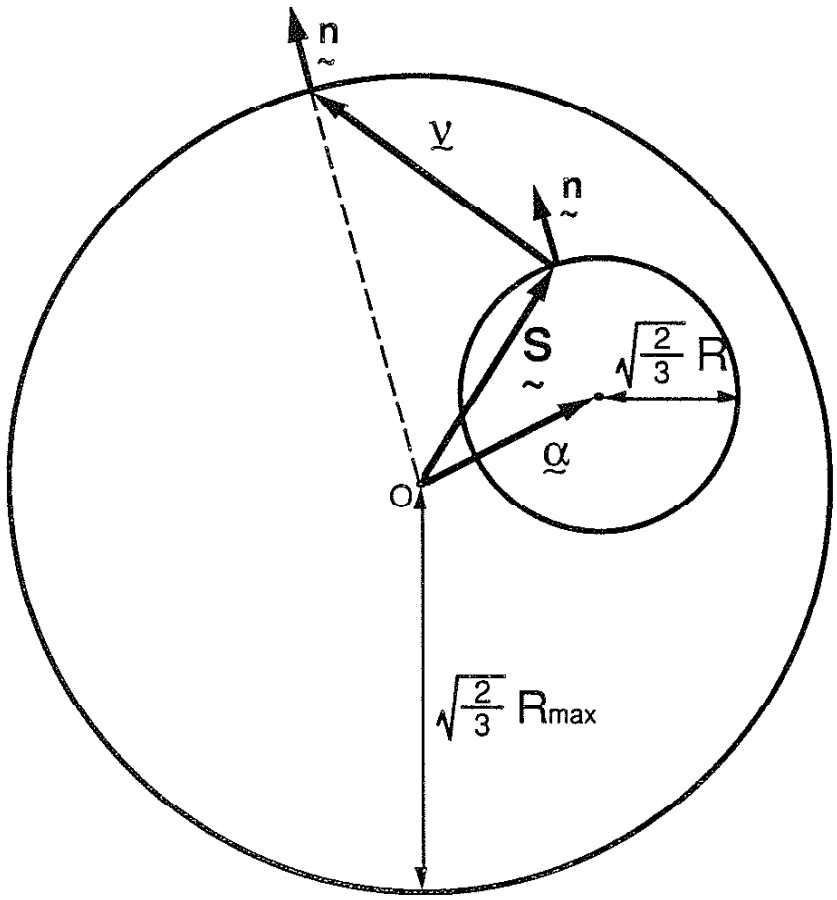

Fig.2 Yield and Bounding Surfaces in Deviatoric Stress Space

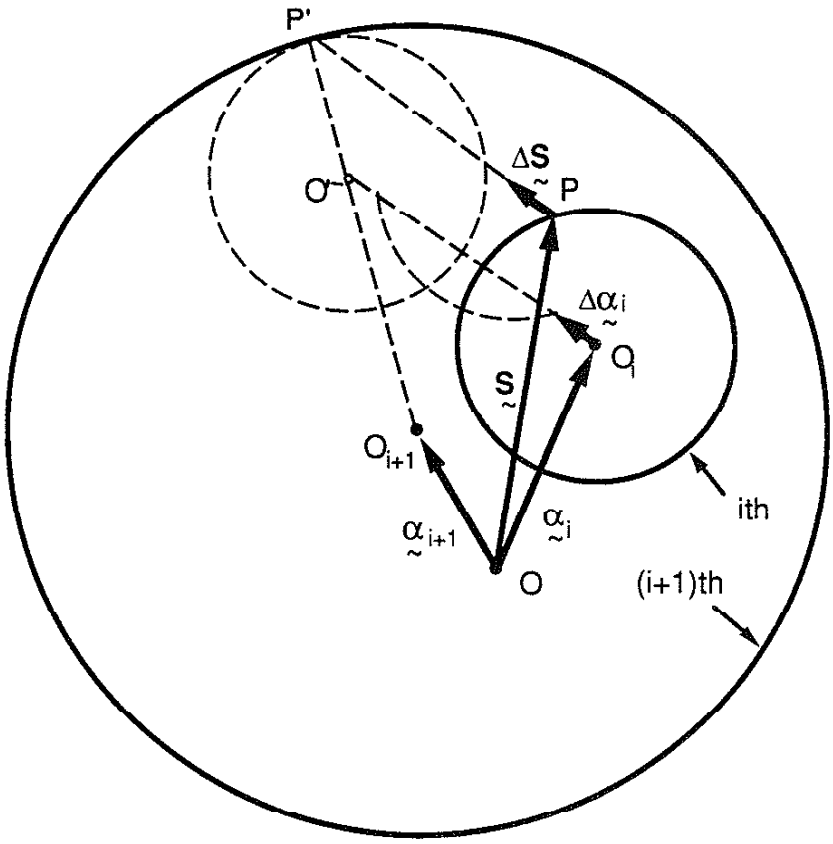

Fig.3 Schematic of Garud Hardening Rule

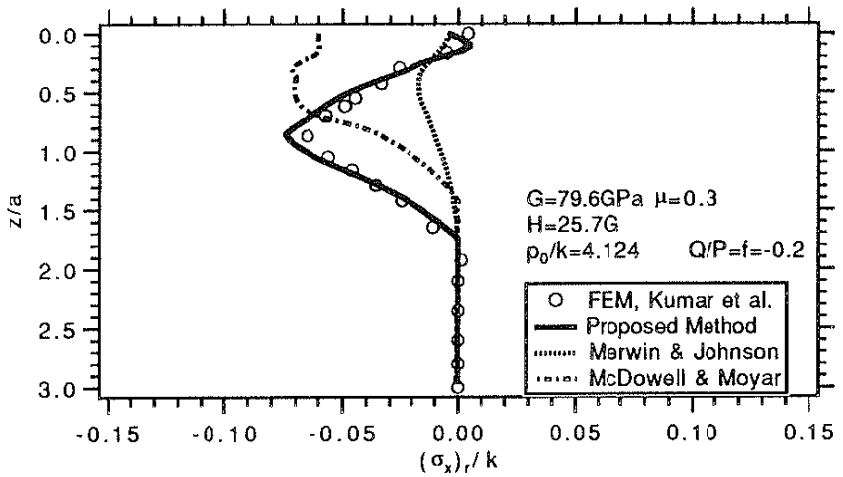

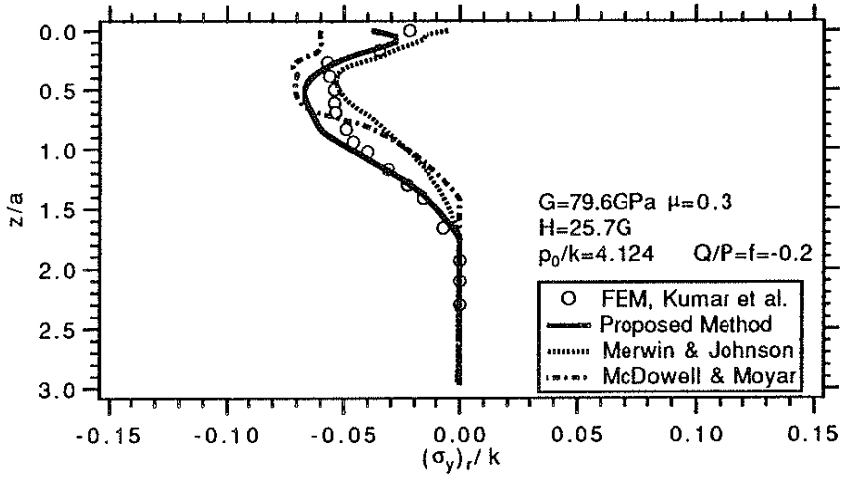

(a) Case I: p_0/k=4.124 Q/P=-0.2 H=25.7G

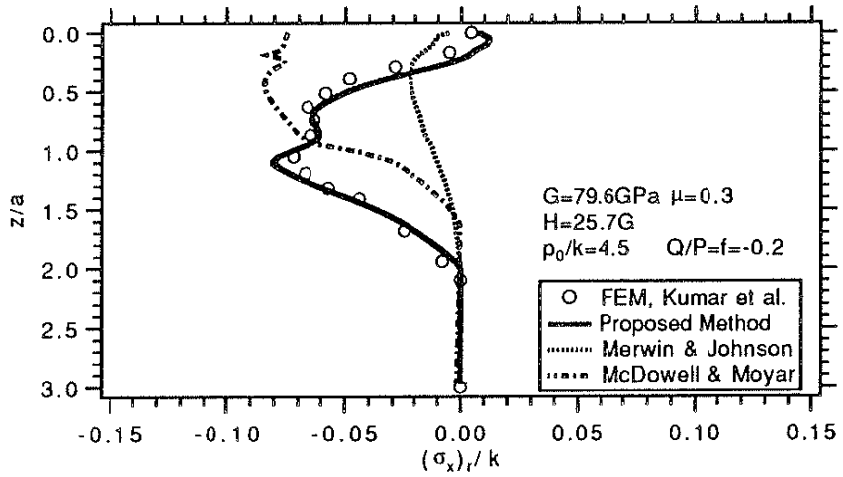

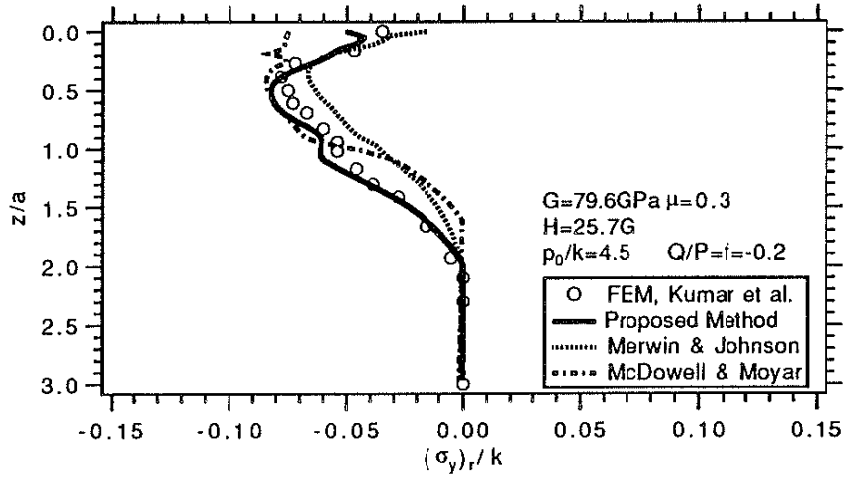

(b) Case II: p_0/k=4.5 Q/P=-0.2 H=25.7G

Fig.4 Variations of Steady State Residual Stresses $(\sigma_x)_r$ and $(\sigma_y)_r$ Predicted by Different Approaches

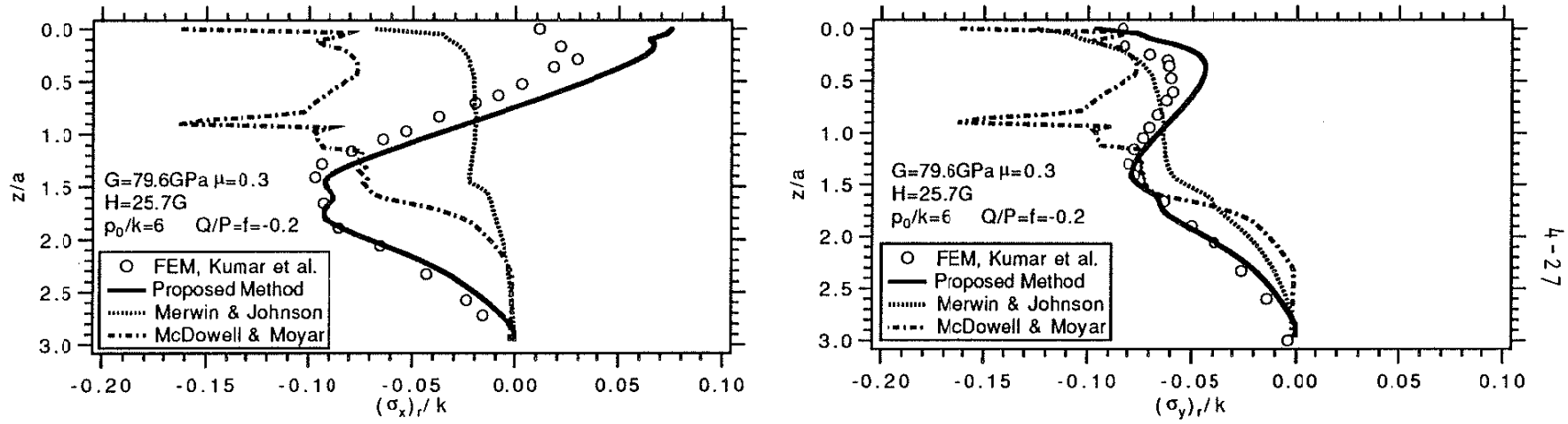

(c) Case III: $p_0/k=6$ Q/P=-0.2 H=25.7G

Fig.4 (con't) Variations of Steady State Residual Stresses $(\sigma_x)_r$ and $(\sigma_y)_r$ Predicted by Different Approaches

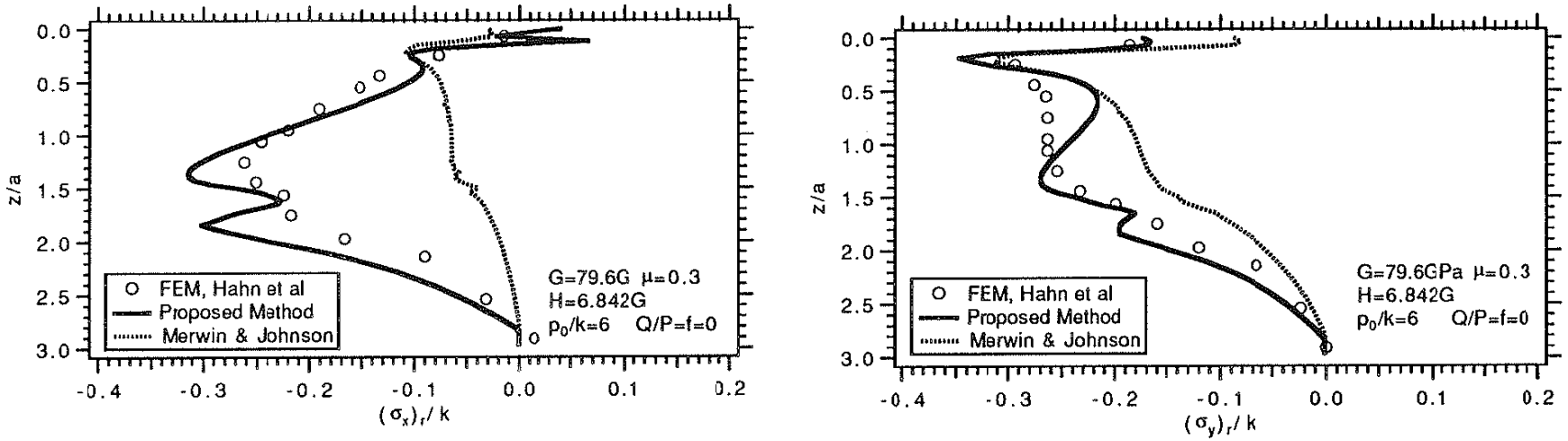

(a) Case I: Pure Rolling p_0/k=6, H=6.84G

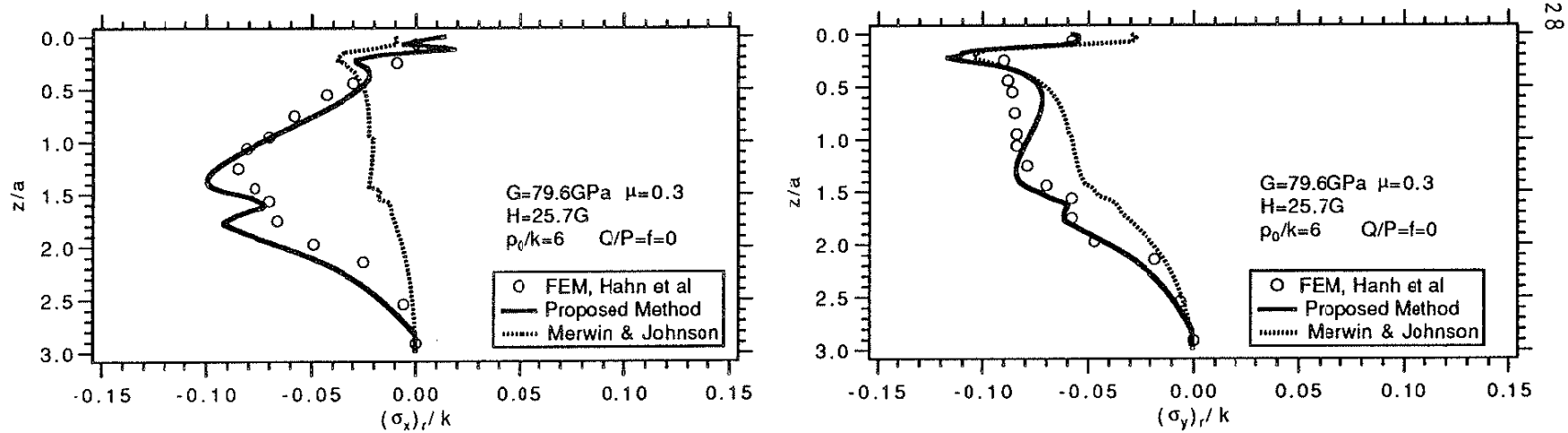

(b) Case II: Pure Rolling p_0/k=6, H=25.7G

Fig.5 Variations of Steady State Residual Stresses $(\sigma_x)_r$ and $(\sigma_y)_r$ Predicted by Different Approaches

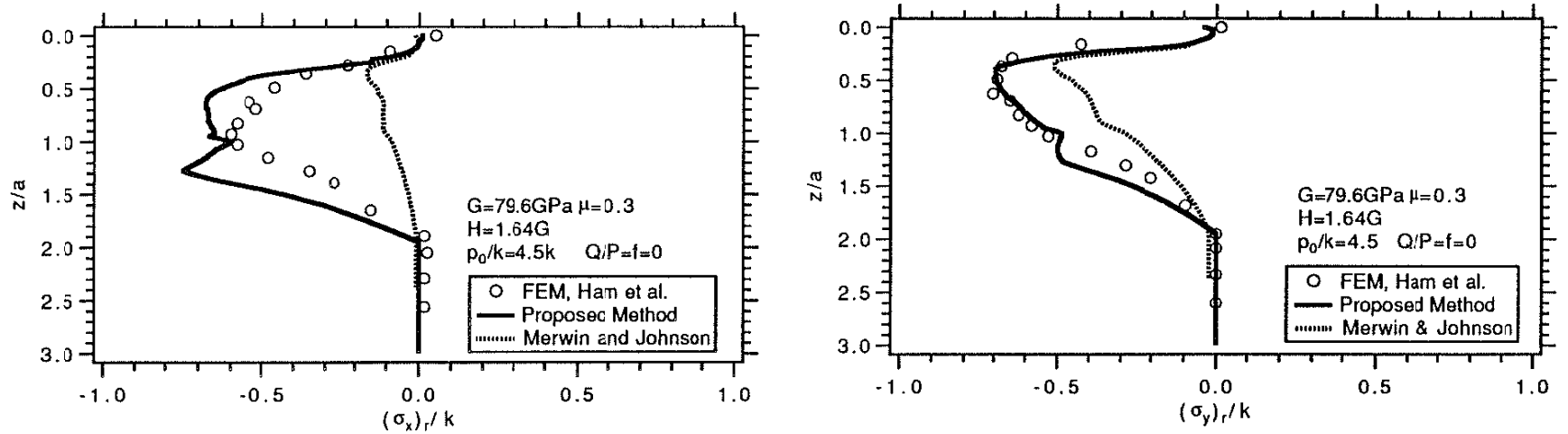

(a) Case I: Pure Rolling p_0/k=4.5 H=1.64G

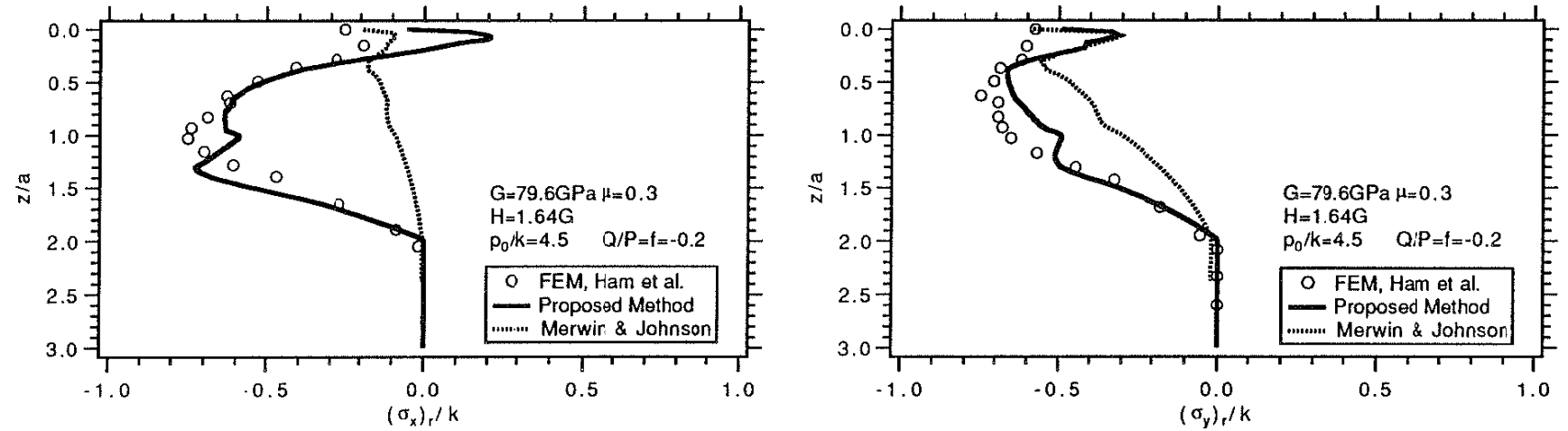

(b) Case II: p_0/k=4.5 Q/P=f=-0.2 H=1.64

Fig.6 Variations of Steady State Residual Stresses $(\sigma_x)_r$ and $(\sigma_y)_r$ Predicted by Different Approaches

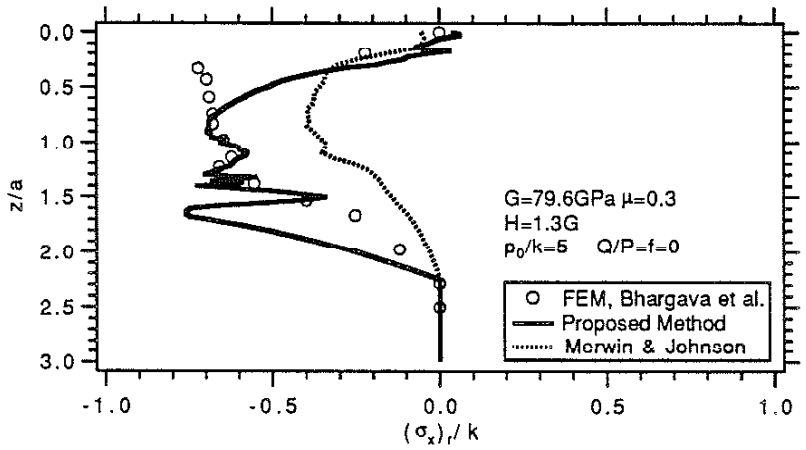

(a) Case I: p_0=5k Q/P=0 H=1.3G

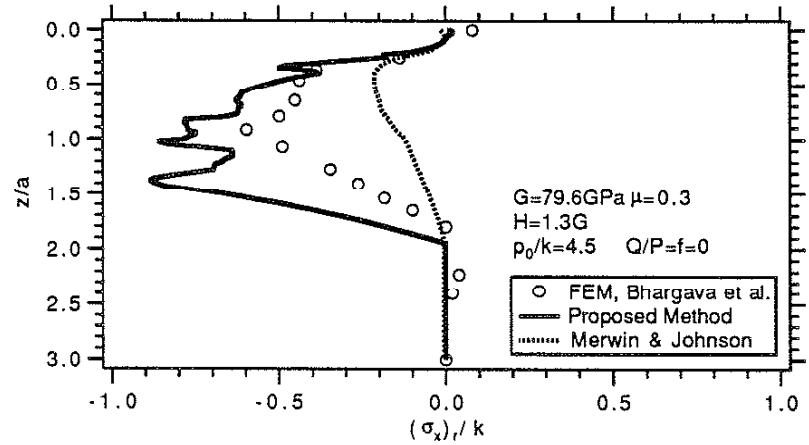

(b) Case II: p_0=4.5k Q/P=0 H=1.3G

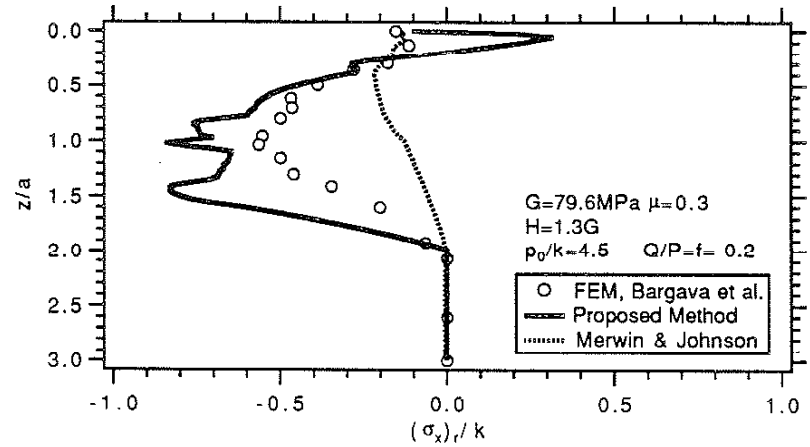

(c) Case III: p_0=4.5k Q/P=f=-0.2 H=1.3G

Fig.7 Variations of Steady State Residual Stress $(\sigma_x)_r$ Predicted by Different Approaches

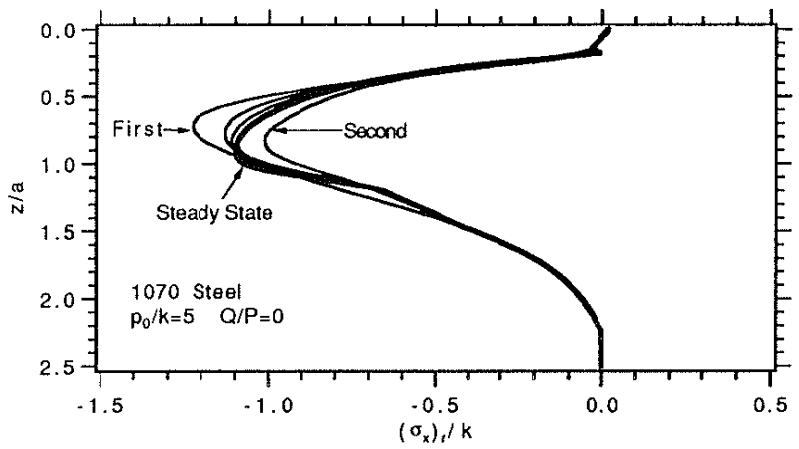

(a) Residual Stress $(\sigma_x)_r$

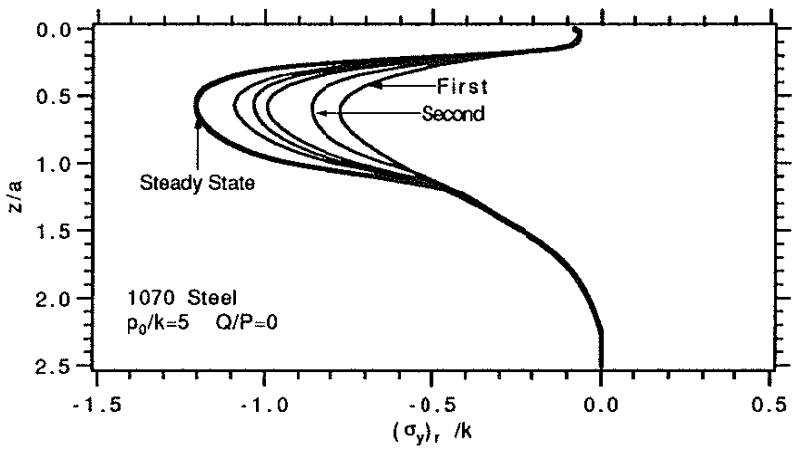

(b) Residual Stress $(\sigma_y)_r$

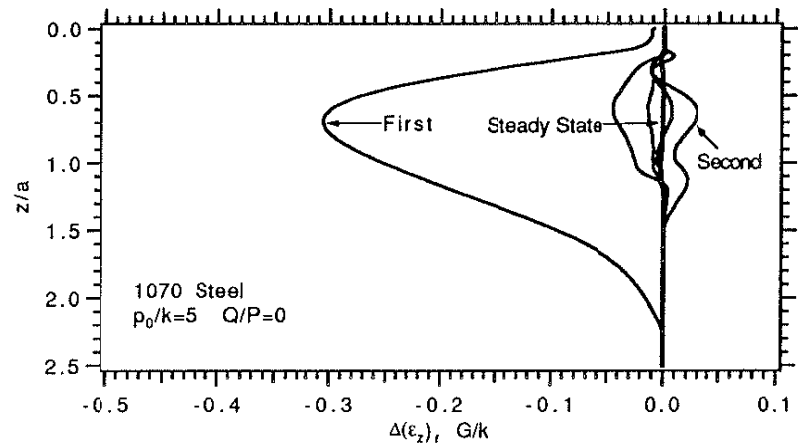

(c) Residual Strain $\Delta(\varepsilon_y)_r$

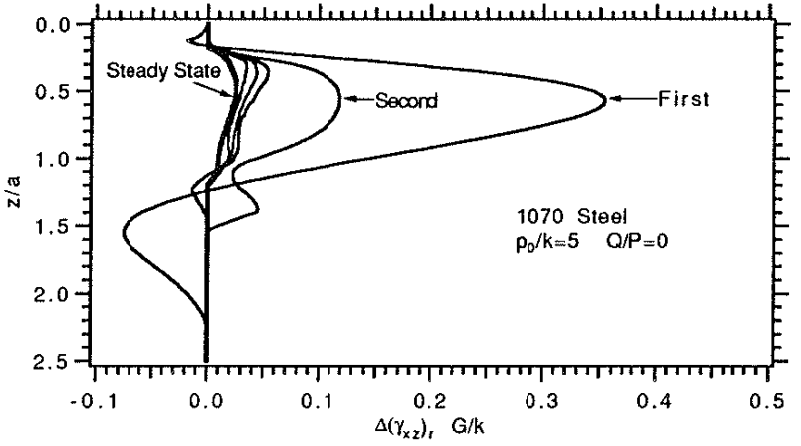

(d) Residual Strain $\Delta(\gamma_{xz})_r$

Fig. 8 Build-up of Residual Stresses and Residual Strains with Repeated Passages of Load

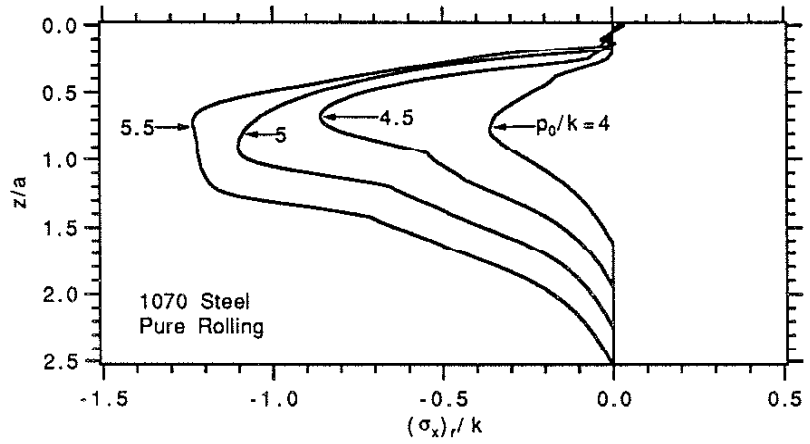

(a) Variation of Residual Stress $(\sigma_x)_r$

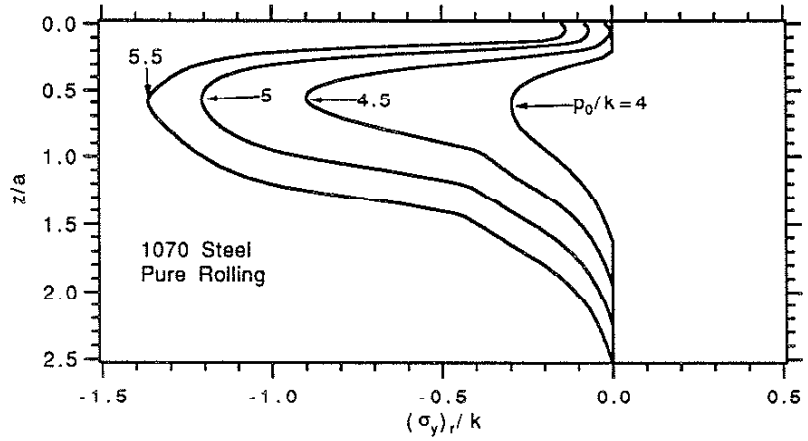

(b) Variation of Residual Stress $(\sigma_y)_r$

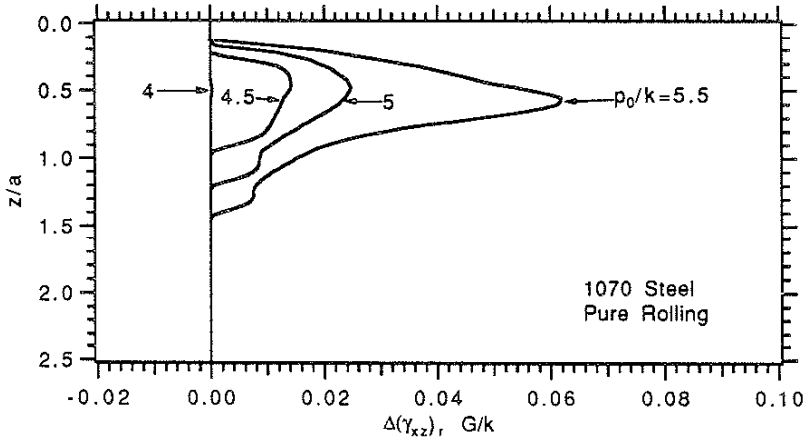

(c) Variation of Residual Shear Strain Rate $\Delta(\gamma_{xz})_r$

Fig.9 Influence of Normal Load on the Variations of Steady State Residual Stresses and Residual Shear Strain Rate

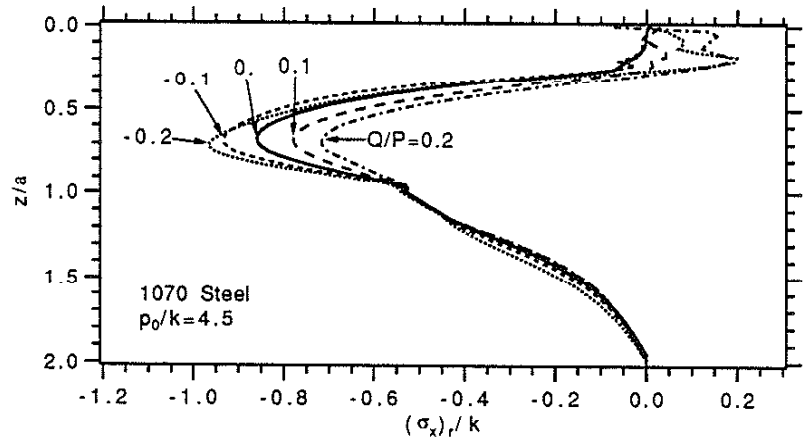

(a) Variation of Residual Stress $(\sigma_x)_r$

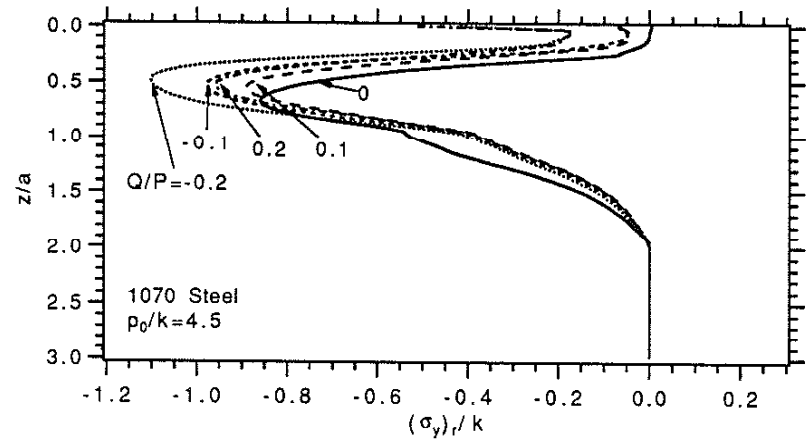

(b) Variation of Residual Stress $(\sigma_y)_r$

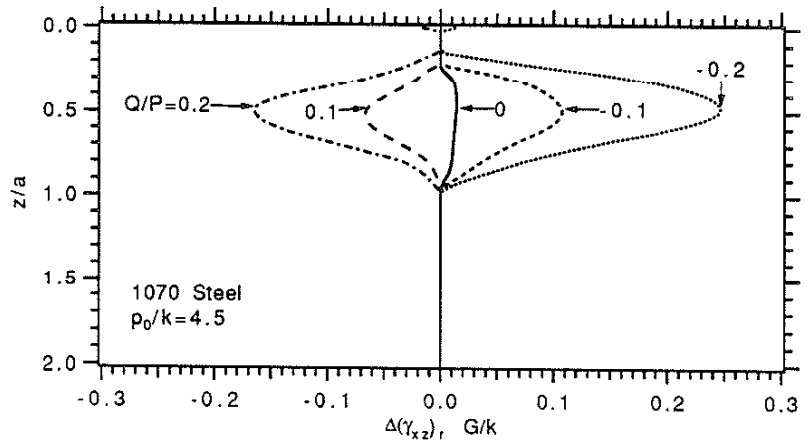

(c) Variation of Residual Shear Strain Rate $\Delta(\gamma_{xz})_r$

Fig.10 Variations of Steady State Residual Stresses and Residual Shear Strain Rate with Tangnetial Load when $p_0/k=4.5$

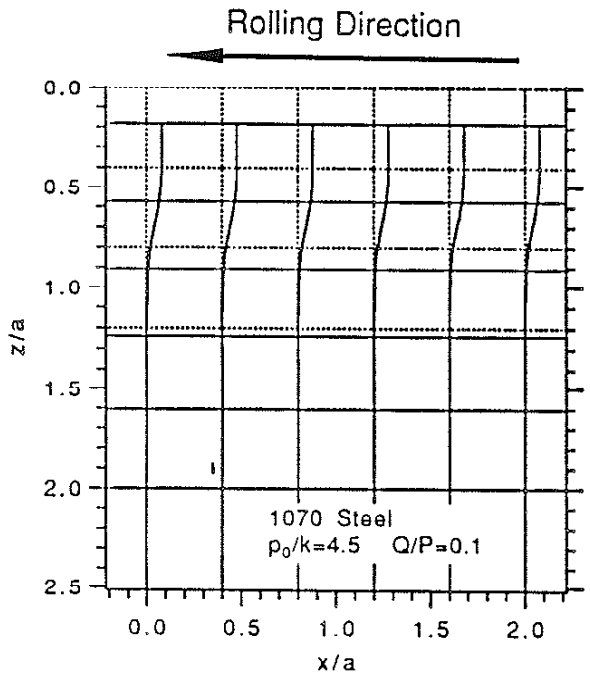

(a) p_0/k=4.5 Q/P=0.1

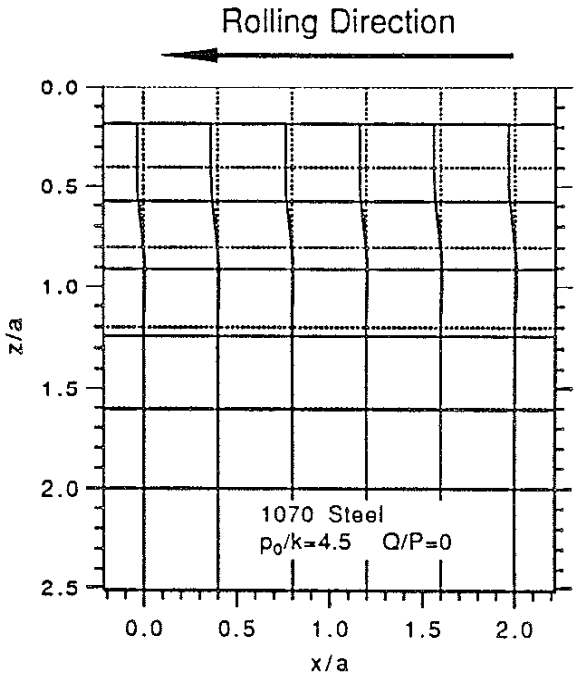

(b) p_0/k=4.5 Q/P=0.

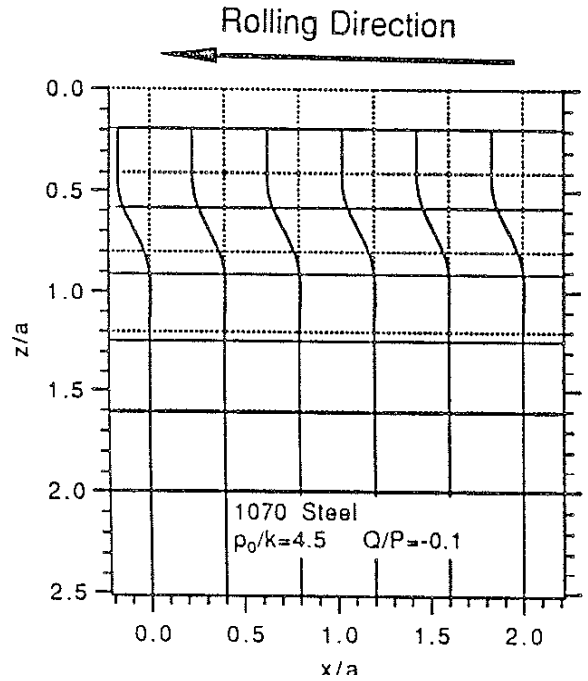

(c) p_0/k=4.5 Q/P=-0.1

Fig.11 Deformed Mesh Predicted by the Proposed Method for 1070 Steel at p_0/k=4.5 with Different Q/P Ratios

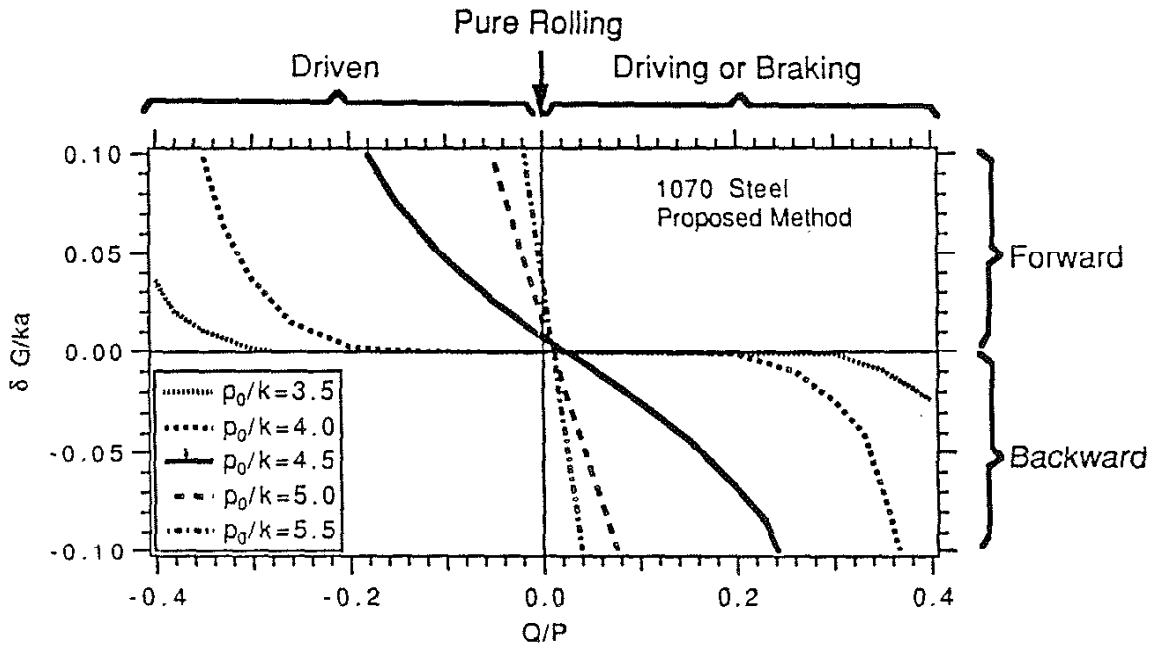

Fig.12 Relative Cyclic Surface Displacement per Passage of Load versus Q/P and p_0/k Ratios

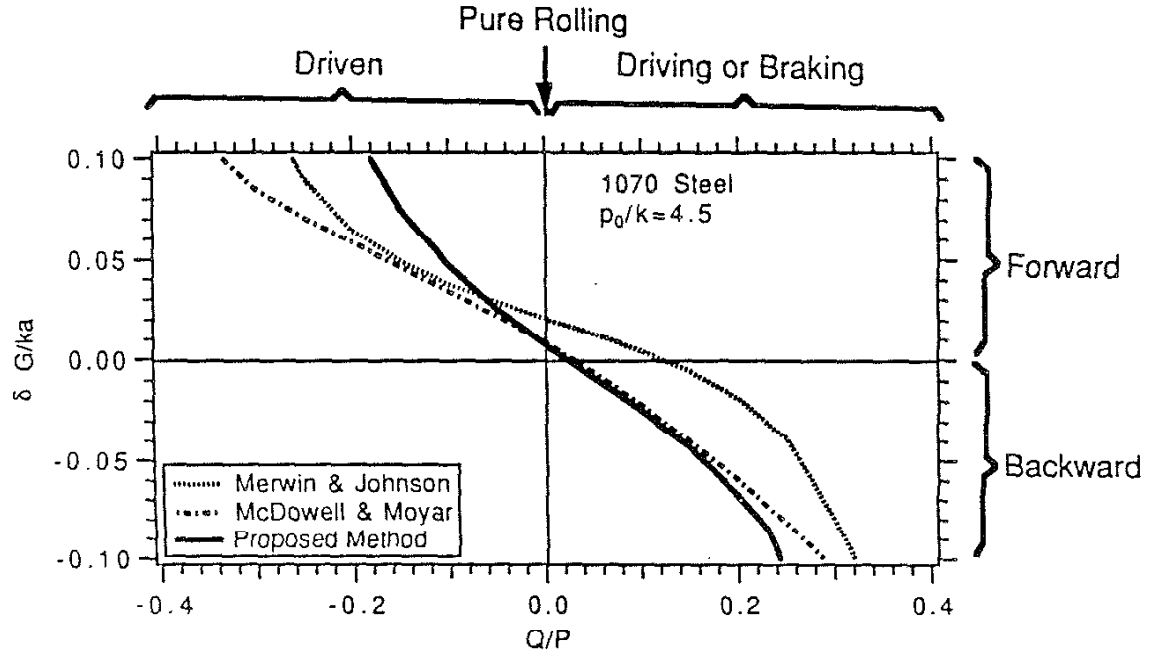

Fig.13 Comparison of the Relative Surface Displacement per Passage of Load Predicted by Different Approaches (1070 Steel $p_0/k=4.5$)

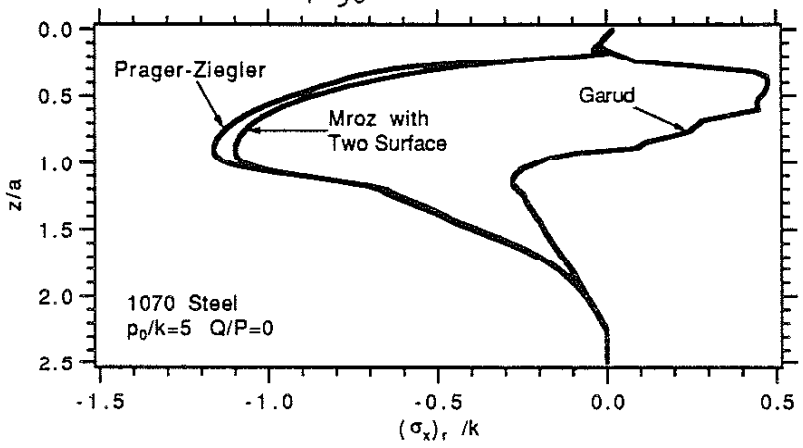

(a) Residual Stress $(\sigma_x)_r$

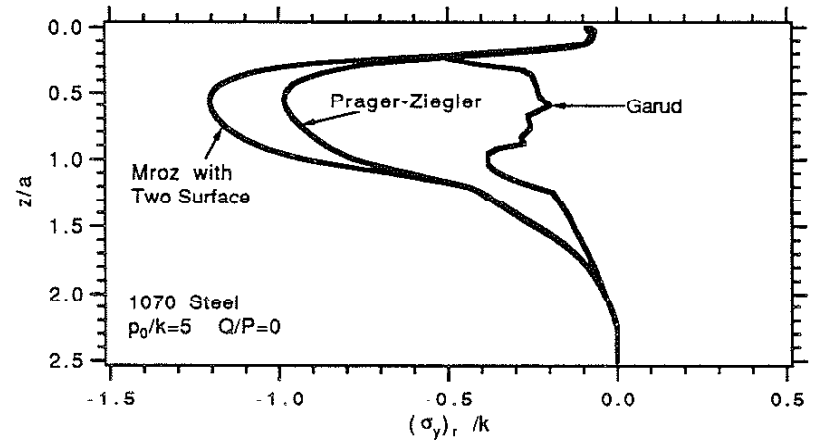

(b) Residual Stress $(\sigma_y)_r$

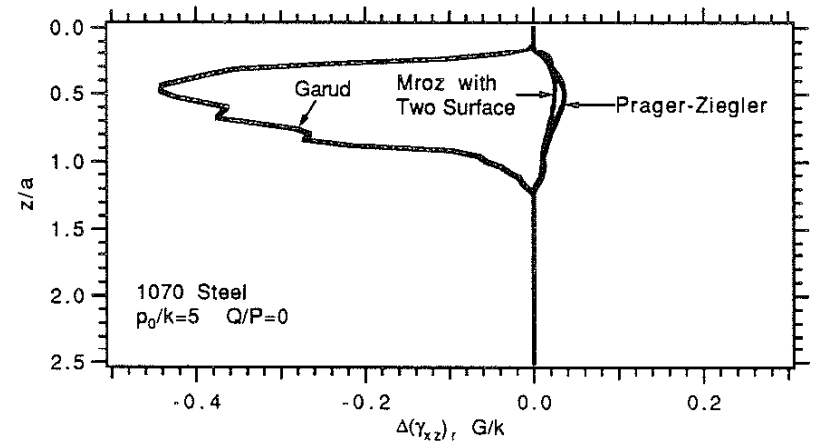

(c) Residual Shaer Strain Rate $\Delta(\gamma_{xz})_r$

Fig.14 Influence of Plasticity Theories on the Analytical Results of Residual Stresses and Strain

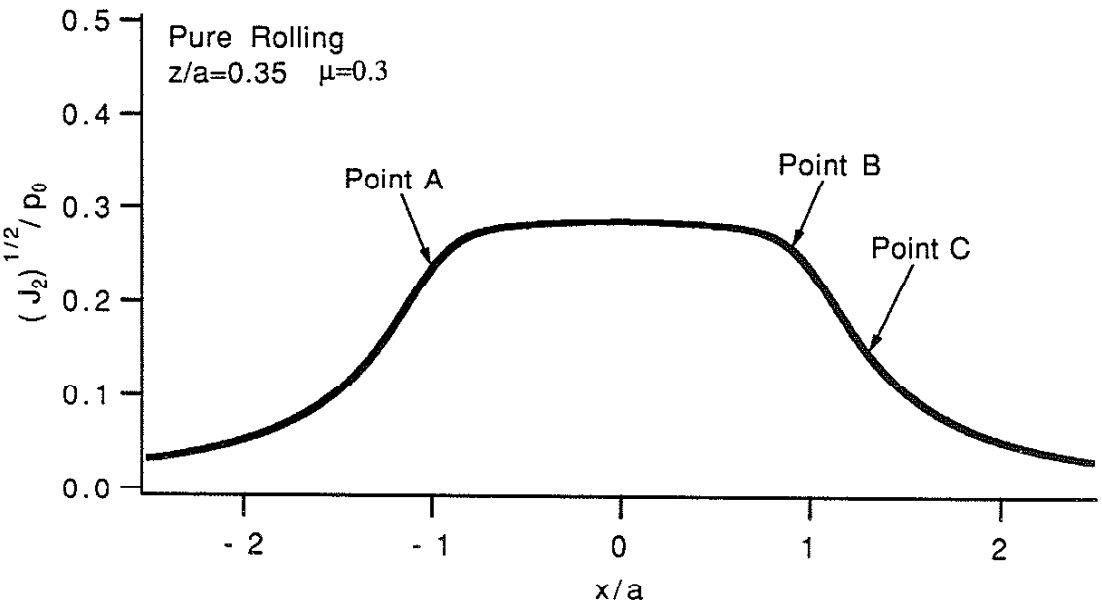

Fig.15 Variation of $(J_2)^{1/2}$ at z/a=0.35 for Pure Rolling

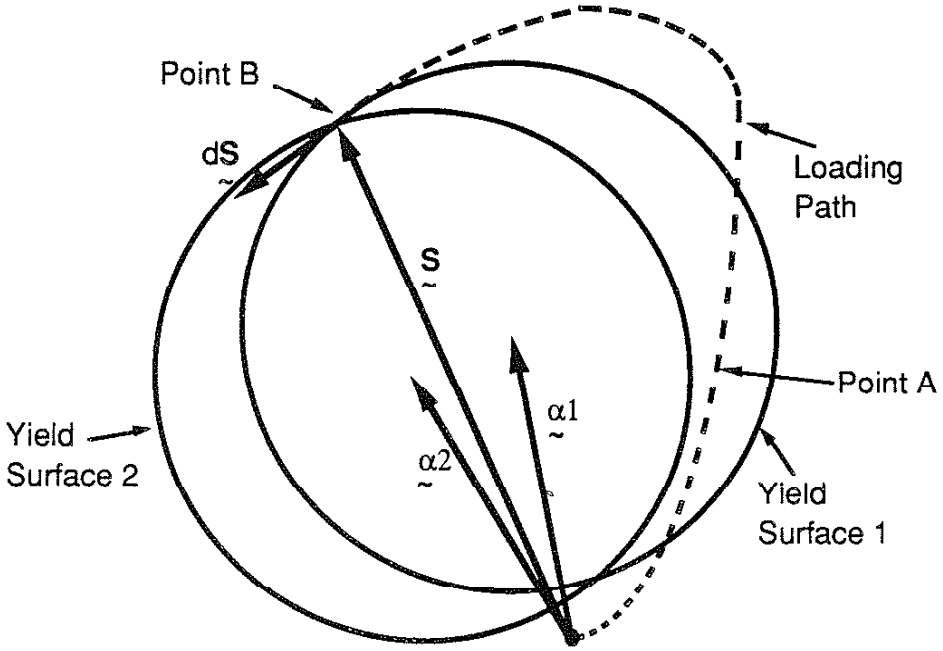

Fig.16 Schematic Illustration of the Influence of Plasticity Theories on the Material Deformation